CHEMIA

STUDIA UNIVERSITATIS BABEȘ-BOLYAI CHEMIA

S T U D I A

UNIVERSITATIS BABEŞ–BOLYAI

CHEMIA

2

CUPRINS – CONTENT – SOMMAIRE – INHALT

Professor **Ioan SILAGHI-DUMITRESCU**
(1950-2009)

We celebrate in June 2020 70 years from the birth of Professor **Ioan SILAGHI-DUMITRESCU**. Born in Botiz (Satu-Mare County) on June 1st 1950, he attended primary school in Botiz and high school in the city of Satu-Mare. He went on to receive a B. Sc. degree in Inorganic Chemistry in 1974 from the Faculty of Chemistry of the Babes-Bolyai University in Cluj-Napoca.

Between 1974 and 1977 he worked at the Intreprinderea de Ceramica Fina pentru Constructii Sanex in Cluj-Napoca, and in 1977 he joined the ranks of the Inorganic Chemistry Chair at the Faculty of Chemistry of the Babes-Bolyai University, where he also obtained a PhD degree in Chemistry in 1981. He was promoted full professor in 1994. It was in this position that he provided essential contributions to the modernization and reformation of the Faculty's curricula, including the transition to the Bologna system and promoting new disciplines of study and new lines of study – including a strong direction in theoretical and computational chemistry. He led the Inorganic Chemistry Chair (1994-2007) and then served as Dean of the Faculty from 2008 to his premature departure on December 25th 2009.

Professor Ioan Silaghi-Dumitrescu's contributions were in the area of inorganic and organometallic chemistry with transition metals and group 13-15 compounds, including cumulenic and heterocumulenic systems with heavy elements, compounds with catalytic activity, compounds with biological activity. He was among the first researchers in Romania to approach chemistry with computing techniques (computational chemistry), starting with studies on the coordination behavior of organothiophosphoric ligands and evolving towards quantum chemistry. His results on the structure of postransitional-element clusters, organometallic clusters, cumulenic and heterocumulenic systems, nanotubes and calixarenes, were reported in almost 200 articles and are found in journals among the most prestigious across the globe. The majority of his research involved establishing strategies for chemical synthesis, rationalization and prediction of properties for a wide range of inorganic, organometallic, and organic compounds, which were obtained experimentally in his own group as well as in the groups of collaborators from within Romania and from abroad.

The Center for molecular modeling and computational quantum chemistry set up by professor Ioan Silaghi-Dumitrescu in 2007 (developed from the Laboratory for structure and molecular modeling he had set up in 1996) offers an infrastructure which is internationally competitive and has allowed for the consolidation of the theoretical chemistry school in Cluj, including collaborations with high-level researchers from the USA and China.

Dr. Ioan Silaghi-Dumitrescu was a visiting professor at Universidad Nacional Autonoma (UNAM) in Mexico (1995-1996), University of Georgia, Athens, Georgia (SUA) (1-2 months per year, 2000-2008), and visiting researcher at University of Nottingham (1992), Heidelberg University (1993-1994). His collaborations spanned Universities in Toulouse, Rouen, Lille, Leipzig, Braunschweig, Koln, Budapest, Pecs, Beijing, Guanjou, Moskow (Idaho).

Professor Ioan Silaghi-Dumitrescu received the *"Gheorghe Spacu"* prize form the Romanian Academy in 1989 and the "Diploma de Onoare and G. Spacu Medal" form the Romanian Chemical Society in 2009. On March 24th 2006 he was elected corresponding member of the Romanian Academy. A scholarhip bearing his name is awarded annually to the top graduate of the Faculty of Chemistry and Chemical Engineering, and one of the largest amphitheaters at the Babes-Bolyai University is named after him.

This editorial was dedicated to the memory of Professor Ioan Silaghi-Dumitrescu, a highly respected member of the chemist's community with many professional achievements, who will be perhaps remembered not only for his pioneering work in implementing the field of computational quantum chemistry and molecular modeling at Babes-Bolyai University, Faculty of Chemistry and Chemical Engineering, but also for the generosity of his academic spirit.

Studia UBB Chemia Editorial Board

THE EFFECT OF HALOGEN SUBSTITUTION ON THE BOWL-TO-BOWL INVERSION, MOLECULAR STRUCTURE AND ELECTRONIC PROPERTIES OF SUMANENE

AKIN AZIZOGLU[a,*], DUYGU EMIR[a]

ABSTRACT. Halogen (X: F, Cl, and Br) substituted sumanene derivatives were subjected to a detailed computational study, exploring the molecular structure, bowl-depths, bowl-to-bowl inversion dynamics, and electronic properties. Hybrid density functional (DFT, B3LYP, X3LYP and PBEKCIS) theoretical calculations were performed with an array of basis sets 6-31+G(d,p) and cc-pVTZ. The bowl shaped geometry and other properties were significantly affected by the introduction of halogens (F, Cl, and Br). Especially, the bond length alternations (Δ^1 and Δ^2) in the *hub* benzene ring and *flank* benzene ring of halogenated sumanenes (2Xa, 2Xb, and 12X) show remarkable sensitivity as a function of halogen with a wide range of fluctuations (0.011 to 0.071 Å). The introduction of fluorine to sumanene influences the bowl-to-bowl inversion energies slightly. The size of halogens seems to chiefly control the bowl depth and bowl-to-bowl inversion dynamic. In contrast, the bond length alternations seem to be controlled by electronic factors and not by the size of the substituted halogen atoms. The frontier molecular orbitals (FMOs) and molecular electrostatic potentials (MEPs) were significantly affected by the introduction of halogen atoms.

Keywords: Sumanene, Halogens, Bowl-to-bowl inversion, DFT

INTRODUCTION

The polycyclic aromatic hydrocarbons (PAHs) are formed by linear fusion and two dimensional growth of benzene [1]. Chemistry of nonplanar π-conjugated carbon molecules has received considerable attention in recent years due to their unique physical, chemical and assembling features [2]. They display unique properties such as bowl-to-bowl inversion, bowl chirality, electron conductivity, and columnar packing structure in the solid state [3].

---

[a] *Balıkesir University, Faculty of Arts and Sciences, Department of Chemistry, TR-10145, Balıkesir, Türkiye*
* *Corresponding author: azizoglu@balikesir.edu.tr*

Buckybowls, also named π-bowls, are typical bowl-shaped aromatic hydrocarbons with open curved π-surface. Sumanene ($C_{22}H_{12}$, C_{3v}, Figure 1) is mainly derived from fullerene (C_{60}), composed of alternating benzenes and cyclopentadienes around the central benzene ring [1,4]. It can be defined as a piece of buckminsterfullerene with 21 carbon atoms and it poses both concave and convex π-surfaces with all vacant valences terminated by hydrogen [1,5]. Sumanene, a representative of the molecular π-bowls, has a bowl structure comprising five- and six-membered cycles. After the successful synthesis of sumanene in 2003, the interest in this compound increased and it has intensively been studied experimentally and theoretically [1-18].
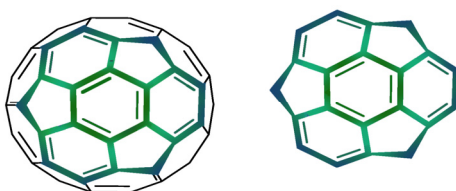
Figure 1. Fullerene (*left*) and Sumanene (*right*)

The bowl-to-bowl inversion is a distinctive character of some PAHs having π-bowl. Reported value of bowl-to-bowl inversion barrier for the sumanene is 16.9 kcal/mol employing B3LYP/cc-pVTZ//B3LYP/cc-pVDZ level of theory [6]. In the experimental works, bowl-to-bowl inversion barrier for sumanene is found to be ca. 20 kcal/mol (19.6 to 20.4 according to solvents) [7,8]. Theoretical and experimental findings suggest that sumanene is indeed rigid. Beside the bowl inversion energy barrier, it exhibited various unique properties such as columnar packing structure in the solid state [9], bowl chirality [10], electron conductivity [11], curved face-dependent stereoelectronic effect [12], and unprecedented coordination ability [13]. Among its interesting properties, Sakurai and et al. extensively studied the substituent effects on the bowl-to-bowl inversion and the correlation between the bowl structure and the bowl inversion energy by means of DFT calculation and experiments [14,15].

Sumanene also posed an appreciable challenge to synthetic chemists owing to its deep bowl depth. Many attractive properties have been studied since first successful synthesis of sumanene by Hirao and co-workers [8]. It has two different sides as concave (inside) and convex (outside) [16]. Furthermore, sumanene having three sp³ hybridized carbon atoms at the benzylic positions is representative example of π-bowls [17. These benzylic positions of sumanene can allow the functionalization of new bowl shaped structure [18]. It is an enticing key structure that was examined by researchers for syntheses of novel bowl-forms [19].

Chemists regarding the influence of hetero-substitution of PAHs have also been extended to graphenes and nanotubes; properties like magnetism and mobility [20], sensing applications [21], electronic, aromatic and optical properties [22-25] have been studied.
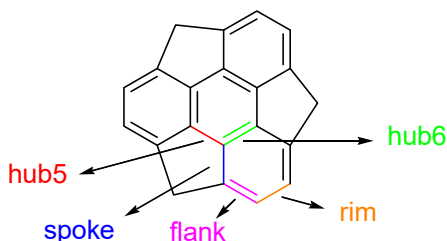
Figure 2. Different carbon bonds of sumanene

All these facts motivated us to investigate theoretically changes of essential properties of sumanene, the consequence of substitution of the aromatic and benzylic CH_2 groups with halogen atoms (F, Cl, and Br). We chose the DFT methods (B3LYP, X3LYP, and PBEKCIS) since this approach have proved to be a good solution when both accuracy and computational time are taken into account [26]. In this study, halogen (F, Cl, and Br) substituted sumanenes are considered for DFT-type calculations. Sumanene has five various C-C bonds, which include the *rim*, *flank*, *spoke*, *hub5* and *hub6*. For "*rim*" carbon atoms shown in Figure 2, three structures were obtained by replacing H with two halogen atoms (F, Cl, and Br). Other three ones were visualized by replacing H atoms of benzylic carbon atom with two halogen atoms. Last three compounds were modelled by substituting halogens (F, Cl, and Br) for all of H atoms of sumanene. The aim of the study was to get information about the selected geometric parameters, bowl depth, bowl-to-bowl inversion barriers, and electronic properties of nine sumanene derivatives by DFT treatments.

RESULTS AND DISCUSSION

After modelling the initial molecular structure of sumanene, its wide range of H atoms were replaced by fluorine, chlorine and bromine atoms, and nine different sumanene derivatives were obtained with the help of Gauss View 5.0 program. Three sumanenes were attained by substituting two halogen atoms for hydrogens at the "*rim*" carbon of sumanene (**2Fa, 2Cla, 2Bra**).

2Xa   **2Xb**   **12X**
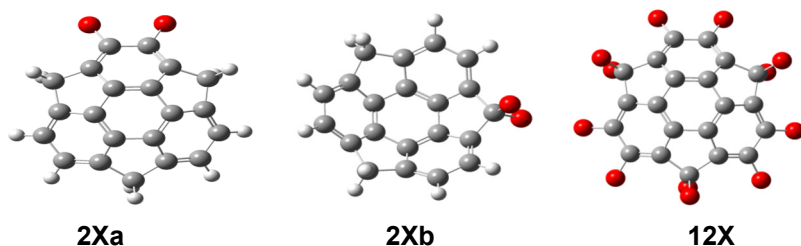
Figure 3. Halogen (**X**: F, Cl, and Br) substituted sumanene derivatives subjected to theoretical calculations (**X**: red; Carbon: grey; Hydrogen: white colour)

Moreover, three sumanenes were achived by adding two halogens atoms to benzylic carbon of sumanene (**2Fb, 2Clb, 2Brb**). Finally, all hydrogen atoms of sumanene were substituted by halogen atoms (**12F, 12Cl, 12Br**), and thus three structures were obtained (Figure 3).

In the first part of the study, geometry optimizations of fluorine (**2Fa**, **2Fb**, **12F**), chlorine (**2Cla**, **2Clb**, **12Cl**), bromine (**2Bra**, **2Brb**, **12Br**) substituted sumanenes were performed at the (restricted) B3LYP/6-31+G(d,p), B3LYP/cc-pVTZ, X3LYP/6-31+G(d,p), X3LYP/cc-pVTZ, PBEKCIS/6-31+G(d,p) and PBEKCIS/cc-pVTZ levels. Then, their geometric parameters were calculated at the corresponding level of theories. The optmized geometries are virtually identical at all DFT levels. The Δ^1 and Δ^2 terms are formulated for the bond alternation of "*hub*" and "*flank*" benzene ring of halogen substituted sumanene, respectively.

$$\Delta^1 = r_{hub5} - r_{hub6} \qquad \textbf{(1)}$$
$$\Delta^2 = r_{rim} - r_{hub6} \qquad \textbf{(2)}$$

Bond alternations in the *hub* benzene ring (Δ^1) and *flank* benzene ring (Δ^2) of halogen (**X**: F, Cl, and Br) substituted sumanenes were given in Table 1. Lowest bond alternation is exhibited for the *hub* benzene ring of **2Bra,** where the electron-donating +I effect and electron-withdrawing –M effects are weak. This is in sharp contrast to the situation in the *hub* benzene ring of **12Cl**, which exhibits significant bond alternation. These results indicate that the electronic factors are chiefly responsible for bond length alternation. The bond alternations of **12F** in *hub* six-membered ring were calculated higher than *flank* ones. Similarly, bond variations in the *hub* of six-membered ring were calculated higher than *flank* six-membered ring for chlorinated sumanene except for **2Clb**. As it had been the same for the theoretical calculations made in advance, for brominated sumanenes, bond alternation in the *hub* of six-membered ring was calculated lower than *flank* position, and it is only the opposite for **12Br**. As indicated in Table 1 that the very slight

bond alternations of the *hub* and *flan*k benzene ring happened with the substitution of sumanene benzylic positions in all cases (**2Xbs**). Besides, improving the basis set quality further to 6-31+G(d,p) does not bring in any significant changes in the geometries and bond alternations.

Table 1. Bond alternations (Å) in the *hub* benzene ring ($Δ^1$) and *flan*k benzene ring ($Δ^2$) of fluorine, chlorine, and bromine substituted sumanenes at DFT levels.

Theoretical Levels	2Fa		2Fb		12F	
	$Δ^1$	$Δ^2$	$Δ^1$	$Δ^2$	$Δ^1$	$Δ^2$
B3LYP/6-31+G(d,p)	0.045	0.047	0.048	0.055	0.059	0.056
B3LYP/cc-pVTZ	0.049	0.049	0.049	0.057	0.061	0.058
X3LYP/6-31+G(d,p)	0.044	0.047	0.048	0.055	0.058	0.056
X3LYP/cc-pVTZ	0.048	0.049	0.049	0.057	0.061	0.058
PBEKCIS/6-31+G(d,p)	0.043	0.041	0.043	0.050	0.057	0.050
PBEKCIS/cc-pVTZ	0.047	0.042	0.044	0.051	0.060	0.052
Theoretical Levels	2Cla		2Clb		12Cl	
	$Δ^1$	$Δ^2$	$Δ^1$	$Δ^2$	$Δ^1$	$Δ^2$
B3LYP/6-31+G(d,p)	0.056	0.048	0.047	0.050	0.071	0.048
B3LYP/cc-pVTZ	0.057	0.049	0.047	0.051	0.070	0.050
X3LYP/6-31+G(d,p)	0.056	0.048	0.047	0.050	0.070	0.049
X3LYP/cc-pVTZ	0.057	0.049	0.047	0.052	0.070	0.050
PBEKCIS/6-31+G(d,p)	0.055	0.042	0.042	0.044	0.071	0.043
PBEKCIS/cc-pVTZ	0.055	0.043	0.042	0.046	0.070	0.044
Theoretical Levels	2Bra		2Brb		12Br	
	$Δ^1$	$Δ^2$	$Δ^1$	$Δ^2$	$Δ^1$	$Δ^2$
B3LYP/6-31+G(d,p)	0.012	0.047	0.044	0.047	0.066	0.046
B3LYP/cc-pVTZ	0.013	0.049	0.046	0.050	0.068	0.047
X3LYP/6-31+G(d,p)	0.012	0.048	0.044	0.047	0.065	0.046
X3LYP/cc-pVTZ	0.013	0.049	0.047	0.050	0.068	0.048
PBEKCIS/6-31+G(d,p)	0.011	0.041	0.042	0.044	0.064	0.041
PBEKCIS/cc-pVTZ	0.012	0.043	0.042	0.045	0.067	0.042

In the next part of the study, bowl depth (BD), depicted in Figure 4, was estimated for only three symmetrical compounds were obtained by substituting halogens (F, Cl, and Br) with all of H atoms of sumanene at the DFT levels studied herein. Bowl depth is known as the interplanar distance between the two planes formed by the central "*hub*" atoms and the "*rim*" carbon atoms [9,27,28].

Figure 4. Bowl depth (BD)

Molecular bowl-depth of sumanene is equal to 1.11 Å in literature [13]. When examined the bowl depth values of halogenated sumanenes given in Table 2, the highest value of bowl depth for halogen substituted sumanene obtained by replacing hydrogen with fluorine atoms was calculated for **12F** compound at the PBEKCIS/6-31+G(d,p) level. **12F**s also have deeper bowl depths than the estimated value of unsubstituted sumanene (1.11Å). However, **12Cl**s and **12Br**s are slightly shallower than unsubstituted one. The lowest bowl depth was calculated to be 0.887 for **12Br** compound at the B3LYP/cc-pVTZ level. Calculated bowl depth values exhibited fluctuations according to the nature of halogen atoms.

Table 2. Bowl Depthes (BD) of twelve halogen substituted sumanene at DFT levels.

Theoretical Levels	BD (Å)		
	12F	**12Cl**	**12Br**
B3LYP/6-31+G(d,p)	1.133	0.922	0.896
B3LYP/cc-pVTZ	1.137	0.985	0.887
X3LYP/6-31+G(d,p)	1.140	0.930	0.900
X3LYP/cc-pVTZ	1.139	0.972	0.896
PBEKCIS/6-31+G(d,p)	1.142	0.987	0.926
PBEKCIS/cc-pVTZ	1.137	0.985	0.913

Then, bowl-to-bowl inversion barrier of studied molecules were estimated at the DFT levels. Bowl-to-bowl inversion activation energies ($\Delta E^{\#}$) including zero-point energy (ZPE) corrections (in kcal/mol), depicted in Figure 5, were calculated from the energy difference between the optimized bowl structure and the planar structure of sumanene as a transition state (**TS**) [2].
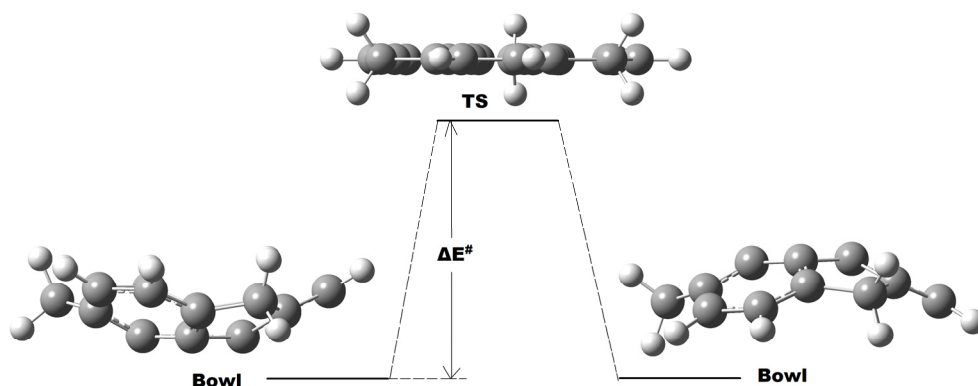
Figure 5. Schematic representation of the bow-to-bowl inversion barrier ($\Delta E^{\#}$, kcal/mol) for sumanene

All bowl-shaped compounds were structurally optimized at the beginning of the study. Then, their planar conformers for the transition states with one imaginary frequency were optimized at B3LYP/6-31+G(d,p), B3LYP/cc-pVTZ, X3LYP/6-31+G(d,p), X3LYP/cc-pVTZ, PBEKCIS/6-31+G(d,p) and PBEKCIS/cc-pVTZ levels. The normal mode corresponding to the one imaginary frequency had a direction corresponding to the bowl-to-bowl inversion process. Their IRC calculations linking planar transition structures to the bowl-shaped sumanenes were also performed to check the **TS** optimization procedures.

It can be easily understood from Table 3 that the highest bowl-to-bowl inversion energy barrier was obtained for **2Brb** as 21.3 kcal/mol at the PBEKCIS/6-31+G(d,p) level, whereas the lowest one was calculated to be 11.1 kcal/mol for **12Br** at the B3LYP/cc-pVTZ level.

Table 3. Bowl-to-bowl inversion barrier energy of fluorine, chlorine, and bromine substituted sumanene at DFT levels (ZPE included).

Theoretical Levels	$\Delta E^{\#}$ (kcal/mol)		
	2Fa	**2Fb**	**12F**
B3LYP/6-31+G(d,p)	17.3	18.7	16.6
B3LYP/cc-pVTZ	17.2	18.5	16.3
X3LYP/6-31+G(d,p)	17.5	18.9	17.1
X3LYP/cc-pVTZ	17.3	18.7	16.7
PBEKCIS/6-31+G(d,p)	18.0	19.3	16.1
PBEKCIS/cc-pVTZ	17.7	19.0	15.8
	2Cla	**2Clb**	**12Cl**
B3LYP/6-31+G(d,p)	17.9	18.6	13.7
B3LYP/cc-pVTZ	17.7	18.5	13.8
X3LYP/6-31+G(d,p)	18.1	18.8	14.1
X3LYP/cc-pVTZ	17.9	18.7	14.2
PBEKCIS/6-31+G(d,p)	18.8	19.3	14.0
PBEKCIS/cc-pVTZ	18.4	19.1	14.1
	2Bra	**2Brb**	**12Br**
B3LYP/6-31+G(d,p)	17.7	20.2	14.5
B3LYP/cc-pVTZ	17.6	18.3	11.1
X3LYP/6-31+G(d,p)	18.0	20.5	14.9
X3LYP/cc-pVTZ	17.8	18.6	11.4
PBEKCIS/6-31+G(d,p)	18.6	21.3	15.5
PBEKCIS/cc-pVTZ	18.4	19.0	11.8

Fluorinated sumanene derivatives exhibit slight changes in the bowl-to-bowl inversion energies at all DFT levels used herein. This is true for **2Cla** and **2Clb**, but the lower inversion barriers are computed for **12Cl**. It can be

also concluded in Table 3 that the slight increase of the bowl-to-bowl inversion barrier happened with the substitution of sumanene benzylic positions in all cases. However, the significant change occured with the substitution of all hydrogens of sumanene with bromine. These changes of the bowl-to-bowl inversion barrier are exclusively controlled by the size of the substituent and are independent of any electronic factors. Similar interpretations were reported by Armakovic and Sastry [7,27].

Compounds with non-linear optical (NLO) responses are of great importance as they find application in optical modulation, optical switching, optical logic, and optical memory for areas such as telecommunication, signal processing and optical interconnections [29,30]. Molecules having delocalized electrons have been observed to possess NLO properties. Hence, we have also undertaken to investigate the molecular orbitals of fully halogenated sumanenes (**12F**, **12Cl**, and **12Br**) with the help of the NBO analysis at the B3LYP/cc-pVTZ theory of level. As known that the relative orders of the highest occupied and lowest unoccupied molecular orbital (HOMO and LUMO, respectively) energies generally define conceivable qualitative indications of chemical stability, which are important criteria for developing organic semiconductor in electronic devices [31]. If the energy of HOMO is high, compounds may give electron more easily. It implies that NLO reactivity increases with rising of HOMO. The other parameter is the LUMO energy. If the E_{LUMO} value is lower, molecules may accept electrons and this result indicates that NLO reactivity of compounds increases with decreasing of E_{LUMO}. Electron mobility is important for reactivity determination. NLO activity increases with decreasing of the energy gap between frontier molecular orbitals (Δ_{gap} values). Theoretical LUMO-HOMO energy gaps also help characterize the chemical reactivity and the kinetic stability of the molecule. According to Fleming, a molecule having a small frontier orbital gap is more polarizable, and generally associated with a high chemical reactivity, low kinetic stability and also called as soft molecule [32-35]. It can be seen in Table 4 that unsubstituted sumanene has the biggest LUMO-HOMO energy gap with 7,74762 *eV*, whereas the **12Br** has the lowest one with 7,39475 *eV*. This smaller LUMO–HOMO gap means low excitation energies for many of excited states and low chemical hardness for **12Br**. The others, **12F** and **12Cl**, have 7,54197 and 7,40510 *eV* LUMO-HOMO gap values, respectively. According to E_{LUMO}, and Δ_{gap} values, **12Br** is the best one between of them in NLO activity except for the energies of HOMO. In other words, NLO activity may increase with the halogen substitution, especially bromine. Moreover, HOMO and LUMO orbitals are mainly on the double bonds, whereas HOMOs are substantially delocalized through the central benzene ring of **12F**, **12Cl**, and **12Br**. Electrons in the LUMO are also localized on the spoke, flank, and rim bonds.

Table 4. Energies of HOMO, LUMO, and Δ_{gap} (in *eV*) for **12F**, **12Cl**, and **12Br** at the B3LYP/cc-pVTZ level.

	Energies (*eV*)			
	Sumanene	**12F**	**12Cl**	**12Br**
LUMO	1.04709	-0.93907	-0.85417	-0.75403
HOMO	-6.70053	-8.48104	-8.25927	-8.14878
Δ_{gap}	7,74762	7,54197	7,40510	7,39475

The molecular electrostatic potential (MEP) map of studied molecules were calculated via electro-static potential (ESP) charges to determine their electron-deficient and electron-rich regions for nucleophlic and electrophilic attack, respectively. MEP maps, calculated at DFT B3LYP level of theory using cc-pVTZ basis set, are depicted in Figure 6.
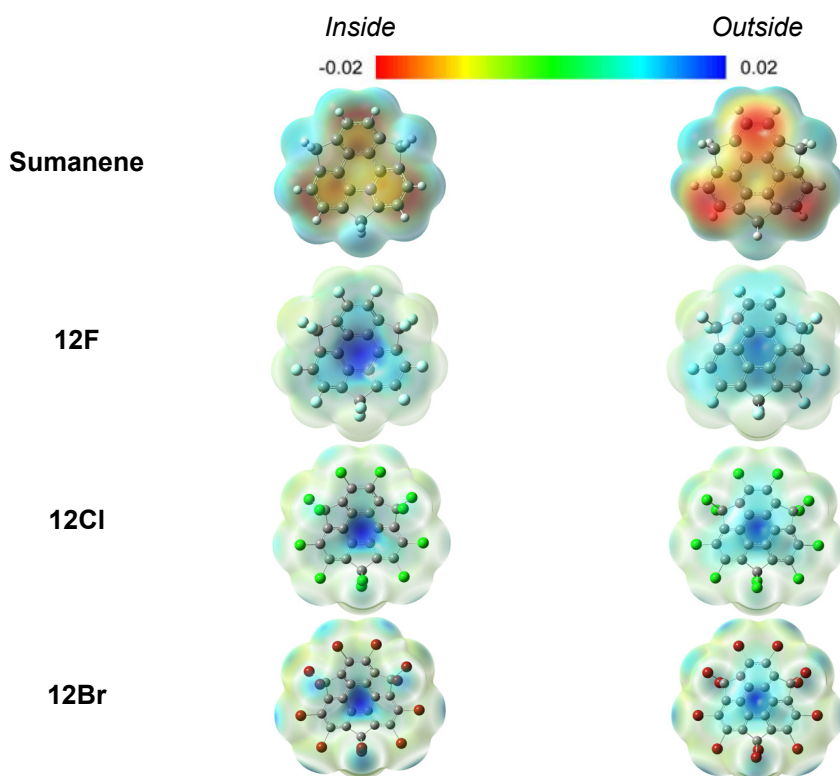
Figure 6. Molecular electrostatic potential maps of the title compounds

The negative (red colour) electrostatic potential regions of MEP were related to electrophilic reactivity and the positive (blue colour) ones to nucleophilic reactivity [36-38]. The regions with zero potential are represented in green. The electrostatic potential increases in the following order: red < orange < yellow < green < blue. The negative electrostatic potential signifies an attraction of the proton by the aggregate electron density in the compound (*shades of red*), and the positive electrostatic potential means the repulsion of the proton by the atomic nuclei (*shades of blue*).

The visualized MEP map depicts clearly that the negative electronic potential is found to be spread towards the concave and convex surface of sumanene; whereas the electronic potential is changed to neutral or even positive with the introduction of the electron-withdrawing halogen substituents. Upon substitution with halogen atoms the negative charge of the five and six membered rings is lost subsequently in the vicinity of halogens. The MEP surfaces on both faces of bowl of central benzene are nearly positive. Thus, it is confirmed that the electronic distribution of title sumanenes can be significantly affected by the presence of halogen substituents.

CONCLUSIONS

The molecular structure, bowl depth, bowl-to-bowl inversion, and electronic structure of the elusive key structural motif of halogenated sumanene are discussed using various density functional methods (B3LYP, X3LYP and PBEKCIS) with the 6-31+G(d,p) and cc-pVTZ basis sets for the first time. Sumanene derivatives were obtained by substitution of hydrogen atoms with fluorine, chlorine, and bromine atoms. The lowest bond alternation is found to be for the *hub* benzene ring of **2Bra,** where the electron-donating +I effect and electron-withdrawing –M effects are weak. However, the *hub* benzene ring of **12Cl** shows significant bond alternations. These results indicate that the electronic factors are chiefly responsible for bond length alternation of halogenated sumanenes. Moreover, improving the basis set quality further to 6-31+G(d,p) does not introduce any significant changes in the geometries and bond alternations of title molecules.

The fluorinated sumanenes (**12F**) have deeper bowl depths than unsubstituted sumanene (1.11Å), whereas the chlorinated (**12Cl**) and brominated (**12Br**) sumanenes are slightly shallower than unsubstituted one. Computed bowl depths at DFT levels exhibited fluctuations according to the nature of halogen atoms. Larger halogen atoms tend to flatten the structure and vice versa.

The lowest bowl-to-bowl inversion barrier is predicted to be 11.1 kcal/mol for **12Br** at the B3LYP/cc-pVTZ level including zero-point energy correction, whereas the highest one is calculated to be 21.3 kcal/mol for **2Brb** at the PBEKCIS/6-31+G(d,p) level. The introduction of fluorine to sumanene affect the bowl-to-bowl inversion energies slightly. Hence, the changes of the bowl-to-bowl inversion barrier are exclusively controlled by the size of the substituent and are independent of any electronic factors. The computational results indicate that halogenated sumanenes are not locked in the bowl geometry and that a bowl-to-bowl inversion could exist.

Moreover, the introduction of halogen substituents benefits the energetic stabilization of both the HOMO and LUMO. Lower values of the Δ_{gap} difference suggest a higher charge carrier mobility [39]. The π-electron-withdrawing halogens generally decrease Δ_{gap} of halogenated sumanene and these usually improve the carrier mobility of sumanene. The present theoretical results could be helpful for further studies on these interesting halogenated sumanenes.

EXPERIMENTAL SECTION

Computational details. The geometries of studied molecules were fully optimized with no symmetry constraints at the restricted B3LYP/6-31+G(d,p), B3LYP/cc-pVTZ, X3LYP/6-31+G(d,p), X3LYP/cc-pVTZ, PBEKCIS/6-31+G(d,p) and PBEKCIS/cc-pVTZ levels in the gas phase [40]. The geometries of title molecules were initially modelled by Gauss View 5.0 [41], and then the related theoretical calculations were done using the Gaussian 09W software [42]. Optimized structures were also checked using corresponding frequency calculations, which also used for calculating zero-point energy corrections (ZPE). Stationary points of outputs were defined as minima or transition structures by way of an analytic evaluation of harmonic vibrational frequencies at the level of geometry optimizations [43-46]. Moreover, the intrinsic reaction coordinates (IRCs) were pursued to prove the energy profiles relating each transition state to the correct local minima, by applying the second-order Gonzalez-Schlegel method [47].

ACKNOWLEDGMENTS

REFERENCES

1. D. Zhou; Y. Gao; B. Liu; Q. Tan; B. Xu; *Org. Lett.*, **2017**, *19*, 4628-4631.
2. T. Amaya; H. Sakane; T. Nakata; T. Hirao; *Pure Appl. Chem.*, **2010**, *82*, 969-978.
3. N. Ngamsomprasert; G. Panda; S. Higashibayashi; H. Sakurai; *J. Org. Chem.*, **2016**, *81*, 11978-11981.
4. T. Amaya; T. Hirao; *Chem. Record,* **2015**, *15*, 310-321.
5. E. Tahmasebi; Z. Biglari; E. Shakerzadeh; *Vacuum*, **2016**, *136*, 82-90.
6. U.D. Priyakumar; G.N. Sastry; *J. Phys. Chem.*, **2001**, *105*, 4488-4494.
7. S. Armaković; S.J. Armaković; J.P. Šetrajčić; I.J. Šetrajčić; *Chem. Phys. Lett.*, **2013**, *578*, 156-161
8. H. Sakurai; T. Daiko; T. Hirao; *Science*, **2003**, *301*, 1878-1878.
9. H. Sakurai; T. Daiko; H. Sakane; T. Amaya; T. Hirao; *J. Am. Chem. Soc.* **2005**, *127*, 11580−11581.
10. S. Higashibayashi; H. Sakurai; *J. Am. Chem. Soc.* **2008**, *130*, 8592−8593.
11. T. Amaya; S. Seki; T. Moriuchi; K. Nakamoto; T. Nakata; H. Sakane; A. Saeki; S. Tagawa; T. Hirao; *J. Am. Chem. Soc.* 2009, 131, 408−409.
12. S. Higashibayashi; S. Onogi; H.K. Srivastava; G.N. Sastry; Y.T. Wu; H. Sakurai; *Angew. Chem., Int. Ed.* 2013, 52, 7314−7316.
13. H. Sakane; T. Amaya; T. Moriuchi; T. Hirao; *Angew. Chem., Int. Ed.* **2009**, *48*, 1640−1643.
14. B.B. Shrestha; S. Karanjit; S. Higashibayashi; H. Sakurai; *Pure Appl. Chem.* **2014**, *86*, 747−753.
15. S. Higashibayashi; R. Tsuruoka; Y. Soujanya; U. Purushotham; G.N. Sastry; S. Seki; T. Ishikawa; S. Toyota; H. Sakurai; *Bull. Chem. Soc. Jpn.* **2012**, *85*, 450−467.
16. A. Reisi-Vanani; M. Hamadanian; S. N. Kokhdan; *Comput. Theor. Chem.*, **2016**. *1082*, 49-57.
17. T. Amaya; T. Ito; S. Katoh; T. Hirao; *Tetrahedron*, **2015**, *71*, 5906-5909.
18. S. Armaković; S.J. Armaković; J.P. Šetrajčić; *Int. J. Hydrog. Energy*, **2013**, *38*, 12190-12198.
19. A. Reisi-Vanani; S. Bahramian; *Comput. Theor. Chem.*, **2016**, *1093*, 40-47.
20. Y. Ma; A.S. Foster; A.V. Krasheninnikov; R.M. Nieminen; *Physical Review B*, **2005**, *72*, 205416.
21. K.P. Prathish; M.M. Barsan; D. Geng; X. Sun; C.M.A. Brett; *Electrochimica Acta*, **2013**, *114*, 533.
22. P. Nath; S. Chowdhury; D. Sanyal; D. Jana; *Carbon*, **2014**, *73*, 275.
23. M. Medeleanua; R. Pop; M. Andoni; *STUDIA UBB CHEMIA*, **2017**, *62(4)*, 105-119.
24. S. Armaković; S.J. Armaković; J.P. Šetrajčić; V. Holodkov; *J. Mol. Model.*, **2014**, *20*, 2538-2551.
25. X. Chen; F.-Q. Bai; Y. Tang; H.-X. Zhang; *J. Comput. Chem.*, **2016**, *37*, 813–824.
26. A. Karton; *J. Comput. Chem.*, **2016**, *38*, 370-382.

27. U.D. Priyakumar; G.N. Sastry; *J. Org. Chem.*, **2001**, *66*, 6523-6530.
28. Y. Sun; X. Hou; Chinese Chem. Lett., **2016**, *27*, 1166-1174.
29. V.M. Geskin; C. Lambert; J.L.Bredas; *J. Am. Chem. Soc.*, **2003**, *125*, 5651-15658.
30. D. Sajan; H. Joe; V.S. Jayakumar; J. Zaleski; *J. Mol. Str.*, **2006**, *785*, 43-53.
31. A. Rockett; Organic Semiconductors, in *The Materials Science of Semiconductors*, A. Rockett, Ed.; Springer, Boston, MA, **2008**, pp 395-453.
32. I. Fleming, "Frontier Orbitals and Org. Chemical Reactions", Wiley, London, **1976**.
33. Y. Tian; W. Chen; Z. Zhao; L. Xu; B. Tong; *J. Mol. Model.,* **2020**, *26*, 67.
34. L. Găină, I. Torje, E. Gal, A. Lupan, C. Bischin, R. Silaghi-Dumitrescu, G. Damian, P. Lönnecke, C. Cristea, L. Silaghi-Dumitrescu; *Dyes Pigments*, **2014**, *102*, 315.
35. A. Azizoglu; *Struct. Chem.*, **2003**, *14*, 575-580.
36. Z. Ozer, T. Kilic, S. Carikci, A. Azizoglu; *Russ. J. Phys. Chem. A*, **2019**, *93*, 2703–2709.
37. C.B. Yildiz; Z.O. Sagir; T. Kilic; A. Azizoglu; *STUDIA UBB CHEMIA*, **2014**, 59(2), 17-32.
38. S. Gosav; N. Paduraru; D. Maftei; M.L. Birsa; M. Praisler; *Spectrochim. Acta A*, **2017**, *172*, 115-125.
39. H. Unlu, *Solid State Electron*, **1992**, *35*,1343-1352.
40. D.C. Young; *Computational Chemistry*. New York, John Wiley & Sons Inc., **2001**, pp. 19-92.
41. R. Dennington; T. Keith; J. Millam; *GaussView*, **2009**, Version 5, Semichem Inc., Shawnee Mission KS.
42. M.J. Frisch; G.W. Trucks; H.B. Schlegel; G.E. Scuseria; M.A. Robb; J.R. Cheeseman; G. Scalmani; V. Barone; B. Mennucci; G.A. Petersson; H. Nakatsuji; M. Caricato; X. Li; H.P. Hratchian; A.F. Izmaylov; J. Bloino; G. Zheng; J.L. Sonnenberg; M. Hada; M. Ehara; K. Toyota; R. Fukuda; J. Hasegawa; M. Ishida; T. Nakajima; Y. Honda; O. Kitao; H. Nakai; T. Vreven; J.A. Montgomery Jr.; J.E. Peralta; F. Ogliaro; M. Bearpark; J.J. Heyd; E. Brothers; K.N. Kudin; V.N. Staroverov; R. Kobayashi; J. Normand; K. Raghavachari; A. Rendell; J.C. Burant; S.S. Iyengar; J. Tomasi; M. Cossi; N. Rega; J.M. Millam; M. Klene; J.E. Knox; J.B. Cross; V. Bakken; C. Adamo; J. Jaramillo; R. Gomperts; R.E. Stratmann; O. Yazyev; A.J. Austin; R. Cammi; C. Pomelli; J.W. Ochterski; R.L. Martin; K. Morokuma; V.G. Zakrzewski; G.A. Voth; P. Salvador; J.J. Dannenberg; S. Dapprich; A.D. Daniels; Ö. Farkas; J.B. Foresman; J.V. Ortiz; J. Cioslowski; D.J. Fox; *Gaussian 09*, revision *D.01*; Gaussian, Inc.: Wallingford, CT, 2009.
43. I.-T. Moraru, G. Nemes, *STUDIA UBB CHEMIA*, **2019**, *64(2)*, 435-446.
44. A.A. Attia; R.S. -Dumitrescu; *Int. J. Quant. Chem.*, **2014**, *114*, 652-665.
45. N. Azizoglu; M. Alkan; Ö. Geban; *J. Chem. Educ.*, **2006**, *83*, 947-953.
46. A. Azizoglu; R. Ozen; T. Hokelek; M. Balci; *J. Org. Chem.*, **2004**, *69*, 1202-1206.
47. C. Gonzalez; H.B. Schlegel; *J. Phys. Chem.*, **1990**, *94*, 5523-5527.

MODELLING OF THE SUGAR BEET PULP DRYING PROCESS

ADINA GHIRIŞAN[a], SIMION DRĂGAN[a], CONSTANTIN COŢA[b], ELENA-MIHAELA NAGY[b], GYORGY ZOLTAN[b], VASILE MICLĂUŞ[a]*

ABSTRACT. The paper presents the drying model proposed for sugar beet pulp in the presence of hydrated lime within a range temperature of 333 and 368 K. The experimental results were used to identify the coefficients in the two-term exponential model, choose as the most appropriated model for our case. The relationships for the variation of the coefficients with temperature were determined. The equations of the mathematical model were used to establish the optimal drying time.

Keywords: sugar beet pulp, drying kinetics, drying rate, mathematical modeling

INTRODUCTION

The sugar beet pulp represents the fibrous material which results as a by-product in the sugar manufacturing process. It is a macromolecular product of the sugar beet cellular membrane made of protopectin, with a high content of proteins, vitamins and minerals, essential elements for the health of animals [1].

The presence of the sugar beet pulp in the feed of ruminants leads to positive effects as: the substitution of grains for lactating dairy cattle, the increase of milk production and fat content, the reduction of pollutants (CO_2, CH_4) during digestion, the improving of metabolic health of animals, etc. [2-9].

The efficiency of the sugar beet pulp in animal feed can be substantially improved by the addition of macro and microelements (Ca^{2+}, Mg^{2+} PO_4^{3-}), respectively (Co^{2+}, Zn^{2+}, Mn^{2+}), the additional administration of Ca^{2+} leading to easy assimilable compounds. In this context the addition of Ca^{2+} in the

---

[a] *Babeş-Bolyai University, Faculty of Chemistry and Chemical Engineering, 11 Arany Janos str., RO-400028, Cluj-Napoca, Romania*
[b] *Institutul Naţional de Cercetare - Dezvoltare Pentru Maşini şi Instalaţii Destinate Agriculturii şi Industriei Alimentare, Sucursala Cluj-Napoca, Str. Al. Vaida-Voievod, Nr. 59, RO-400458, Romania*
* *Corresponding author miclausv@yahoo.com*

form of hydrated lime $Ca(OH)_2$ in the sugar beet pulp subjected to drying leads to the formation of organo-mineral complexes in which the assimilation is superior to that of carbonates [10].

These products with high perishable cannot be stored for longer periods of time. So, their processing is required in order to ensure the properties maintenance. Drying of the sugar beet pulp, as the most common form of preservation, is imposed too, by the seasonal functioning character of the sugar factories, when it results in large quantities that cannot be used in full [11].

In the literature, different mathematical models are proposed, in order to fit the experimental measurements (see Table 1).

Table 1. Thin layer drying models [12, 13]

Model name	Model equation	References
Exponential model	$MR = \exp(-kt)$	El-Beltagy et al. (2007)
Generalized exponential model	$MR = A\exp(-kt)$	Shittu and Raji (2008)
Logarithmic model	$MR = a\exp(-kt)+c$	Akpinar and Bicer (2008)
Page's model	$MR = \exp(-kt^n)$	Singh et al. (2008)
Midilli–Kucuk model	$MR = a\exp(-kt^n)+bt$	Midilli and Kucuk (2003)
Parabolic model	$MR = a+bt+ct^2$	Doymaz (2010)
Two-term exponential	$MR = A_1 e^{K_1 t} + A_2 e^{K_2 t}$	Henderson (1974)

In the present work, a mathematical model was developed based on the drying kinetic data of sugar beet pulp, considering the influence of drying temperature and the addition of hydrated lime. The proposed model allows the calculation of the drying time, in order to reach a certain moisture content that will allow the storage without alteration.

RESULTS AND DISCUSSION

Solving the main engineering problems of the drying process, choosing and sizing the dryer, automation, optimization and computerized management, implies to know the mathematical model after which it is carried out. There are two methods to establish the model that show the evolution in time of a physical or chemical process:
- Theoretical modelling, which assumes that the kinetic equation of the studied phenomenon is known;
- Empirical modelling that involves experimental measurements of the rates, the numerical values obtained being subsequently correlated in a kinetic equation.

The large number of parameters that influence the drying, as well as the large number of phenomena that occur during the drying process (internal and external diffusion of water vapours, thermal transfer from the drying agent to the material or through the crust of solid material, mass transformation processes, water evaporation, desorption, etc.) makes theoretical modelling difficult to access.

Modelling of drying process can be carried out not only after simple models but also after a combined model, when two or even three elementary processes have the rates of the same order of magnitude [14]. Therefore, in the case of solids drying, empirical modelling is required. These models implied experimental measurements in conditions as close to those to be used in industrial practice [15-19].

The experimental values of the moisture content M_t, calculated by Equation 1, are processed first as a function of time in the form of drying curves (Figure 1).

$$M_t = \frac{m_i - m_t}{m} = \frac{m_i(X_i - X_t)}{m_i(1 - X_i)} = \frac{X_i - X_i \cdot \eta}{1 - X_i} \qquad (1)$$

where: M_t is the moisture content at any drying time (Kg water/Kg dry material); m_i – the initial mass of the sample (Kg); m_t – the mass of sample at any time t (Kg); m - the mass of the dry material (Kg); η - degree of moisture removal; X_i - the fraction of the initial water content; X_t - the fraction of the water content at any drying time.

In Figure 1, the influence of the temperature on the drying was performed comparatively for the raw sugar beet pulp (P1) and the sugar beet pulp with the addition of $Ca(OH)_2$ (P2).

The analysis of the drying curves shows that the drying occurs during the falling-rate period for both cases, the diffusion of the moisture from inside to the surface of material being the limitative process.

The drying results show the strong influence of the temperature on the time required for the total remove of the moisture, Table 2.

Table 2. The time required for the total removal of the moisture

Sample Temperature, [K]	Time, s			
	333	343	358	368
P1	5500	4500	3360	2400
P2	3800	2250	1700	1650
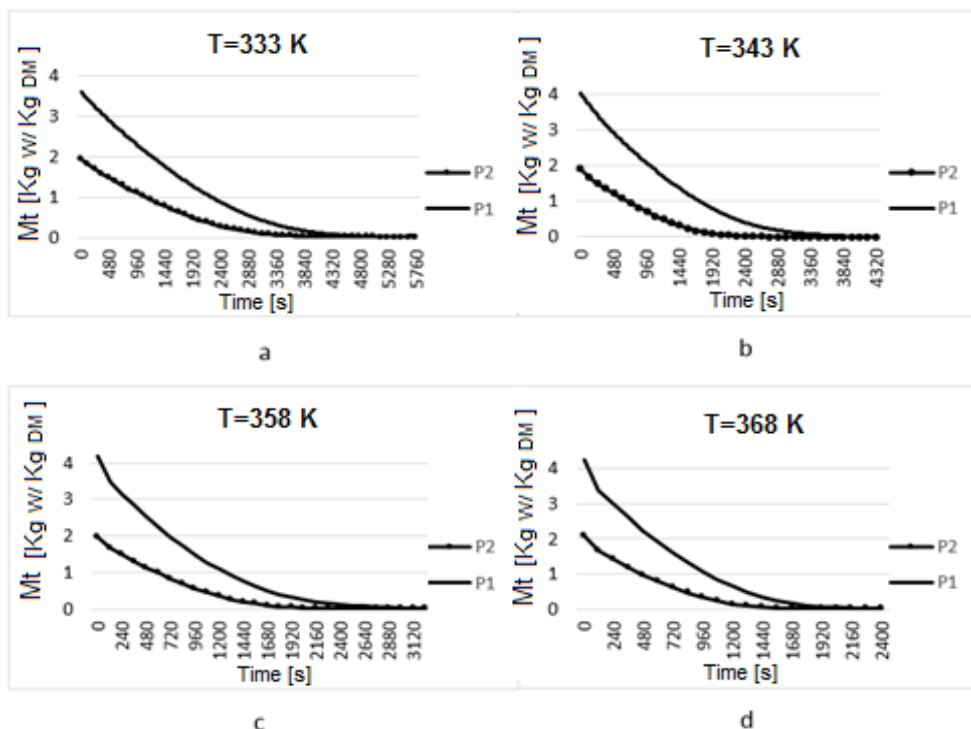
Figure 1. Evolution of moisture content in time at temperatures of:
a)T=333 K; b) T= 343 K; c) T=358 K; d) T=368 K

The curves from Figure 1 show too, the positive influence the addition of $Ca(OH)_2$ on the time required for the total removal of moisture. At each thermal regime, for samples with the addition of $Ca(OH)_2$, the total removal time is reduced with 30-40%.

The validation of the mathematical model implies the identification of the coefficients. For the two-term exponential model, used in the present analysis, the numerical values of the K and A coefficients obtained by the mathematical processing of the experimental are presented in Table 3.

The values of A and K coefficients increase with temperature, in both cases for sample P1 and for P2.

The evolution of the drying rate over the time determined with the experimental data using the finite difference method, and those obtained by the equation of the mathematical model are shown in Figure 2.

The drying rate was calculated as follows:

$$r = \frac{M_t - M_{t+dt}}{dt} \qquad (2)$$

where: r is the drying rate (Kg water/Kg dry material.m^2.h), M_t is the moisture content at time t (Kg water/Kg dry material); M_{t+dt} - the moisture content at t+dt (Kg water/ Kg dry material); and t - time (h).

Table 3. The numerical values of the coefficients for two-term exponential model

Coefficient	T [K] Sample	333	343	358	368
K_1	P1	0.985	1.770	2.900	3.705
	P2	1.250	2.330	3.020	4.030
K_2	P1	3.750	6.150	6.470	12.390
	P2	5.510	9.790	10.710	16.370
A_1	P1	6.780	7.270	7.650	7.910
	P2	6.330	6.820	7.040	7.350
A_2	P1	9.390	9.940	9.123	11.090
	P2	9.020	10.030	9.770	10.820
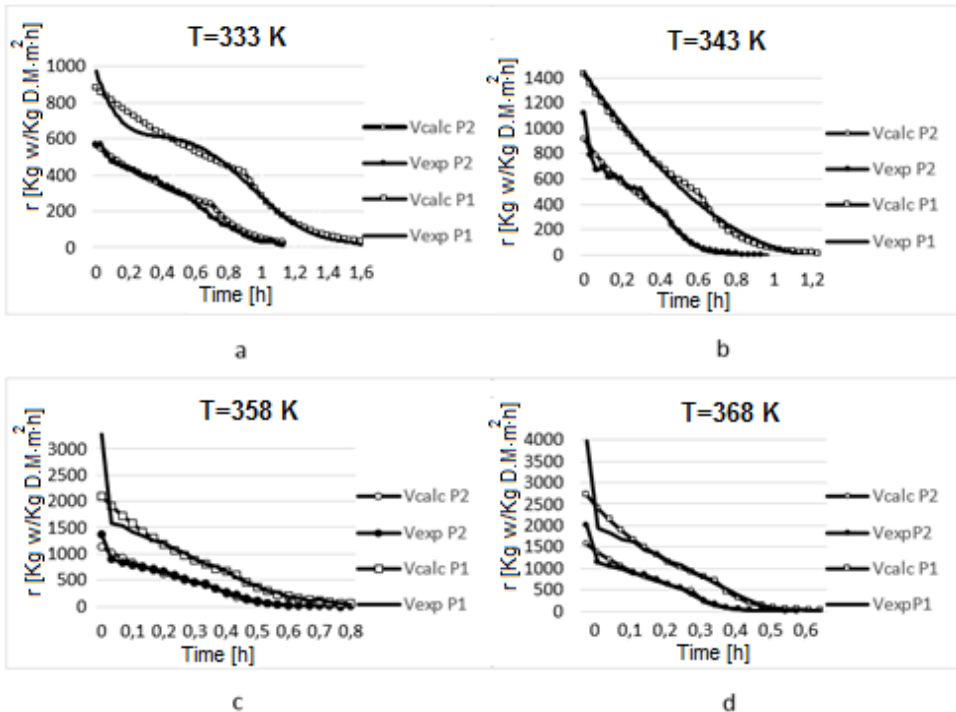
Figure 2. The comparative values of the drying rate resulted from experimental measurements with those calculated by the proposed model

Validation of the proposed mathematical model by means of the numerical values of the K and A coefficients, has shown that the drying rate determined experimentally does not agree with the one calculated with the proposed equation, during the entire process. Thus, at degrees of moisture removal greater than 90% (+/-1.5%) it is observed that takes place the modification of the mechanism, during the remove of the moisture. There are two areas:

- a) first area corresponds to the time interval until the elimination of approx. 90% (+/-1.5%) of the total moisture content of the material. This drying period is carried out at a rate corresponding to the values K_1 and A_1 from the proposed mathematical model. The duration of this period is t_1;

- b) second area corresponds to the elimination of the rest of approx. 10% of the total moisture of the material. This area is characterized by the numerical values K_2 and A_2 of the proposed mathematical model and corresponds to the duration of development t_2. The time required to eliminate the total moisture is obtained by summing the time for the two areas: $t_t = t_1 + t_2$.

Comparing the experimental measurements results of the drying rate with those calculated on the basis of the mathematical model (Figure 2) it was found a good agreement in the temperature range 343-368 K. At the temperature of 333 K there are deviations that correspond to a certain moisture content of the sugar beet pulp. This deviation is determined by the more complex mechanism of the drying process, mainly determined by the complex porous structure of the sugar beet pulp.

At low temperatures, the cell walls membranes are less destroyed in time. That determines the existence of pores of different sizes in which the water is retained with different forces, hence the different drying rate. At temperatures higher than 333 K, at samples with lime addition, macro-pores are formed from the first moments of the process, which causes the elimination of water to be done by simpler mechanisms.

Determining the time required for drying at temperatures other than those at which experimental measurements have been made requires establishing the temperature dependence of the K coefficients of the mathematical model. The mathematical processing of the numerical values in Table 3 leads to the equations presented in Table 4.

Table 4. The equations for the coefficients K depending on the temperature range

Sample	Equations for the coefficient K calculation	
	Validity range η=0-0.9	Validity range η=0.9-1
P1	$K_{11}=0.85+0.0816*\Delta T$	$K_{12}=3.75+0.247*\Delta T$
P2	$K_{21}=1.25+0.0794*\Delta T$	$K_{22}=5.51+0.310*\Delta T$

where: $\Delta T = T_i - 333$

T= temperature in the range 333-368 K.

By combining Equation (1) with Equation of drying rate (2), as well as with those which reproduce the variation of the coefficients with the temperature (Table 4), one can obtain the relationships which allow the determination of the drying time for temperatures other than those for which were performed experimentally (Equations 3 and 4).

$$\frac{X_i - X_t \cdot \eta}{1 - X_t} = 7,11 \cdot e^{-(0,85 + 0,0816 \cdot \Delta T)} + 9,49 \cdot e^{-(3,75 + 0,247 \cdot \Delta T)} \tag{3}$$

$$\frac{X_i - X_t \cdot \eta}{1 - X_t} = 6,88 \cdot e^{-(1,25 + 0,0794 \cdot \Delta T)} + 9,61 \cdot e^{-(5,51 + 0,31 \cdot \Delta T)} \tag{4}$$

CONCLUSIONS

The study of the sugar beet pulp drying has shown that the addition of $Ca(OH)_2$ leads to the breakdown of the cell walls of the sugar beet pulp which caused the acceleration of the process.

The mathematical models for the drying of raw sugar beet pulp and in the presence of lime were developed.

From the experimental measurements data, the coefficients K_1 and K_2 used in the proposed model equations were calculated.

The numerical values of the K coefficients allow to establishing their variation equations with the temperature, and forward to apply the developed equation in the case of other process temperatures.

The equations established for the drying time calculation necessary to remove a certain amount of moisture are presented.

EXPERIMENTAL SECTION

The experiments were performed using industrial sugar beet pulp resulting from the TEREOS-Ludus sugar factory, Romania.

The source for Ca^{2+} ions was hydrated lime $Ca(OH)_2$ obtained in laboratory by hydrating the industrial lime used in sugar factories.

The experimental study of drying was carried out with an AXIS-100 moisture analyzer with natural convection and maximum capacity of 100 g at the weighing accuracy of 0.01%. The heat contribution required for the evaporation of water is achieved by means of two halogen lamps with which the moisture analyzer is provided. The moisture analyzer is provided too, with an automatic temperature control system and the software for automatically measuring of the sample mass in time. Its software allows the collection and storage of measured values on the PC connected to the moisture analyzer.

The sample P1 contained 18.7% dried organic substances. The sample P2 contained 30% of CaO, reported to the dried material.

ACKNOWLEDGMENTS

REFERENCES

1. M. Asadi; *Sugar Beet Handbook*, *John Wiley&Sons Inc*., Hoboken, New Jersey, **2006**.
2. E. Evans; U. Messerschmidt; *J. Anim, Sci. Biotechnol.*, **2017**, *8,* 1-10.
3. C. Ibáñez; M.C. López; P. Criscioni; C. Fernández; *Anim. Prod. Sci.*, **2015**, *55(1),* 56-63.
4. M. Münnich; F. Klevenhusen; Q. Zebeli; *J. Sci. Food and Agric.*, **2018**, 98(3), 991-997.
5. M. Münnich; R. Khiaosaard; F. Klevenhusen; A. Hilpold; Q. Zebeli; *Anim. Feed Sci. Tech.*, **2017**, *224*, 78-89.
6. A.P.A. Monteiro; J.K. Bernard; J.R. Guo; X.S. Weng; S. Emanuele; R. Davis; G.E. Dahl; S. Tao; *J. Dairy Sci.*, **2017**, *100(2)*, 1063-1069.
7. A. Jokić; Z. Zavargo; N. Lukić; B. Ikonić; J. Marković; J. Dodić; J. Grahovac; *J. on Process and Energy in Agri.,* **2013**, *17(1)*, 24-30.
8. L. Mogensen; T. Kristensen; *Acta. Agric. Scand. (A),* **2003**, *53*, 86–96.
9. P. Melendez, P.J Pinedo; *J. Appl. Anim. Res.*, **2015**, *43(3),* 261–265.
10. E.M. Nagy; C. Coţa; N. Cioica; Z. Gyorgy; T. Deac; *Proceedings* INMATEH-AGRICULTURAL ENGINEERING *Conferences*, **2019**, *112*, 03023.
11. L. Yang; Z. Hu; L. Yang; S. Xie; M. Yang; *INMATEH - Agricultural Engineering*, **2018**, *55(2)*, 53-62.
12. T.Y. Tende-Akintunde; G.O. Ogunlakin; *J. Food Sci. Technol.*, **2013**, *50(4)*, 705-713.
13. A. Ghirisan; S. Dragan; C. Cota; E.M. Nagy: V. Miclaus; *Studia UBB Chemia*, **2018**, *63(2)*, 53-62.
14. E.K. Akpinar; S. Toraman; *Heat Mass Trans.,* **2015**, *8(2),* 110-123.
15. I. Doymaz, *Energy Conv. and Manag.,* **2012**, *56*, 199-205.
16. D.G. Overhults; H.E. White; H.E. Hamilton; I.J. Ross; *Trans. of ASAE,* **1973**, *16*, 112-113.
17. S.M. Henderson; *Trans. of ASAE,* **1974**, *17,* 1167-1172.
18. E.K. Akpinar; *J. Food Eng.*, **2006**, *73(1),* 75-84.
19. A. Ghirisan; S. Dragan; *Studia UBB Chemia*, **2013**, LVIII(2), 35-42.

MODELLING AND SIMULATION OF
METHANOL PRODUCTION FROM COKE OVEN GAS

LETITIA PETRESCU[a]*, DUMITRITA-AURA CRISAN [a]

ABSTRACT. Coke Oven Gas (COG) is highly rated as a valuable by-product of coke production used in the steel industry. The production of methanol from COG-derived syngas has been investigated in the last period due to its practicality as well as to the recent interest in methanol over the past years. Two case studies, using COG and CO_2 as raw-materials, are simulated and compared in the present study. In the first case the intermediate step is the dry methane reforming (DMR) while in the second case the intermediate step is steam methane reforming (SMR). The syngas obtained is furthermore converted to methanol. Beside the transformation of COG into methanol, the present study deals also with the CO_2 emissions reduction, the CO_2 generated in the COG combustion is captured using amine based gas-liquid absorption technology (e.g. methyl diethanolamine - MDEA)). ChemCAD process flow-modelling software was used as a tool to produce 250 t/day of methanol with purities higher than 99%. The results showed that the most advantageous technological route of COG and CO_2 utilization is DMR, in which, a lower quantity of raw material (COG) and lower number of equipment is required to obtain the same amount of final product.

Keywords: *Coke Oven Gas, Process Modelling and Simulation, Methanol production, Technical evaluation.*

INTRODUCTION

Methanol is an important raw material synthetized in large quantities in the chemical industry. It is an important material in the production of various chemical solvents, antifreeze and fuels. One of the most common uses of methanol is in the formaldehyde production. Formaldehyde is further used in the production of plastics, including those for construction, car paints, explosives or as a preservative for organisms in biological laboratories. Other

---

[a] *Department of Chemical Engineering Babeş-Bolyai University, Faculty of Chemistry and Chemical Engineering, 11 Arany Janos str., RO-400028, Cluj-Napoca, Romania*
* Corresponding author letitiapetrescu@chem.ubbcluj.ro

substances using methanol as a raw material / intermediate are: acetic acid, methyl tert-butyl ether (MTBE), dimethyl ether (DME), methylamine, dimethyl carbonate (DMC), chloromethane. Besides its applications in the chemical and power industry, methanol attracted attention through its potential for use in the automotive industry, where it can be used as a fuel or it can lead to other fuels generation (i.e. biodiesel). Storing energy in the form of methanol could put an end to fossil fuel dependence, transforming carbon dioxide into a raw material for an economy based on methanol. This status is expected to last in the near future or even to improve it in order to transform it in a central participant in the worldwide economic landscape [1]. For these reasons, every improvement to methanol production process, in terms of energy savings, optimization, and minimization of its environmental impact has potential to promote relevant economic progress.

Coke oven gas (COG), a by-product of the coking process, can be used in effectively reducing the CO_2 emissions caused by the steel industry. The production of methanol from COG-derived syngas has been investigated in the last period due to its practicality to obtain a liquid fuel instead of a gaseous product as well as to the recent interest in methanol over the past years [2]. The CO_2 emissions reduction in the steel industry can also be performed through transforming COG into valuable products such as synthesis gas, hydrogen or methanol [3]. The process to transform COG to methanol is quite complex. The COG has a complex composition at the exit of the coke oven. It suffers several transformations in order to be converted into synthesis gas and furthermore to methanol. Firstly, the COG is cooled to remove pitch, which may form deposits on the gas lines, and then the NH_3, H_2S, benzene, toluene and xylene are removed from the COG. Chemically speaking COG has the following composition: H_2 55 - 60%; CH_4 23 - 27%; CO 5 - 8%; N_2 3 - 6%; CO_2 2%. Traces of other hydrocarbons can also be present in the COG. The high calorific value of COG (e.g. 17 - 18 MJ/m^3) is due to the substances from its composition: H_2, CH_4, CO, C_2H_6.

Dry methane reforming (DMR) is a technology that converts two stable molecules, CH_4 and CO_2, into syngas. The process occurs at 700 – 900°C, at one atmosphere pressure or lower, using Ni, Rh and Ru catalysts. It is considered to be an effective method for methanol synthesis, due to the possibility of obtaining an optimal H_2/CO ratio in a single step, as long as the reaction takes place under stoichiometric conditions of CH_4 and CO_2. In addition, the process involves partial recycling of CO_2, half of the carbon dioxide produced by the system being recycled. COG–DMR is investigated as a first option in the present study [4].

The most common way of obtaining methanol is through methane steam reforming (SMR). In the present study, the methane used for methanol generation comes from COG produced in a steel plant, so COG-SMR is

considered as a second option. The conversion of COG into synthetic natural gas (SNG) is an efficient method to supply the high demand for natural gas on the market. The natural gas is a non-renewable energy source with a heat capacity between 20.1 and 38.26 MJ/m^3 and it is not accessible in the long term. The SNG can be used in the chemical, energetic and transportation industries. Compared to the equivalent coal mass, the natural gas use reduces carbon dioxide emissions by approximately 40%. COG is too rich in hydrogen to be used in the methanation reaction for producing SNG. The $(H_2-CO_2)/(CO+CO_2)$ ratio in the COG is between 5 and 6, the optimum value for the methanation being approximately 3 a high quantity of hydrogen remaining unconverted. The various studies on the technologies where an additional carbon source is needed revealed that, the use of an internal carbon source, produced within the system, instead of using an external gas source, can be a convenient solution to solve this problem. A considerable amount of carbon dioxide results from the combustion of coke oven gas for heat generation. This carbon dioxide is separated and reintroduced into the process using the gas-liquid absorption (e.g. MDEA) [5]. The SNG obtained is further used in the methanol production process, using syngas as an intermediary product.

As already mentioned, two different methods of obtaining methanol are presented and compared in the present work (see Figure 1):

- DRM using COG and CO_2 as raw materials and
- SMR, with SNG as a raw material for SMR. SNG is obtained through COG methanation and CO_2 recycling.
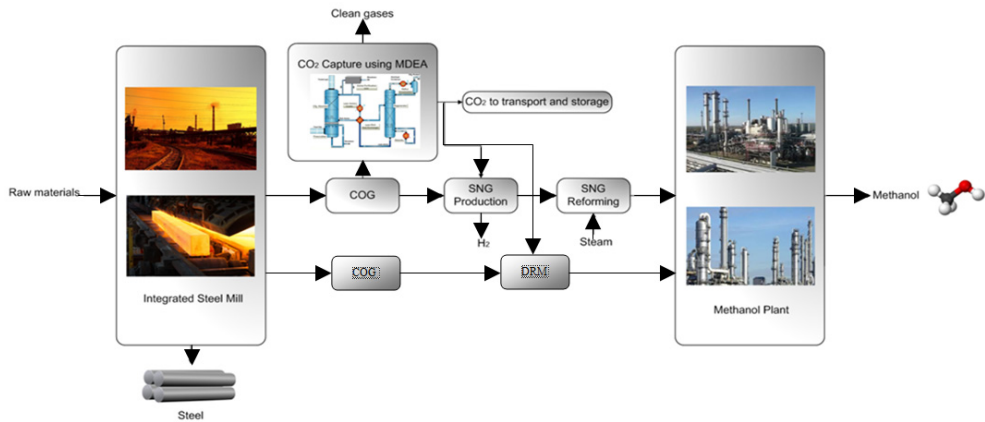
Figure 1. Methanol production from COG

The novelty of the present work consists on the technological comparison of the above mentioned technologies for methanol synthesis using COG and CO_2 as raw-materials.

RESULTS AND DISCUSSION

The cases investigated in the present work with their correspondent sub-processes are presented in Table 1.

Table 1. Cases investigated and their correspondent sub-processes

Case Name	Sub-process considered
Case A	COG combustion
	CO_2 capture using amine based gas-liquid absorption (i.e. MDEA)
	DMR for syngas generation
	Methanol synthesis from syngas
Case B	COG combustion
	CO_2 capture using amine based gas-liquid absorption (i.e. MDEA)
	SNG production
	SMR of SNG for syngas generation
	Methanol synthesis from syngas

A schematic representation of the two cases under study is illustrated in Figure 2 and Figure 3 under EXPERIMENTAL SECTION.
The main streams for *Case A* are reported in Table 2.

Table 2. Main inputs and outputs for syngas production (*Case A*)

Parameters	Unit of measure	Streams			
		COG	CO_2 from CO_2 capture unit	Before DRM	After DRM
Pressure	atm	0.98	0.98	0.98	0.98
Temperature	ºC	25	35	980	1000
Vapour fraction	-	1	1	1	1
Liquid fraction	-	0	0	0	0
Component mole flow-rate					
Carbon Monoxide	kmol/h	53.95	0.00	32.46	327.55
Hydrogen		535.94	0.00	324.60	613.00
Carbon dioxide		27.25	133.77	150.28	1.07
Water		0.00	0.06	0.06	3.41
Nitrogen		45.41	0.38	27.89	27.89
Methane		245.46	0.00	148.54	2.66
Methanol		0.00	0.00	0	0.00
Total flow-rate	kmol/h	907.82	134.23	683.83	975.58
Total flow-rate	kg/h	8997.99	5899.79	11343.09	11343.09

As noticed from Table 2, starting from 907.82 kmol/h of COG and 134.23 kmol/h of CO_2 captured a molar flow-rate of 975.58 kmol/h gaseous stream is obtained in the DRM. The DMR stream has a high content of hydrogen (e.g. 613.00 kmol/h) and CO (e.g. 327.55 kmol/h). Small traces of N_2, CO_2, CH_4 and CO_2 can be also found in the outlet of DMR. This stream is furthermore sent to methanol synthesis step. The main inputs and outputs streams for methanol production using DRM as intermediary step are presented in Table 3.

Table 3. Main inputs and outputs for methanol production (*Case A*)

Parameters	Unit of measure	Streams			
		After DRM	Before methanol synthesis	After methanol synthesis	Main product
Pressure	atm	0.98	107.08	106.1	0.98
Temperature	°C	1000	267	267	64.00
Vapour fraction	-	1	1	1	1
Liquid fraction	-	0	0	0	0
Component mole flow-rate					
Carbon Monoxide	kmol/h	327.55	499.35	179.77	0.01
Hydrogen		613.00	1392.61	736.25	0.03
Carbon dioxide		1.07	33.68	27.96	0.02
Water		3.41	0.19	5.92	0.34
Nitrogen		27.89	1338.08	1338.08	0.03
Methane		2.66	18.30	18.30	0.002
Methanol		0.00	4.44	329.76	325.09
Total flow-rate	kmol/h	975.58	3286.69	2636.05	325.58
Total flow-rate	kg/h	11343.09	56201.58	56201.58	10425.88

The gaseous stream obtained in the DMR (e.g. 975.58 kmol/h) is mixed with a recycled stream coming from methanol purification section. As noticed from Table 3, the inlet of the methanol reactor is about 3286.69 kmol/h. The ratio between H_2 and CO at the inlet of the reactor is around 3. CO and H_2 conversion in the methanol reactor is higher than 45%, more exactly 47.13%. A quantity of 325.58 kmol/h of methanol was produced in the above presented process.

The main inputs and outputs derived from process modeling and simulation in the second option investigated (*Case B*) are summarized in Table 4.

Table 4. Main inputs and outputs for SNG production (*Case B*)

Parameters	Unit of measure	Streams			
		COG	CO_2 from CO_2 capture unit	After methanation	SNG after purification
Pressure	atm	0.98	0.98	23.50	39.50
Temperature	°C	25	35	35	400
Vapour fraction	-	1	1	0.65	1
Liquid fraction	-	0	0	0.35	0
Component mole flow-rate					
Carbon Monoxide	kmol/h	60.94	0.00	0.00	0.00
Hydrogen		596.30	0,00	7.17	0.00
Carbon dioxide		30.32	59.88	0,00	0.00
Water		0.00	0.03	221.87	0.00
Methane		272.88	0.00	366.13	366.02
Nitrogen		50.53	0.19	42.72	19.22
Oxygen		0.00	0.005	0.00	0.00
Total flow-rate	kmol/h	1010.68	60.10	637.90	385.25
Total flow-rate	kg/h	10028.55	2641.26	11082.21	6410.86

As noticed from Table 4, starting from 1010.68 kmol/h of COG and 60.10 kmol/h of CO_2 a quantity of 385.25 kmol/h of SNG was obtained. A total conversion of COG to SNG was considered. This high conversion leads to a high purity SNG (e.g. 95% mole fraction). The SNG stream obtained from COG is furthermore used in methanol production. The main inputs and outputs streams for methanol production from SNG are presented in Table 5.

As reported in Table 5, a flow-rate of 385.25 kmol/h of SNG is sent to the SMR for syngas production. SNG is converted into syngas using about 1004.10 kmol/h of steam. A flow-rate of 2072.86 kmol/h syngas is obtained. This stream is mixed with some recycled stream coming from methanol purification section. The flow-rate of the recycled stream is 348.44 kmol/h. The mixed stream is sent to methanol synthesis reactor. CO, CO_2 and H_2 are transformed into methanol, which is furthermore separated using a flash and a distillation column. The final flow-rate of methanol is 327.71 kmol/h, as noticed from Table 5.

Table 5. Main inputs and outputs for methanol production (*Case B*)

Parameters	Unit of measure	Streams			
		SNG	After reforming reactor	After methanol synthesis	Main product
Pressure	atm	39.50	38	107.5	0.98
Temperature	°C	400	1000	267	64.49
Vapour fraction	-	1	1	1	1
Liquid fraction	-	0	0	0	0
Component mole flow-rate					
Carbon Monoxide	kmol/h	0.00	261.18	143.60	$2*10^{-3}$
Carbon dioxide		0.00	805.87	348.23	0.05
Hydrogen		0.00	1105.83	15570.88	0.10
Nitrogen		19.22	19.22	34.07	$2*10^{-4}$
Methane		366.02	24.27	1111.38	0.03
Water		0.00	581.77	80.72	2.44
Methanol		0.00	0.00	331.91	325.09
Total flow-rate	kmol/h	385.25	2072.86	17636.87	327.71
Total flow-rate	kg/h	6410.86	24499.58	81670.13	10463.54

The main technical key performance indicators obtained in the two investigated cases are reported in Table 6.

Table 6. Comparative results obtained in *Case A* and *Case B*

Parameter	Component	*Case A*	*Case B*
Raw-material (kmol/h)	COG	907.82	1010.68
	CO_2	134.23	60.10
Final product (t/day)	CH_3OH	250	250
MeOH (wt.%)		99.92	99.55
CO_2 capture rate (%)		84.53	84.77
No. of unit operations involved in the whole process		48	66
Energy consumption (MW)		13.50	14.20
CO_2 emissions (kg/h)		48.76	395.20

As presented in Table 6, different quantities of raw-materials (i.e. COG and CO_2) are used in the two investigated technologies in order to obtain the same quantity of methanol (e.g. 250 t/day). Higher quantities of COG are used in *Case B* compared to *Case A* (e.g. 1010.68 kmol/h vs. 907.82 kmol/h). The CO_2 flow-rate is two times lower in *Case B* compared to

Case A. High methanol purities are obtained in both cases. Almost pure methanol is obtained in *Case A*. The CO_2 capture rates are about 85% in both cases. The energy consumption in *Case A* is lower compared to the energy consumption used in *Case B* (e.g. 13.50 MW vs. 14.20 MW). The number of unit operations involved in *Case A* is lower compared to *Case B* (e.g. 48 units operations vs. 66 units operations). The CO_2 emissions in *Case A* are about eight times lower compared to the CO_2 emissions from *Case B*.

CONCLUSIONS

The aim of the present paper was to compare, from technological point of view, two processes for methanol production using COG and CO_2 as raw materials. In order to reach the proposed goal process flow-modeling tools (i.e. ChemCAD process simulator software) was used. The plant capacity in each case was set to 250 t / day. The simulations results are in accordance with the data from the scientific literature, fact which was demonstrated by models validation.

From a technological point of view, the most advantageous route, between the two investigated cases, is methanol production from COG through DMR – *Case A*, in which a lower quantity of COG is required to obtain the same amount of final product. The other solution investigated was methanol production from COG through SMR, denoted as *Case B*.

The two cases are compared using various key performance indicators. Less unit operations are involved in *Case A* compared to *Case B*. Considering the CO_2 emissions released in the two investigated cases it can be concluded that these emissions are eight times less in *Case A* compared to *Case B*. The technologies of methanol production from COG are in line with the current environmental problems, due to the following two aspects:1) they valorize a by-product of steel plants (i.e. COG), turning it into valuable products (SNG and methanol); 2) they reduce the CO_2 released into the atmosphere.

It can be concluded that methanol production from COG and CO_2 capture through DMR offers several advantages.

EXPERIMENTAL SECTION
GENERAL PRESENTATION

Figure 2 illustrates the block flow diagram for *Case A*. The first intermediate step considered in this case is the DRM. The COG is mixed with a CO_2 stream which was previously generated during the total combustion of

some COG and captured using amine based gas-liquid absorption technology (using MDEA as a solvent). The methane-carbon dioxide mixture is introduced into the catalytic reforming reactor leading to syngas. The obtained syngas is cooled, compressed and sent to methanol synthesis step, where CO, CO_2 and H_2 are converted to methanol. The final step is the methanol separation. A methanol stream having a flow-rate of 250 t / day and a purity of 99.92% is obtained after the separation step.
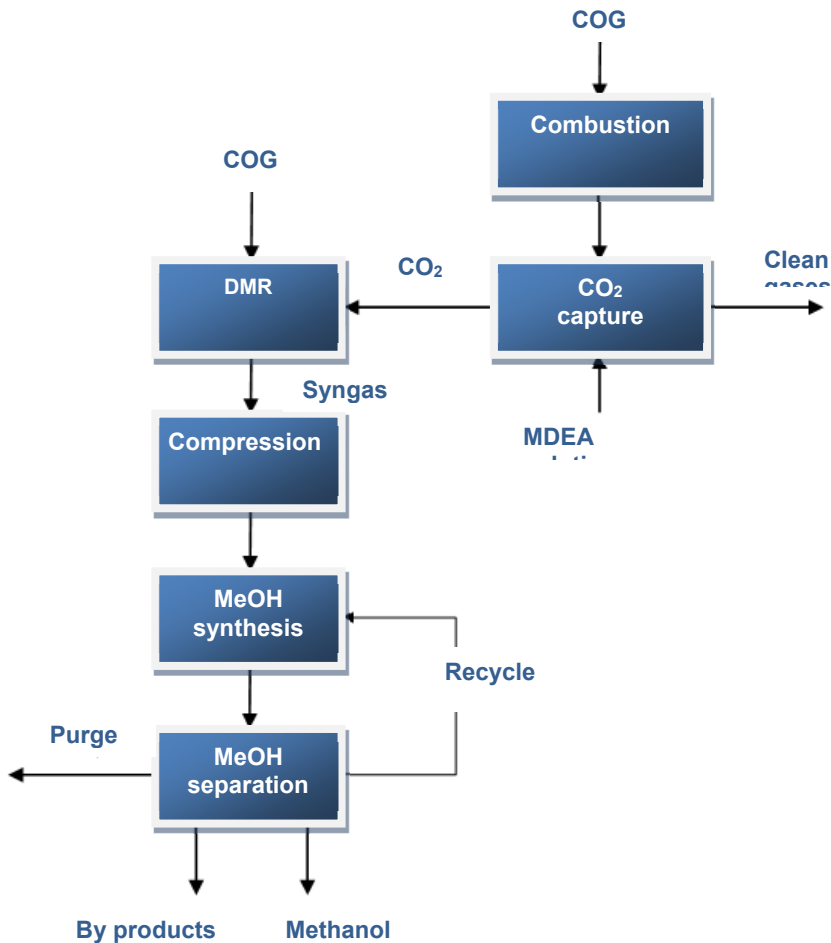
Figure 2. Simplified block flow diagram for *Case A*
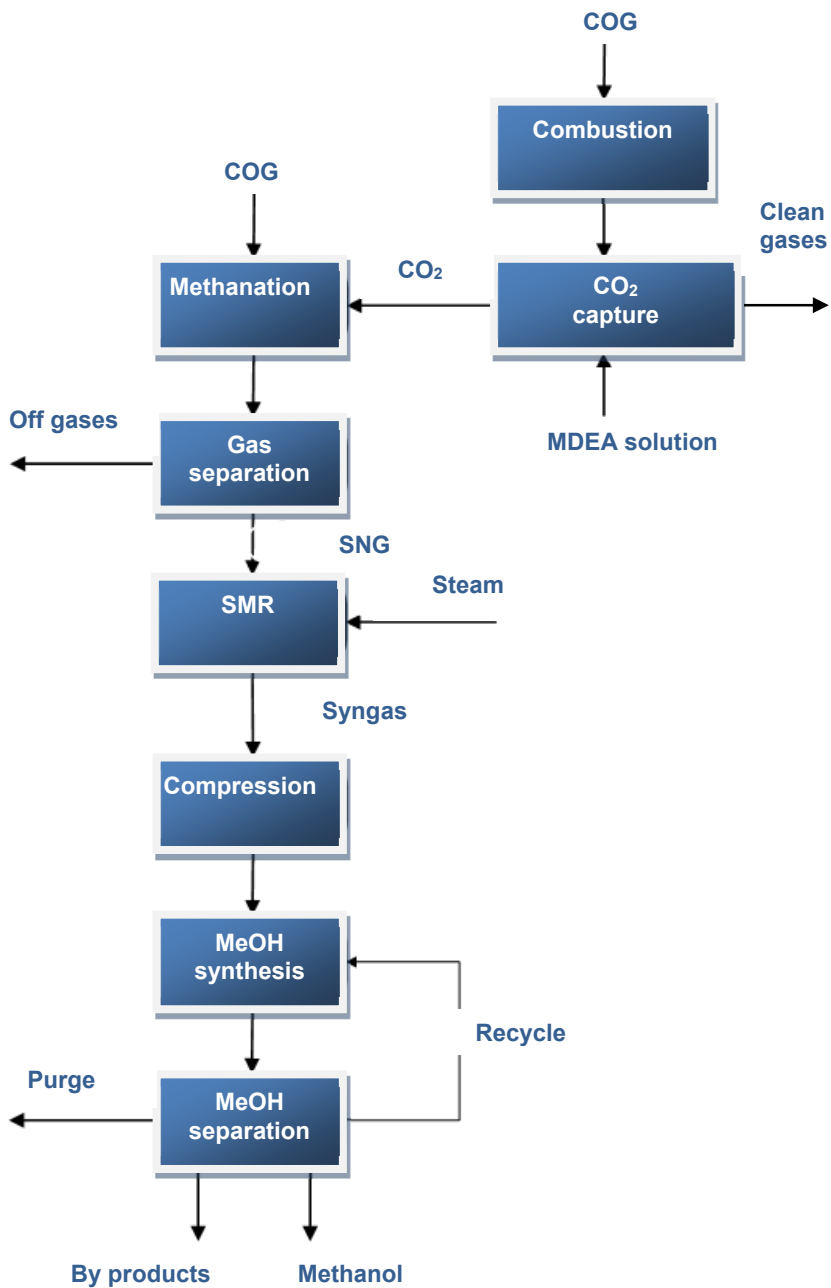
Figure 3. Simplified block flow diagram for *Case B*

Figure 3 shows the simplified block diagram for *Case B*. COG is the raw material also used in this case. It is divided into two streams, one part is sent to the combustion chamber and the rest to the methanation step. The combustion gases are sent to a CO_2 capture unit. As in the previous case, CO_2 capture is based on gas-liquid absorption. MDEA is the solvent used for CO_2 removal. After separation, pure CO_2 is reintroduced into the system together with the COG stream. The COG - CO_2 gas mixture obtained is sent to the methanation unit which leads to a rich CH_4 stream. This is furthermore separated in a stream containing 91.59% CH_4 called also SNG. Furthermore, SNG is fed to a SMR unit where, using steam, CH_4 is converted to syngas. The syngas is sent to the cooling unit, compressed and sent to the methanol synthesis step. The result of this step is a methanol rich product, which is purified in a separation system. The same productivity of methanol (e.g. 250 t / day) is obtained in *Case B*. Methanol purity in this case study is 99.55%.

The reactions tacking place in the combustion step are (R_1 - R_3) presented below [5]:

(R_1): $H_2 + 0.5O_2 \rightarrow H_2O$ ΔH_{298K} = -285.83kJ/mol
(R_2): $CH_4 + 2\ O_2 \rightarrow CO_2 + 2\ H_2O$ ΔH_{298K} = -890.36 kJ/mol
(R_3): $2CO + O_2 \rightarrow 2\ CO_2$ ΔH_{298K} = -566 kJ/mol

All reactions are exothermic, generating heat for the process in which coal is turned into coke. The process temperature varies between 1250 - 1300°C. In general, the excess air coefficient is between 1.2 - 1.3. For the simulation of the process, the air coefficient was set to 1.25. The reactions take place completely, all the components (H_2, CH_4, CO) being transformed into water and carbon dioxide.

The reactions occurring in the methanation step are (R_4 - R_6) [5]:

(R_4): $CO + 3\ H_2 \rightarrow CH_4 + H_2O$ ΔH_{298K} = -206 kJ/mol
(R_5): $CO_2 + 4\ H_2 \rightarrow CH_4 + 2H_2O$ ΔH_{298K} = -165 kJ/mol
(R_6): $CO + H_2O \rightarrow CO_2 + H_2$ ΔH_{298K} = -41 kJ/mol
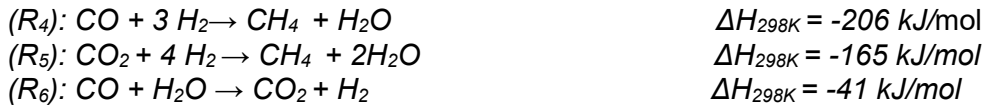
The first two reactions are strongly exothermic, and the third reaction occurs only when the carbon monoxide concentration is low and the hydrogen is in excess. In the industry, the catalysts used for the methane process are nickel-based. They maintain high activity in a wide temperature range (200 - 700°C) and can convert almost 100% of CO and over 98% of the CO_2.

The reactions taking place in the CO_2 capture section are ($R_7 - R_{10}$) [5]:

(R_7): $MDEAH^+ + H_2O = MDEA + H_3O^+$
(R_8): $CO_2 + OH^- = HCO_3^-$
(R_9): $HCO_3^- + H_2O = H_3O^+ + CO_3^{2-}$
(R_{10}): $2H_2O = H_3O^+ + OH^-$
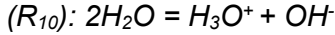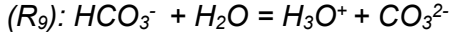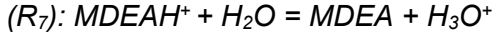
The reaction considered for DRM is R_{11} [2, 3]:

(R_{11}): $CH_4 + CO_2 \leftrightarrow 2H_2 + 2CO$ $\qquad\qquad \Delta H_{298K} = 247.30 \ kJ/mol$

The interest for DRM technology is due to the low energy consumption, compared to the SMR, because it uses two greenhouse gases: CO_2 and CH_4 generating valuable products. CO_2 reforming allows the production of a synthesis gas with low H_2 / CO ratios, theoretically 1/1.
The reaction considered in SMR is R_{12} [2, 3]:

(R_{12}): $CH_4 + H_2O \rightarrow 3H_2 + CO$ $\qquad\qquad \Delta H_{298K} = 206.20 \ kJ/mol$

SMR is currently the main process for obtaining synthesis gas. This involves the catalyzed reaction between methane and steam to obtain the synthesis gas with an increased H_2 / CO ratio, the optimum value being 3/1.

The reactions taking place in the methanol synthesis are (R_{13} - R_{15}) [2, 3]:

(R_{13}): $CO + 2H_2 \leftrightarrow CH_3OH$ $\qquad\qquad \Delta H_{298K} = -90.79 \ kJ/mol$
(R_{14}): $CO_2 + 3H_2 \leftrightarrow CH_3OH + H_2O$ $\qquad \Delta H_{298K} = -49.79 \ kJ/mol$
(R_{15}): $CO_2 + H_2 \leftrightarrow CO + H_2O$ $\qquad\qquad \Delta H_{298K} = 41.00 \ kJ/mol$
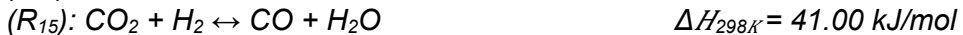
All of these reactions are reversible and depend on the reaction conditions. Methanol synthesis reactions are exothermic and maximum conversion is achieved under high pressure and low temperature.

DETAILS ON PROCESS MODELLING AND SIMULATION

The two cases have been modelled using ChemCAD process simulator developed by Chemstations [6]. *Case A* sub-processes have been listed in Table 1 and the assumptions used in process modelling and simulation are presented in Table 7.

Table 7. Process modelling assumptions for *Case A*

Case A	Assumptions

Input data specifications	COG molar composition:
	  $CO = 0.06$
	  $H_2 = 0.59$
	  $CO_2 = 0.03$
	  $CH_4 = 0.27$
	  $N_2 = 0.05$
	COG temperature: 25˚C
	COG pressure: 1 atm

COG combustion	Total combustion is considered. Combustion temperature: 1300˚C Excess air is used for combustion.
CO₂ capture	MDEA solution (50% wt.) is used for gas-liquid absorption. Absorption column: 30 trays. Desorption column: 10 trays.
DMR	The DMR catalytic reforming reactor is operated at 1000˚C and 0.98 atm. The flow obtained is cooled to 50˚C.
Syngas compression	After water removal and compression, the synthesis gas reaches 145˚C and 29.6 atm. The gas is furthermore compressed to 108.56 atm. The compressor efficiency is 75%.
Methanol synthesis	The methanol synthesis reactor is operated at 267˚C and 107 atm. The pressure drop in the reactor is 0.98 atm.
Methanol separation	The methanol purification unit consists of two separators whose resulting gaseous fluxes are compressed at 108.56 atm and returned to the process. The compressors are adiabatic and their efficiencies are 75%. The first separator is operated at 105 atm and 38°C. The second separator is operated at 1.97 atm and 38°C.The distillation column has 42 plates, the feed is made on plate 27. The pressure at the top of the column is 0.98 atm.

Case B sub-processes have been listed in Table 1 and the assumptions used in process modelling and simulation are presented in Table 8.

Table 8. Process modelling assumptions for *Case B*

Case B	Assumptions
Input data specifications	COG molar composition:CO = 0.06; H_2 = 0.59; CO_2 = 0.03; CH_4 = 0.27; N_2 = 0.05 COG temperature: 25°C COG pressure: 1 atm
COG combustion	Total combustion is considered. Combustion temperature: 1300°C Excess air is used for combustion.
CO_2 capture	MDEA solution (50% wt.) is used for gas-liquid absorption. Absorption column: 30 trays. Desorption column: 10 trays.
Methanation section	Three reactors are used for this section. The first reactor is operated at 620°C, the mixture obtained being furthermore cooled to 300°C. The second reactor is operated at 300°C, the mixture obtained being subsequently cooled to 240°C. The third reactor is operated at 240°C, the mixture obtained then cooled to 168°C. The gaseous product obtained by separation is rich in hydrogen and methane gas.
Gas separation	SNG with composition 95% CH_4 and 5% N_2 is obtained in this section.
SMR	High pressure steam (p = 118.4 atm, T = 360°C) is used in the SMR. The methane-steam mixture is preheated to 870°C before being introduced into the reforming reactor. The reforming reactor is a Gibbs type reactor, operating at 1000°C and 37.5 atm.
Syngas compression	The gas mixture leaving the reforming reactor is cooled and compressed in two steps to the desired pressure of 107 atm. Compressors efficiencies are 75%.
Methanol synthesis	The methanol synthesis reactor is operated at 267°C and 107 atm. The pressure drop in the reactor is 0.98 atm.
Methanol separation	The methanol purification unit consists of two separators whose resulting gaseous fluxes are compressed at 108.56 atm and returned to the process. The compressors are adiabatic and their efficiencies are 75%. The first separator is operated at 105 atm and 38°C.The second separator is operated at 1.97 atm and 38°C. The distillation column has 42 plates, the feed is made on plate 27. The pressure at the top of the column is 0.98 atm.

The developed models were validated using literature date, the error between the proposed models and those found in the literature being less than 5%.

A comparative simulation-literature study was performed for the main flows obtained in Case B in order to validate the SNG production model developed in ChemCAD. The data obtained for the SNG production is in accordance with those from the literature (see Table 9).

Table 9. Model validation for SNG production process

Parameter	Unit of measure	SNG production	
		Present work	Literature [5]
Pressure	atm	19.70	19.73
Temperature	°C	25	25
Vapour fraction	-	1	1
Liquid fraction	-	0	0
Composition			
Carbon Monoxide		0	0
Hydrogen		0	0
Carbon dioxide		0	0
Water	Mole fractions	0	0
Methane		0.95	0.95
Nitrogen		0.05	0.05
Oxygen		0	0

For methanol synthesis, the data obtained from process modelling and simulation was validated in comparison with scientific literature data (see Table 10).

Table 10. Model validation for methanol production process (*Case B*)

Parameter	Unit of measure	MeOH production	
		Simulation	Literature [7]
Carbon Monoxide		0.00	0.00
Hydrogen		$3 \cdot 10^{-5}$	0.00
Carbon dioxide		$1.45 \cdot 10^{-5}$	0.009
Water	Mole fractions	0.007	0.001
Methane		$9.07 \cdot 10^{-5}$	198 ppm
Nitrogen		$7.58 \cdot 10^{-5}$	727 ppm
Methanol		0.99	0.98

REFERENCES

1. G.A. Olah, and G.K.S. Prakash. "Beyond oil and gas: the methanol economy", **2011**, John Wiley & Sons.
2. G. Bozzano, F. Manenti. *Prog. Eneg Combust.*, **2016**, *56*, 71-105.
3. J.M. Bermúdez, A. Arenillas, R. Luque, J.A. Menéndez. *Fuel Process. Technol.,* **2013**, *110*, 150-159.
4. J.M. Bermúdez, N. Ferrera-Lorenzo, S. Luque, A. Arenillas, Menéndez, J.A. *Fuel Process. Technol.*, **2013**, *115*, 215-221.
5. Q. Yi, G. Wu, M. Gong, Y. Huang, J. Feng, Z. Hao, W. Li. *Appl. Energ.*, **2017**, *193,* 149-16.
6. ChemCAD Chemical Process Simulation – Chemstations, Huston, USA, *http://www.chemstations.com* (accessed on April 2020).
7. W.L. Luyben. *Ind. Eng. Chem. Res.*, **2010**, *49*, 6150-6163.

MINERAL WATERS CLASSIFICATION USING FUZZY LINEAR DISCRIMINANT ANALYSIS

ALEXANDRINA GUIDEA[a], RADU D. GĂCEANU[b], HORIA F. POP[b], COSTEL SÂRBU[a*]

ABSTRACT. Fuzzy linear discriminant analysis is efficiently applied for the characterization and classification of some Romanian and German mineral waters according to their mineral composition. The samples were successfully classified according to the degrees of membership and canonical scores. A correct classification rate of 88% was obtained when the samples were divided into four groups corresponding to origin and nature of samples. The proposed methodology based on the fuzzy sets theory may be considered as a promising tool with future applications in analytical chemistry and other related fields.

Keywords: *Fuzzy discriminant analysis, chemometrics, mineral waters, mineral composition*

INTRODUCTION

One of the most acute problems facing the world today is the water quality and quantity, because water is a limiting factor of the environment, both for biological systems and human societies [1-3]. As a consequence, there are many national and international initiatives and vigorous efforts to protect ground and surface water and to increase water quality and resources [4]. Mineral waters, as natural waters usually obtained from springs, contain an appreciable quantity of salts and gases deriving from their passage through rocks and soil. From the physiological point of view, mineral waters

---

[a] *Babeş-Bolyai University, Faculty of Chemistry and Chemical Engineering, 11 Arany Janos str., RO-400028, Cluj-Napoca, Romania*
[b] *Babeş-Bolyai University, Department of Computer Science, str. Mihail Kogalniceanu nr. 1, 400084, Cluj-Napoca, Romania*
* *Corresponding author: csarbu@chem.ubbcluj.r*

must contain a sufficient amount of inorganic salts, with or without dissolved gases, to enable them to have an efficient effect [5]. There are many mineral waters, presently being bottled all around the World. The most famous in Europe, for example, are from France, Italy, Germany, Austria and Switzerland. Compared to Europe's mineral waters, Romanian natural mineral waters take a very high position by their diversity, quality and quantity. Romanian mineral waters are a gift of untouched nature in close surroundings of the Carpathian Mountains from North to South [6, 7]. Tradition of utilization of these waters for drinking originates from the Roman period in Dacia and is connected for practical comprehension of its healing activity on the work of heart and digestive organs, for example. In the past, many of these waters were neither present on the market, nor subject of any substantial examinations. It is interesting that despite the existence of a general chemical analysis (macro components) of the majority of these waters it has not been noticed that many of them contain increased contents of some micro elements as, for example, magnesium, zinc, copper or fluoride and bromine. Relatively recent, research has shown that the status of these elements in the human organism in its development phases has extremely great importance in prevention of numerous illnesses. For example, the prominent role of Mg in water as a cardiovascular protective factor is largely accepted [8].

The classical discriminant analysis method is known to provide maximum likelihood estimations under certain assumptions (normality of the class distributions etc.) [9-11]. As the experiments will illustrate, and as previous research on data analysis methods based on fuzzy sets have also shown, the fuzzy discriminant analysis method is robust with respect to outliers and distribution of data [12, 13].

We underline once again the robustness achieved by using fuzzy membership values and their relevance. The main advantage of fuzzy sets over crisp sets and of fuzzy logic over binary logic is the availability of gradual membership degrees. On one side, the classes input provided by the human expert is fuzzified, allowing robust treatment of outliers. On the other side, the output of the method is fuzzy as well, allowing for a more detailed view of the relationships between data objects (samples) and classes. These fuzzy degrees of membership (DOMs) are not actually related to uncertainty, because there is nothing uncertain about the classification of a certain data element (sample), but have to be regarded as a measure of 'typicality' [12-14].

The fuzzy linear discriminant analysis (FLDA) method presented and applied here is a multiclass method by design, as no restrictions with respect to the number of classes are introduced. This is a parameter to be set by the human experts as they establish the a-priori classes split.

RESULTS AND DISCUSSION

The data used in this study are summarized in **Table 1** and **Figure 1a-b.** It can be easily observed from the Box and whiskers plots that only in the case of major ions (Na^+, Ca^{2+}) including Mg^{2+}, Sr^{2+} and Cu^{2+} and also conductivity and salinity are not highlighted outliers and extremes values (Fig. 1a-b). In all these cases, all values are within the robust confidence interval (neither outliers nor extremes) and the distributions appear to be more or less asymmetric. In all other cases are highlighted outliers and extremes values. The concentrations of Li^+, K^+, NH_4^+, Sr^{2+}, Ba^{2+}, Cu^{2+} and Br^- are the highest in samples from Sângeorz Băi area and the concentration of SO_4^{2-} is the highest in mineral waters from Germany.

Table 1. The statistics of data corresponding to all mineral waters discussed in this study

Variable	Mean	Median	Minimum	Maximum	Range	SD	Skewness	Kurtosis
Li^+	2.3	0.2	0.0	14.4	14.4	4.4	1.8	2.0
Na^+	514.4	145.0	0.9	1814.0	1813.1	696.2	1.1	-0.6
K^+	35.0	13.0	0.5	166.0	165.5	49.2	1.6	1.2
NH_4^+	3.0	0.1	0.0	18.0	18.0	5.1	1.7	2.2
Mg^{2+}	52.2	42.5	1.7	142.0	140.3	41.0	0.5	-0.9
Ca^{2+}	214.4	171.0	8.8	546.0	537.2	172.7	0.4	-1.3
Sr^{2+}	0.8	0.6	0.0	2.6	2.6	0.8	0.8	-0.8
Ba^{2+}	0.5	0.0	0.0	2.5	2.5	0.9	1.6	0.6
Zn^{2+}	34.0	3.5	0.0	664.0	664.0	132.0	4.9	24.4
Cu^{2+}	24.9	16.0	0.0	89.0	89.0	29.4	0.8	-0.8
Cl^-	514.6	76.3	0.2	2824.0	2823.8	819.5	1.5	1.3
F^-	0.5	0.3	0.0	2.6	2.6	0.6	2.4	6.8
Br^-	0.8	0.0	0.0	4.2	4.2	1.5	1.8	1.6
SO_4^{2-}	56.9	9.8	0.6	398.0	397.4	97.8	2.4	5.7
NO_3^-	0.8	0.3	0.0	3.8	3.8	1.1	1.9	2.7
pH	6.8	6.9	5.2	8.4	3.3	0.9	0.0	-1.0
Cond	3407.4	1802.0	104.0	10680.0	10576.0	3560.5	1.1	-0.4
Salinity	1.8	0.9	0.0	6.0	6.0	2.0	1.1	-0.4

All concentrations are in mg.L^{-1}, excepting Cu^{2+} and Zn^{2+} which are in µg.L^{-1}
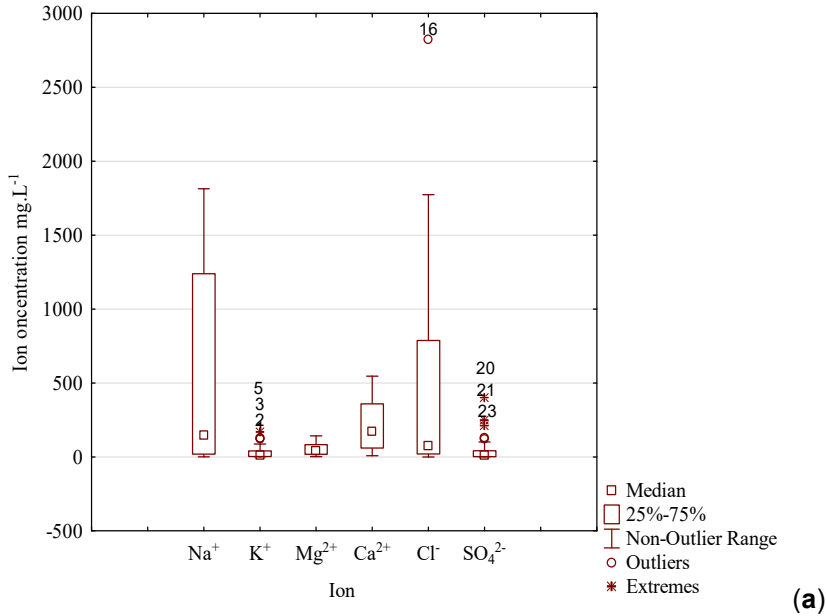
(a)
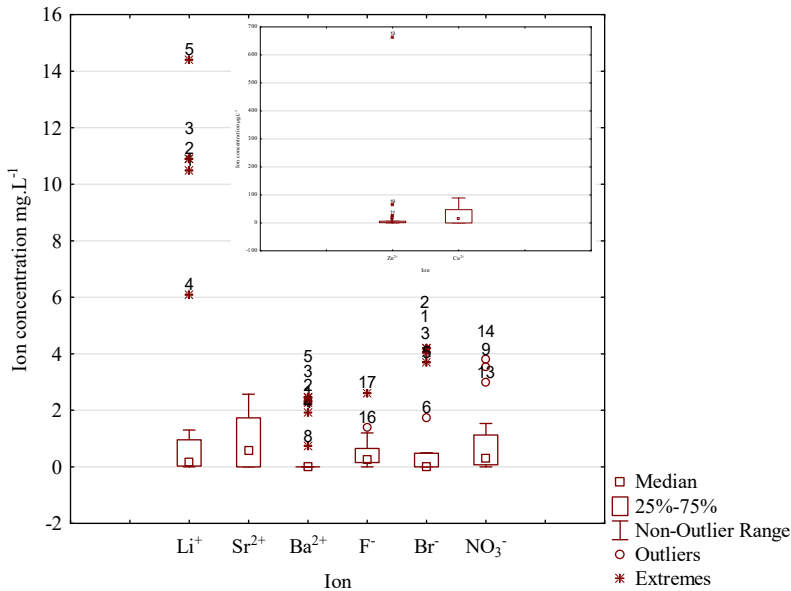
(b)

Figure 1. Box and whiskers plot of the physicochemical parameters (**a**, **b**) excepting sample S1 assigned also to German mineral water group (**A4**) but with a very small DOM (0.2654). This sample appears as a strong outlier with an equal DOM to other fuzzy partitions. All the German mineral water samples were assigned to fuzzy partition **A4** with DOM-range between 0.8959 and 0.9970, excepting in this case the sample G2 (**21**-Schiller Brunnen) assigned to the Olăneşti group with a high DOM (0.8782).

According to the origin and nature of mineral water samples, the number of classes for FLDA was chosen to be 4. FLDA produced four fuzzy partitions, which were all represented by a prototype (a cluster center with the parameters corresponding to the fuzzy robust means of the original physicochemical characteristics for the 25 samples weighted by DOMs corresponding to each partition) depicted in **Table 2**. To compare the partitions and the similarity and differences of the investigated mineral waters, we have to analyze both the characteristics of the prototypes corresponding to the four fuzzy partitions (**A1**-**A4**) obtained by applying FLDA and DOMs of samples corresponding to all fuzzy partitions, including also the canonical scores used usually in classical linear discriminant analysis. The results presented in Table 2 clearly illustrate the most specific characteristics of each fuzzy partition and their similarity and differences. The values of prototype corresponding to the first partition (**A1**) assigned to medicinal waters from Sângeorz Băi are the highest excepting the value of Zn^{2+}, F^- and SO_4^{2-}. The highest value of Zn^{2+} corresponds to the prototype of **A2** partition (assigned to the table Romanian waters-M), the highest value of F^- to the prototype of **A3**

Table 2. The parameters of prototypes

Physicochemical parameter	Parameters of prototype			
	A1	A2	A3	A4
Li^+	10.38	0.35	0.06	0.23
Na^+	1720.84	91.60	250.41	33.98
K^+	124.56	12.44	5.07	7.12
NH_4^+	10.56	1.08	0.72	0.09
Mg^{2+}	90.55	42.02	28.31	31.96
Ca^{2+}	435.74	187.02	47.98	126.67
Sr^{2+}	1.69	0.61	0.00	0.66
Ba^{2+}	2.19	0.07	0.00	0.00
Zn^{2+}	1.16	83.12	33.60	4.16
Cu^{2+}	57.71	22.58	0.00	15.93
Cl^-	1564.11	47.68	409.55	31.18
F^-	0.66	0.28	0.98	0.17
Br^-	3.57	0.16	0.00	0.00
SO_4^{2-}	1.89	10.60	107.34	142.10
NO_3^-	0.65	1.67	0.03	0.16
pH	6.98	6.28	7.78	6.89
Cond	9544.16	1479.77	1713.96	852.26
Salinity	5.35	0.73	0.81	0.37

(assigned to the mineral waters from Olăneşti-O area) and the highest concentrations of SO_4^{2-} characterize the German mineral waters-G assigned to the **A4** partition.

The results presented in **Table 3** and **Figure 2a-c** point out the mineral waters assigned to each partition (**A1**-**A4**) according to their DOMs.

The fuzzy partition **A1** includes all the *samples* from Sângeorz Băi area with the DOM-range between 0.9411 and 0.9611 for the first five samples and 0.7705 for the **6**-Anies sample. This is not surprisingly because Anies is located at seven kilometers far from Sângeorz Băi. The fuzzy partition **A2** contains eight table Romanian waters (M1, M8) with the DOM-range between 0.8975 and 0.9971 excepting the sample M9 assigned to **A4** (German mineral water group) but with a relatively small DOM (0.5570). The fuzzy partition **A3** includes three samples from Olăneşti area (S2, S3 and S4) with the DOM-range between 0.8439 and 0.9594,

a)

b)

c)
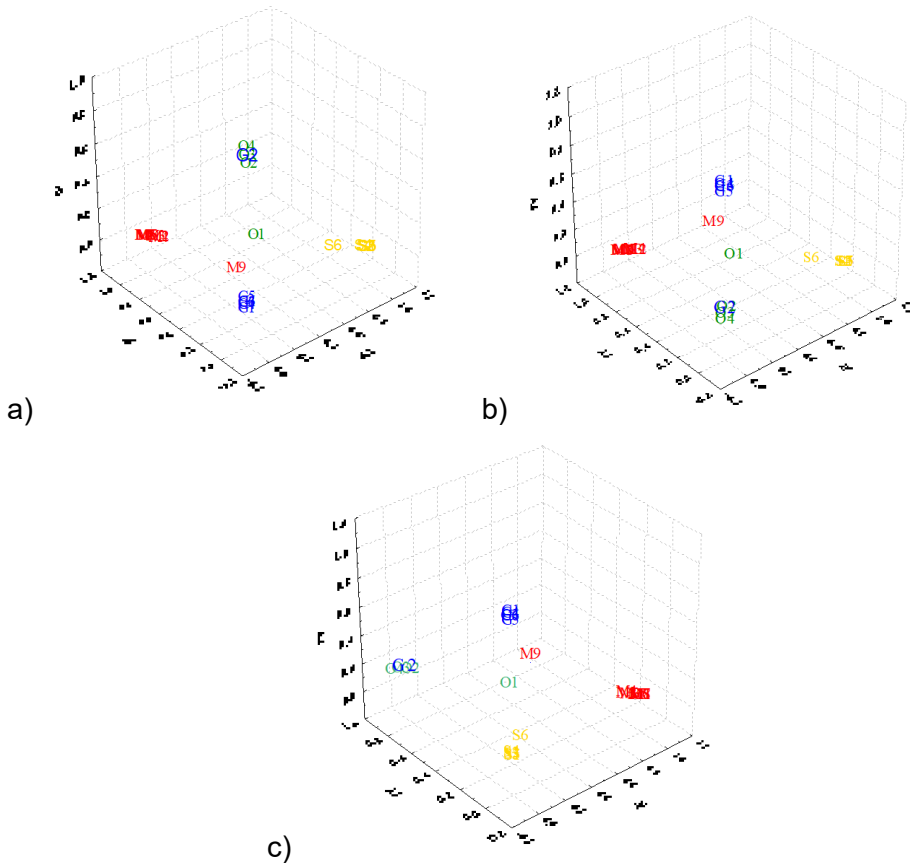
Figure 2. 3-D scatterplot of DOMs

Table 3. The degrees of membership (DOMs) to the
four fuzzy classes obtained applying FLDA

No	Water sample	A1	A2	A3	A4
1	**S1**	**0.9695**	0.0111	0.0075	0.0119
2	**S2**	**0.9540**	0.0125	0.0142	0.0193
3	**S3**	**0.9659**	0.0093	0.0103	0.0145
4	**S4**	**0.9411**	0.0153	0.0186	0.0250
5	**S5**	**0.9711**	0.0104	0.0071	0.0114
6	**S6**	**0.7705**	0.1066	0.0451	0.0778
7	**M1**	0.0010	**0.9971**	0.0005	0.0014
8	**M2**	0.0380	**0.8992**	0.0203	0.0426
9	**M3**	0.0291	**0.9242**	0.0149	0.0318
10	**M4**	0.0313	**0.8975**	0.0184	0.0528
11	**M5**	0.0081	**0.9775**	0.0044	0.0100
12	**M6**	0.0050	**0.9865**	0.0026	0.0060
13	**M7**	0.0027	**0.9925**	0.0014	0.0034
14	**M8**	0.0025	**0.9928**	0.0014	0.0033
15	M9	0.1101	0.2332	0.0997	0.5570
16	O1	*0.2584*	*0.2242*	*0.2520*	*0.2654*
17	**O2**	0.0354	0.0224	**0.8439**	0.0982
18	**O3**	0.0135	0.0094	**0.9080**	0.0691
19	**O4**	0.0064	0.0039	**0.9594**	0.0303
20	**G1**	0.0006	0.0007	0.0017	**0.9970**
21	G2	0.0141	0.0100	*0.8782*	*0.0977*
22	**G3**	0.0116	0.0147	0.0240	**0.9497**
23	**G4**	0.0064	0.0075	0.0143	**0.9718**
24	**G5**	0.0265	0.0343	0.0433	**0.8959**
25	**G6**	0.0143	0.0169	0.0269	**0.9419**

All of the above statements concerning the efficiency of FLDA are well supported also by scatterplot of canonical scores in the space defined by Froot 1 - Froot 2 - Froot 3 (**Figure 3**) and the values of quality performance features obtained for the correct classification rate of the original data and by applying the leave-one-out (LOO) cross-validation approach (**Table 4**).
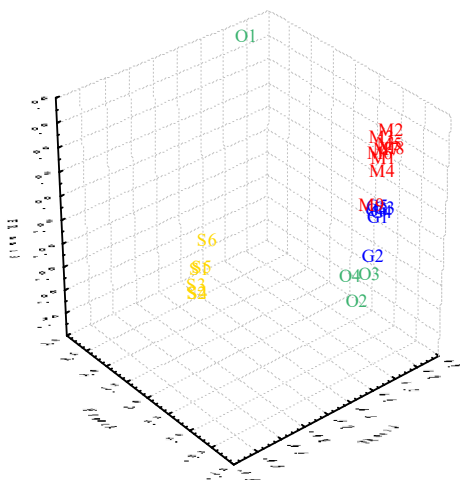
Figure 3. 3-D scatterplot of canonical scores obtained applying FLDA

Table 4. Matrix classification of mineral waters

Class	Total	Samples					%			
		A1	A2	A3	A4	A1	A2	A3	A4	
A1	**6**	**6**	0	0	0	**100.00**	0.00	0.00	0.00	
A2	**9**	0	**8**	0	1	0.00	**88.89**	0.00	11.11	
A3	**4**	0	0	**3**	1	0.00	0.00	**75.00**	25.00	
A4	**6**	0	0	1	**5**	0.00	0.00	16.67	**83.33**	
Leave-one-out cross-validation										
A1	**6**	**3**	2	1	0	**50.00**	33.33	16.67	0.00	
A2	**9**	0	**5**	2	2	0.00	**55.56**	22.22	22.22	
A3	**4**	0	0	**1**	3	0.00	0.00	**25.00**	75.00	
A4	**6**	0	0	2	**4**	0.00	0.00	33.33	**66.67**	

CONCLUSION

In this study, the advantages of the fuzzy linear discriminant analysis for the characterization and classification of various mineral waters on the basis of their mineral composition have been explored. The parameters of the prototypes (class centers) illustrate much better than, for example, arithmetic means the specific characteristics of each class, and the degrees of membership allow a rationale comparison of the similarities and differences of mineral water samples investigated.

EXPERIMENTAL SECTION

Mineral water samples and analytical methods

A large diversity of natural mineral waters from Romania (19 types) were analyzed and compared (**1-19**): **1**-Sângeorz Băi spring 1 (S1), **2**-spring 3 (S2), **3**-spring 5 (S3), **4**-spring 7 (S4), **5**-spring 9 (S5) and **6**-Anies (S6); **7**-Olăneşti spring 30 (O1), **8**-spring 14 (O2), **9**-spring 24 (O3) and **10**-spring 10 (O4); **11**-Borsec (M1), **12**-Biborţeni (M2), **13**-Bucovina (M3), **14**-Anavie (M4), **15**-Dorna (M5), **16**-Poiana Negri (M6), **17**-Buziaş (M7), **18**-Izvorul Alb (M8) and **19**-Izvorul Minunilor (M9).

Only six types of German mineral waters (**20-25**) were included in this study: **20**-Fuldataler (G1), **21**-Schiller Brunnen (G2), **22**-Lauchaer Minnerall Brunnen (G3), **23**-Schönborn Quelle (G4), **24**-Lausitzer (G5) and **25**-Schildetaler Mineralquelle (G6).

It is needed to mention that all Romanian M type waters are bottled nowadays on the market and are very appreciated by the public people. The waters from Sângeorz Băi and Olăneşti region respectively, well-known as natural medicinal waters, are recommended especially in the cure of gastroenterolitic disorder, cholecysitis, hyperuricemia, consequences of liver disease, disorder of biliar tract and gastroenterolitic disorder.

All samples were analyzed for the anions, chloride, fluoride, bromine, sulfate, nitrate and cation lithium, sodium, potassium, ammonium, magnesium, calcium, strontium and barium by ion chromatography using a DIONEX DX 120 system (Methrom anion and cation columns, deionized water and acetonitrile as eluent and a conductivity detector). The concentration of cooper was determined by standard flame atomic absorption spectrometry (Perkin Elmer FIAS 400), using specific line and the concentration of zinc by standard striping voltammetry (Metrohm Polarecord 626); pH and conductivity were determined electrochemically [9, 15]. The results obtained for the samples presented above are depicted in Tables 1 and 2.

Fuzzy Linear Discriminant Analysis

The Fuzzy Linear Discriminant Analysis problem is defined as follows: let $\mathbf{X} = \{x^1, ..., x^n\} \subset \mathbf{R}^s$ be a finite set of characteristic vectors, where n is the number of items and s is the number of the original variables (predictors), $\mathbf{x}^j = [x^j_1, x^j_2, ..., x^j_s]^T$ and let A_i (with $i = 1, ..., k$) be fuzzy sets on X, corresponding to the k a-priori sets composing the partition substructure of the given data set. A new vector (or characteristic) c is to be determined, that maximizes the fuzzy between-class variance of the projected data items, and minimizes the fuzzy within-class variance of the projected data items.

The total variance/covariance matrix may be decomposed into two components: the between-group variance **B** and within-group variance **W**, namely,

$$V = B + W.$$

Considering a new characteristic defined as **c** = **Xu**, this becomes

$$\frac{\mathbf{u}^T\mathbf{B}\mathbf{u}}{\mathbf{u}^T\mathbf{V}\mathbf{u}} + \frac{\mathbf{u}^T\mathbf{W}\mathbf{u}}{\mathbf{u}^T\mathbf{V}\mathbf{u}} = 1$$

With the first ratio maximized we get

$$\lambda = \frac{\mathbf{u}^T\mathbf{B}\mathbf{u}}{\mathbf{u}^T\mathbf{V}\mathbf{u}}$$

Or, since matrix **V** of the total variance is symmetrical and positive definite,

$$\mathbf{V}^{-1}\mathbf{B}\mathbf{u} = \lambda\mathbf{u},$$

where λ ($0 \le \lambda < 1$) and **u** represent the eigenvalues (known, as well, as characteristic roots) and eigenvectors of the matrix $\mathbf{V}^{-1}\mathbf{B}$.

The vector $\mathbf{u}^1$, named *the first discriminant factor* corresponds to the highest value of λ; the higher this value the higher will be the discriminant power of this factor.

Considering this new characteristic defined as **c** = **Xu**, the fuzzy between-group variance **B** and fuzzy within-group variance **W**, are defined as:

$$\mathbf{W} = \frac{1}{n-k}\sum_{i=1}^{k}\left(\sum_{j=1}^{n}A_i\left(x^j\right)^m\left(x^j-L^i\right)^T\left(x^j-L^i\right)\right),$$

$$\mathbf{B} = \frac{1}{k-1}\sum_{i=1}^{k}\left(\sum_{j=1}^{n}A_i\left(x^j\right)\right)^m\left(L^i-L\right)^T\left(L^i-L\right),$$

where the class means L^i are the fuzzy central locations of classes A_i, and L is the central location for the whole data set. The weighting exponent m (so-called "fuzzifier") is any real number in $[1, \infty]$, which determines the fuzziness of the clusters (for m→1 the μ_{ij} approach 0 or 1, for m→∞ the memberships tend to be "totally fuzzy" μ_{ij}→1/c). Usually, m = 2.

As the fuzzy sets A_i form a sub-partition of the given data set, we formulate the problem of determining the optimal direction $\mathbf{u}$ as maximizing the ratio

$$\lambda = \frac{\mathbf{u}^T(\mathbf{V} - \mathbf{W})\mathbf{u}}{\mathbf{u}^T\mathbf{V}\mathbf{u}}$$

with ($0 \leq \lambda < 1$). In a different form, since matrix $\mathbf{V}$ of the total variance is symmetrical and positive definite,

$$\mathbf{V}^{-1}(\mathbf{V}-\mathbf{W})\mathbf{u} = \lambda\mathbf{u},$$

where λ and $\mathbf{u}$ represent the eigenvalues (known, as well, as characteristic roots) and eigenvectors of the matrix $\mathbf{V}^{-1}(\mathbf{V}-\mathbf{W})$.

The vector $\mathbf{u}^1$, named *the first fuzzy discriminant factor* corresponds to the highest value of λ; the higher this value the higher will be the discriminant power of this factor. After obtaining the first discriminant characteristic $\mathbf{c}_1 = \mathbf{X}\mathbf{u}^1$, in a similar way can be obtained the discriminant characteristic $\mathbf{c}_2 = \mathbf{X}\mathbf{u}^2$, uncorrelated with the first and so on. It appears clearly that eigenvectors corresponding to the matrix $\mathbf{V}^{-1}(\mathbf{V}-\mathbf{W})$ namely $\mathbf{u}^1$, $\mathbf{u}^2$, .., $\mathbf{u}^{k-1}$, ranked in decreasing order of the positive values λ_1, …, λ_{k-1}, are successive solutions of the above matrix equation. The quality of discrimination and the selection of the most discriminant independent variable is given by the value of the largest eigenvalue, λ.

Finally, the original class means are projected in the new system of coordinates, and the final fuzzy membership degrees are determined from square-distances to the class means, as with the Fuzzy c-Means algorithm.

The final fuzzy classification table is then computed by counting cardinals of fuzzy sets: instead of counting the number of data items classified in a particular class, we are actually computing an overall fuzzy membership degree. The fuzzy count of all items from the i-th original fuzzy set A'_i classified in the l-th fuzzy set A_l denoted as C_{il}, is given by

$$C_{il} = \sum_{j=1}^{n} A'_i\left(x^j\right) \cdot A_l\left(x^j\right)$$

or, by scaling the values above as the percentages of all items in A'_i classified in A_l :

$$C_{il}^{[\%]} = \frac{\sum_{j=1}^{n} A'_i\left(x^j\right) \cdot A_l\left(x^j\right)}{\sum_{j=1}^{n} A'_i\left(x^j\right)} \times 100.$$

A crisp classification matrix is as well determined by first defuzzifying the final fuzzy partition and then using the cardinals of the crisp classes. After this learning phase, testing follows in various ways, including use of separate testing data, or by cross-validation.

All the graphs and some statistics were performed using Statistica 8.0 (StatSoft, Inc. 1984–2007, Tulsa, USA) software. All the other results were obtained using our own fuzzy software package.

REFERENCES

1. J.H. Lehr; J. Keeley; Water Encyclopedia - Ground Water, Wiley-Interscience, New York, **2005**.
2. S. Ahuja; Handbook of Water Purity and Quality, Academic Press, **2009**.
3. S. Maxwell; S. Yates; The Future of Water: A Startling Look Ahead, American Water Works Association, **2011**.
4. C.E. Boyd; Water Quality. An Introduction, Second Edition, Springer, **2015**.
5. I. Rosborg; F. Kozisek; (Eds). Drinking Water Minerals and Mineral Balance. Importance, Health Significance, Safety Precautions, Second Edition, Springer Nature Switzerland AG, **2019**.
6. C. Berca; Water and Health, Ceres Publishing House, Bucharest, **1994**.
7. L. Munteanu; C. Stoicescu; L. Grigore; The Guide of Romanian Resting Stations, Sport Turism Publishing House, Bucharest, **1978**.
8. J. Durlach; Magnesium in Clinical Practice, Publ. John Libbey, London-Paris, **1988**.
9. C. Sârbu; *Rev. Chim.* (Bucharest), **2002**, *53*, 442-449.
10. C. Sârbu; H.F. Pop; R. Elekes; G. Covaci; *Rev. Chim.* (Bucharest), **2008**, *59*, 1237-1241.
11. G.J. McLachlan; Discriminant Analysis and Statistical Pattern Recognition, John Wiley & Sons, Inc., **2004**.
12. C. Sârbu; H.F. Pop; Fuzzy Soft-Computing Methods and Their Applications in Chemistry in Reviews in Computational Chemistry, K.B. Lipkowitz, R. Larter and T.R. Cundari (Eds.), Wiley-VCH, 2004, Chapt. 5, 249-332.
13. H.F. Pop; C. Sârbu; A New Fuzzy Discriminant Analysis Method, *MATCH Commun. Math. Comput. Chem.*, **2013,** *69*, 391-412.
14. O. Horovitz; C. Sârbu; H.F. Pop; Clasificarea raţională a elementelor chimice, Editura Dacia, Cluj-Napoca, **2000**.
15. C. Sârbu; H.W. Zwanziger; *Anal. Lett*, **2001**, *34*, 1541--1552.

ANTIMICROBIAL ACTIVITY AND CHEMICAL COMPOSITION OF TWO EXPERIMENTAL GELS BASED ON ESSENTIAL OILS

LAURA MONICA DASCALU (RUSU)[a], MARIOARA MOLDOVAN[b], DOINA PRODAN[b], IRINA CIOTLAUS[b], RAHELA CARPA[c], RAZVAN ENE[d,e], SORINA SAVA [a]*, RADU CHIFOR[f], MINDRA EUGENIA BADEA[f]

ABSTRACT. In this study, the comparative testing of the antimicrobial efficacy of 2 experimental photosensitizers (PS-H; PS-T) based on natural compounds with a commercial one based on toluidine blue O (TBO) FotoSan® was performed, by antimicrobial tests with G- and G+ bacterial strains and through SEM microscopy on dental enamel, using LED phototherapy. For the formulation of the experimental natural photosensitizers we used Frankincense (T) and Thieves (H) essential oils (EO), used as photosensitizing agents in antimicrobial photodynamic therapy in the control of the microbial biofilm of the oral cavity. We also tested the composition of experimental photosensitizers by GC-MS chromatography. Our results suggest that EO should be further investigated as a promising source of natural compounds that can be used to combat bacterial strains. Essential oils can inhibit growth of a broad range of pathogens correlating to their presence in aromatic plants.

Keywords: GC-MS, SEM, antibacterial effect

[a] *Department of Prosthodontics and Dental Materials, Iuliu Hatieganu University of Medicine and Pharmacy, 31 Avram Iancu str., RO-400083, Cluj-Napoca, Romania*

[b] *Department of Polymer Composites, Babes-Bolyai University, Institute of Chemistry Raluca Ripan, 30 Fantanele str., RO-400294, Cluj-Napoca, Romania*

[c] *Department of Molecular Biology and Biotechnology, Babeș Bolyai University, Faculty of Biology and Geology,1 M. Kogălniceanu str.,400084, Cluj-Napoca, Romania*

[d] *University of Medicine and Pharmacy Carol Davila Bucharest, 8 Eroii Sanitari str., RO-050474 Bucharest, Romania*

[e] *Orthopedics and Traumatology Department, Bucharest Emergency University Hospital, 8 Calea Floreasca str., RO- 050098 Bucharest, Romania*

[f] *Department of Preventive Dental Medicine, Iuliu Hatieganu University of Medicine and Pharmacy,31 Avram Iancu Street, 400083 Cluj-Napoca, Romania*

*Corresponding author: savasorina@yahoo.com

L. M. DASCALU (RUSU), M. MOLDOVAN, D. PRODAN, I. CIOTLAUS, R. CARPA,
R. ENE, S. SAVA, R. CHIFOR, M. E. BADEA

INTRODUCTION

Since ancient times, essential oils and other plant extracts have proven their potential as sources of natural products. They have been examined for their possible uses as alternative remedies for the treatment of many infectious diseases. The natural alternative to conventional treatment includes the use of medicinal and aromatic plants, which are a major source of natural organic compounds, for the cure of certain diseases [1,2].

Essential oils obtained from medicinal and aromatic plants are complex organic (carbon-containing) chemical entities, which are generally composed of hundreds of chemical compounds, including terpenes, aldehydes, alcohols, esters, phenols, ethers and ketones, which are responsible for the many characteristic properties of the essential oil.

The antimicrobial impact of essential oils and their chemical components have been recognized in the past by several researchers. Literature studies attest the medicinal properties of essential oils, such as anti-inflammatory, healing or antimicrobial activities, but may also be responsible for negative qualities such as photosensitivity and toxicity [3-5].

Understanding the chemistry of essential oils is important for monitoring the composition, which subsequently allows a better understanding of their biological properties. It has been shown that there is a strong correlation between chemical composition and antimicrobial activity.

According to Xiaoqing Hu et al. [6], photosensitizers (PS) are usually unsaturated, double-conjugated organic molecules, which absorb in the visible spectrum, even close to the IR range and which ensure a good penetration of light into tissues. They are chosen according to the way they bind to the surface (membrane) of microbial cells, so that photodynamic therapy can be effective.

The introduction of essential oils in the composition of gels, leads to a slight increase in water retention in conditions of pH = 4-5. This behavior suggests the formation of homogeneous materials and can be attributed to the physical interaction through intermolecular hydrogen bonds between the phenolic groups of essential oils and the $-NH_2$ and $-OH$ groups of the polymer matrix. These intermolecular hydrogen bonds lead to the stabilization of the macromolecule by the formation of a flexible secondary network that allows the diffusion of water molecules through the polymer chains.

The chemical composition of essential oils is relatively complex and about 20 to 60 different bioactive components are observed such as terpenes, terpenoids and other aromatic and aliphatic constituents with low molecular

weights. Usually, the chemical characterization of many essential oils reveals the presence of only 2-3 major components at a fairly high concentration (20–70%) compared to other components present in trace amounts. Many of these compounds have antimicrobial activity and the presence of the compounds together can be more powerful than the action of only one compound [7-9].

The *novelty* of the study consists in the formulation and evaluation of two experimental natural photosensitizers: PS-T with incense essential oil (Frankincense) and PS-H with a mixture of essential oils (Thieves) that combines several essential oils (Clove, Cinnamon Bark, Lemon, Eucalyptus Radiata and Rosemary), used as photosensitizing agents in antimicrobial photodynamic therapy in the control of the microbial biofilm of the oral cavity.

In this study, the comparative testing of the antimicrobial efficacy of 2 experimental photosensitizers (PS-H; PS-T) with a commercial one FotoSan® was performed. In clinical practice FotoSan® (CMS Dental A/S, DK-2800 Kgs. Lyngby) is used for light-activated disinfection in combination with a photosensitizer (FotoSan Agent) containing toluidine blue O (TBO) as an active ingredient, used to catalyse the photochemical process.
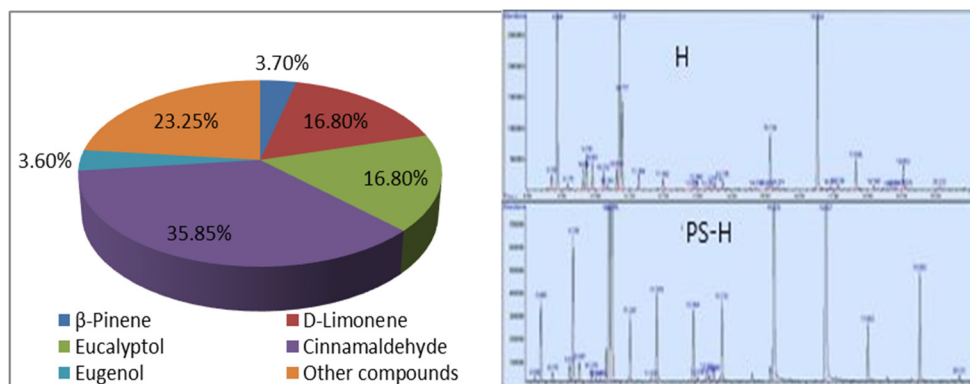
RESULTS AND DISCUSSION

GC-MS analysis shows the volatile compounds specific to experimental PS containing Frankincense essential oil PS-T and Thieves PS-H. The volatile compounds identified from the composition are presented in figure 1 and 2.
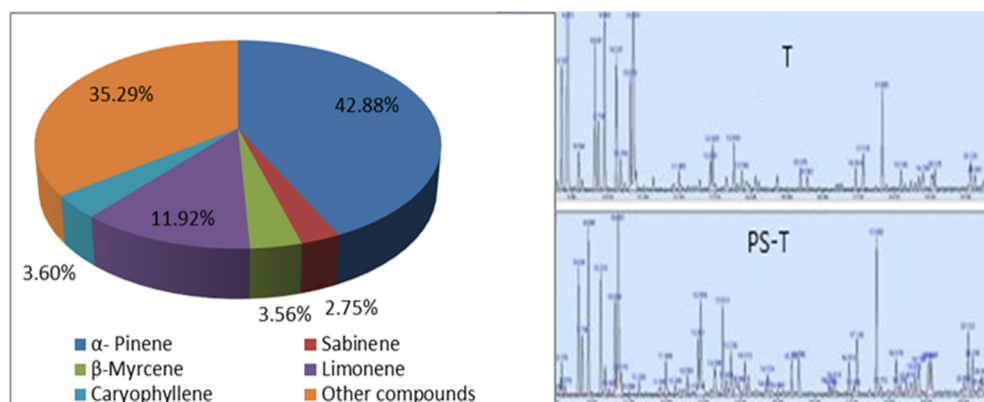
Figure 1. Composition and GC-MS spectra of volatiles identified from photosensitizer (PS-T) and Frankincense (T) essential oil

L. M. DASCALU (RUSU), M. MOLDOVAN, D. PRODAN, I. CIOTLAUS, R. CARPA,
R. ENE, S. SAVA, R. CHIFOR, M. E. BADEA

Figure 2. Composition and GC-MS spectra of volatiles identified from
photosensitizer (PS-H) and Thieves (H) essential oil

According to several published reports the Frankincense essential oil shows antibacterial and antifungal activity [10,11]. This herbal oil with anti-inflammatory effect may be applied in the treatment of gingivitis, which is a periodontal tissue inflammatory disease [12,13].

In this study the essential oil was characterized by the high content of monoterpenes, which constituted 84.86% in which α-Pinene and limonene were the major constituents. The remaining 14.53% was accounted for the sesquiterpenes in which the E-caryophyllene was the major constituent (fig.1).

GC-MS analysis (fig. 2) shows the volatile compounds specific to the mix of essential oils: clove, lemon, cinnamon, eucalyptus, rosemary contained in PS-H gel. Composition of volatiles recovered from PS-H was presented in figure 2. Clove oil (*Syzygium aromaticum*) is a mixture of different constituents, with three main active ingredients being eugenol, eugenyl acetate and caryophyllene (fig. 2). It is contributed to the antimicrobial and antioxidant properties of the oil [14,15].

The main compounds were limonene, γ-terpinene, β-pinene, myrcene, sabinene and citral (fig. 2). Lemon oil is also used for its germicidal, antioxidant and anticarcinogenic properties [16,17].

The major compound of cinnamon EO (essential oil) is cinnamaldehyde, which possesses the strongest antifungal activities [18].

Eucalyptus oil (*Eucalyptus radiata*), constituent from the oil mix analysed includes: Eucalyptol (1, 8- cineole), beta-pinene, alpha-pinene, alpha-phellandrene, para-cymene camphor, isoborneol, levomentol (fig.2). Eucalyptus oil is recognized for its antibacterial and antioxidant properties [19]. The volatile profile of the rosemary essential oil (Rosmarinus officinalis), is given by: alpha pinen, 1.8-cineol (eucalyptol), camphor, camphene, β-myrcene, limonene. The rosemary essential oil is known to possess insecticidal, antifungal, acaricidal, antibacterial and cytotoxic activities [20,21].

The preliminary analysis of the GC chromatograms of the studied EO (essential oils) showed an abundance of several volatile compounds. The main components of Frankincense EO identified in our study were α-Pinene, Limonene and Caryophyllene, while the main constituents of Thieves EO were cinnamaldehyde, eucalyptol and D-limonene.

Major constituents of essential oils with antimicrobial activity include terpenoids such as thymol, carvacrol, para-cymene and cinnamaldehyde. These compounds were demonstrated as components in several of the essential oils tested. α- and β-pinene are well-known representatives of the monoterpenes group and are found in many essential oils [22]. Pinene ($C_{10}H_{16}$) is a bicyclic, double bond, terpenoid hydrocarbon. They are among the best-known representatives of a broad family of monoterpenes.

Antimicrobial activity

Most photosensitizing agents showed antimicrobial activity for both Gram-positive (G+) and Gram-negative (G-) strains.
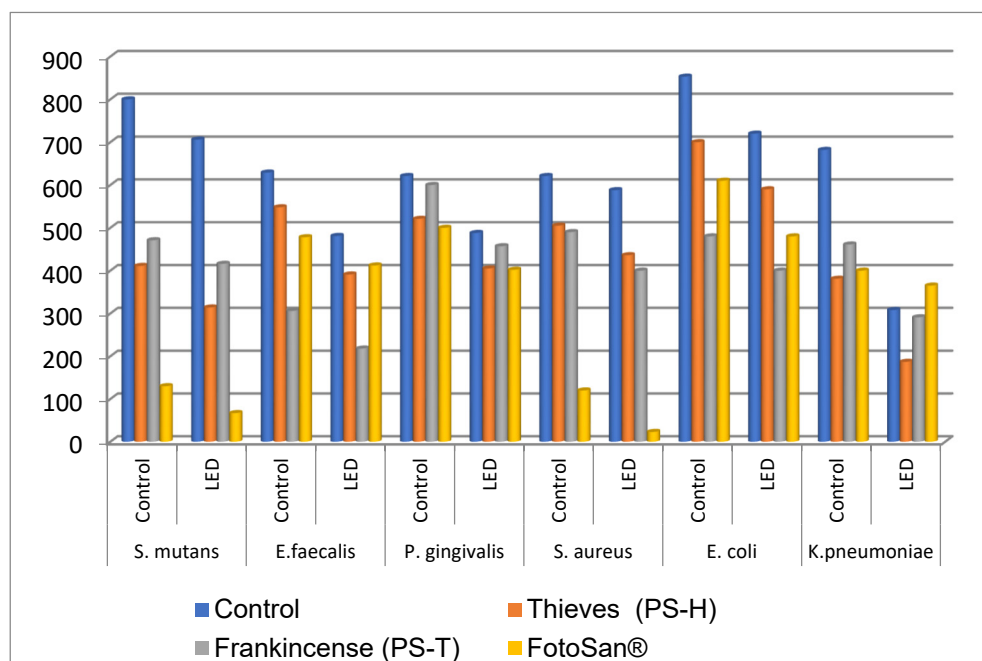
Figure 3. Antimicrobial activity of experimental (PS-T; PS-H) and commercial (FotoSan) photosensitizers

In the absence of irradiation, in Control samples, the number of Gram-positive and Gram-negative colonies formed was very high (Fig. 3), in all bacterial strains. In figure 3 can be observed that both experimental photosensitizers showed antibacterial activity compared to the control gel and the effect is comparable to that of the commercial product. The photosensitizer (PS-T) based on incense essential oil (T) had a more pronounced antibacterial effect on *E. faecalis*, *S. aureus* and *E. coli* strains. In contrast, the photosensitizer PS-H with a mixture of essential oils (H) showed a more pronounced antibacterial effect on *S. mutans*, *P. gingivalis* and *K. pneumoniae* strains.

Compared to the commercial photosensitizer, the experimental photosensitizers showed a better antimicrobial effect on *E. faecalis*, *P. gingivalis*, *E.coli* and *K. pneumoniae* strains. Eucalyptol is a major component of the EO from several species, in particular the *Eucalyptus* genus and is a recognized antimicrobial agent [23].

According to the antimicrobial results, both samples displayed notable activity towards all tested strains. Frankincense EO exhibited the highest antimicrobial activity on *E. Faecalis* (Gram positive) strain and Thieves EO on *K. pneumoniae* (Gram negative) strain. The antibacterial effect was increased when the use of the gel based on essential oils was associated with a LED light source. The results of this study are consistent with the data found in the literature. Xiao S. [24] states that Thieves essential oil has an antimicrobial effect on the *S. aureus* strain. The efficacy of photodynamic antimicrobial therapy on extracted teeth, without enamel lesions, was analyzed by SEM, after bacterial colonization and after treatment with PS-T and PS-H.

Representative images of the samples after bacterial colonization and after treatment with experimental and commercial PS are shown in figure 4.

Scanning by electron microscopy (SEM) allows the visualization of three-dimensional surface structures at very different resolutions. In our study, we observed a sensitivity of bacteria to this form of testing, by applying the photosensitizers for 4 minutes and then phototherapy for 1 min.

In figure 4 (a,c,e) it could be observed initially a well-defined intact bacterial wall, without discontinuities. In figure 4, (b, d, f) it could be observed the interrupted bacterial wall both longitudinally and transversely, after a single application of therapy according to the described protocol. Bacterial wall damage is observed following LED phototherapy.
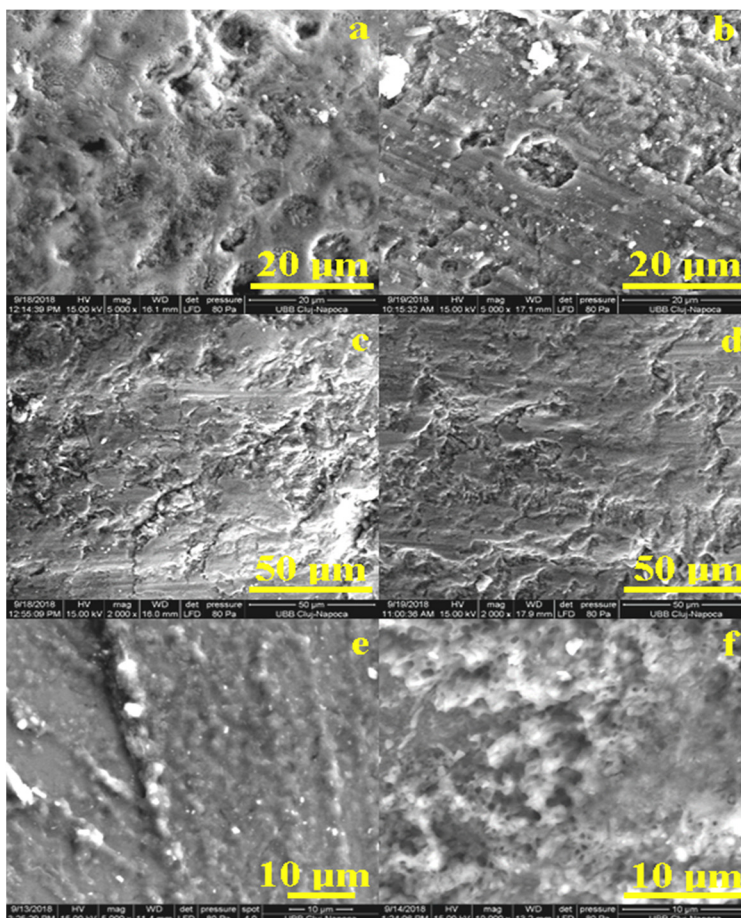
Figure 4. SEM images of enamel teeth at different magnifications: a,c,e) after bacterial colonization and b) after treatment with experimental PS–T and LED; d) after treatment with experimental PS-H and LED; f) after treatment with commercial FotoSan and LED lamp.

CONCLUSIONS

Frankincense and Thieves EO as traditional natural medicines, have extensive and significant pharmacological effects and important antimicrobial properties. In this regard, antimicrobial activity of two experimental gels based on essential oils was tested in several strains with a wide range of observed results; the inhibition of *6 bacteria strains* has been reported. Single bacteria, as well as monolayer chains or three-dimensional aggregates of bacteria were observed by SEM, confirming the bacterial population in saliva.

Our results suggest that EO should be further investigated as a promising source of natural compounds that can be used to combat bacteria strains. Essential oils can inhibit growth of a broad range of pathogens correlating to their presence in aromatic plants.

EXPERIMENTAL SECTION

Obtaining the experimental natural photosensitizers (PS)

For PS formulation, we used 2 essential oils Frankincense (T) and Thieves (H) from Young Living, 9727 AJ Groningen, Netherlands. Thieves contains a mixture of Clove, Cinnamon Bark, Lemon, Eucalyptus Radiata and Rosemary essential oils.

Gels based on natural compounds used as photosensitizers in photodynamic therapy (PDT) were used in the experimental study.

The experimentally PS were prepared from a mixture of gelatin: glycerol (Sigma-Aldrich Inc., St. Louis, USA) in a weight ratio of 1:1 and 60 ml Kaqun® water (Harghita, 535600, Romania), using the following procedure: gelatine and glycerol with 0.015% salicylic acid solution were added to the water.

Experimental photosensitizers were characterized by chromatographic analysis (GC-MS) and the antibacterial effect was evaluated on six gram-positive and gram-negative bacterial strains. The effect of antimicrobial photodynamic therapy on tooth enamel was evaluated by SEM microscopy.

The gas chromatography - mass spectrometry (GC-MS)

For this study were used two type of gels, gel with Frankincense essential oil (T) and Thieves (H), a mixture of essential oils, as antibacterial agents with applications in dentistry. By the GC–MS analysis technique we identified the chemical composition of the tested essential oils.

GS-MS, sample processing: (0.5 g) were dispersed in hexan (10 mL) for 2h, then was ultrasonicated for 15 minutes and centrifuged at 4400 rpm for 15 minutes. The volatile fraction in hexan was filtered and then dried over sodium sulfate. The essential oil recovered from gel was injected into GC-MS.

GC-MS Method: Agilent GC-MS Gas Chromatograph - 7890A/5975/ 2008 (Agilent Technologies, Inc. Europe, Waldbronn, Germany) was used for analysis; GC-MS analyzes were performed in scan mode on a DB-5MS (30m x 0.25mm x 0.25μm) capillary column (Agilent 19091S-433M), high

purity He carrier gas at a flow rate of 1 mL /min. Temperature program: initial temperature 40°C with a ramp of 8°C / min up to 220°C, then with 20°C up to 280°C and maintained 5 min, injector temperature 250°C, injection volume of 1 µL, 100: 1 slides, MS 70eV, mass range u.a.m. 30-400. NIST library was used for identification/ confirmation of the structure components. In addition, a C8-C20 standards alkanes (Alkane Standard Solution C8-C20, Sigma Aldrich) was used for calculation of the linear retention index (RI), and matching the experimental values with those reported in the literature for similar chromatographic columns, in the same condition.

Antimicrobial activity

Microbial strains

The essential oils were tested against 6 Gram positive and Gram negative bacteria. The Gram positive bacteria strains were: *Staphylococcus aureus* ATCC 6538, *Streptococcus mutans* ATCC 25175, *Enterococcus faecalis* ATCC 29212. The Gram negative bacteria strains were: *Escherichia coli* ATCC 25922, *Klebsiella pneumoniae* ATCC 4352, *Porphyromonas gingivalis* ATCC 33277.

Determination of bactericidal activity

For each bacterial strain, 96-well plates were used. For each plate 3 types of photosensitizing agents were inoculated in triplicate and for each bacterial strain to be tested. From fresh colonies of bacteria grown on Mueller-Hinton medium, bacterial suspensions were made in BHI broth adjusted to a turbidity of 0.5 McFarland. 150 µL of bacterial suspension and 125 µL of photosensitizing agents were placed in each well. The inoculated plates were placed in the dark 5 minutes before irradiation. One board was kept for CONTROL and one was subjected to LED lighting with Fotosan lamp (630nm, 40 mW/cm^2).

SEM analysis

The irradiation time for each well was 60 sec. After irradiation, the 96-well plates were placed in an incubator at 37°C for 24 h.To assess bacterial viability, 50 µL of each sample was mixed with 200 µL sterile PBS and placed on Petri dishes with Mueller-Hinton solid culture medium. These plates were again incubated at 37°C for 24 h. After incubation, the colonies appeared for each sample of the 3 experimental variants and were counted.

In order to evaluate the efficiency of photodynamic therapy and the formulated experimental PS, we used enamel teeth with no lesions (n = 30). The extracted teeth were immersed in natural saliva, collected from subjects with high carioreceptivity. They were then incubated at 37°C for at least 48 hours. After the initial examination, photosensitizers (PS-T; PS-H, FotoSan) were applied on the teeth for 4 minutes. After this time, PS was removed by rinsing with 0.9% saline, taking care that the jet did not act directly on the area of interest to avoid mechanical removal of bacteria.

Dental surfaces were subjected to photodynamic therapy using the LED phototherapy with Fotosan lamp (630nm, 40 mW/cm^2). for 1 minute. To evaluate the antibacterial effect, dental surface was examined by SEM (Inspect S, FEICompany) before and after the application of photosensitizers and LED irradiation.

The researches were on extracted teeth and all subjects gave their informed consent for inclusion before they participated in the study. The study was conducted in accordance with the Declaration of Helsinki and the protocol was approved by the Research Ethics Committee of the University of Medicine and Pharmacy "Iuliu Hatieganu", Cluj-Napoca, Romania (authorization no. 578/10.12.2019).

REFERENCES

1. G.N. Teke; K. . Elisée; K.J. Roger; *BMC Complement. Altern. Med*.,**2013**,*13*, 130.
2. M.K. Swamy; U.R. Sinniah; *Molecules*, **2015**, *20*, 8521-8547.
3. M.K. Swamy; M.S. Akhtar; U.R. Sinniah; *Evid. Based. Complement. Alternat. Med*., **2016**, *2016*, 3012462, 21 p.
4. A. Orchard; S. van Vuuren; *Evid. Based. Complement. Alternat. Med.,* **2017**, **2017**, 4517971, 92 p
5. M. Valdivieso-Ugarte; C. Gomez-Llorente; J. Plaza-Díaz; Á. Gil; *Nutrients*., **2019**, *11*, 2786.
6. X. Hu; Y.Y. Huang; Y. Wang; X. Wang; M.R. Hamblin; *Front Microbiol*., **2018**, *9*, 1299.
7. J.E. Patterson; L. McElmeel; N.P. Wiederhold; *Open Forum Infect. Dis*., **2019**, *6*, ofz502.
8. N.A. Mahizan; S.K. Yang, C.L. Moo, A.A.L. Song; C.M. Chong; C.W. Chong; A. Abushelaibi; S.H.E. Lim; K.S. Lai; *Molecules*.,**2019**, *24*, 2631.
9. B. Salehi; S. Upadhyay; I. Erdogan Orhan; A.K. Jugran; S.L.D. Jayaweera; D.A. Dias; F. Sharopov; Y. Taheri; N. Martins; N. Baghalpour; W.C. Cho; J. Sharifi-Rad; *Biomolecules*, **2019**, 9, 738.

10. T. Umezu; *Jpn. J. Pharmacol*., **2000**, *83*, 150-153.
11. A. Ali; M. Wurster; N. Arnold; A. Teichert; J. Schmidt; U. Lindequist; L. Wessjohann; *Rec. Nat. Prod*., **2008**, *2*, 6-12.
12. M.K. Samani; H. Mahmoodian; A. Moghadamnia; A.P.B. Mir; M. Chitsazan; *DARU J. Pharmaceutical Sci*., **2011**, *19*, 288–294.
13. T. Lakshmi; R. Rajesvari; A. Selvaraj; R. Parameswari; *J. Adv. Pharmacy Education & Res.*, **2017**, *7*, 182-186.
14. B. Amelia; E. Saepudin; A.H. Cahyana; D. U. Rahayu; A. S. Sulistyoningrum; J. Haib; *AIP Conference Proceedings, **2017**, *1862*, 030082.
15. L. Jirovetz; G. Buchbauer; I. Stoilova; A. Stoyanova; A.E. Krastanov; J. Schmidt; *J. Agric. Food Chem*., **2006**, *54*, 6303–6307.
16. A. Gök; Ş. Ismail Kirbaşlar; F. Gülay Kirbaşlar; *J.Essent. Oil Res*., **2015**, *27*, 17-22.
17. F. Spadaro; C. Circosta; R. Costa; F. Pizzimenti; D.R. Palumbo; F. Occhiuto; *J. Essent. Oil Res*., **2012**, *24*, 187–193.
18. K. Małgorzata Brodowska; A.J. Brodowska; K. Śmigielski; *Eur. J. Biol. Res.*, **2016**, *6*, 310-316.
19. R.K. Bachheti; *Der Pharma Chemica*, **2015**, *7*, 209-214.
20. S.A. Socaci; M. Tofană; C. Socaciu; *Bulletin UASVM, Agriculture*, **2008**, *65*, 405-409.
21. V. Miclea; I. Donca; M. Culea; N. Fiţ; P. Podea; *Studia UBB Chemia*, **2019**, *2*, 127-138.
22. M. Soškić; D. Bojović, V. Tadić; *Studia UBB Chemia*, **2016**, *2*, 127-136.
23. A. Nafis; A. Kasrati; C.A. Jamali; L. Custódio; S. Vitalini; M. Iriti; L. Hassani; *Antibiotics, **2020**, *9*, 140.
24. S. Xiao; P. Cui; W. Shi, Y. Zhang; *BMC Complement Med. Ther*., **2020**, *20*, 99.3.

ELEMENTAL ANALYSIS OF CULINARY HERBS AND SPICES BY ICP OES: CLASSIFICATION BY CHEMOMETRICS

ALEKSANDRA N. PAVLOVIĆ[a, *], JELENA M. MRMOŠANIN[a], SNEŽANA Č. JOVANOVIĆ[a], SNEŽANA S. MITIĆ[a], SNEŽANA B. TOŠIĆ[a], JOVANA N. KRSTIĆ[b] and GORDANA S. STOJANOVIĆ[a]

ABSTRACT. The inductively coupled plasma optical emission spectrometry method (ICP OES) was optimized and validated for the quantification of 21 elements in 88 samples of 23 types of culinary herbs and spices. All analyzed samples were low in Na, but rich in Ca, K and P. Among the microelements, the most abundant was Fe, followed by Cu, Zn, Cr, and Se. The concentrations of toxic elements (Cd and Pb) were below the permissible limits given by the World Health Organisation (WHO). Chemometrics was performed by the principal component analysis (PCA) and cluster analysis (CA). PCA generated two principal components that explained 43.82% of the total variance in the data and all samples were classified into six groups based on the element content. Also, PCA and CA allowed the differentiation and classification of culinary herbs and spices based on the concentration of five major elements.

Keywords: *culinary herbs, spices, macro and microelements, ICP OES, chemometrics, classification*

INTRODUCTION

Spices have been an irreplaceable part of traditional and modern cuisines since ancient times. Herbs are plants with aromatic leaves and represent a subset of spices [1]. Not only do spices give a specific flavour to food, but they also have a beneficial effect on human health. In a study conducted by Naveed et al. [2], essential oils from four Pakistani spices

---

[a] *University of Niš, Faculty of Sciences and Mathematics, Department of Chemistry, Višegradska 33, P.O. Box 224, 18000 Niš, Serbia*

[b] *University of Union Nikola Tesla, Faculty of Applied Science, Department of Contemporary Food Technology, Dušana Popovića 22a, 18000 Niš, Serbia.*

* *Corresponding author aleksandra.pavlovic@pmf.edu.rs*

cumin, cinnamon, cardamom and clove showed the antibacterial activity against multi-drug resistant bacteria: *S. typhi, S. paratyphi, E. coli, S. aureus, P. fluorescens* and *B. licheniformis.* El-Ghorab et al. [3] pointed out the antioxidant properties of ginger and cumin. The use of essential oils and extracts from spices as preservatives in food protection has also been described [4, 5]. Sgorbini et al. [6] characterized and quantified biologically active markers in some herbs and species (clove, American peppertree, black pepper, white pepper, rosemary, sage and thyme) using separative (HS-SPME-GC-MS) and non-separative (HS-SPME-MS) approaches. They used aromatic markers, eugenol for cloves, carvacrol and thyme for thyme, and thujones for saga which were directly quantified on the solid matrix through the multiple headspace extraction-HS-SPME. Paleari et al. [7] characterized spices and aromatic herbs using GC/MS. They separated components which came from spices/aromatic herbs from the others which came from phenomena due to lipolytic endoenzymatic processes.

Apart from the importance of the organic components, the importance of major and trace elements in spices must not be neglected. The results obtained by Khan et al. [8] indicated that the essential trace elements that were found in aromatic spices have a good nutritional contribution. In contrast, the concentrations of toxic elements (As, Cd, Pb) were low and did not pose a threat to human health. Ghanjaoui et al. [9] have developed and validated the inductively coupled plasma optical emission spectrometry (ICP OES) method for the determination of trace elements in basil powder samples from Spain and Morocco. In a study conducted by Tahri et al. [10], 14 elements were determined by inductively coupled plasma atomic emission spectrometry (ICP AES) in rosemary samples collected in eastern Morocco. Özcan and Akbulut [11] have estimated the content of major and minor elements in medicinal and aromatic plants grown in Turkey which are used as spices, condiments and herbal tea by ICP AES, concluding that mineral content varied significantly depending on the species and location of the plant, while the content of heavy metals was very low in all of the samples. Kumaravel and Alagusundaram [12] reported 15 trace elements in five Indian spices, with the absence of As and Hg in all of the samples.

However, Abou-Arab and Abou Donia [13] noted that heavy metals present in some spices exceeded the permissible levels, which could be a consequence of the use of contaminated irrigation water, the addition of some fertilizers and herbicides, or the contamination from traffic. The mineral and trace elements content were determined in culinary herbs and spices in many studies. Some of these studies deal with the determination of a small number of elements in a specific type of fresh herbs or spices. Also, before any chemometric technique can be used, it is important to ensure that

accurate analytical data are being obtained since the conclusions drawn from chemometric techniques can only be as reliable as the data. In this study, all samples were analysed under analytical control with the optimization of the operating parameters of the instrument and with the analysis of a certified reference material. Based on the lack of comprehensive studies of all well-known macro and microelements involving large number of culinary herb and spice samples, the aim of this work was to determine macro and microelements (Al, B, Ba, Be, Ca, Cd, Co, Cr, Cu, Fe, K, Mg, Mn, Na, Ni, P, Pb, Se, Si, V, Zn) in 88 commercially available samples of culinary herbs and spices after the optimization and validation of the ICP OES method, as well as their classification using the principal component analysis (PCA) and cluster analysis (CA).

RESULTS AND DISCUSSION

Optimization of the Method

According to Mermet [14], the Mg II/Mg I line intensity ratio higher than 10 was selected to evaluate ICP operating conditions and the plasma robustness. The highest Mg II/Mg I ratio was obtained for RF power of 1150 W and nebulizer gas flow of 0.5 L/min. As in previous works [15, 16], the results showed a higher Mg II/Mg I ratio for the radially viewed configuration (Table S1).

A final selection of wavelength lines was taken into consideration after the study of ratio $slope_{cal}/slope_{sam}$ as well as the accuracy obtained for each line and spectral interferences. As can be seen in Table 1 the slopes of both kinds of lines were statistically comparable, which indicates the lack of matrix effects. ME data up to 7.6% indicates that the method of evaluation of the matrix effect generates reliable results.

Validation of the Method

The accuracy of the method was checked by analyzing the SRM. The recovery percentages for all elements were in the range 91-105% except for Na, Cd, Pb, Se and Si which were < 91%. The percent coefficient of variation (CV%) obtained for the precision evaluation for all analyte elements was ranged from 1.7% for Ca to 14.9% for Cr. Nevertheless, in all cases, the accuracy and precision were within the acceptable recoveries and CV percentages obtained from the Horwitz function [17-19] and the AOAC Peer-Verified Methods (PVM) program on the analyte level [20].

Table 1. The analyte line selected with the ratio $slope_{cal}/slope_{sam}$ and matrix effect (ME), as well as coefficient of determination (R^2), LOD and LOQ of the calibration for each element determination

Element	Wavelength (nm)	Plasma view mode	$Slope_{cal}/Slope_{sam}$	ME (%)	R^2	LOD (ng/g)	LOQ (ng/g)
Al	309.271	axial	0.976	-2.4	0.9990	77.5	260
B	249.773	axial	1.013	1.3	0.9982	8.00	26.6
Ba	455.403	axial	0.981	-1.9	1	0.50	1.90
Be	234.861	axial	0.968	-3.2	0.9998	0.80	2.40
Ca	393.366	radial	a	a	0.9984	0.10	0.50
Cd	226.502	axial	1.019	1.9	1	2.40	7.80
Co	228.616	axial	0.971	-2.9	1	4.10	13.6
Cr	283.563	axial	0.952	-4.8	0.9996	7.80	25.9
Cu	324.754	axial	0.988	-1.2	1	7.60	25.5
Fe	259.940	axial	1.009	0.9	1	7.50	25.1
K	766.490	radial	a	a	0.9990	6.60	22.1
Mg	279.553	radial	a	a	0.9990	0.20	0.60
Mn	257.610	axial	1.023	2.3	1	1.20	4.40
Na	589.592	radial	a	a	1	0.10	0.50
Ni	221.647	axial	1.054	5.4	0.9996	7.40	25.0
P	213.618	radial	a	a	1	49.0	163
Pb	220.353	axial	1.063	6.3	1	25.4	84.5
Se	196.090	axial	1.049	4.9	1	41.8	139
Si	251.611	axial	0.924	-7.6	0.9974	20.6	68.8
V	309.311	axial	0.988	-1.2	1	7.40	24.8
Zn	213.856	axial	1.044	4.4	0.9996	1.50	4.80

[a]It was not necessary to optimize $slope_{cal}/slope_{sam}$ and matrix effect for the major elements Ca, K, Mg, P and Na because of their relatively high concentration in the samples

Macro and Microelements in Culinary Herbs and Spice Samples

The results of the elemental analysis of spice and herb samples (Supplementary materials) indicate that Ca and K were the most abundant macro elements, followed by P, Mg, and Na. The mean concentrations of Ca

are ranged from 0.6 mg/g in garlic to 17.4 mg/g in lovage, while the mean concentrations of K are ranged from 1.45 mg/g in cinnamon to 10.9 mg/g in parsley. The highest mean concentrations of P and Mg were found in white mustard and celery yielding 7.83 mg/g and 4.75 mg/g, respectively.

The lowest mean concentrations of P and Mg were found in cinnamon yielding 0.570 mg/g and 0.381 mg/g, respectively. The mean concentration of Na varied and ranged from 2.85 µg/g in chive to 138 µg/g in clove. All analyzed samples are low in Na, but rich in Ca, K and P. The macro element contents are in good agreement with the reported data on macro element content of spices and condiments used in Turkey, but lower for Na (1.16-16.45 mg/g Ca, 3.57-27.67 mg/g K, 0.48-4.31 mg/g Mg, 0.44-9.37 mg/g P, and 1.1-20.91 mg/g Na) [11].

Among the essential elements, Fe was the most abundant, followed by Cu, Zn, Cr and Se. The results obtained for these metal concentrations are in accordance with the literature data for aromatic spices [8] and medicinal herbs [21]. The mean content of Se, which has a role in the antioxidant defence system of the body, ranged from n.d. in thyme, basil, dill, parsnip, nutmeg, garlic, chive, rosemary and caraway to 0.255 µg/g in ginger. According to Aras and Ataman [22], the differences in the content of Se can be a consequence of the soil composition in which the food is grown.

The manganese, cobalt, silicon, nickel, boron and vanadium were detected in all samples and levels were among 9.51-249 µg/g, 0.076-0.813 µg/g, 7.68-936 µg/g, 0.843-4.89 µg/g, 2.57-30.1 µg/g and 1.05-19.9 µg/g, respectively. Boron is essential for plants and tends to accumulate in plant tissues. Rich sources of B are nuts, leafy vegetables and fruits [22]. According to WHO [23] the mean daily intake of B for adults is 1.2 mg per day.

In this study, the levels of Be and Ba were in the range of n.d.-0.077 µg/g and 3.98-314 µg/g, respectively. Ba was detected in all samples. When grown in Ba-rich soils, plants can accumulate higher levels of Ba, which further increases the potential dietary Ba intakes [24].

Lead and cadmium have no essential function in plants and at high concentrations are toxic for plants and animals as well as for humans. The uptake of Pb and Cd by plant roots depends on the concentration, the oxidation state of this metal in the solution, and the physical-chemical characteristics of the soils such as pH content of clay, minerals, and organic matter [25, 26]. The Joint FAO/WHO [27] provisionally recommends that the weekly intake of lead should not exceed 25 µg/kg of body weight per week and 7 µg/kg of body weight should be regarded, provisionally, as the maximum tolerable weekly intake of Cd. The results obtained for Pb (0.38-2.67 µg/g) and Cd (0.032-0.221 µg/g) are in accordance with the literature data [8,12] and below the limits given by the FAO/WHO [27].

ALEKSANDRA N. PAVLOVIĆ, JELENA M. MRMOŠANIN, SNEŽANA Č. JOVANOVIĆ,
SNEŽANA S. MITIĆ, SNEŽANA B. TOŠIĆ, JOVANA N. KRSTIĆ, GORDANA S. STOJANOVIĆ

Pearson's Correlation Analysis

In this study, the correlation analysis was performed at a 0.05 probability level to evaluate the relationship among the element concentrations. The results are included in Supplementary material (Table S2 (Supplementary material). According to Cohen, a strong correlation exists when r ≥│0.5│[28]. Among the elements, K showed a positive correlation with Ca, Mg, B and V; P with Zn; Al with Ni and Si; Cr with Si; and Fe with Ni, Pb and Si.

The elements showing the significant positive correlation are Fe and Si (0.80), Al and Si (0.74) and Fe and Pb (0.73). Of all macro elements Mg shows a good correlation with V (0.84), B (0.74) and Ca (0.71). It is assumed that a good correlation indicates a similar origin of the elements in the tested plants [21]. There were some correlations which were very close to 0, for example, Na with Pb, K, Mg, Cu, Zn, B, Be with Al, Cd with Cr, Ni and Se, which indicates weak relations between these elements.

Chemometric Data Processing

PCA was used for extracting the data from variables and reducing the number of inter-correlated variables to uncorrelated variables (PC), thereby allowing a more accurate estimate [29]. The principal components are rotated so that the total sum of squares of the loading along each axis is maximised [30]. For this chemometric calculation, a data matrix (21×88) was constructed using 88 samples as rows and content of 21 metals as columns. Six principal components with eigenvalues > 1, as suggested by the Kaiser criterion [30], were extracted by PCA. These six components explained about 74.3% of the variation in the data. The first component (PC1) had the highest eigenvalue of 5.44 and explained 25.89% of the total variance. The eigenvalue of the second component (PC2) was 3.76 and explained 17.93% of the total variance in data. As the first two factors explain 43.82% of the total variations and the contributions of the third, fourth, fifth and sixth are considerably lower, PC1 and PC2 were used for a further analysis. Figure 1 shows the score plot for all 88 samples. The first group, in the lower right quadrant, consists of spices from the *Lauraceae* family (cinnamon and bay laurel). This group is extracted by the high concentrations of Cd and Be (Figure 2). The second group, the *Zingiberaceae* family (turmeric and ginger), is located on the negative side of PC1 and the negative side of PC2. This group is extracted by the high concentrations of Cr, Si and Pb. Next to these elements, Al, Ni, and Fe are grouped in the lower left quadrant with the significant positive correlation between Fe and Si (0.80), Al and Si (0.74) and Fe and Pb (0.73). Al and Si are highly present in the soil. Silicon gives strength to the cell wall and increases the resistance of the plant to insects and fungal diseases, while the available Al, despite its toxicity in plants [31], in some species such as *Camellia sinensis* and *Melastoma malabathricum*

has a beneficial effect on plant growth [32]. The third group consists of spices from the *Lamiaceae* family (basil, one sample of marjoram, and one sample of oregano) is located in the negative side of PC1, and in the positive side of PC2. This group is extracted by the high concentrations of V and Zn, and relatively high concentrations of macroelements K, Ca, and Mg (Figure 2). Potassium and phosphorus (negative loadings on PC1 and positive loadings on PC2) in some spices probably originate from artificial fertilizers NPK [33]. Potassium, phosphorus and magnesium are grouped in the same quarter as the elements necessary for photosynthesis. The fourth group includes spices from the *Lamiaceae* family (Breckland thyme, thyme, marjoram, oregano, and rosemary) and it is located near zero of PC1 and PC2. The fifth group, *Apiaceae* (dill, parsley, coriander, caraway, celera, lovage, and parsnip), is between the two groups of *Lamiaceae* and this group is extracted by the high content of P (Figure 2). The sixth group is *Amaryllidaceae* (garlic and chive) and it is located on the positive side of PC1 and near zero of PC2. It can be seen that the samples from the *Brassicaceae* family (white mustard) do not belong to any group. The *Brassicaceae* family was reported as a hyperaccumulator of Cd, Zn and Ni [26, 34].
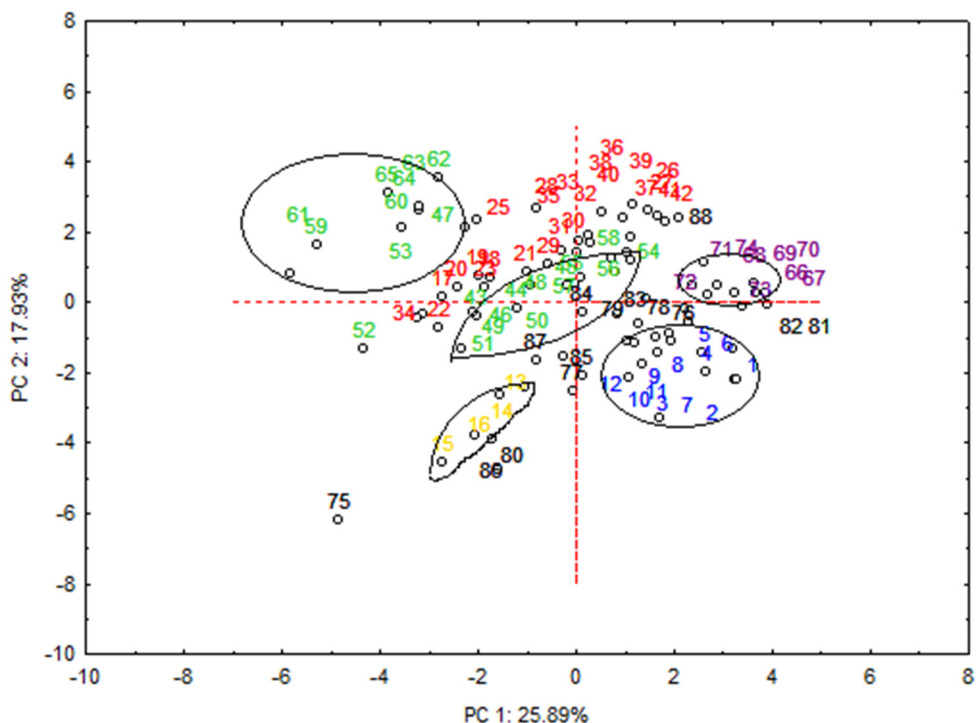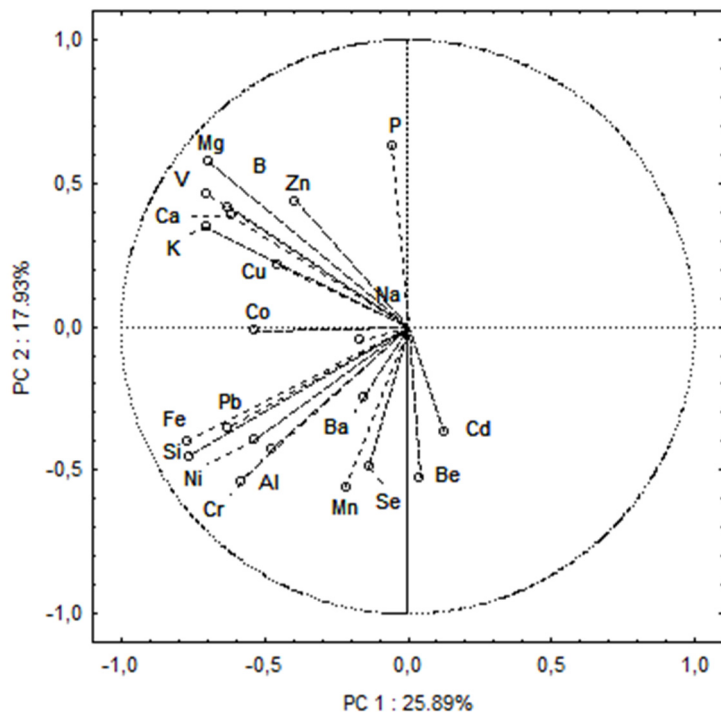

Figure 1. PCA score plot obtained for classification of culinary herbs and spices

ALEKSANDRA N. PAVLOVIĆ, JELENA M. MRMOŠANIN, SNEŽANA Č. JOVANOVIĆ,
SNEŽANA S. MITIĆ, SNEŽANA B. TOŠIĆ, JOVANA N. KRSTIĆ, GORDANA S. STOJANOVIĆ

Figure 2. PCA loading plot of the elemental composition of culinary herbs and spices

When macro elements were considered as the elements with bigger loadings on PC1 and PC2, the scores of PC1 and PC2 in Figure 3 indicate that the macro elements affect the separation of the samples. The first and second components reported 48.65% and 21.58% variance, respectively. The first two components described 70.23% variances for all data. From the higher scores of the first principal component, it can be interpreted that the concentrations of Na on PC1 are higher for the samples from the *Myrtaceae* family (clove) and are lower for all other samples, the concentrations of Ca are similar and the concentrations of Na are high for the samples from the *Apiaceae* family (parsley, dill), the concentrations of Mg are higher for the samples from the *Apiaceae* family (lovage, celery) and the samples from the *Lamiaceae* family (basil). When the second principal component is interpreted, P concentrations on the PC2 loadings are higher for samples from the *Apiaceae* family (coriander, caraway) and for one sample from the *Brassicaceae family* (white mustard) and they are lower for all other samples. The cinnamon and bay laurel samples from the *Lauraceae* family have the lowest content of Mg,

K and P. The turmeric and ginger samples from the *Zingiberaceae* family, the parsnip samples from the *Apiaceae* family, the garlic samples from the *Amaryllidaceae* family, the black pepper samples from the *Piperaceae* family and the nutmeg samples from the *Myristicaeae* family have the lowest content of Ca and K.
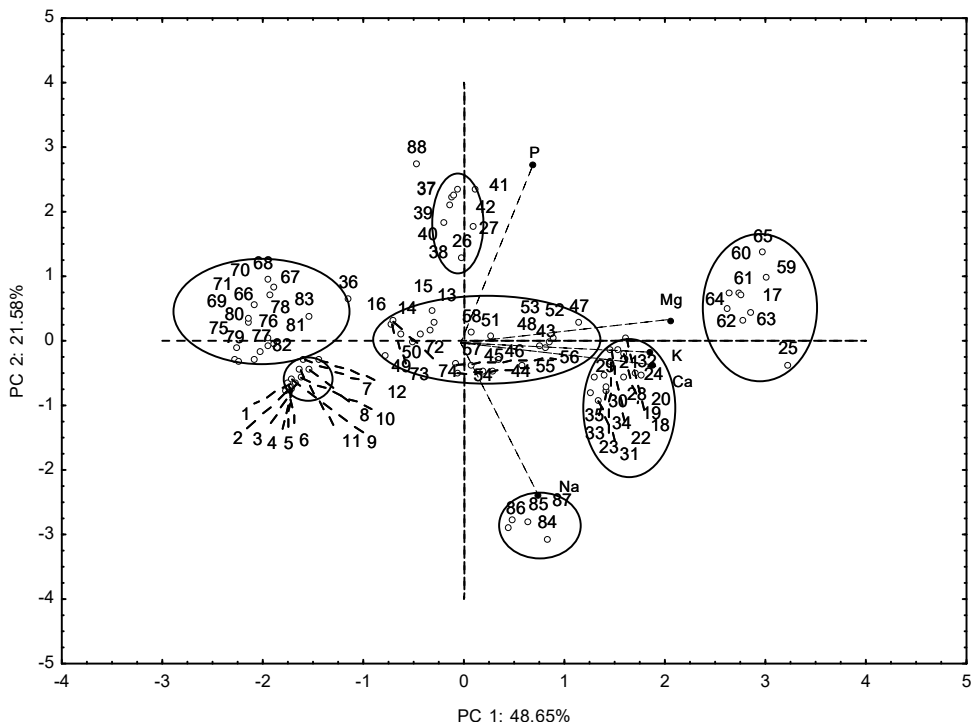
Figure 3. PCA score plot for classification of culinary herbs and spices based on macro element contents

The cluster analysis was performed using the same variables as in PCA, obtaining a second correct classification (Supplementary material) with six clusters. The first cluster on the right consists of samples from the *Lauraceae* family (cinnamon and bay laurel). The second cluster includes samples from the *Amaryllidaceae* (garlic), *Apiaceae* (parsnip), *Myristicaceae* (nutmeg) and Piperaceae (black paper) family. The third cluster consists of two subclusters. The first subcluster includes the samples from the *Myrtaceae* family (clove), the second subcluster contains the samples from the Apiaceae family (parsley, dill). The fourth cluster consists of the samples from the *Apiaceae* (25 celery and 17 lovage) and *Lamiaceae* (59-65 basil) family. The fifth cluster includes the samples from the *Zingiberaceae* (turmeric, ginger) *Lamiaceae* (oregano, Breckland thyme, thyme, marjoram, rosemary), Amaryllidaceae (chive) family.

The sixth cluster includes the samples from the *Apiaceae* family (coriander, caraway). White mustard from the Brassicaceae family is joined to this cluster. Based on the CA results, the samples from the Lamiaceae family are grouped in cluster five, the only base is in cluster four, the Apiaceae family samples are grouped in three clusters (three, four and six) which are next to each other, and this grouping of samples is in accordance with the results obtained from PCA.

CONCLUSIONS

This study contributes to the analysis of element concentrations in 88 culinary herb and spice samples. All of the analyzed samples were found to be high in Ca and K compared to other elements. Among microelements, Fe was the most abundant, followed by Cu, Zn, Cr and Se. The concentrations of toxic elements (Pb and Cd) were below the limits given by FAO/WHO [27]. The correlation analysis showed that strong positive correlations exist between Fe and Si, Al and Si and Fe and Pb. Of all macro elements, Mg showed a good correlation with V, B and Ca. The data analysis was done using chemometrics such as PCA and CA. According to PCA, all samples were classified into six groups. The first group consists of the spices from the family of *Lauraceae* (cinnamon and bay laurel), the second group includes the family of *Myrtaceae* (clove), the third group consists of the spices from the family of *Lamiaceae* (basil, Breckland thyme, thyme, marjoram, rosemary, and oregano), the fourth group includes the spices from the family of *Apiaceae* (dill, parsley, coriander, caraway) and *Amaryllidaceae* (chive), the fifth group is the *Zingiberaceae* family (turmeric and ginger) and the sixth group is the *Amaryllidaceae* family (garlic). The samples from the family of *Brassicaceae* (white mustard) do not belong to any group. CA confirms the results obtained by PCA. Also, the chemometric analysis allowed the classification of culinary herbs and spices based on the concentration of five major elements. Due to their simplicity, PCA and CA can be useful to classify culinary herbs and spices according to their species.

MATERIALS AND METHODS

Reagents

Ultra-scientific (USA) ICP multi-element standard solutions of about 20.00 ± 0.10 mg/L were used as a stock solution for calibration. The glass containers used for storing the samples were treated with a 20% nitric acid and washed with ultra-pure water 0.05 μS/cm (MicroMed high purity water system, TKA Wasseraufbereitungssysteme GmbH) to avoid the contamination of the samples with traces of any metals. The nitric acid (65%) (Merck, Darmstadt, Germany) was of analytical grade.

Instrumentation

The entire analysis was carried out on an iCAP 6000 inductively coupled plasma optical emission spectrometer (Thermo Scientific, Cambridge, UK) which uses the Echelle optical design and a charge injection device solid-state detector. The nebulizer was glass concentric. An iTEVA software from Thermo Scientific (Cambridge, UK) was used to collect and analyze the data. The digestion was performed in a microwave digestion system ETHOS 1 (Milestone, Bergamo, Italy).

Samples

Eighty-eight commercially available samples of twenty-three different culinary herbs and spices were purchased at local markets in Serbia. All samples were bought as pulverized/ground and dried by the manufacturer. No further drying was applied. The English and botanical names of the analyzed culinary herbs and spices are listed in Table 4.

Sample Preparation

The samples were digested according to Khan et al. [8] with the following modifications: 1 g of each sample was accurately weighed and then 7 ml concentrated HNO_3 (70%) and 1 mL H_2O_2 were added and digested using the microwave system. The conditions were as follows: 500 W at 80 °C for 5 min; 500 W at 50 °C for 5 min; 500 W at 180 °C for 10 min, and 0 W for 30 min for cooling. After cooling the content of the tubes was transferred to 25 mL volumetric flask and diluted to 25 mL with a 0.5% HNO_3. The same procedure was carried out for a blank sample and SRM NCS ZC73036. All samples were analyzed in triplicates.

Optimization of the Method

Before the metal analysis, the operating parameters were conducted to check the instrument performance. Using a 27.12 MHz ICP, RF power, and nebulizer, the argon flow rate was varied under the constant values of other plasma conditions: flush pump-rate 100 min^{-1}, analysis pump-rate 50 min^{-1}, coolant gas flow-rate 12 L/min, auxiliary gas flow-rate 0.5 L/min, dual-viewed plasma mode (axial/radial) and sample uptake delay of 30 s.

The standard addition method was used to overcome the matrix effect [35, 36]. A ratio of two elemental signals was used to calculate the matrix effect [37]. The analytic lines were evaluated according to the ratio of the slope of the calibration curve and slope of the standard addition method line ($slope_{cal}/slope_{sam}$).

ALEKSANDRA N. PAVLOVIĆ, JELENA M. MRMOŠANIN, SNEŽANA Č. JOVANOVIĆ,
SNEŽANA S. MITIĆ, SNEŽANA B. TOŠIĆ, JOVANA N. KRSTIĆ, GORDANA S. STOJANOVIĆ

Table 4. Culinary herbs and spices studied

No	n[a]	English name	Species	Family
1-6	6	Cinnamon	*Cinnamomum verum* J.Presl	Lauraceae
7-12	6	Bay laurel	*Laurus nobilis* L.	Lauraceae
13-14	2	Turmeric	*Curcuma longa* L.	Zingiberaceae
15-16	2	Ginger	*Zingiber officinale* Roscoe	Zingiberaceae
17	1	Lovage	*Levistricum officinale* W.D.J. Koch	Apiaceae
18-24	7	Parsley	*Petroselinum crispum* (Mill.) Fuss	Apiaceae
25	1	Celery	*Apium graveolens* L.	Apiaceae
26-27	2	Coriander	*Coriandrum sativum* L.	Apiaceae
28-35	8	Dill	*Anethum graveolens* L.	Apiaceae
36	1	Parsnip	*Pastinaca sativa* L.	Apiaceae
37-42	6	Caraway	*Carum carvi* L.	Apiaceae
43-48	6	Oregano	*Origanum vulgare* L.	Lamiaceae
49-50	2	Breckland thyme	*Thymus serpyllum* L.	Lamiaceae
51	1	Thyme	*Thymus vulgaris* L.	Lamiaceae
52-53	2	Marjoram	*Origanum majorana* L.	Lamiaceae
54-58	5	Rosemary	*Rosmarinus officinalis* L.	Lamiaceae
59-65	7	Basil	*Ocimum basilicum* L.	Lamiaceae
66-71	6	Garlic	*Allium sativum* L.	Amaryllidaceae
72-74	3	Chive	*Allium schoenoprasum* L.	Amaryllidaceae
75-80	6	Black pepper	*Piper nigrum* L.	Piperaceae
81-83	3	Nutmeg	*Myristica fragans* Houtt.	Myristicaceae
84-87	4	Clove	*Syzygium aromaticum* L. Merrill & Perry	Myrtaceae
88	1	White mustard	*Sinapis alba* L.	Brassicaceae

[a] number of samples from each selected spice.

Validation

The validation process involved the linearity of the calibration curve which was tested from 0 to 5 mg/kg, detection (LOD) and quantification limit (LOQ). Both limits were expressed in ng/g. All calibration curves were prepared with four standard solutions, including the blank. The linearity was assessed by the coefficients of the determinations (R^2) of calibration curves. The certified reference material (green tea), supplied by The China National Analysis Center for Iron and Steel, Beijing, China (NCS ZC73036), was analyzed for the determination of B, Ba, Be, Ca, Cd, Co, Cr, Cu, Fe, K, Mg, Mn, Na, Ni, P, Pb, Se, Si, V and Zn in order to the check the accuracy of the method. The samples were handled according to the supplier's specifications.

Supplementary materials containing the standard reference material analysis results and cluster analysis dendrogram can be obtained upon request from the authors.

Data Analysis

All correlations (Pearson's correlation analysis) and chemometric analyses such as principal component analysis (PCA) and cluster analysis (CA) were performed using Statistica 8.0 (StartSoft, Tusla, Oklahoma, USA). PCA is a chemometric technique used to reduce the dimensionality of large datasets, with an increasing interpretability and minimization of data lost. The new PC variables are linear functions of the origin data. PCA is used to reduce solving an eigenvalue problem [38]. Cluster analysis, also called numerical taxonomy, is a chemometric technique used for grouping similar objects in the same clusters. Cluster analysis examines all relationships between variables and does not differentiate between dependent and independent variables [39]. The chemometric techniques are used to evaluate whether or not there is a relationship between the metal contents in different types of herbs which belong to the same family, as well as for grouping samples based on the metal contents.

ACKNOWLEDGMENTS

REFERENCES

1. The United Nations Industrial Development Organization and Food and Agriculture Organization (UNIDO/FAO), "Spices and essential oils: Post-harvest operations indeveloping countries", **2005**. Available from: *http://www.fao.org/3/a-ad420e.pdf.*
2. R. Naveed, I. Hussain, A. Tawab, M. Tariq, M. Rahman, S. Hameed, S. Mahmood, A.B. Siddique, M. Iqbal, *BMC Complem. Altern. M.,* **2013**, *13(1),* 265.
3. A.H. El-Ghorab, M. Nauman, F.M. Anjum, S. Hussain, M. Nadeem, *J. Agric. Food Chem.,* **2010**, *58(14),* 8231-8237.
4. L. Hernández-Ochoa, Y.B. Aguirre-Prieto, G.V. Nevárez-Moorillón, N. Gutierrez-Mendez, E. Salas-Muñoz, *J. Food Sci. Technol.,* **2014**, *51(5),* 957-963.

5. N. Celikel, G. Kavas, *Czech J. Food Sci.*, **2008**, *26(3),*174-181.
6. B. Sgorbini, C. Bicchi, C. Cagliero, C. Cordero, E. Liberto, P. Rubiolo, *J. Chromatography*, **2015**, *1376*, 9-17.
7. M.A. Paleari, V.M. Moretti, C. Bersani, G. Beretta, T. Mentasti, *Meat Sci.*, **2004**, *67(4)*, 549-557.
8. N. Khan, J.Y. Choi, E.Y. Nho, N. Jamila, G. Habte, J.H. Hong, I.M. Hwang, K.S. Kim, *Food Chem.*, **2014**, *158,* 200-206.
9. M.E. Ghanjaoui, M.L. Cervera, M. El Rhazi, M. de la Guardia, *Food Chem.,* **2011**, *125,*1309-1313.
10. M. Tahri, B. Imelouane, F. Aouinti, H. Amhamdi, A. Elbachiri, *Res. Chem. Intermed.,* **2014**, *40*, 2651-2658.
11. M. Özcan, M. Akbulut, *Food Chem.*, **2007**, *107(2)*, 852-858.
12. S. Kumaravel, K. Alagusundaram, *Orient. J. Chem.,* **2014**, *30(2)*, 631-636.
13. A.A.K. Abou-Arab, M.A. Abou Donia, *J. Agric. Food Chem.,* **2000**, *48(6),* 2300-2304.
14. J.M. Mermet, *Anal. Chim. Acta, 1991, 250,* 85-94.
15. M. Mitić, A. Pavlović, S. Tošić, P. Mašković, D. Kostić, S. Mitić, G. Kocić, J. Mašković, *Microchem. J.,* **2018**, *141,* 197-203.
16. J.M. Mrmošanin, A.N. Pavlović, J.N. Krstić, S.S. Mitić, S.B. Tošić, M.B. Stojković, R.J. Micić, M.S. Đorđević, *J. Food Compost. Anal.*, **2018**, *67,* 163-171.
17. W. Horwitz, *Anal. Chem.,* **1982**, *54*, 67-76.
18. M. Thompson, The amazing Horwitz function. AMC Technical Brief No.17., London, UK: Royal Society of Chemistry, **2004**. Available from: *https://www.rsc.org/images/horwitz-function-technical-brief-17_tcm18-214859.pdf.*
19. A.G. Gonzalez, M.A. Herrador, *Trend. Anal. Chem.*, **2007**, *26(3)*, 227.
20. Method Validation Program (OMA/PVM Department), including Appemdix D: Guidelines for collaborative study procedures to validate characteristics of a method of analysis, Rockville, MD, USA: AOAC International, **2000**, Available from:*http://www.aoac.org/aoac_prod_imis/AOAC_Docs/StandardsDevelopme nt/Collaborative_StudyValidation_Guidelines.pdf.*
21. Ş. Tokalioğlu, *Food Chem.*, **2012**,*134(4),* 2504-2508.
22. N.K. Aras, O.Y. Ataman, "Trace element analysis of food and diet", RSC Food Anal Monographs, Cambridge, United Kingdom, The Royal Society of Chemistry, **2006**.
23. World Health Organization (WHO), "Boron", Environmental Health Criteria 204: International programme on chemical safety [online]. Geneva, Switzerland, **1998**. Available from: *http://www.inchem.org/documents/ehc/ehc/ehc204.htm/*.
24. World Health Organization (WHO), "Barium and barium compounds", Concise International Chemical Assessment Document 33 [online]. Geneva, Switzerland, **2001**. Available from: *https://apps.who.int/iris/bitstream/handle/10665/42398/9241530332.pdf?sequ ence=1/.*
25. M. Brokbartold, M. Wischermann, B. Marschner, *Water Air Soil Pollut.,* 2011, *223(1),* 199-213.

26. D.K. Gupta, F.J. Corpas, J.M. Palma, "Heavy metal stress in plants". Springer-Verlag, Berlin Heidelberg, Germany, **2013**.

27. Food and Agriculture Organization and World Health Organization (FAO/WHO), "Trace elements in human nutrition and health", International Atomic Energy & Food and Agriculture Organization of the United Nations Geneva, Geneva, Switzetland, **1996**. Available from:
https://www.who.int/nutrition/publications/micronutrients/9241561734/en/.

28. J. Cohen, "Statistical power analysis for the behavioral science" 2nd edition, Lawrence Erlbaum Associates, New York, **1988**.

29. T.W. Anderson, "An introduction to multivariate statistical analysis" 3rd edition, John Wiley and Sons, Hoboken, New Jersey, **2003**.

30. H.F. Kaiser, *Educ. Psychol. Meas.*, **1960**, *20,* 141-151.

31. S.R. Imadim, S. Wasee, A.G. Kazi, M.M. Azooz, P. Ahmad, "Aluminum toxicity in plants" An overview. In: Ahmad, P. (Ed.): Plant metal interactions, 1st edition, Elsevier Inc, Amsterdam, **2016**, pp. 1–20.

32. R. Hajiboland, S. Bahrami-Rad, J. Barcelo, C. Poschenrieder, *J. Plant Nutr. Soil Sc.,* **2013**, *176,* 616-625.

33. A. Azizi, F. Yan, B. Honermeier, *Ind. Crops Prod.,* **2009**, *29(2/3),* 554-561.

34. R. Reeves, NATO Science Series IV: Earth Environmental Sciences, **2006**, 68, 25.

35. J.L. Todoli, L. Gras, V. Hernandis, J. Mora, *J. Anal. Atomic Spectrom.,* **2002**, *17(2)*,142-169.

36. M.L. Salit, G.C. Turk, A.P. Lindstrum, T.A. Butler, C.M. Beck, B. Norman, *Anal. Chem.*, **2001**, *73(20)*, 4821-4829.

37. K.E. Sharpless, J.B. Thomas, S.J. Christopher, R.R. Greenberg, L.C. Sander, M.M. Schantz, M.J. Welch, S.A. Wise, *Anal. Bioanal. Chem.*, **2007**, *389(1)*,171-178.

38. I.T. Jolliffe, J. Cadima, *Philos. T.R. Soc. A*, **2016**, *374*:*20150202*.

39. F. Zolfaghari, H. Khosravi, A. Shahriyari, M. Jabbari, A. Abolhasani, *PLoS one,* **2019**, *14(12)*, e0226355.

THE COMPARATIVE OVERVIEW OF HPLC ANALYSIS OF DIFFERENT EXTRACTS FROM *MORUS* SPECIES FROM SOUTHEAST SERBIA

DANICA DIMITRIJEVIĆ[a]*, DANIJELA KOSTIĆ[b], MILAN MITIĆ[b], DUŠAN PAUNOVIĆ[a], BRANKA STOJANOVIĆ[a], JOVANA KRSTIĆ[a], SLAVICA STEVANOVIĆ[a], JASMINA VELIČKOVIĆ[a]

ABSTRACT. The aim of this work was to evaluate the content of phenolic compounds (phenols, flavonoids and anthocyanins) of *Morus alba* L. fruit (white mulberry), *Morus rubra* L. (red mulberry) and *Morus nigra* L. fruit (black mulberry) by the HPLC analysis. In the extracts of white, red and black mulberry identified the four phenolic acids by HPLC analysis: chlorogenic, 4-caffeoylquinic, 5-caffeoylquinic and caffeic acid. 5-caffeoylquinic acid was identified in all tested extracts of white, red and black mulberry. 4-caffeoylquinic acids contain all the extracts except methanol extract of red mulberry. Caffeic and chlorogenic acid containing methanol extracts of white and red mulberry.

Keywords: Morus species, HPLC analysis.

INTRODUCTION

The mulberry belongs to the genus *Morus* of the family *Moraceae*. Mulberry is found from temperate to sub-tropical regions of the Northern hemisphere to the tropics of the Southern hemisphere and they can grow in a wide range of climatic, topographical and soil conditions. These are widely spread throughout all regions from the tropics to the sub-arctic areas. Genus Morus is widespread in Asia, Europe, North and South America and Africa as well.

Morus species are deciduous and in a period of low temperatures during the winter require to break dormancy. Mulberry fruit may be colored white, red or black when they are ripe. Deep-colored fruits are good sources of phenolics, including flavonoids, anthocyanins and carotenoids [1–4], and

---

[a] *Faculty of Applied Sciences, University of Belgrade, Serbia*
[b] *Faculty of Sciences and Mathematics, University of Nis, Serbia*
*Corresponding author: danicadimitrijevic7@gmail.com

mulberries are rich in phenolics [5]. Mulberry has an unique delicious fruit, sour and refreshing taste. It has been used as a folk remedy to treat oral and dental diseases, diabetes, hypertension, arthritis and anemia [6]. The bright black and purple mulberry fruits, which have a very pleasant taste when eaten fresh, are also used in jams, juices, liquors, natural dyes as well as in the cosmetics industry [7]. The plant has high level of anthocyanins; hence it has a very important role in the food industry. It is considered that the fresh fruit color comes from anthocyanins present in the fruit. This has contributed to the positive effects of fruit on the people health. The mulberry is found to be especially rich in anthocyanins, flavonoid and phenol compounds. The total content and the yield (percentage) of these compounds is dependent on geographic location and soil on which the mulberry tree grows. Despite the previous research on this plant, there is no information about its contents. Accordingly, the results obtained in this study differ from the results of *Morus* species found in other countries.

RESULTS AND DISCUSSION

Table 1 shows a comparative overview of HPLC analysis of three types of mulberry.

A total of four phenolic acids have been identified in white, red and black mulberry extracts: chlorogenic, neochlorogenic, cryptochlorogenic and caffeic acid. Neochlorogenic acid was confirmed in both methanolic and acetone extracts of white, red and black mulberry. Cryptochlorogenic acid contains all extracts except methanolic red mulberry extract. Caffeine and chlorogenic acid contain methanolic extracts of white and red mulberry. The lowest content was found of caffeic acid in methanolic extract of white mulberry (3.80 mg / kg), while the highest amount of neochlorogenic acid in methanolic extract of black mulberry fruit (231.41 mg / kg).

HPLC analysis confirmed the presence of the following flavonoids in the tested extracts: quercetin-3-*O*-rutinoside, quercetin-3-*O*-glucoside, quercetin-3-*O*-rhamnoside, kaempferol-3-*O*-rutinoside and quercetin. All tested extracts of the three types of mulberry contain quercetin-3-O-rutinoside and quercetin-3-*O*-glucoside. Quercetin-3- *O*-rhamnoside contains all tested extracts except methanolic extracts of white and red mulberry. Kaempferol-3-*O*-rutinoside contains methanolic white and red mulberry extracts and acetone white mulberry extract. Quercetin contains only methanolic extract of black mulberry. The lowest amount of quercetin-3-*O*-glucoside (5.02 mg / kg) was recorded in acetone extract of white mulberry, while the highest amount of quercetin-3-*O*-rutinoside was recorded in methanolic extract of black mulberry (123.17 mg / kg).

Table 1. A comparative overview of HPLC analysis of three types of mulberry

| Phenolic acid mg/kg (320 nm)	Black mulberry		Red mulberry		White mulberry	
	methanol	acetone	methanol	acetone	Methanol	acetone
Chlorogenic acid	-	-	9.22	-	7.36	-
Caffeic acid	-	-	3.87	-	3.80	-
Neochlorogenic acid	231.41	22.29	6.76	15.18	25.21	22.99
Criptochlorogenic acid	143.28	18.34	-	8.57	24.15	8.92
Flavonoids (360nm)						
Quercetin-3-*O*-rutinoside	123.17	29.12	12.59	13.94	16.91	26.58
Quercetin-3-*O*-glucoside	64.88	18.96	6.10	5.78	26.04	5.02
Quercetin-3-*O*-ramnoside	38.89	44.62	-	22.85	-	24.91
Kaempherol-3-*O*-rutinoside	-	-	18.52	-	8.12	5.13
Quercetin	4.21	-	-	-	-	-
Anthocians (520nm)						
Cyanidine-3-*O*-glucoside	888.32	32.72	11.17	-	-	-
Cyanidine-3-*O*-rutinoside	349.94	5.36	-	-	-	-
Pelargonidine-3-*O*-glucoside	12.19	1.73	-	-	-	-
Pelargonidine-3-*O*-rutinoside	2.98	-	-	-	-	-

Qualified and quantified anthocyanins in the extracts of the three types of mulberry are: cyanidin-3-*O*-glucoside, cyanidin-3-*O*-rutinoside, pelargonidin-3-*O*-glucoside, and pelargonidin-3-*O*-rutinoside. Cyanidin-3-*O*-glucoside contains the methanolic and acetone extracts of red and black mulberry. Cyanidin-3-*O*-rutinoside and pelargonidin-3-*O*-glucoside contain only methanolic and acetone extracts of black mulberry fruit. Pelargonidine-3-*O*-rutinoside is only present in methanolic extract of black mulberry fruit. White mulberry does not contain anthocyanins.
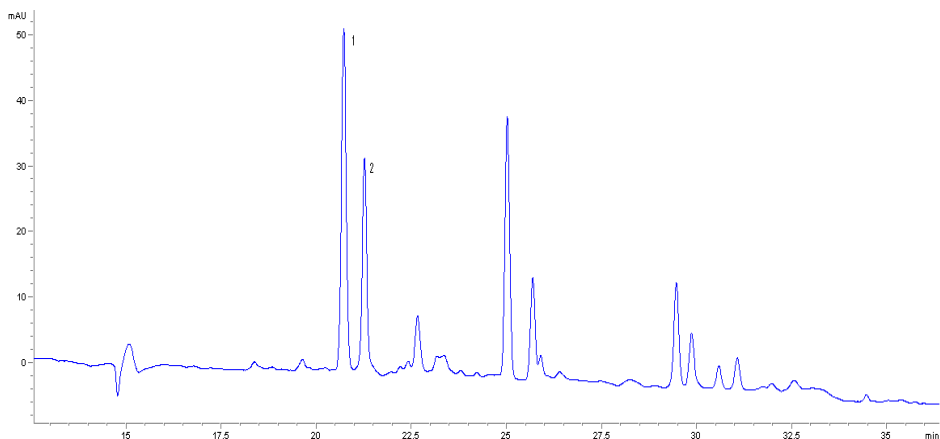
Figure 1. HPLC analysis of acetone extract of black mulberry (*Morus nigra* L.) at 320 nm: neochlorogenic acid (1), cryptochlorogenic acid (2).
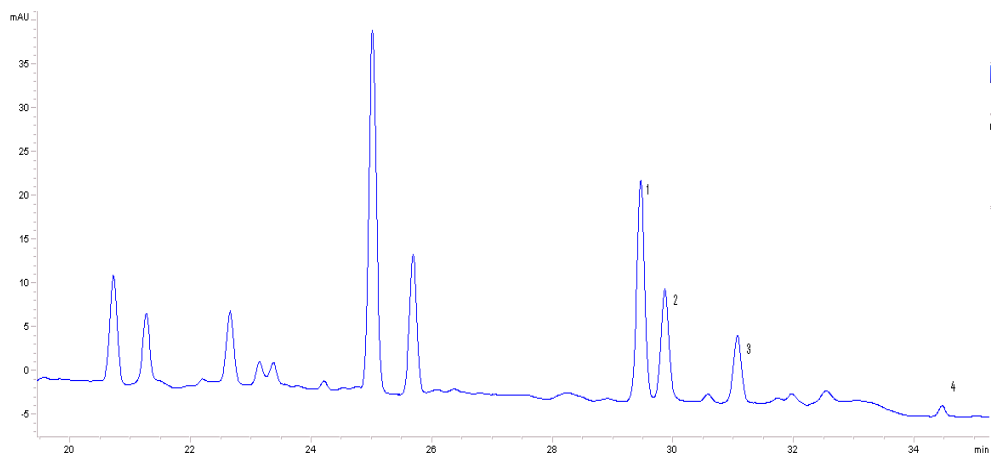
Figure 2. HPLC analysis of acetone extract of black mulberry fruit
(*Morus nigra* L.) at 360 nm: quercetin-3-*O*-rutinoside (1), quercetin-3-*O*-glucoside
(2), quercetin-3-*O*-rhamnoside (3), quercetin (4).
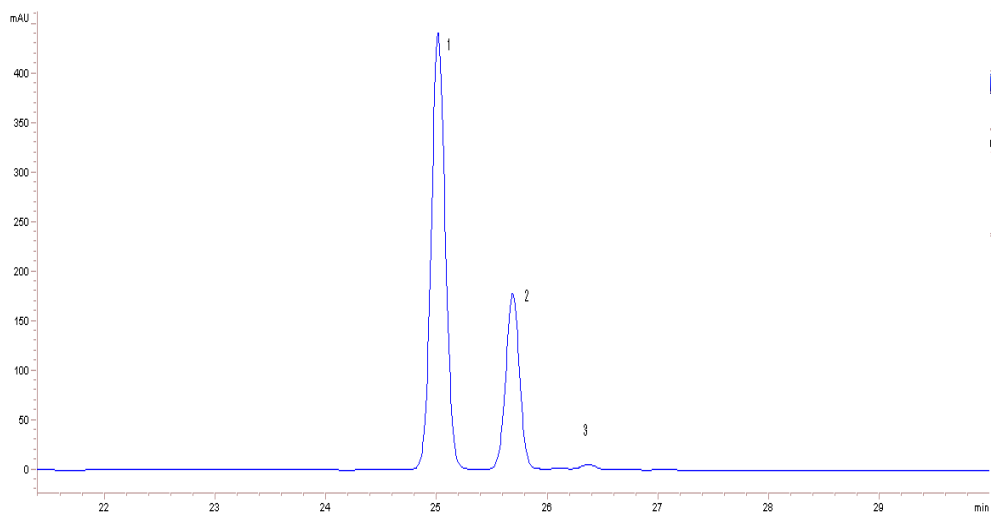
Figure 3. HPLC analysis of acetone extract of black mulberry fruit
(*Morus nigra* L.) at 520 nm: cyanidin-3-*O*-glucoside (1),
cyanidin-3-*O*-rutinoside (2), pelargonidin-3-*O*-glucoside.

Phenolic compounds isolated from different parts of the mulberry
(fruit, leaf, root, tree) and then identified by HPLC analysis are shown in
Table 2.

Table 2. Compounds isolated from mulberry (fruit, leaf, root, tree) by HPLC analysis

Compound	*Morus Nigra L.*	*Morus rubra L.*	*Morus alba L.*	Ref.
Cyanidin- 3-*O*-*β*-D-glucopiranoside	-	-	+	[8]
Cyanidin-3-*O*-*β*-D-galactopiranoside	-	-	+	[8]
Cyanidin- 7-*O*-*β*-D-glucopiranoside	-	-	+	[8]
Cyanidin-3-*O*-glucoside	+	-	-	[9]
	+	-	+	[10]
	+	-	-	[11]
Quercetin-3-*O*-ramnosid-7-*O*-glucoside	-	+	+	[12]
Quercetin-3,7-di-*O*-*β*-D-glucopiranoside	-	+	+	[12]
Kaempferol-7-*O*-glucoside	-	+	+	[12]
Kaempferol-3-*O*-rutinoside	+	-	+	[10]
Kaempferol	-	-	+	[13]
Rutin	+	+	+	[14]
	-	-	+	[13]
	+	+	+	[12]
	+	+	+	[15]
	+	-	+	[16]
Quercetin	+	+	+	[14]
	+	-	+	[16]
	-	-	+	[13]
	+	+	+	[15]
Catechine	+	+	+	[14]
Quercetin-3-*O*-glucoside	+	+	+	[12]
Quercetin-3-*O*-rutinoside	+	-	-	[9]
Taxifolin	+	-	-	[17]
Chlorogenic acid	+	-	+	[7]
	+	+	+	[14]
	-	-	+	[13]
	+	-	+	[16]
p-coumaric acid	+	+	+	[14]
	+	-	+	[7]
m-coumaric acid	+	-	+	[14]
	+	-	+	[7]
o-coumaric acid	+	+	+	[14]
Vanillic acid	+	+	+	[14]
	+	-	+	[7]
Gallic acid	+	-	+	[16]
	+	+	+	[14]
	-	-	+	[13]
	+	-	+	[7]
Caffeic acid	-	-	+	[13]
	+	+	+	[14]
	-	+	+	[12]
Ferullic acid	+	-	+	[13]
	+	-	+	[16]
Criptochlorogenic acid	-	+	+	[12]
Neochlorogenic acid	-	+	+	[12]

DANICA DIMITRIJEVIĆ, DANIJELA KOSTIĆ, MILAN MITIĆ, DUŠAN PAUNOVIĆ, BRANKA STOJANOVIĆ, JOVANA KRSTIĆ, SLAVICA STEVANOVIĆ, JASMINA VELIČKOVIĆ

The following compounds were isolated from a white mulberry picked in China: cyanidin-3-*O*-β-D-glucopyranoside, cyanidin-3-*O*-β-D-galactopyranoside and cyanidin-7-*O*-β-D-glucopyranoside [8]. Cyanidin-3-glucoside and quercetin-3-*O*-rutinoside were isolated from a black mulberry harvested in Spain [9], whereas by HPLC-PDAESI-MS analysis of a black and white mulberry from Poland isolated cyanidin-3-glucoside and kaempferol-3-*O*-rutinoside [10].

Tunisia red and white mulberry were analyzed by injecting a solution of known concentration of chlorogenic acid (250 μg / ml), caffeic acid (100 μg / ml), routine (235 μg / ml) and quercetin (200 μg / ml) [12]. Chlorogenic and caffeic acid were selected because they had already been identified with their derivatives in red and white mulberry extracts. Rutine was used as an equivalent for the quantification of quercetin and kaempferol-diglycoside. Caempferol derivatives differ from quercetin derivatives only by the position of the hydroxyl group at the 3 'position of the flavan ring. Quercetin was used as the standard to quantify the monoglycoside derivatives of quercetin and kaempferol [12].

The HPLC method, as the primary analytical method, was applied for the analysis of flavonoids, coumarins and chlorogenic acid in the fruit, bark and leaves of white mulberry from China from which camepferol, rutin, chlorogenic and gallic acid were isolated [13]. This analytical method was also used to isolate routines, quercetin, catechins, chlorogenic, caffeic, gallic, vanillinic acid and m- and o-coumaric acids from black, red and white mulberry extracts from Turkey [14]. Quercetin and rutin were also isolated from white, red and black mulberry from China [15].

White and black mulberries from Serbia contain rutin, quercetin and phenolic acids: gallic, caffeic, chlorogenic, vanillin, ferulic, dihydroxybenzoic and p-coumaric acid [16]. Chlorogenic, p- and m-coumaric, vanillin, gallic and ferulic acids were isolated from the fruits and leaves of white and black mulberry from Pakistan [19].

CONCLUSION

In the extracts of white, red and black mulberry identified the four phenolic acids by HPLC analysis: chlorogenic, 4-caffeoylquinic, 5-caffeoylquinic and caffeic acid. 5-caffeoylquinic acid was identified in all tested extracts of white, red and black mulberry. 4-caffeoylquinic acids contain all the three extracts except methanol extract of red mulberry. Caffeic and chlorogenic acid containing methanol extracts of white and red mulberry.

In the tested extracts, the following flavonoids were confirmed by HPLC analysis: quercetin-3-*O*-rutinoside, quercetin-3-*O*-glucoside, quercetin-3-*O*-ramnoside, kaempherol-3-*O*-rutinoside and quercetin. All of the three tested

species of mulberry extracts containing quercetin-3-*O*-rutinoside and quercetin-3-*O*-glucoside. Quercetin-3-*O*-ramnoside containing all tested extracts except methanol extract of white and red mulberry. Quercetin contains only the methanol extract of black mulberry.

The methanolic extract of black mulberry contains the following anthocyanins: cyanidin-3-*O*-glucoside, cyanidin-3-*O*-rutinoside, pelargonidin-3-*O*-glucoside and pelargonidin-3-*O*-rutinoside. The acetone extract of black mulberry contains all of these anthocyanins except pelargonidin-3-*O*-glucoside. The methanolic extract of red mulberry contains cyanidin-3-*O*-glucoside. In the extracts of white mulberry anthocyanins have not been identified.

EXPERIMENTAL

Preparation of materials: Plant material was collected in the South East Serbia in early July 2011. Fresh fruit maturity was estimated on the basis of the color. Samples were stored in plastic bags and kept frozen until extraction. The frozen fresh fruit material homogenized using a blender. Black, red and white mulberry fresh fruits (10 g) was extracted with water, methanol-water (50/50, v/v%), methanol, ethanol-water (50/50, v/v%), ethanol, acetone-water (50/50, v/v%) and acetone. All solvents were acidified with 1 ml conc. HCl. The extraction was performed with 100 ml of solvents using the ultrasonic bath for 30 minutes. The suspension was gravity filtered through a Buchner funnel and Whatman No. 1 filter paper. Extracts were stored in the fridge at 5ºC until their analysis.

High-performance liquid chromtagraphy (HPLC) analysis: High performance Liquid Chromatography (HPLC) liquid chromatography with UV / Vis and a high resolution fluorescence detector (HPLC) was applied to separate and quantify the phenolic compounds in the prepared samples. The HPLC method was developed, with the following parameters showing the best results. Chromatographic separation was performed on an Eclipse XDB-C18 column (4.6 mm x 150 mm) using a solvent system: A - (H2O + 5% HCOOH) and B - (80% ACN + 5% HCOOH + H2O).

Separation of components was performed using the following linear gradient: 0-28 min, 0.0% B; 28-35 min, 25% B; 35-40 min, 50% B; 40-45 min, 80% B, and finally 0% B again for the last 10 min. The mobile phase flow was 0.8 cm^3 / min. 5 µl of sample solution was injected automatically using autosamplers. The column was thermostatically controlled at 30° C.

DANICA DIMITRIJEVIĆ, DANIJELA KOSTIĆ, MILAN MITIĆ, DUŠAN PAUNOVIĆ, BRANKA STOJANOVIĆ, JOVANA KRSTIĆ, SLAVICA STEVANOVIĆ, JASMINA VELIČKOVIĆ

The phenolic components present in the samples were identified by comparing their retention times and spectra with the retention time and spectrum of standards for each component. The following standards were used: malvidin-3-glucoside, cyanidin-3-glucoside, halogen acids, p-coumaric, caffeic and ferulic acids, catechin, epicatechin, quercetin and caempherol. The quantitative determination of the components was performed by the external standard method.

For each individual standard, a stock solution of a mass concentration standard of 1.0 mg/cm^3 was prepared by dissolving in 10% methanol solution. A calibration curve, for each standard, was constructed based on the obtained surfaces, depending on the mass concentration of the standard. From the obtained linear dependence equation, mass concentrations of the components in the samples were calculated. For components in samples for which no standard was available, quantification was performed based on a calibration curve, by the structure of the corresponding standard. All analyzes were performed in triplicate.

REFERENCES

1. E.A. Cieslik; A.W. Grada; W. Adamus; *Food Chem.*, **2006**, *94,* 135-142.
2. A. Sass-Kiss; J.P. Kiss; M.M. Milotay; M. Kerek; M. Toth-Markus; *Food Res. Inter.,* **2005**, *38,* 1023-1029.
3. L.K. Liu; F.P. Chou; Y.C. Chen; C.S. Chyan; *J Agric Food Chem.*, **2009**, *57.* 7605-7611.
4. A. Trappey; H. Bawadi; R.R. Bansode; N.J. Losso; *Food Chem.*, **2005**, *91*, 665-672.
5. J.Y. Lin; C.Y. Tang; *Food Chem.*, **2007**, *101,* 140-147.
6. M. Ozgen; S. Serce; K. Kaya; *Sci. Hortic.*, **2009**, *119*, 275-279.
7. S. Ercisli; E. Orhan; *Sci. Hortic.*, **2008**, *116,* 41-46.
8. Q. Du; J. Zheng; Y. Xu; *J. Food Compos. Anal.*, **2008**, *21,* 390–395.
9. M.R. Perez-Gregorio; J. Reguiero; E. Alonso-Gonzales; L.M. Pastrana-Castro; J. Simal-Gandara; *LWT*, **2011**, *40*, 1793–1801.
10. A.M. Pawlowska; W. Oleszek; A. Braca; *J. Agric. Food Chem.*, **2008**, *56*, 3377–3380.
11. N.M.A. Hassimotto; M.I. Genovese; F.M. Lajolo; *Food Sci.Technol. Int*., **2007**, *13*, 17–25.
12. I. Thabti; W. Elfalleh; H. Hannachi; A. Ferchichi; M. Da Graca Campos; *J. Funct. Foods*, **2012**, *4*, 367–374.
13. Q. Chu; M. Lin; H. Tian; J. Ye; *J. Chromatogr. A,* **2006**, *1116*, 286–290.
14. M. Gundogdu; F. Muradoglu; R.I. Gazioglu Sensoy; H. Yilmaz; *Sci. Hortic.,***2011**, *132,* 37–41.

15. M. Isabelle; B. Lan Lee; C. Nam Ong, X. Liu; D. Huang; *J. Agric. Food Chem.*, **2008**, *56,* 9410–9416.
16. M.M. Radojković; Z.P. Zeković; S.S. Vidović; D.D. Kocar; P.Z. Masković; *Hem. Ind.,* **2012***, 66*, 547–552.
17. O. Mazimba; R.R.T. Majinda; D. Motlhanka; *Afr. J. Pharm. Pharmacol.*, **2011**, *5*, 751–754.
18. O. Ercsli; E. Orhan; *Sci. Hortic.,* **2008***, 116,* 41–46.
19. A.A. Memon; N. Memon; L.D. Luthria; I.M. Bhanger; A.A. Pitafi; *Pol. J. Food Nutr. Sci.,* **2010***, 60*, 25–32.

INVERTED VERSUS DIRECT STRUCTURE BULK HETEROJUNCTION ORGANIC SOLAR CELLS INVOLVING A TRIPHENYLAMINE-BASED SMALL MOLECULAR DONOR

GAVRIL-IONEL GIURGI[a,b], **LORANT SZOLGA**[a,b,*], **ISTVAN KOVACS**[c],
ELENA BOGDAN,[a] **NICULINA DANIELA HĂDADE**,[a]
ANAMARIA TEREC,[a] **ION GROSU**[a,*], **JEAN RONCALI**[a,*]

ABSTRACT. Bulk heterojunction solar cells involving a triphenylamine-based molecular donor and $PC_{61}BM$ with direct and inverted structures have been fabricated and optimized. The devices have been characterized under simulated solar illumination and the conversion efficiency and stability of the two kinds of organic solar cells are discussed.

Keywords: Organic solar cells, bulk heterojunction, inverted structure, molecular donors, triphenylamine derivatives

INTRODUCTION

In a general context marked by the foreseeable exhaustion of fossil energy resources and rising of environmental concerns, photovoltaic (PV) energy is expected to acquire a growing importance in the near future. While the PV industry is largely dominated by the silicon technology, recent years have witnessed an increasing research effort focused on the development of possible alternative technologies potentially more environmentally friendly and cost-effective such as, dye sensitized solar cells (DSSCs), perovskite solar cells and organic photovoltaic cells (OPV). [1, 2]

[a] *Babes-Bolyai University, Faculty of Chemistry and Chemical Engineering, Department of Chemistry and SOOMCC, Cluj-Napoca, 11 Arany Janos str., 400028, Cluj-Napoca, Romania*
[b] *Optoelectronics Group, Base of Electronics Department, ETTI, Technical University of Cluj-Napoca, Str.Memorandumului, Nr.28, Cluj-Napoca, 400114, Romania*
[c] *IPA SA, Cercetare, Proiectare si Productie de Echipamente si Instalatii de Automatizare, Sucursala CIFATT Cluj, 15 Zorilor str., 400335, Cluj-Napoca, Cluj, Romania*
* *Corresponding authors: lorant.szolga@bel.utcluj.ro, igrosu@chem.ubbcluj.ro, jeanroncali@gmail.com*

GAVRIL-IONEL GIURGI, LORANT SZOLGA, ISTVAN KOVACS, ELENA BOGDAN,
NICULINA DANIELA HĂDADE, ANAMARIA TEREC, ION GROSU, JEAN RONCALI

OPV cells can be fabricated by different techniques such as vacuum deposited multi-layer planar heterojunctions and solution-processed bulk heterojunction solar cells (BHJ). [3-7] This latter kind of device which combines low-cost, simplicity and efficiency has progressively become the most widely developed and most successful technology of fabrication of OPV cells. BHJs were initially fabricated with a "direct" structure namely by spin-casting a solution of donor and acceptor materials on an indium-tin oxide (ITO) conducting electrode coated with a spin-cast layer of poly(3,4-ethylenedioxythiophene): polystyrene sulfonate (PEDOT:PSS) in order to smooth the surface and facilitate hole-extraction. However the acidity of PEDOT:PSS has been identified as one of the cause of instability of direct BHJ cells. An alternative technique consists in the realization of an inverted structure in which a solution-processed ZnO interlayer is inserted between the ITO electrode and the active layer thus removing the use of PEDOT:PSS. [8-11]

In this work we present a comparative analysis of the BHJ cells fabricated by the two techniques using a small molecular donor (**D**) consisting of a triphenylamine connected to a dicyanovinyl group by a thienyl ring (**1**) [12] and [6,6]-phenyl-C_{61}-butyric acid methyl ester (PC$_{61}$BM) as the acceptor (**A**). Donor **1** was selected for its easy synthesis and relevant properties among the other small donors investigated in our group. [13-16] Various parameters involved in the fabrication of direct and inverted BHJ cells have been investigated including the donor/acceptor ratio, the thickness of the active layer and the conditions of its deposition by spin-coating (nature of the solvent and speed of rotation).
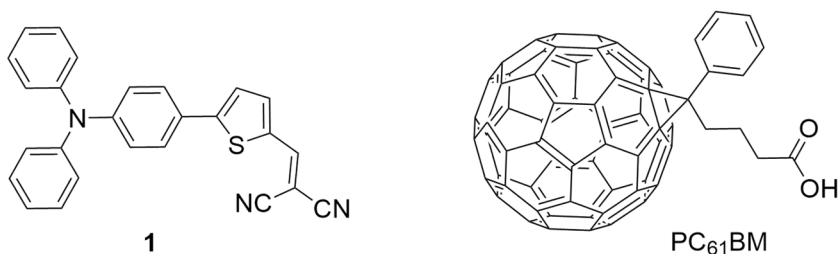
Figure 1. Chemical structures for donor **1** and PC$_{61}$BM

RESULTS AND DISCUSSIONS

OPV cells based on donor **1** and fullerene C_{60} fabricated by successive vacuum deposition of the donor and C_{60} have already been reported. A power conversion efficiency (*PCE*) of 2.50% was reported for a bilayer cell while a

hybrid cell fabricated by co-evaporation of the donor and C_{60} gave a *PCE* of 4.0%. [17-19] However, the fabrication of solution-processed BHJ cells based on donor **1** has not been investigated in detail yet.

Figure 2 shows the structure of the direct and inverted devices investigated here. Except for the deposition of the metal electrodes, all experiments related to the fabrication and characterization of the cells were carried out in ambient conditions.

BHJ with direct structure (ITO/PEDOT:PSS/1, PC$_{61}$BM /Al).

In a first step two solvent systems have been compared for the processing of the active layer namely chloroform (CF) / chlorobenzene (CB) (1/1) and chloroform (CF) / dichlorobenzene (DCB) (1/1). Although the donor **1**/PC$_{61}$BM blend is readily dissolved in both systems, the CF/CB mixture produced more uniform and more compact films on the PEDOT:PSS layer. The CF / DCB mixture lead to hollow spin-cast films unsuitable for OSC fabrication.

Using the 1/1 CF / CB solutions BHJs with active layers of 80, 125 and 170 nm thickness were fabricated. The best results (*PCE* = 1.02%) were obtained with the thinnest film (80 nm), while *PCE* decreases to 0.66 % when increasing film thickness to 170 nm (Table 1).
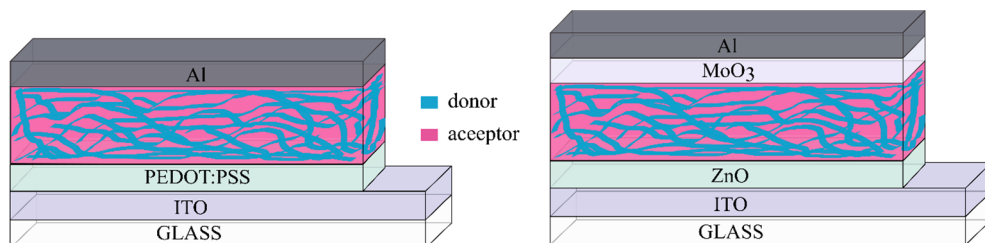
Figure 2. Simplified representations of direct (left) and inverted (right) BHJ organic solar cells

Table 1. Effect of the thickness of the active layer on the average values of the photovoltaic characteristics of direct BHJ cells with 1:1 **1**/PC$_{61}$BM ratio

Spin-coating program and rotation speed	Thickness [nm]	V_{oc} [V]	J_{sc} [mA cm^{-2}]	FF [%]	PCE [%]
1000rpm/40s + 8000rpm/20s	80	0.85	4.46	29	1.02
700rpm/60s + 3000rpm/20s	125	0.85	3.60	27	0.85
500rpm/60s + 3000rpm/20s	170	0.85	3.00	27	0.66

GAVRIL-IONEL GIURGI, LORANT SZOLGA, ISTVAN KOVACS, ELENA BOGDAN,
NICULINA DANIELA HĂDADE, ANAMARIA TEREC, ION GROSU, JEAN RONCALI

Using the spin-casting conditions leading to 80 nm thick films, a series of cells with D/A ratios of 2:1; 1:1; 1:2; 1:3 and 1:4 were fabricated and characterized. Figure 3 shows the UV-Vis absorption spectra of the films obtained with these various D/A ratios. The different D/A ratios are clearly illustrated by the variation of the relative intensities of the absorption band around 380 nm ($PC_{61}BM$) and 520 nm (**1**). Figure 4 shows the current density *vs* voltage curves for the best cells obtained with various D/A ratios, while the corresponding data are listed in Table 2.

The best *PCE* value (1.50 %) is obtained with a D/A ratio of 1:3, while D/A = 2:1 and 1:1 lead to lower values (*PCE* = 0.66 % and 1.02 %). An open-circuit voltage (V_{oc}) of 1.04 V is obtained with D/A = 2:1 and decreases to 0.86 V for D/A = 1:4. On the other hand, the short-circuit current density (J_{sc}) increases from 2.70 mA cm^{-2} for D/A = 2:1 to 4.94 mA cm^{-2} for D/A = 1:3, this D/A ratio leading to the maximum *PCE* of 1.54%. All devices show relatively low fill factors (*FF*) in the range of 30%, such modest *FF* values frequently observed with TPA-based push-pull donor have been attributed to their low hole mobility and to problems related to the extraction of charges at the active layer/electrode interfaces.
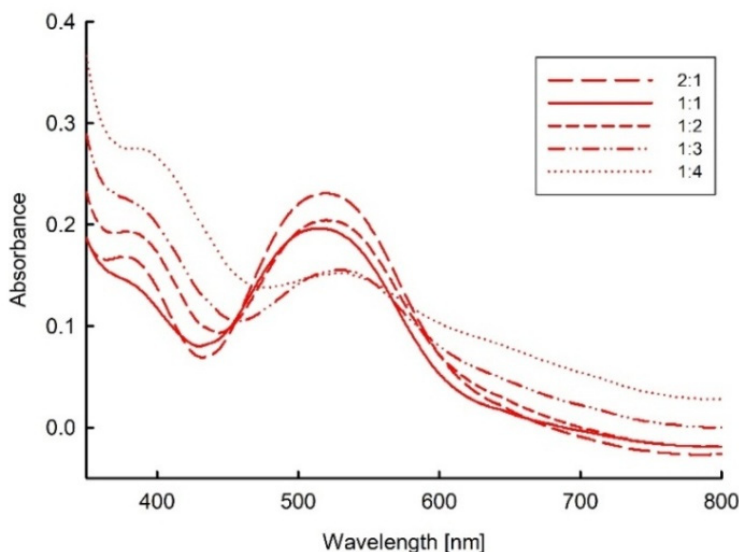
Figure 3. UV-VIS spectra of the films spun-cast with different D/A ratios
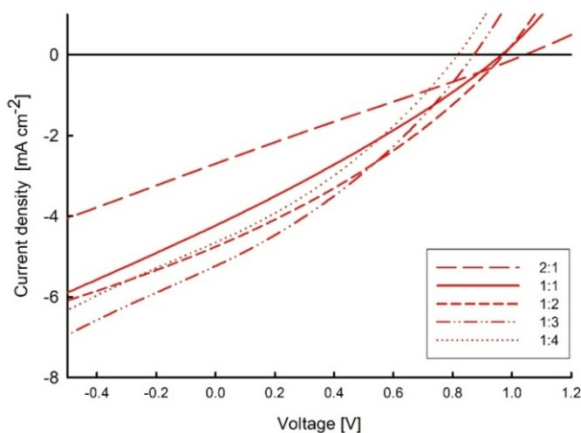
Figure 4. Current density *vs* voltage curves for direct BHJ cells fabricated with various D/A ratios, AM 1.5 simulated solar light with a power light intensity of 100 mWcm^{-2}.

The external quantum efficiencies of the cells under monochromatic irradiation (*EQE*) are shown in Figure 5.

These action spectra show a first band around 380 nm which increases with the PC$_{61}$BM content and corresponds to its contribution to the photocurrent. The main band extending from 450 to 650 nm corresponds to the charge transfer band of the donor and shows a maximum intensity for D/A = 1:3, in good agreement with the results obtained under simulated solar light. It is noted that this ratio also corresponds to the maximum contribution of PC$_{61}$BM, suggesting that the morphology of the bi-phase D/A blend is optimum at this ratio.

Table 2. Optical and photovoltaic characteristics of direct BHJ cells fabricated with various D/A ratios

D/A Ratio	V_{oc} [V]	J_{sc} [mA cm^{-2}]	*FF* [%]	*PCE* [%]	*EQE*$_{max}$ [%]
2:1	1.04	2.70	25	0.71	22
1:1	0.96	4.23	28	1.16	25
1:2	0.97	4.76	31	1.44	33
1:3	0.93	4.94	33	1.54	34
1:4	0.86	4.69	31	1.28	25
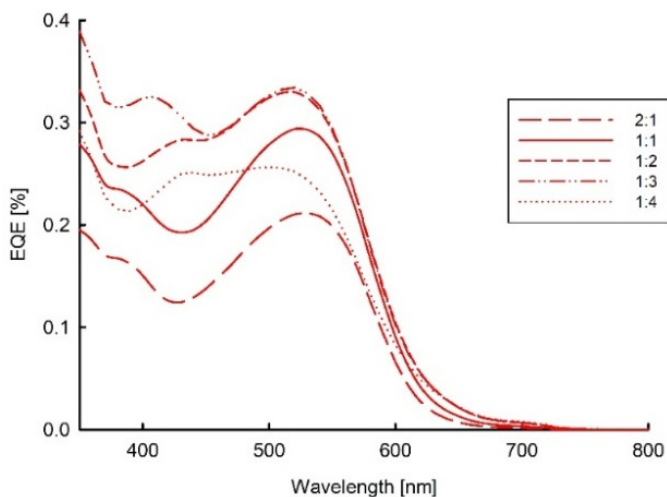
Figure 5. *EQE* responses for the best direct BHJ cells fabricated
with the various D/A ratios

BHJ with inverted structure (ITO/ZnO/1,PC$_{61}$BM/MoO$_3$/Al)

As a next step, a series of inverted cells of structure (ITO/ZnO/**1**, PC$_{61}$BM/MoO$_3$/Al) with D/A ratios of 1:1, 1:2 and 1:3 and a thickness of the active layer of 80 nm have been fabricated. The ZnO layer improves the charge extraction from the blend D/A layer by enhancing electron transport to the ITO electrode while the MoO$_3$ layer improves hole-transport and contributes to protect the active layer from oxygen and moisture that play a major role in the device degradation. For ZnO a layer thickness of 25-30 nm is optimum, while for MoO$_3$ the optimal thickness depends on the nature of the metal electrode. Au presents the highest electrical conductivity, but Al and Ag have better optical transparency. [20] The inverted cells have been fabricated with Ag and Al electrodes with a constant thickness of the MoO$_3$ layer. In a first set of experiments a 7 nm of MoO$_3$ was used, but it results in short-circuited cells with both type of electrodes. Increasing the thickness of the MoO$_3$ to 10 nm, leads to working cells with Al electrodes but attempt to fabricate cells with silver electrodes remain unsuccessful, presumably because of the experimental set-up for silver vacuum deposition was not adapted.

The current density *vs* voltage curves of the inverted cells fabricated with various D/A ratios and a 10 nm MoO$_3$ layer are shown in Figure 6 and the corresponding photovoltaic parameters are listed in Table 3. The highest

average *PCE* of 1.83 % was obtained with the 1:3 D/A ratio while the highest *PCE* value (2.00%) was measured on a cell based on a 1:2 D/A ratio. As for direct cells, a small increase of V_{oc} with the donor content is observed, but on the characteristics of the various cells are rather similar with in particular J_{sc} values of 5.40-5.70 mA cm^{-2}. The most noticeable difference with direct cells is a significant improvement of *FF* from *ca* 25% for direct cells to 35 % for the inverted ones, suggesting that the inverted structure leads to a better extraction of photo-generated charges.
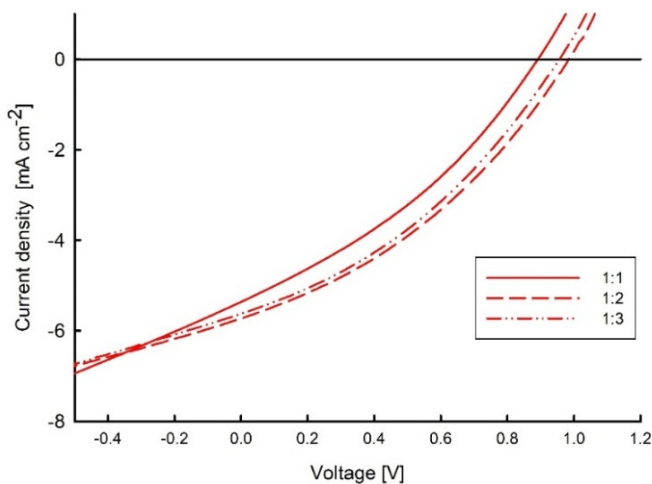
Figure 6. Current density *vs* voltage curves for best inverted BHJ cells fabricated with various D/A ratios, AM 1.5 simulated solar light with a power light intensity of 100 mWcm^{-2}.

The *EQE* spectra of the various cells recorded under monochromatic irradiation show a maxim of ca 35% around 520 nm (Figure 7). Except for an increase of the short wavelength band reflecting the increase of the acceptor content, the three spectra are very similar which agrees well with the results obtained under white light irradiation.

In order to investigate the long term stability of the two types of devices direct and inverted cells were stored in ambient conditions and the conversion efficiency was recorded at various time intervals (Figure 8). Figure 8 compares the variation of *PCE vs* time for direct and inverted cells. The *PCE* of the direct cells drops down from 0.93 to 0.18 % after 24 hours and to 0.08 % after 10 days.
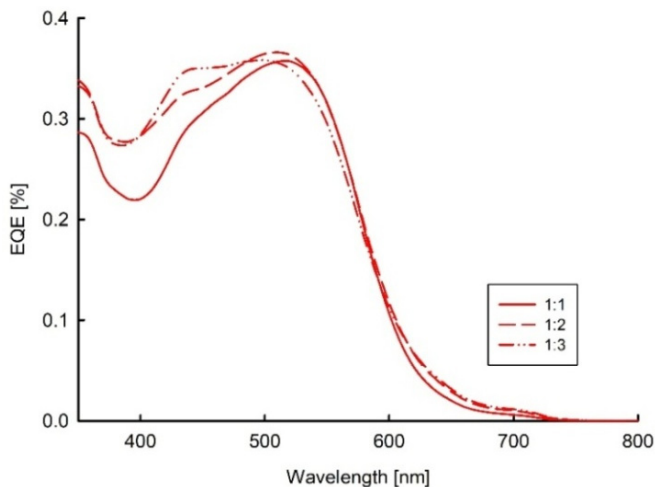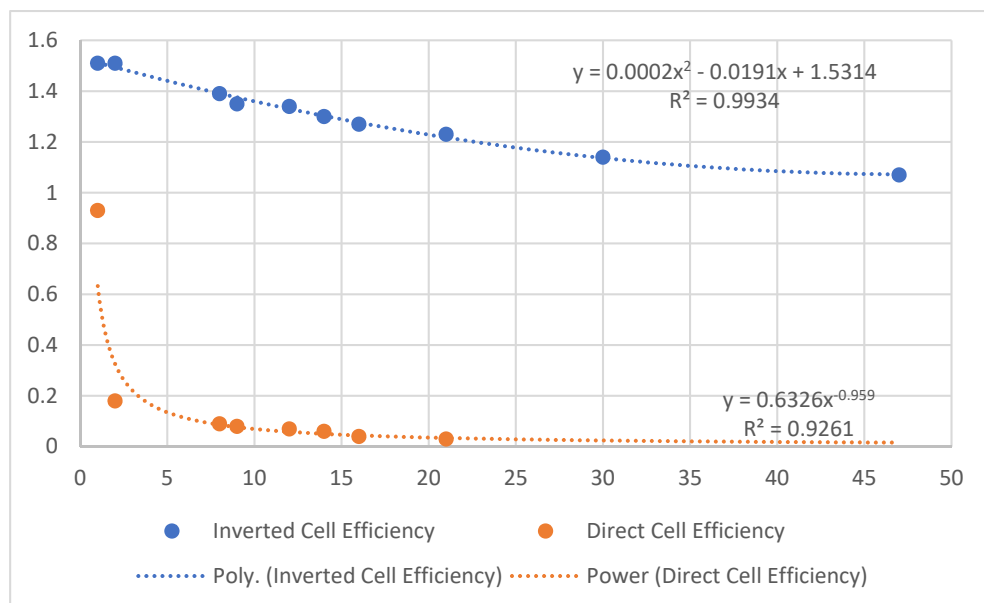
Figure 7. *EQE* spectra recorded under monochromatic illumination
for the best inverted BHJ cells fabricated with various D/A ratios

Table 4. Photovoltaic characteristics under AM 1.5 simulated solar light for inverted
BHJ cells fabricated with various D/A ratios.

D/A Ratio	V_{oc} [V]	J_{sc} [mA cm^{-2}]	*FF* [%]	*PCE* [%]	*EQE*$_{max}$ [%]
1:1	0.89	5.36	34	1.62	34
1:2	0.98	5.72	35	2.00	36
1:3	1.04	5.40	35	1.99	34

For the inverted cells *PCE* shows a much slower decrease since the
initial value of 1.50 % decreases to 1.35 % after 10 days and to 1.07 % after
50 days. To summarize, the results clearly show that in the absence of
encapsulation, the inverted structure leads to a considerable improvement of
the stability of BHJ cells in ambient atmosphere.

The chart displays two fitted curves:

$$y = 0.0002x^2 - 0.0191x + 1.5314$$
$$R^2 = 0.9934$$

$$y = 0.6326x^{-0.959}$$
$$R^2 = 0.9261$$

Legend: Inverted Cell Efficiency · Direct Cell Efficiency · Poly. (Inverted Cell Efficiency) · Power (Direct Cell Efficiency)

Figure 8. Variation of the *PCE* of direct and inverted BHJ cells over a period of 50 days storage in ambient conditions

CONCLUSIONS

A comparative analysis of the photovoltaic performances of BHJ cells of direct and inverted structures and based on a small molecular donor and $PC_{61}BM$ has been presented. The results obtained after optimization of the thickness of the active layer and donor *vs* acceptor ratio show the inverted cells present a higher efficiency that direct devices, due essentially to an improvement of the fill factor which probably reflect a more efficient collection of charges at the electrodes. Furthermore, the performances of inverted cells are much less dependent on the donor/acceptor ratio than direct structures and exhibit higher efficiencies and considerably better stabilities than BHJ cells with direct structure based on the same active components.

GAVRIL-IONEL GIURGI, LORANT SZOLGA, ISTVAN KOVACS, ELENA BOGDAN,
NICULINA DANIELA HĂDADE, ANAMARIA TEREC, ION GROSU, JEAN RONCALI

EXPERIMENTAL PART

Materials and equipment

The cells were obtained using commercially available ITO-coated glass substrates of 24×25 mm. These substrates were sonicated for 10 minutes in distilled water, cleaned with Deconex (10 min), ethanol (10 min), isopropanol (10 min) and finally using an UV Ozone Cleaner for 20 minutes. $PC_{61}BM$, PEDOT, PSS, MoO_3, $CHCl_3$, C_6H_5Cl and Al were commercially available. The active material and ZnO were prepared accordingly to literature data. [21] The deposition of different layers of the cells were carried out either using a classic spin-coater or a high vacuum deposition equipment (MANTIS DEPOSITION- model QUBE). The characterization of the cells was performed with an Artificial Sun system LCS-100 (94011A-ES) and a monochromator equipment IQE 200B Quantum Efficiency Measurement Solution, while the thickness of the layers was measured using a profilometer Tencor Alpha-Step D500. The absorption spectra of the film were analyzed by UV-VIS 1900 Shimadzu spectrometer.

General procedure for the fabrication of direct BHJs

A PEDOT/PSS layer of 35-40 nm was spun-cast at 5000 rpm for 30 s on clean ITO plates. The active layer was then deposited by spin-casting and the thickness was controlled by the spin-casting conditions (for 80 nm: t_1= 40 s, S_1= 1000 rpm, t_2= 20 s, S_2= 8000 rpm; for 125 nm: t_1= 60 s, S_1= 700 rpm, t_2= 20 s, S_2= 3000 rpm; for 170 nm: t_1= 60 s, S_1= 500 rpm, t_2= 20 s, S_2= 3000 rpm). The 100 nm Al electrodes were deposited by thermal evaporation under high-vacuum deposition system at 1×10^{-6} mbar.

General procedure for the fabrication of inverted BHJs

A layer of 40 nm ZnO was deposited by spin-casting [S = 3000 rpm, t = 40 s) on clean ITO plates and then the plates were heated at 200 °C for 1h. The films of **donor 1: $PC_{61}BM$** with a thickness of 80 nm were deposited by spun-cast (t_1= 40 s, S_1= 1000 rpm, t_2= 20 s, S_2= 8000 rpm) on top of ZnO layer. The hole transporter layer (HTL) consisting in a 10 nm thick MoO_3 layer and the Al electrodes (100 nm) were deposited by thermal evaporation under high vacuum at 10^{-6} mbar.

ACKNOWLEDGEMENTS

REFERENCES

1. J.A. Luceño-Sánchez, A.M. Díez-Pascual, R P. Capilla, *Int. J. Mol. Sci*. **2019**, *20*, nr. 976.
2. M. Hiramoto, Y. Shinmura, *Organic Solar Cells* in Springer Handbook of Electronic and Photonic Materials, S. Kasap, P. Capper eds. Springer Handbooks. Springer, **2017**, Chapter 54, p 1329-1338.
3. S. Chambon, L. Derue, M. Lahaye, B. Pavageau, L. Hirsch, G. Wantz, *Materials* **2012**, *5*, 2521 – 2536.
4. J. Lee, Y.K. Jung, D.Y. Lee, J.W. Jang, S. Cho, S. Sone, J. Jeong, S.H. Park, *Synth. Met.*, **2015**, *199*, 408-412.
5. Z. Wang, Z. Hong, T. Zhuang, G. Chen, H. Sasabe, D. Yokoyama, J. Kido, *Appl. Phys. Lett.*, **2016**,*106*, 053305.
6. S. Rafiquea, S.M. Abdullah, K. Sulaiman, M. Iwamoto, *Renew. Sustain. Energy*, **2018**, *84*, 43-53.
7. M.C. Scharber, N.S. Sariciftci, *Progr. Polym. Sci.*, **2013,** *38*, 1929-1940.
8. M.S. White, D. S. Olson, *Appl. Phys. Lett.* **2006**, *89*,143517.
9. K. Wang, C. Liu, T. Meng, C. Yia, X. Gong, *Chem. Soc. Rev*., **2016**, *45*, 2937-2975.
10. B. Gholamkhass, N.M. Kiasari, P. Servati, *Org. Electron.*, **2012**, *13*, 945-953.
11. Y. Wang, H. Cong, B. Yu, Z. Zhang, X. Zhan, *Materials*, **2017**, *10*, 1064.
12. A. Leliège, C.H. Le Régent, M. Allain, P. Blanchard, J. Roncali, *Chem. Commun*. **2012**, *48*, 8907–8909.
13. A. Diac, D. Demeter, S. Jungsuttiwong, I. Grosu, J. Roncali, *Tetrahedron Lett*. **2015**, *56*, 4607 – 4612.
14. A. Diac, D. Demeter, M. Allain, I. Grosu, J. Roncali, *Chem. Eur. J.,* **2015**, *21*, 1598 – 1608.
15. D. Demeter, S. Mohamed, A. Diac, I. Grosu, J. Roncali, *ChemSusChem* **2014**, *7*, 1046-1050.

16. A.P. Diac, L. Szolga, C. Cabanetos, A. Bogdan, A. Terec, I. Grosu, J. Roncali, *Dyes and Pigments*, **2019**, *171*, nr. 107748.
17. J.W. Choi, C.H. Kim, J. Pison, A. Oyedele, D. Tondelier, A. Leliège, E. Kirchner, P. Blanchard, J. Roncali, B. Geffroy, *RSC Advances*, **2014**, *4*, 5236–5242.
18. S. Mohamed, D. Demeter, J.-A. Laffitte, P. Blanchard, J. Roncali, *SciRep* **2015**, *5*, nr. 9031.
19. Y. Jiang, C. Cabanetos, M. Allain, S. Jungsuttiwong, J. Roncali, *Org. Electron*., **2016**, *37*, 294-304.
20. H.R. Yeom, J. Heo, G.-H. Kim, S.-J. Ko, S. Song, Y. Jo, J.Y. Kim, B. Walker, J.Y. Kim, *Phys. Chem. Chem. Phys.,* **2015**, *17*, 2152-2159.
21. Y.M. Sun, J.H. Seo, C.J. Takacs, J. Seifter, A.J. Heeger, *Adv. Mater*, **2011**, *23*, 1679-1683.

AMINO-SUBSTITUTED PORPHYRINS AT THE BORDER OF HYBRID MATERIALS GENERATION AND PLATINUM NANOPARTICLES DETECTION

**DIANA ANGHEL[a], MIHAELA BIRDEANU[b], ANCA LASCU[a],
CAMELIA EPURAN[a], EUGENIA FAGADAR-COSMA[a]***

ABSTRACT. Two amino substituted porphyrins, namely: 5,10,15,20-tetrakis(4-aminophenyl)porphyrin (TAPP) and 5,10,15,20-tetrapyridyl-21H,23H-porphine (TPyP) have been used for complexation reaction of platinum nanoparticles (PtNPs) with the main purpose to recover or detect them from diluted leaching solutions, after transformation in colloidal solutions. The complexation reactions were monitored by UV-vis spectroscopy and revealed that both porphyrins have the capacity to complex PtNPs in different detection domains ranging from 2.776 to 40.457×10^{-6} M in the case of TAPP, and in a larger range of 8.07×10^{-6} – 7.03×10^{-5} M in the case of TPyP. Excellent correlation coefficients of 99.35 % and 99.57 % respectively have been obtained in each case. During complexation a nanomaterial based on TAPP and a micromaterial composed from TPyP both having as second partner PtNPs were obtained and thoroughly characterized by atomic force microscopy (AFM). The aggregation phenomena that occurred for each amino-porphyrin in DMF, in their acidified solutions and in their hybrid materials, revealed that the TAPP-PtNPs hybrid is a nanomaterial, based on triangular prisms aggregates of acidulated TAPP, and the TPyP-PtNPs hybrid is a micromaterial that is based on pyramidal shaped aggregated from the acidulated solution of TPyP.

Keywords: amino-substituted porphyrins, PtNPs, Pt-NPs detection, UV-vis spectroscopy, AFM characterization

---

[a] *Institute of Chemistry "Coriolan Dragulescu", Mihai Viteazu Ave. 24, 300223 - Timisoara, Romania*
[b] *National Institute for Research and Development in Electrochemistry and Condensed Matter, P. Andronescu Street 1, 300224- Timisoara, Romania*
  * Corresponding author: efagadar@yahoo.com

INTRODUCTION

In the last few years, the chemistry of porphyrins and metalloporphyrins has received increased interest. The conjugated electron system of the tetrapyrrolic macrocycle leads to unique optical properties used in a large range of applications in: medicine (for photodynamic therapies) [1], analytical chemistry (molecular recognition) [2], catalysis (mediators in electrochemistry and in organic synthesis) [3, 4], artificial photosynthesis [5] and as photosensitizers for organic solar cells [6, 7, 8] and in automotive industry [9].

This interest also covers the field of platinum nanoparticles due to the many uses of nanosized sensors [10, 11], catalysts [12] and drugs [13]. Platinum colloidal particles can be obtained by using different types of reduction agents [14], such as: trisodium citrate [15], aminodextrans [16], NaBH4, is used to initiate the reaction, forming small particles [17].

For instance, the synthesis in ethylene glycol applying UV-induced reduction offers both a higher stability and a lower size of the particles [18, 19]. The stabilization of colloidal particles is possible by encapsulation in polymers, such as: polyvinyl alcohol) (PVA), polyvinylpyrrolidone (PVP), polyacrylates, polyacrylamides, poly(ethylene glycol) (PEG) or by using surfactant agents, such as: cetyltrimethyl ammonium bromide (CTAB) that allow the formation of micelles [20, 21]. When stabilized with biocompatible polymers, like PVP, platinum nanoparticles have a beneficial effect upon the blood fluidity, under oxidative stress conditions [22].

The protective layer of the metal nanoparticles can be done also by covering them with different dyes that might improve the catalytic or sensitive properties of the colloids [23, 24]. Porphyrin molecules can perform this task with multiple benefits. For example, nanocomposites based on *meso*-tetrakis(p-sulfonatophenyl)porphyrin and PtNPs are photocatalytically active for water reduction to produce hydrogen under UV-vis irradiation [25]. An efficient hydrogen reduction photocatalyst was obtained from PtNPs and Zn(II)-protoporphyrin IX as photosensitizer [26]. Photosensitizer nanocomposites, formed from platinum nanoparticles functionalized with multibranched-porphyrins are reported to generate donor-bridge-acceptor conjugates, thus facilitating the electron transfer [27].

The interest in recovery or detection of platinum is nowadays continuously increasing, as the natural resources are limited and the consumption as catalyst in various chemical reactions, especially in automotive industry, is very large. The best performance of 600mg/g recovery imply biosorption of platinum using cellulose nano- fibers and nanocrystals modified with polyethylene imine [28]. Biomass materials [29], zeolites bearing hydrazine groups [30] or hybrids of oxalic acid [31] gave lower recovery performances of maximum 150 mg/g.

Other reported methods used in the last five years for platinum recovery are microwave-assisted with cloud point extraction [32], complexation [33-34] and ion exchange techniques, all from leaching solutions [35-37].

As most methods for the recovery of platinum that are economically feasible and environmentally friendly rely on adsorption phenomena, the purpose of our study was to design efficient materials based on porphyrins, capable to detect/recover PtNPs from leaching solution.

This novel approach relies on complexation phenomena between suitable porphyrins and platinum nanoparticles being both a facile method for the recovery of platinum from dilute solutions and a source of new platinum complexes.

Two amino-functionalized free-base porphyrins, an aliphatic one: 5,10,15,20-tetrakis(4-aminophenyl)porphyrin (TAPP) (Figure 1a) and an aromatic one: 5,10,15,20-tetrapyridyl-21H,23H-porphine (TPyP) (Figure 1b), were chosen to compare their distinctive abilities to recover platinum.

$\qquad\qquad$ (a) $\qquad\qquad\qquad\qquad$ (b)
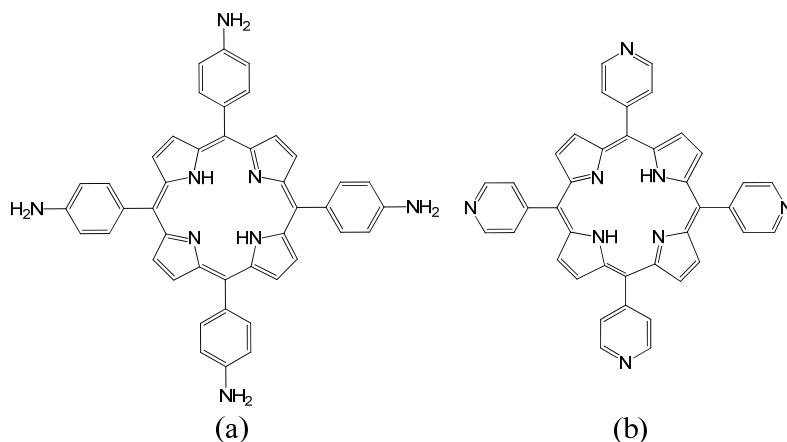
Figure 1. Structures of 5,10,15,20-tetrakis(4-aminophenyl)porphyrin (**TAPP**) (a) and 5,10,15,20-tetrapyridyl-21H,23H-porphine (**TPyP**) (b)

RESULTS AND DISCUSSION

1. UV-vis spectroscopy of Pt-colloid and amino-porphyrins in DMF and in acid solutions

The UV-vis spectra of Pt-colloid and amino-porphyrins both in DMF and in acid solutions are presented in Figure 2 A and B.
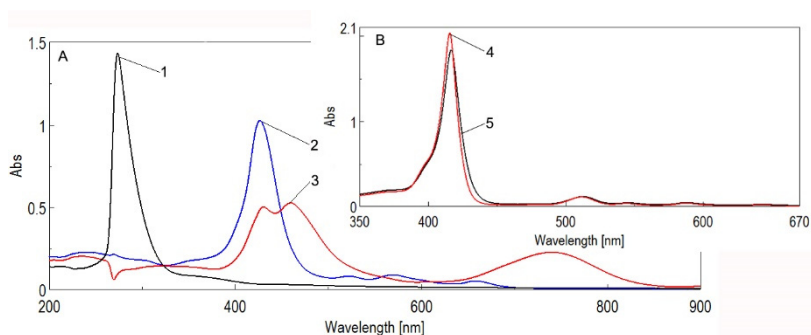
Figure 2. Overlapped UV-vis spectra of: Pt colloid in water **(A1)**; **TAPP** in DMF
(c = 1.989 x 10^{-5}M) **(A2)**; **TAPP** in acid environment (pH = 2.5) **(A3)**; **TPyP** in DMF
(c = 8.834 x 10^{-5}M) **(B4)**; **TPyP**in acid environment (pH = 2.5) **(B5)**

From Figure 2A-line 1, it can be observed that the maximum absorption peak for the platinum colloidal solution, located at λ_{max} = 274 nm, (figure T line 1) does not belong to the visible region of the spectrum.
The TAPP porphyrin shows (Figure 2A-line 2), as expected, the intense Soret band at 426 nm accompanied by only three Q bands, located at: 522 nm, 569 nm and respectively 658 nm.

In the case of TAPP (Figure 2A-line 3), when reaching a pH=2.5, after HCl 0.5 N solution was added, the splitting of the Soret band occurs due to the protonation of the two imino nitrogens from the inner structure of porphyrin. The deprotonation is accompanied by the disappearance of the Q2 and Q3 bands accompanied by both a significant hyperchromic effect and highly bathochromic shift of the Q1 band up to 740 nm. All these aspects are indicative for an J–type aggregation process (side-by side arrangement of molecules) that is investigated further by AFM. Regarding TPyP (Figure 2B-line 4), at the same pH = 2.5, only a shift of the Soret band from 416 nm to 418 nm can be noticed, that might be the sign for a beginning of J-type aggregation.

2. Platinum colloid detection

2.1. Uv-vis monitoring of the complex generation between TAPP and PtNPs in acidulated medium

The complex generation between TAPP and PtNPs in acid medium was continuosly monitored by UV-vis spectroscopy (Figure 3).
By continuously adding of controlled amounts of PtNPs to the acidulated TAPP solution, a few complex phenomena took place. The first effect is the decrease in the intensity of the Soret band situated around 460 nm that is accompanied by a hypsochromic shift of around 5 nm.
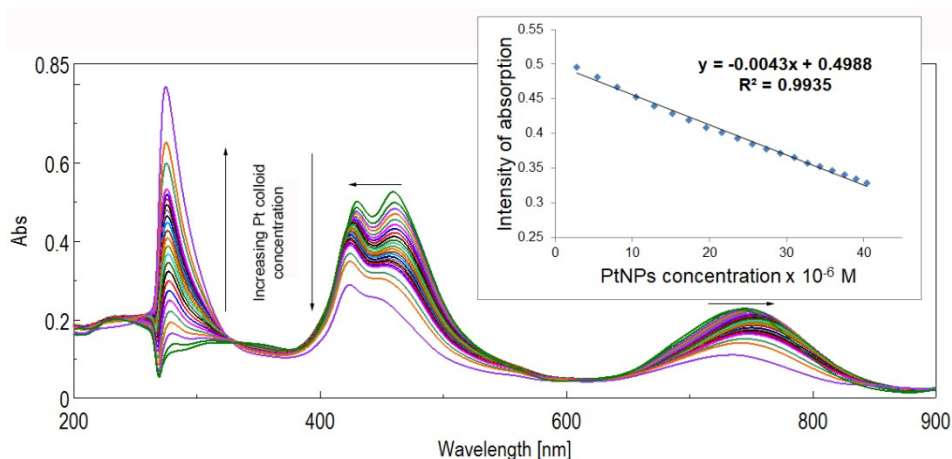
Figure 3. Overlapped UV-vis spectra monitoring the complex formation. In detail: linear dependence between the intensity of absorption of the hybrid Pt-TAPP read at 460 nm and PtNPs concentration

The same effect might be observed regarding the second Soret band initially located at 430 nm that is also blue shifted from 430 to 425 nm.

A clear isosbestic point, located around 325 nm, and another one at 630 nm, indicate the formation of PtNPs-porphyrin complex, so that these optical effects cannot be explained by simple dilution.

The absorption maximum corresponding to the Pt plasmon is also hypsochromically shifted, from 274 nm to 276 nm.

In the range of PtNPs concentrations from 2.776 to 40.457 x 10^{-6} M the dependence between the intensity of absorption of the plasmonic band read at 460 nm and the increasing concentration of PtNPs is linear, characterized by an excellent correlation coefficient of 99.35 % (Figure 3-detail).

2. 2. *Uv-vis monitoring of the complex generation between TPyP and PtNPs in acidulated medium*

The successive adding of platinum colloid to the TPyP acidulated solution in DMF (c = 8.834 x 10^{-5} M) leads to the formation of a complex nanomaterial, Pt-TPyP, evidenced by the presence of two isosbestic points, at 391 nm and 426 nm respectively, on both branches of the Soret band of the spectrum. A simple dillution phenomenon is excluded due to both the isosbestic points existence and because of the increasing in intensity of the Q bands (Figure 4 and A and B details).
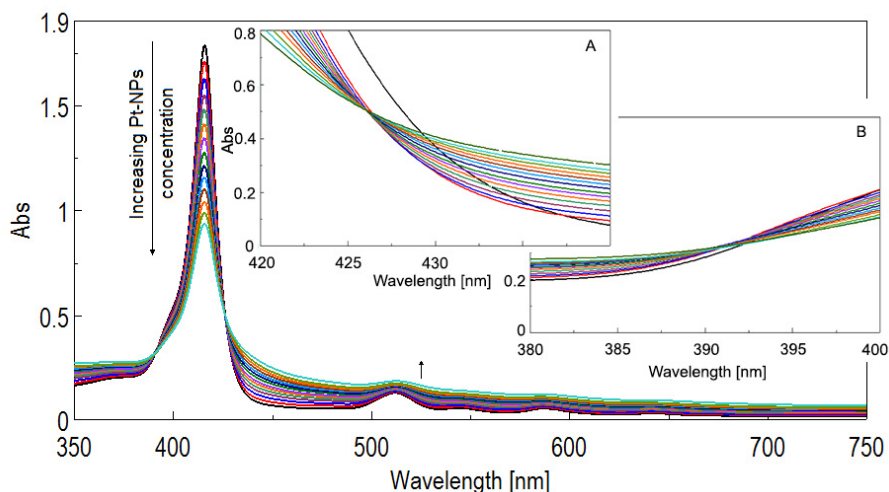
Figure 4. Overlapped UV-vis spectra after successive adding of of Pt-NPs solution to acidulated TPyP and isosbestic points detail: isosbestic point at 426 nm **(A)** and isosbestic point at 391 nm **(B)**

The dependence between the intensity of absorption of the Soret band read at 416 nm and PtNPs concentration is linear with an excellent corelation coefficient of 99.57 % in the platinum concentration range: $8.07 \times 10^{-6} – 7.03 \times 10^{-5}$ M, as represented in Figure 5. These values are comparable to those detectable by TAPP porphyrin, proving that both porphyrins containing amino groups, either aliphatic or aromatic, are capable to form complexes with platinum nanoparticles.
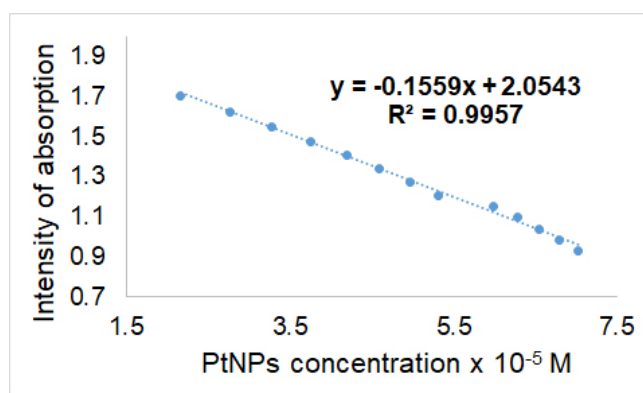
Figure 5. Linear dependence between the intensity of absorption of the Soret band read at 416 nm and PtNPs concentration

3. AFM investigation of the Pt colloid, bare porphyrins and hybrid nanomaterials

Table 2 (A, B, C) presents the main results from AFM investigation, regarding surface features, morphology and aggregation architectures.
Table 2A reveals that the dimension of Pt-colloid ovoid-like particles is varying in the range of 65 - 80 nm (Table 1A, a and b) having the height distribution in the domain of 6 - 14 nm. In the sized image of 4.59 x 4.59 µm the formation of some large platinum spherical shaped aggregates around 220 nm can be noticed, as expected from an unstabilized colloid.
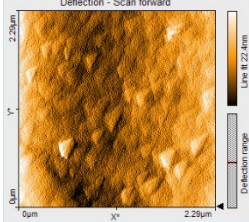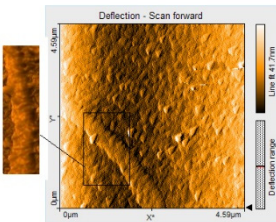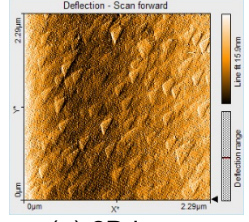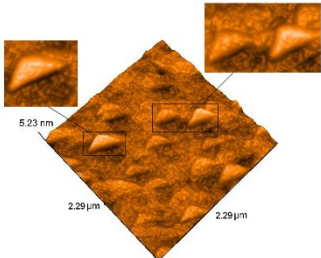
Table 1A. AFM images of PtNPs (a,b)
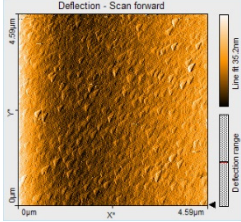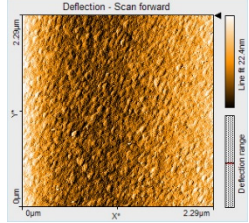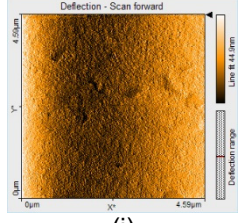
	Scanning 2.29×2.29µm	Scanning 4.59×4.59µm
PtNPs	(a)	(b)
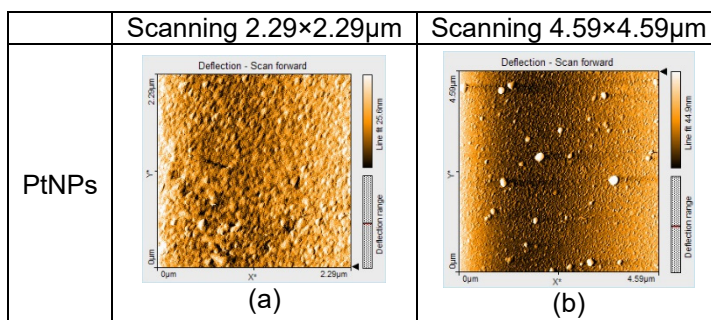
The microscopy analysis was performed for TAPP porphyrin both solely and in acid pH medium. TAPP deposited by drop-casting from DMF on silica plates presents equilateral triangular building–block units (Table 1B, c and d), with dimensions larger than those generated in acid medium (Table 2B, e, f), having the sizes around 165 nm. The larger image (4.59 × 4.59 µm) puts into evidence besides the continuous covering of the surface with triangular architectures preserving the same orientation, a novel type of organization in bow-type wires, implying that both types of aggregation processes, an initial H-type aggregation followed by the J- type phenomenon, are occurring.
Acidulated TAPP deposited on silica plates (Table 1B, e and f) presents the same orientation of triangular-shaped aggregates having sizes around 135 nm. The height distribution is tighter, in the region from 2.2 to 5.3 nm. In the 3-D image of acidulated TAPP (Table 1B, g) it can be seen triangular prisms randomly covering the surface and having the heights of 12 nm. This aspect is a novelty, because the usual aggregation of porphyrins in acid media is in the pyramidal form [38].

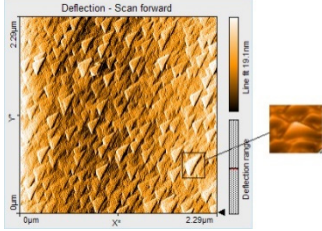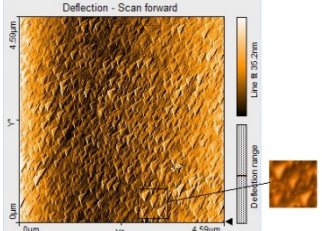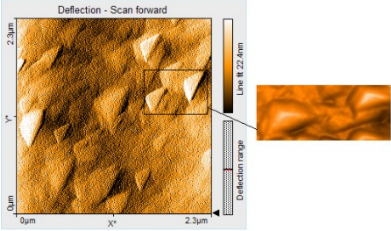**Table 1B:** AFM images of investigated compounds:TAPP (c, d); acidulated TAPP (e, f, g); TAPP-PtNPs hybrid (h, i)
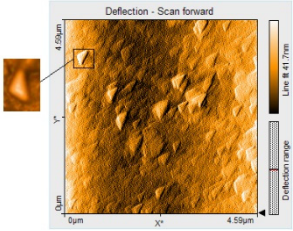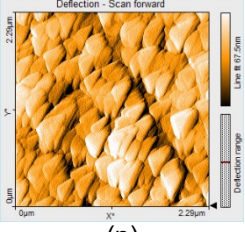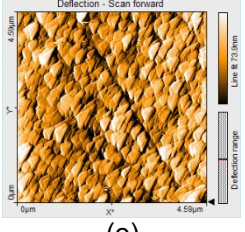
	Scanning 2.29×2.29µm	Scanning 4.59×4.59µm
TAPP	(c)	(d)
acidulated TAPP	(e)-2D image / (g)-3D image	(f)
TAPP-PtNPs hybrid	(h)	(i)

Regarding the rugosity, a comparison between the porphyrin-base in DMF and in acidulated DMF-water medium reveals that the acid surfaces have a smaller rugosity (Sa varying from 2 nm to 4.6 nm) than those in DMF solution (Sa from 3 nm to 6.4 nm).

114

In the case of the hybrids obtained between porphyrin and Pt colloid (Table 1B, h and i), the height distribution is smaller and narrower and the sizes are varying from 5 to 8.3 nm. The hybrid nanomaterial has the whole structure reorganized showing smaller triangular particles with dimension of 35 nm. In conclusion, the generation of complex between the TAPP and the PtNPs in acid media gave rise to a very well-structured nanomaterial, characterized by a slightly higher rugosity than that of TAPP in different media, that is around 3.2 nm.

Regarding the pyridyl substituted derivative, TPyP, a roof type aggregation can be seen (Table 1C, j and k) at the interface DMF-air, generated by H- and J-type processes using as building blocks triangular isosceles with dimensions of 122nm and 204 nm, respectively and height distribution in the range of 4-10 nm.

Table 1C: AFM images of the investigated compounds: TPyP (j, k); acidulated TPyP (l, m); TPyP-PtNPs hybrid (n, o)

	Scanning 2.29×2.29µm	Scanning 4.59×4.59µm
TPyP	 (j)	 (k)
TPyP acidulated	 (l)	 (m)
TPyP -PtNPs hybrid	 (n)	 (o)

When the TPyP is deposited from DMF acid medium (Table 1C, l and m), the rugosity is increasing, this aspect being divergent with the behavior of TAPP.

In the 3-D images (Table 1C, l-detail), the architecture of the aggregates is a pyramidal one, that is another different aspect as compared to TAPP.

The hybrid micromaterial, TPyP-PtNPs (Table 1C, n and o) has the surface morphology constituted from equilateral triangles having dimensions of around 320 - 450 nm, that are amazingly organized as the bricks in a wall (generated by sandwich-type aggregation) and showing distinct rows (generated by J-type aggregation).

The height distribution is in this particular case larger, in the range of 22 - 70 nm.

The recovery of PtNPs

The recovery of PtNPs was performed as previously reported [34] by precipitating PtNPs from the two obtained hybrid materials using 1 N HCl solution (Figure 6A).
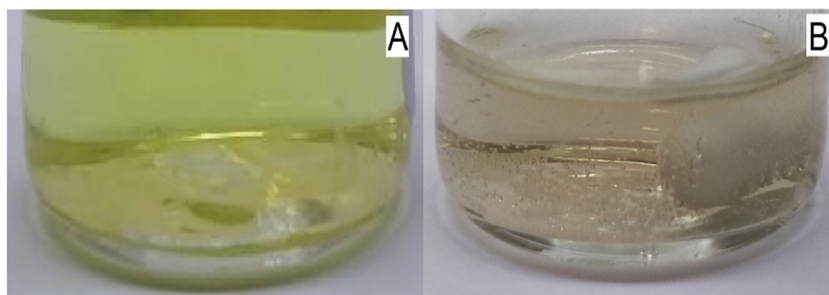
Figure 6. Reduction of the PtNPs-porphyrin complexes using 1N HCl (A) and $NaBH_4$ (B)

The recovery efficiency of these two aminoporphyrins was evaluated from the capacity of complexation and the results are promising: 602 mg Pt /g TAPP and 212 mg Pt /g TPyP, corresponding to approximately 3 mole PtNPs/ 1 mole TAPP and 1 mole PtNPs/ 1 mole TPyP. A plausible explanation might be that TAPP is capturing PtNPs in the inner part of the molecule and also between the $-NH_2$ functional groups (from 5,10 and 15, 20) but the TPyP creates coordinative bonds only in the center of the molecule.

CONCLUSIONS

The design of efficient materials based on different amino-substituted porphyrins, capable to detect or recover PtNPs from leaching solution was the main aim of this study.

This novel approach relies on complexation phenomena between suitable porphyrins and platinum nanoparticles being both a facile method for the recovery of platinum from dilute solutions and a source of new platinum complexes.

Two amino-functionalized free-base porphyrins, an aliphatic one: 5,10,15,20-tetrakis(4-aminophenyl)porphyrin (TAPP) and an aromatic one: 5,10,15,20-tetrapyridyl-21H,23H-porphine (TPyP) were chosen to compare their distinctive abilities to recover platinum. The platinum from the synthetic leaching solution containing $H_2PtCl_6x6H_2O$ was transformed in colloidal Pt by reducing with $NaBH_4$.

The complexation reactions were monitored by UV-vis spectroscopy and revealed that each of these porphyrins have the capacity to complex PtNPs in different detection domains ranging from 2.776 to 40.457 x 10-6 M in the case of TAPP, and in a larger range of 8.07 x 10-6 – 7.03 x 10-5 M in the case of TPyP. Excellent correlation coefficients of 99.35% and 99.57 respectively have been obtained in each case.

During complexation a nanomaterial based on TAPP and a micromaterial composed from TPyP both having as second partner PtNPs were obtained and thoroughly characterized by AFM. The aggregation phenomena that occurred for each amino-porphyrin in DMF, in their acidified solutions and in their hybrid materials, revealed that the TAPP-PtNPs hybrid is a nanomaterial, and the TPyP-PtNPs hybrid is a micromaterial. Both hybrid materials have as building block units TAPP or TPyP already aggregated in triangular geometries of different sizes (with two or all three sides equal), but always uniformly oriented.

The recovery efficiency of these two aminoporphyrins was evaluated from the capacity of complexation and the results are promising: 602 mg Pt /g TAPP and 212 mg Pt /g TPyP, corresponding to approximately 3 moles PtNPs/ 1 mole TAPP and 1 mole PtNPs/ 1 mole TPyP.

EXPERIMENTAL SECTION

Reagents

Hexachloroplatinic acid and trisodium citrate were purchased from Sigma-Aldrich (St. Louis, USA). Sodium borohydride was provided by Merck (Darmstadt, Germany) and doubly distilled water was used for all experiments.

The synthesis of TAPP was done in two steps involving the obtaining of 5,10,15,20-*meso* –tetrakis-(p-nitrophenyl) porphyrin, followed by the reduction of nitro-groups with $SnCl_2$ x $2H_2O$ [39].

The synthesis of TPyP was done in accordance with published results [40] starting from 4-pyridinecarboxaldehyde and pyrrole in propionic acid.

Synthesis of the platinum colloid

In order to check the viability of PtNPs complexation and its total recovery after the reduction of complexes, we used for the platinum colloid generation H_2PtCl_6 x $6H_2O$, thus creating an ideal situation. In real leaching solutions, a mixture of valuable metal ions, such as: Pt (in the form of $(NH_4)_2PtCl_6$), Pd and Rh are present, besides Ni and Mn ions that are not interfering.

So, the platinum colloid was synthesized after previously reported data [41], as follows: a solution was prepared from 0.01697 g (3.276 x 10^{-5} mole) of H_2PtCl_6 x $6H_2O$ dissolved in 77.9 mL distilled water with molar concentration of $c = 1.416$ x 10^{-4} M. To this solution 2 mL trisodium citrate with $c = 0.04$ M were added and stirred for 30 minutes at room temperature. After 30 minutes of vigorous stirring 0.409 mL $NaBH_4$ solution with concentration 0.05 M, was added dropwise. The mixture was stirred and allowed to react at ambient temperature for 1 h.

The solution color changed from yellowish to brownish yellow due to optical phenomena associated to the formation of nanometric particles [42].

Obtaining the TAPP-Pt-colloid complex

To a volume of 5 mL TAPP in DMF ($c = 1.808$ x 10^{-5} M) 0.1 mL portions of Pt colloid solution ($c = 1.416$ x 10^{-4} M) in water were added. The mixture was stirred for 30 seconds and then the UV-vis spectra were recorded and overlapped (as shown in Figure 3).

Obtaining the TPyP-Pt-colloid complex

The experiment was done in a similar way, changing only the concentration of TPyP solution in DMF ($c = 8.834$ x 10^{-5} M). The overlapped UV-vis spectra were registered (as shown in Figure 4).

Method for the recovery of PtNPs

The two obtained complexes PtNPs-TAPP and PtNPs-TPyP were subjected to a reduction reaction using 1N HCl and $NaBH_4$ solutions and it was clearly proven that the platinum nanoparticles were precipitated.

Apparatus

For recording UV-visible spectra a V-650 - JASCO spectrometer (Pfungstadt, Germany) having 1 cm wide quartz cuvettes was used. Atomic force microscopy (AFM) images were obtained on a Nanosurf®EasyScan 2 Advanced Research AFM microscope (Liestal, Switzerland). The samples were deposited on pure silica plates by drop casting from DMF solution.

ACKNOWLEDGMENTS

REFERENCES

1. J. Kou; D. Dou; L. Yang; *Oncotarget,* **2017**, *8(46)*, 81591-81603.
2. J.S. Rebouças; B.R. James; *Inorg Chem.*, **2013**, *52(2)*, 1084–1098.
3. M.R. Civic; P.H. Dinolfo; *ACS Appl. Mater. Interfaces*, **2016**, *8(31),* 20465–20473.
4. J. Barona-Castaño; C. Carmona-Vargas; T. Brocksom; K. de Oliveira; *Molecules,* **2016**, *21(3)*, 310.
5. G. Bottari; O. Trukhina; M. Ince; T. Torres; *Coord. Chem. Rev.*, **2012**, *256(21-22)*, 2453–2477.
6. X. Qian; L. Lu; Y.-Z. Zhu; H.-H. Gao; J.-Y. Zheng; *RSC Advances*, **2016**, *6(11)*, 9057–9065.
7. O. Rezazgui; G. Marchand; P. Trouillas; B. Siegler; S. Leroy-Lhez; *Chemistry Select*, **2018**, *3(39)*,10959–10970.
8. X. Sun; G. Chen; J. Zhang; *Dyes Pigm.*, **2008**, *76(2)*, 499–501.
9. C. Liu; S.C. Sun; X.P. Zhu; G.F. Tu; J.Y. Zhang; *IOP Conf. Series: Materials Science and Engineering*, **2019**, *479*, 012058.
10. G.V. Fedorenko; L.P. Oleksenko; N.P. Maksymovych; I.P. Matushko; *Russ. J. Phys. Chem. A,* **2015**, *89(12)*, 2259–2262.
11. E. Fagadar-Cosma; I. Sebarchievici; A. Lascu; I. Creanga; A. Palade; M. Birdeanu; B. Taranu; G. Fagadar-Cosma; *J. Alloys Compd.*, **2016,** *686*, 896–904.
12. C.A. Mak; M.A. Pericas; E. Fagadar-Cosma; *Catal. Today,* **2018**, *306*, 268–275.
13. T.C. Johnstone; K. Suntharalingam; S.J. Lippard; *Chem. Rev.*, **2016**, *116(5)*, 3436–3486.
14. A.L. Stepanov; A.N. Golubev; S.I. Nikitin; Y.N. Osin; *Rev. Adv. Mater. Sci.*, **2014**, *38*, 160-175
15. A.S. Dehnavi; A. Raisi; A. Aroujalian; *Synth. React. Inorg. Met.-Org. Nano-Metal Chem.*, **2013**, *43(5)*, 543–551.
16. L. Dykman; A. Lyakhov; V.A. Bogatyrev; S. Shchyogolev; *November Colloid Journal*, **1998**, *60(6)*, 700-704.
17. A. Martínez-Abad; *Multifunctional and Nanoreinforced Polymers for Food Packaging*, **2011**, 347–367.

18. L. Kacenauskaite; J. Quinson; H. Schultz; J.J.K. Kirkensgaard; S. Kunz; T. Vosch; M. Arenz; *Chem Nano Mat*, **2016**, *3(2)*, 89–93.
19. J. Quinson; M. Inaba; S. Neumann; A.A. Swane; J. Bucher; S.B. Simonsen; L.T. Kuhn; J.J.K. Kirkensgaard; K.M.O. Jensen; M. Oezaslan; S. Kunz; M. Arenz; *ACS Catalysis*, **2018**, *8(7)*, 6627–6635.
20. T.M. Tolaymat; A.M. El Badawy; A. Genaidy; K.G. Scheckel; T.P. Luxton; M. Suidan; *Sci Total Environ.*, **2010**, *408(5),* 999–1006.
21. L.S. Nair; C.T. Laurencin*; Prog. Polym. Sci.*, **2007**, *32(8-9)*, 762–798.
22. S. Kato; R. Hokama; H. Okayasu; Y. Saitoh; K. Iwai; N. Miwa; *JNN*, **2012**, *12(5)*, 4019–4027.
23. X. Wang; P. Sonström; D. Arndt; J. Stöver; V. Zielasek; H. Borchert; K. Thiel; K. Al-Shamery; M. Bäumer; *J. Catal.* **2011**, *278(1)*, 143–152.
24. D.A. Gregory; S.J. Ebbens; *Langmuir*, **2018**, *34(14)*, 4307–4313.
25. L. Zhang; Y. Lu; Y. Du; P. Yang; X. Wang; *J Porphyr Phthalocya*, **2010**, *14(06)*, 540–546.
26. E.R. Clark; D.M. Kurtz; *Inorg. Chem.*, **2017**, *56(8)*, 4584–4593.
27. K. Ladomenou; M. Natali; E. Iengo; G. Charalampidis; F. Scandola; A.G. Coutsolelos; *Coord. Chem. Rev.*, **2015**, *304-305*, 38–54.
28. H.-J. Hong; H. Yu; M. Park; H.S. Jeong; *Carbohydr. Polym.*, **2019**, *210*, 167–174.
29. D.J. Garole; B.C. Choudhary; D. Paul; A.U. Borse*; Environ Sci Pollut Res*, **2018**, *25(11)*, 10911–10925.
30. A.K. Mosai; L. Chimuka; E.M. Cukrowska; I.A. Kotzé; H. Tutu; *Miner. Eng.*, **2019**, *131*, 304–312.
31. H. Malekian; M. Salehi; D. Biria; *Waste Manag.*, **2019**, *85*, 264–271.
32. T. Suoranta; O. Zugazua; M. Niemelä; P. Perämäki; *Hydrometallurgy*, **2015**, *154*, 56–62.
33. D. Anghel, I. Frațilescu, A. Lascu; *New trends and strategies in the chemistry of advanced materials with relevance in biological systems, technique and environmental protection*, **2019**, 6-7.
34. A. Lascu; Proceedings of the 25thInternational Symposium on Analytical and Environmental Problems, **2019**, 18-22.
35. M.S. Safarzadeh; M. Horton; A.D. Van Rythoven; *Min Proc Ext Met Rev*, **2017**, *39(1)*, 1–17.
36. Y. Ding; H. Zheng; J. Li; S. Zhang; B. Liu; C. Ekberg; Z. Jian; *Metals*, **2019**, *9(3)*, 354.
37. A.N. Nikoloski; K.L. Ang; D. Li; *Hydrometallurgy*, **2015**, *152*, 20–32.
38. E. Fagadar-Cosma; G. Fagadar-Cosma; M. Vasile; C. Enache; *Curr. Org. Chem.*, **2012**, *16*, 931–941
39. A. Bettelheim; B.A. White; S.A. Raybuck; R.W. Murray; *Inorg. Chem.,* **1987**, *26,* 1009-1017.
40. E. Fagadar-Cosma; C. Enache; I. Armeanu; G. Fagadar-Cosma; *Dig. J. Nanomater. Bios.*, **2007**, *2*, 175 – 183.
41. G.W. Wu; S.B. He; H.P. Peng; H.H. Deng; A.L. Liu; X.H. Lin; X.H. Xia; W. Chen; *Anal. Chem.*, **2014**, *86(21)*, 10955–10960.
42. B. Escobar Morales; S.A. Gamboa; U. Pal; R. Guardián; D. Acosta; C. Magaña; X. Mathew; *Int. J. Hydrog. Energy*, **2010**, *35(9)*, 4215–4221.

SPIN LABELLED HEMOGLOBIN-BASED OXYGEN CARRIERS (HBOC): PREPARATION AND EVALUATION OF IN VIVO / IN VITRO STABILITY

**RADU SILAGHI-DUMITRESCU[a,*], CRISTINA GRUIAN[b],
CRISTINA PUSCAS[a], ALEXANDRA SIMON[a], EVA FISHER-FODOR[c],
VLAD AL. TOMA[d,e], ANCA FARCAS[d,e], IOANA ROMAN[d],
VIOLETA-FLORINA SCURTU[a], AMR A.A. ATTIA[a],
GRIGORE DAMIAN[f]**

ABSTRACT. Site-directed spin labeling and EPR characterization (continuous wave as well as DEER) of two blood substitute candidates is described for the first time: glutaraldehyde-polymerized bovine hemoglobin and the related hemoglobin-albumin copolymer. In vitro, with two different types of cell cultures, these spin-labeled candidates are relatively stable; however, they appear to be rapidly reduced in vivo, most likely via removal or reduction of the spin label (as opposed to removal of the blood substitute candidate from the circulatory system altogether).

Keywords: hemoglobin, albumin, blood substitute, HBOC, EPR, spin label, MTSSL, in vivo, cell culture, free radical

---

[a] *Department of Chemistry and Chemical Engineering, "Babes-Bolyai" University, 11 Arany Janos street, Cluj-Napoca 400028, Romania*
[b] *Institute for Interdisciplinary Research on Bio-Nano-Systems, "Babes-Bolyai" University, 11 Arany Janos street, Cluj-Napoca 400028, Romania*
[c] *Ion Chiricuta Cancer Institute – Comprehensive Cancer Center, 34-36 Republicii street, Cluj-Napoca 400015, Romania*
[d] *Institute of Biological Research, "Babes-Bolyai" University, 48 Republicii street, Cluj-Napoca 400015, Romania*
[e] *National Institute for Research and Development of Isotopic and Molecular Technologies, 400293 Cluj-Napoca, Romania*
[f] *Department of Physics, Babes-Bolyai University, Cluj-Napoca 400028, Romania*
* *Corresponding author: rsilaghi@chem.ubbcluj.ro*

R. SILAGHI-DUMITRESCU, C.A GRUIAN, C. PUSCAS, A. SIMON, E. FISHER-FODOR, V. AL. TOMA, A. FARCAS, I. ROMAN, V.-F. SCURTU, AMR A.A. ATTIA, G. DAMIAN

INTRODUCTION

Site-directed spin labeling (SDSL) in combination with EPR spectroscopy is a complementary method to X ray crystallography and NMR spectroscopy, widely used for monitoring the structure and dynamics of the proteins.[1] The paramagnetic center (spin label) is typically added specifically at cysteine residues – native as well as purposefully introduced by site-directed mutagenesis.[2] The most used spin labelled for this purpose is methanethiosulfonate (MTS), due to its small volume and its sulfhydryl specificity.[1,3] Continuous wave EPR spectroscopy (CW) offers information about the solvent accessibility of the spin labels (and implicitly of the amino acid where they are attached), their mobility, polarity of the surroundings, as well as on intra and intermolecular distances between two spin labels or between spin labels and any other paramagnetic centers situated at a distance below 2 nm.[1,4–6] Complementary to this, pulse EPR can detect inter-spin distances between 2 and 8.[1,7–11]

Bovine hemoglobin (Hb) has two native cysteines in the β chains, both accessible for spin labeling. The crystal structure of the protein displays a distance of approximately 21 Å between the two β-93 positions within the tetramer.[2,12–15] Bovine Hb is often cited as a promising starting material for Hb-based artificial oxygen carriers. The synthetic strategies to this goal often entail increasing the apparent molecular weight, such as by polymerization of with glutaraldehyde or copolymerization with an antioxidant/protective molecule (ranging from small organics to proteins such as serum albumin).[16–20] The present study reports an application of EPR in combination with SDSL on bovine Hb and on two blood substitute candidates – a version obtained by simple polymerization of Hb with glutaraldehyde and a copolymer of Hb with BSA, both of which have previously been extensively tested as potential blood substitute materials. [16–19,21] The structural information derived from such measurements is the more useful when one considers their inherent heterogeneity, which makes them much less amenable to traditional methods such as x-ray crystallography.

RESULTS AND DISCUSSIONS

Continuous-wave EPR spectra of blood spin-labelled blood substitute candidates

Bovine hemoglobin has a native cysteine accessible for spin labels in position β-93, which was labelled with MTS. The crystal structure of the protein displays a distance of approximatively 21 Å between the two β-93 positions within the tetramer. (Figure 1)
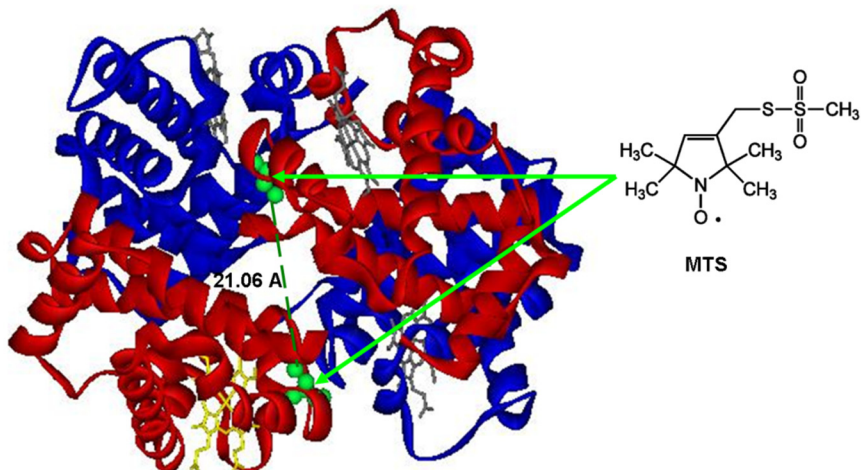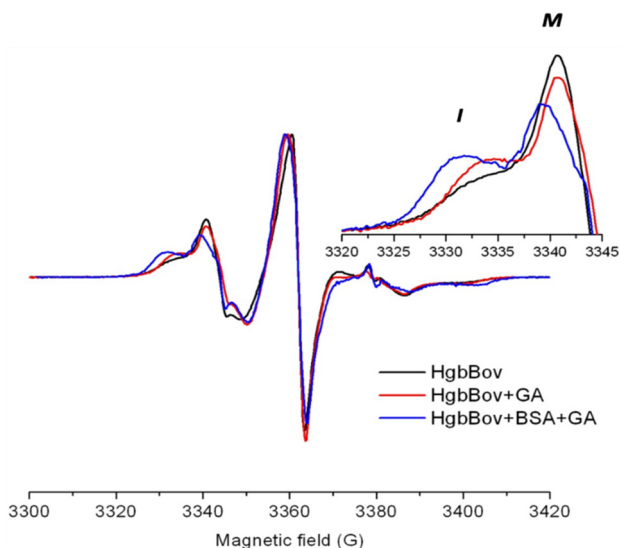
Figure 1. Structure of hemoglobin (2QSS from Protein Data Bank). The α-chains
are colored in blue and the β-chains are colored in red; heme group are indicated
in stick representation and cysteine-93 from the both β-chains are shown in
green ball, with dashed lines between them.

Figure 2 shows the EPR spectra of native, polymerized and
copolymerized hemoglobin labelled with MTS, in buffer. The cw-EPR spectra
of labelled proteins have two components, associated with different mobility
states of the attached spin labels. The immobile component is associated
with a fraction of spin labels engaged in secondary and tertiary interactions
that restrict their reorientation freedom, while the mobile component (M)
corresponds to the signal provided by spin labels that have less constrains
in their surroundings and that are exposed to aqueous environment. The
populations corresponding to these two states are in thermodynamic
equilibrium with the mobile phase more pronounced in solution.[1,22] The two
spectral components are clearly visible in the polymerized and copolymerized
hemoglobin, showing an increase of the immobilization component following
the glutaraldehyde polymerization procedure. When BSA is added, the protein
immobilization is even more pronounced, and it also affects the mobile
component of the spectrum. This may be interpreted as proof that that
hemoglobin molecules are surrounded by BSA in the copolymer – hence a
true heteropolymer, not a mixture or aggregation of a BSA polymer with a Hb
polymer. This assumption is, as seen below, supported by the pulse DEER
measurements.

R. SILAGHI-DUMITRESCU, C.A GRUIAN, C. PUSCAS, A. SIMON, E. FISHER-FODOR, V. AL. TOMA, A. FARCAS, I. ROMAN, V.-F. SCURTU, AMR A.A. ATTIA, G. DAMIAN

Figure 2. Superposed cw-EPR spectra recorded at room temperature for native hemoglobin, polymerized with glutaraldehyde (GA) and copolymerized with BSA and labelled with MTS. The spectra were recorded in PBS, pH 7.4.

DEER experiments

The DEER analyses of the samples show a high modulation depth of the DEER traces (Figure 3a), indicating the dipolar interaction of a considerable number of spin labels. The distance distribution obtained for all three samples (native, polymerized and polymerized hemoglobin) exhibits a peak at 28.6 Å, slightly longer than the Cys---Cys distance seen within the Hb tetramer in the X-ray structure (21 Å). This difference is caused likely by the dynamics of the protein domains, as well as by added size of the spin label. Interestingly, a second peak situated at a distance longer than the first peak, at 44 Å, appears in the distance distribution curve after the polymerization of hemoglobin. This peak reflects the interaction of spin labels of neighboring hemoglobin molecules within the formed cluster; Figure 4 reveals that hemoglobin tetramers can indeed be organized at close distance, amenable for crosslinking with glutaraldehyde, where inter-protein Cys-Cys distances are in good agreement with the DEER data. In the Hb-BSA copolymer, this 44-Å distance peak does not appear anymore, suggesting that in this case the hemoglobin molecules are surrounded by BSA within the formed cluster, so that spin labels from neighboring Hb are not within the (maximum) 8 nm range of a DEER measurement. Such data allow one to get insight on the structure of the polymer and copolymer, which, considering their inherent heterogeneity is very difficult to obtain by traditional methods such as x-ray crystallography.
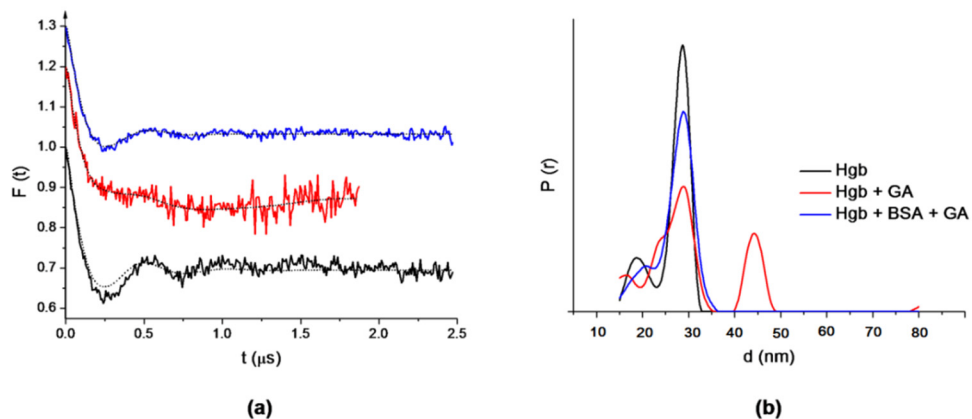
Figure 3. DEER characterization of MTS) spin-labelled of native hemoglobin and
polymerized and copolymerized one: a) background corrected dipolar evolution
data; b) data analysis performed by Tichonov regularization.
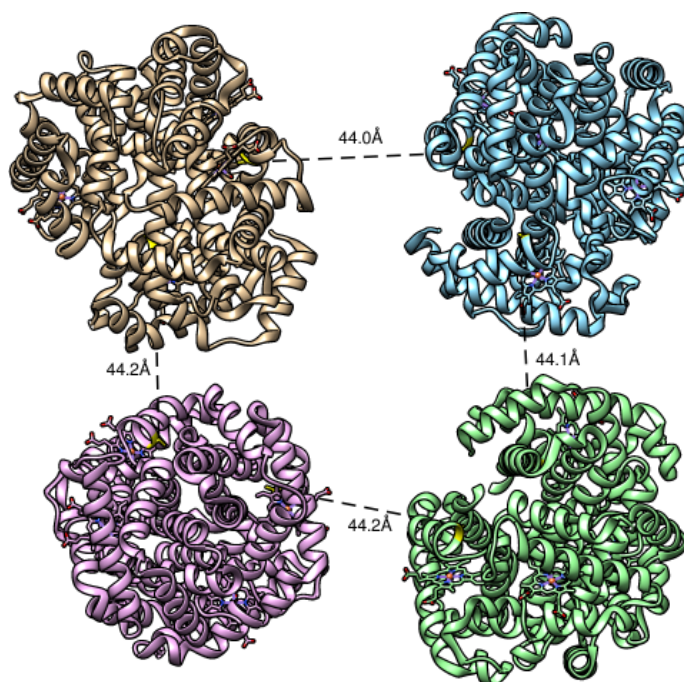
Figure 4. Evaluation of relative distances between cysteines in
glutaraldehyde polymerized hemoglobin.

125

Cell cultures

Samples containing native (simple tetrameric) spin-labelled Hb were mixed with *E. coli* cells at various different ratios that were chosen to be similar to those that might occur between blood substitutes and human cells during an actual transfusion experiment. EPR spectra were recorded immediately after mixing, as well as after 1 and 4 days, respectively. Figure 5 shows illustrative spectra; apparently, when Hb is in contact with cells, the signal intensity decreases; nevertheless, it is clearly detectable even after 24 hours.
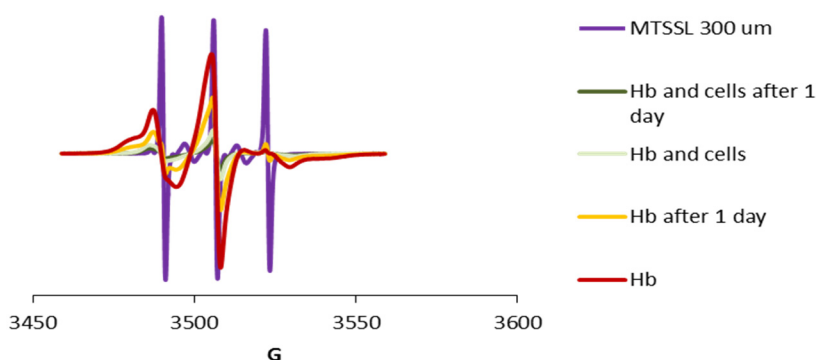
Figure 5. EPR spectra of the spin label and spin-labeled Hb in the presence of *E.coli* cells

HB-BSA and Hb-HSA (bovine hemoglobin co-polymerized with bovine and human serum albumins, respectively) were then tested in similar protocols to those presented above for native Hb, cf. Figure 6. As expected, the lineshapes of both albumin copolymers are very similar to those of the non-polymerized native Hb – though with some apparent loss in mobility in the spin label, as expected in a polymer versus the "monomer". The signal is clearly detectable even after 48 h. In the presence of cells, a severe reduction of the immobile component is also noticeable from the shape of the spectra at 3480 G. These data appear to suggest that the copolymer with BSA is more stable in the environment outside the cells compared to the copolymer with HSA. UV-vis measurements of supernatant and cells separately after exposure to Hb and its copolymerized species were also recorded after mixing and in time, at 24 and 48 hours. As shown in Figure 7, the characteristic Soret band of Hb is intact and restricted to the supernatatnt – suggesting that the copolymers do not enter or adhere to the surface of the cells.
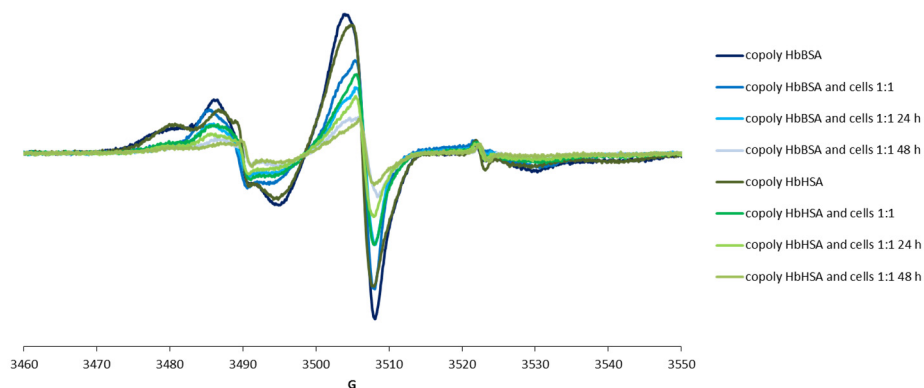
Figure 6. EPR spectra of the two Hb-albumin complexes in the presence
of *E.coli* cells in time.
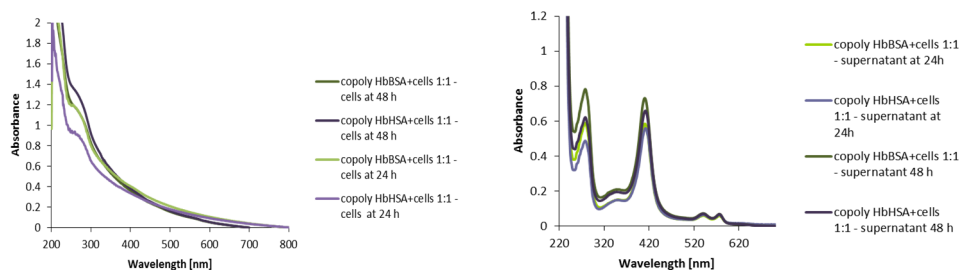
Figure 7. UV-vis spectra of the *E.coli* cell culture (left) and the supernatants (right)
at 24 and 48 hours after exposure to both Hb copolymers.

HUVEC line cells are regular cells which exist in veins collected from
the umbilical cord and they would be the first to be affected if the products
enters the bloodstream when tested *in vivo*. Therefore, EPR spectra were
also collected on such cell cultures after inoculation with the Hb-BSA
copolymer. Figures 8 and 9 show that there is only insignificant trace of the
spin label inside these cells, whereas the proteins are detected in the
surrounding environment. The effect of the contact of these artificial
hemoglobins with human cells at 24 and 48 hours suggests the reduction of
the disulfide bond between the proteins and the spin label, which can be
clearly seen by the line shape of the spectra which are reminiscent of the
free, non protein-bound, spin label.
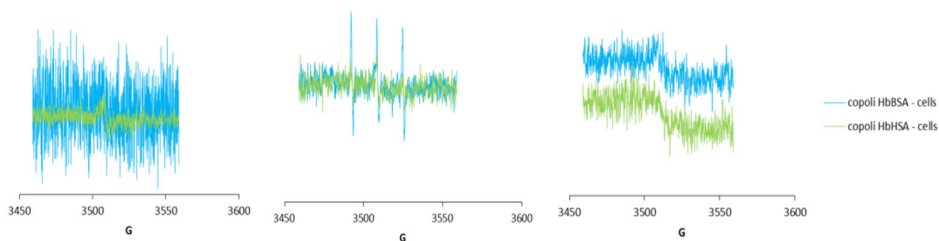
Figure 8. EPR spectra of the HUVEC cellular suspension in time - at the moment of mixing (left), at 24 (center) and 48 hours (right).
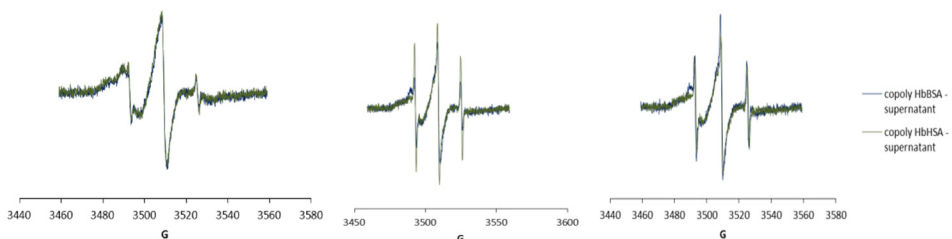
Figure 9. EPR spectra of the survival of the bound spin label in the supernatant in time - at the moment of mixing (left), at 24 (center) and 48 hours (right)

In vivo results

EPR spectra collected on the blood of Wistar rats at 10 minutes, 2 hours and 24 hours after injection with the Hb polymer are shown in Figure 10. The intensity of the EPR signal is very low even at 10 minutes after injection, when the physiological mechanisms would not have had time to remove the product from the bloodstream, but mostly to distribute it homogeneously in the blood vessels. Also, the line shapes are typical of the free form of the spin label. Overall, these data lead to the conclusion that Hb bound to MTSSL has a very short lifetime when exposed to human living systems and further *in vivo* investigation of HBOC with this spin label is not feasible. Possible alternatives with spin labels which can form a more stable adduct with globins (e.g., involving iodoacetamide) are currently considered.
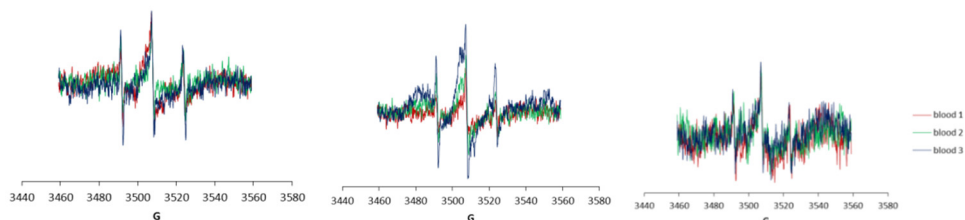
Figure 10. EPR spectra of the Hb polymer at 10 minutes (left), 2 hours (center)
and 24 hours (right) after its injection in rats (3 experiments).

CONCLUSIONS

Three hemoglobin (Hb) based HBOC candidates (Hb polymerized
with glutaraldehyde, Hb copolymerized with BSA, and Hb copolymerized with
HSA) were investigated using EPR spectroscopy combined with site-directed
spin labeling (SDSL), a method widely used for investigating the dynamics
and structure of the proteins. The spin labeling procedure entails the specific
addition of MTSSL to a site at the two native β93 cysteines residues in the
hemoglobin tetramer.

These products were then tested in vitro by exposing them to living
cells, *Escherichia coli* cultures and human umbilical vein endothelial cells
(HUVEC). Also, in vivo tests on animals were performed which provided
information about the lifetime of the copolymer into the circulatory system,
and the undergone structural changes. The Hb (co)polymers are stable in
the investigated in vitro and in vivo conditions; however, their spin labels
were only stable when exposed to *E. coli* cells. In human cell cultures and in
vivo the spin labels were essentially depleted immediately upon exposure
(e.g., 10 minutes). This suggests that spin labeling of HBOC for the purpose
of in vivo monitoring may require more robust attachment procedures than
with MTSSL.

EXPERIMENTAL SECTION

Hemoglobin and its (co)polymers with glutaraldehyde and albumin
were obtained and characterized as previously described.[16,17] Structural
protein analysis and visualization was performed within the Chimera
software package.[23]

R. SILAGHI-DUMITRESCU, C.A GRUIAN, C. PUSCAS, A. SIMON, E. FISHER-FODOR, V. AL. TOMA, A. FARCAS, I. ROMAN, V.-F. SCURTU, AMR A.A. ATTIA, G. DAMIAN

Hemoglobin spin labeling. The proteins were incubated with 10 mM dithiothreitol (DTT) at 4°C for 2 hours to break the disulfide bridges. Buffer condition were 100 mM KCl, 50 mM Tris-DCl (pH 7.5) and 5 mM MgCl$_2$ in D$_2$O. Afterwards, in order to remove the DTT and to replace the acidic conditions, the samples were washed by repeated dilution step with phosphate buffer (pH 8.2), using centrifugal filter units with 30 kDa molecular weight cutoff. Afterwards, the protein solutions were incubated with ten-fold molar excess of MTSSL overnight. The excess of spin labels was removed by consecutive washing and centrifugation steps. Labeling efficiency was estimated to be 90 %. Hb was subsequently (co)polymerized as previously described,[19] and prepared for in vitro and in vivo experiments as a stock solution of 1 mM in phosphate buffer, saline (PBS).

Cw-EPR measuremens. The room temperature X-band cw-EPR measurements were conducted on a home-made EPR spectrometer equipped with a Bruker dielectric resonator. Glass capillaries of 0.9 mm inner diameter were filled with a sample volume of 15 μL, sufficient for a total active resonator volume of 10 μL. The microwave power was set to 1.0 mW, the B-field modulation amplitude was 0.15 mT.

DEER measurements. DEER measurement were recorded at a X-band frequency with a Bruker Elexsys 580 spectrometer equipped with a Bruker Flexline split-ring resonator ER4118xms3 and a continuous flow helium cryostat ESR900 (Oxford Instruments) controlled by an Oxford Intelligent temperature controller ITC 503S. Prior to freezing the protein in 3 mm inner diameter EPR tubes, 20 % (v/v) glycerol was added to each sample in order to increase viscosity. All data were collected at 50 K following the four-pulse DEER sequence. The total measurement time for each sample was 8–24 h. Data analysis was performed with DeerAnalysis2011/2013.[22]

Cell culture and in vivo experiments

Initial experiments were made with the *E. coli* strain BL 21 (DE3), freshly cultivated on LB medium. Samples of both native (simple tetrameric) and albumin-copolymerized Hb were mixed with these culture cells at various different ratios chosen to be similar to those that might occur between blood substitutes and human cells during an actual transfusion experiment.

HUVEC cells were cultivated as previously described and exposed to HBOC candidates in a ratio of 1:1 (v:v).

Wistar rats were selected and prepared/treated as previously described in HBOC top-up experiments;[19,24] the experiments and animals welfare were conducted according to the *Guide for the Care and Use of Laboratory Animals 8*[th] *ed.* (Department of Health Education, and Welfare, National Institute

of Health, 1996), and followed the guidelines of the *Directive 2010/63/UE of the European Parliament and of the Council* with ethical approvals. The animal testing and experiments were approved by the Ethics Committee and Animal Protection for experiments from the Institute of Biological Research, NIRDBS branch, Cluj-Napoca, Romania. (Decision 1/28.02.2013). Following injection with the HBOC candidate, blood for EPR measurements was collected at 10 minutes, 2 hours and 24 hours.

EPR measurements were performed on cell cultures and on venous blood samples collected from the rats under conditions previously described.[19]

ACKNOWLEDGMENTS

REFERENCES

1. Klare, J.P.; Steinhoff, H.J. *Photosynth. Res.* **2009**, *102*, 377–390.
2. Horváth, L.I.; Török, M.; Hideg, K.; Dux, L. *J. Mol. Recognit.* **1997**, *10*, 188–193.
3. Berliner, L.J.; Grunwald, J.; Hankovszky, H.O.; Hideg, K. *Anal. Biochem.* **1982**, *119*, 450–455.
4. Hubbell, W.L.; Cafiso, D.S.; Altenbach, C. *Nat. Struct. Biol.* **2000**, *7*, 735–739.
5. Banham, J.E.; Baker, C.M.; Ceola, S.; Day, I.J.; Grant, G.H.; Groenen, E.J. J.; Rodgers, C.T.; Jeschke, G.; Timmel, C.R. *J. Magn. Reson.* **2008**, *191*, 202–218.
6. Grote, M.; Bordignon, E.; Polyhach, Y.; Jeschke, G.; Steinhoff, H.J.; Schneider, E. *Biophys. J.* **2008**, *95*, 2924–2938.
7. Borbat, P.P.; Freed, J.H. *Chem. Phys. Lett.* **1999**, *313*, 145–154.
8. Pannier, M.; Veit, S.; Godt, A.; Jeschke, G.; Spiess, H.W. *J. Magn. Reson.* **2000**, *142*, 331–340.
9. Schiemann, O.; Prisner, T.F. *Q. Rev. Biophys.* **2007**, *40*, 1–53.
10. Klare, J.P. *Biol. Chem.* **2013**, *394*, 1281–1300.
11. Jeschke, G. *Annu. Rev. Phys. Chem.* **2012**, *63*, 419–446.
12. Gruian, C.; Steinhoff, H.J.; Simon, S. *Studia UBB Chemia* **2011**, 71–81.
13. Gruian, C.; Vulpoi, A.; Steinhoff, H.J.; Simon, S. *J. Mol. Struct.* **2012**, *1015*, 20–26.

14. Takacs, I.M.; Mot, A.; Silaghi-Dumitrescu, R.; Damian, G. *J. Mol. Struct.* **2014**, *1073*, 18–23.
15. Takacs, M.I.; Mot, A.; Silaghi-Dumitrescu, R.; Damian, G. *Studia UBB Chemia* **2013**, *58***,** 61–69.
16. Iacob, B.; Deac, F.; Cioloboc, D.; Damian, G.; Silaghi-Dumitrescu, R. *Artif. Cells Blood Substitutes Biotechnol.* **2011**, *39***,** 293–297.
17. Scurtu, F.; Zolog, O.; Iacob, B.; Silaghi-Dumitrescu, R. *Artif. Cells Nanomedicine Biotechnol.* **2014**, *42***,** 13–17.
18. Hathazi, D.; Scurtu, F.; Bischin, C.; Mot, A.; Attia, A.; Kongsted, J.; Silaghi-Dumitrescu, R. *Molecules* **2018**, *23*, E350.
19. Toma, V.A.; Farcas, A.D.; Roman, I.; Sevastre, B.; Hathazi, D.; Scurtu, F.; Damian, G.; Silaghi-Dumitrescu, R. *PLoS One* **2016**, *11***,** e0153909.
20. Hathazi, D.; Mot, A.C.; Vaida, A.; Scurtu, F.; Lupan, I.; Fischer-Fodor, E.; Damian, G.; Kurtz Jr., D.M.; Silaghi-Dumitescu, R. *Biomacromolecules* **2014**, *15*, 1920–1927.
21. Scurtu, V.-F.; Moţ, A.C.; Silaghi-Dumitrescu, R. *Pharmaceuticals* **2013**, *6***,** 867–880.
22. Bridges, M.D.; Hideg, K.; Hubbell, W.L. *Appl. Magn. Reson.* **2010**, *37*, 363–390.
23. Pettersen, E.G.; Goddard, T.D.; Huang, C.C.; Couch, G.S.; Greenblatt, D.M.; Meng, E.C.; Ferrin, T.E. *J. Comput. Chem.* **2004**, *25*, 1605–1612.
24. Toma, V.A.A.; Farcas, A.D.D.; Roman, I.; Sevastre, B.; Hathazi, D.; Scurtu, F.; Damian, G.; Silaghi-Dumitrescu, R. *Int. J. Biol. Macromol.* **2017**, *107*, 1422–1427.

COMPARATIVE CHARACTERIZATION OF SOMATIC HYBRIDS OF *SOLANUM BULBOCASTANUM + S. TUBEROSUM* CV. 'RASANT' WITH THEIR PARENTS IN RELATION TO BIOCHEMICAL RESPONSES TO WOUND STRESS AND TRICHOME COMPOSITION

DANIEL CRUCERIU[a], IMOLA ERDELY-MOLNAR[a], ZORITA DIACONEASA[b], ANTONIA MARIA MARGINEANU[a], ADRIANA AURORI[a,c], ELENA RAKOSY-TICAN[a,*]

ABSTRACT. Potato production is severely affected worldwide due to its susceptibility to pathogens and pests. *Solanum bulbocastanum*, a potential source of resistance genes, is sexually incompatible with potato. Therefore, somatic hybridization is an alternative tool for enrichment of the potato resistance gene pool. Some important mechanisms involved in resistance are trichomes and various plant secondary metabolites. These resistance mechanisms were recorded in *S. bulbocastanum*, potato cv. 'Rasant' and two of their somatic hybrids with different chromosome numbers in order to evaluate the acquisition of these resistance traits by somatic hybridization. The foliar trichomes were characterized microscopically for morphology and density. Total polyphenolic (TPC) and flavonoid (TFC) content and antioxidant activity (AA) were quantified, both before and after mechanical wounding. Wounding increased TPC, TFC and AA in all tested genotypes. *S. bulbocastanum* was far superior for all parameters when compared with *S. tuberosum* cv. Rasant. The 1508/5 somatic hybrid proved to be similar to the wild species for trichome morphology and density, whereas it has intermediate phenotype for the TPC, TFC and AA compared to the genitors. Therefore, somatic hybridization proves to be a useful tool for resistance mechanisms transfer from a wild species to a somatic hybrid, the 1508/5 genotype being a good candidate for future use in pre-breeding programs.

Keywords: *antioxidant activity, cytogenetic, flavonoids, polyphenols, somatic hybrids, trichomes*

[a] *"Babes-Bolyai" University, Department of Molecular Biology and Biotechnology, 5-7 Clinicilor Street, Cluj-Napoca 400006, Romania*

[b] *University of Agricultural Sciences and Veterinary Medicine, Faculty of Food Science and Technology, 3-5 Calea Mănăştur, Cluj-Napoca 400372, Romania*

[c] *University of Agricultural Sciences and Veterinary Medicine, Advanced Horticultural Research Institute of Transylvania, 3-5 Calea Mănăştur, Cluj-Napoca 400372, Romania*

*Corresponding author: Elena Rakosy-Tican, Email: rakosy.elena@gmail.com

DANIEL CRUCERIU, IMOLA ERDELY-MOLNAR, ZORITA DIACONEASA,
ANTONIA MARIA MARGINEANU, ADRIANA AURORI, ELENA RAKOSY-TICAN

INTRODUCTION

Potato is an important food source for the world population, ranking fourth in terms of worldwide crop production, after wheat, corn and rice [1]. However, *S. tuberosum* is highly susceptible to a wide variety of pests and pathogens, like viruses [2], bacteria [3] or fungi [4].In this context, several wild potato species with broad resistance to biotic and abiotic stress factors were identified as reliable genetic resources for the potato gene pool enrichment [5]. One of such species is *S. bulbocastanum*, a wild diploid Mexican potato species, with accessions which retain resistance to a multiple pests and pathogens [6].

It is difficult to improve the cultivated potato species by classical breeding, due to its sexual incompatibility with most of the wild *Solanum* species, caused by differences in ploidy level and/or endosperm balanced numbers (EBN). Somatic hybridization, an alternative to classical breeding and transgenesis, is a biotechnological tool by which multiple resistance genes and derived mechanisms may be transferred between two distinct species by protoplasts fusion, protoplasts being isolated from each parent [5, 7-9].

Wild plants hold several different resistance mechanisms to each specific environmental factor. Among the structural features, an important defensive role is played by trichomes, specialized hairs found on the surface of vascular plants. Direct correlations between trichomes density and resistance to insects have been repeatedly reported [10, 11]. Furthermore, there is evidence that glandular trichomes from *Solanum* species are involved in resistance to *P. infestans* [12]. Trichomes of the *Solanaceae*, intensively studied in tomato, are distinguished by eight different types, of which four are glandular and four are non-glandular [13]. However, potato and its somatic hybrids were less investigated in respect to their trichome types and densities [14].

Polyphenols are plant important secondary metabolites, which are known to be involved in plant responses to biotic and abiotic stresses. They take part in the non-enzymatic antioxidant system, with an important role in maintaining the redox state of the cell, due to their strong antioxidant capacity [15]. These compounds are found constitutively in plant tissues, their concentration being sometimes critical for an organism to be resistant to a specific pathogen [16, 17]. Moreover, there is evidence that their concentration is rapidly increasing if a stress factor appears in the environment, further highlighting their relevant role in plant defense [18]. Polyphenol and flavonoid *de novo* synthesis is associated with both abiotic factors like strong light, wounding or exposure to UV light [19-21], and biotic stresses such as bacteria [22], insects [23] and other pathogens [24].

Physical wounding occurs in plants at each herbivore attack, process that stimulates polyphenol accumulation as a defense mechanism at the affected site. A recent report indicates that different polyphenols are synthesized when an insect starts consuming the plant [25]. Furthermore there is evidence proving that the accumulation of these secondary metabolites is related to mechanical wounding, even in the absence of herbivore feeding [26].

In this paper, we evaluate two previously obtained somatic hybrids between *S. tuberosum* cv. 'Rasant' and the wild species *S. bulbocastanum* [9], with the main goal to characterize their resistance mechanisms to several environmental factors in comparison with their parents. We determined the trichome morphology and density found on the surface of their leaves in order to assess the differences between genotypes from a physical defense mechanism perspective. Moreover, we evaluated the total phenolic content (TPC), total flavonoid content (TFC) and their antioxidant activity (AA) constitutively found in all genotypes and also after wounding, in order to determine both the differences among genotypes and their response to mechanical wounding. These data, correlated with the SHs chromosome number, reveal and confirm clear differences between the two somatic hybrids and highlight the role of analyzed secondary metabolites in wound stress.

RESULTS AND DISCUSSION

Ploidy and chromosome counts results

The indirect cytogenetic analysis based on the number of chloroplasts per guard cell proved to be a very simple and cost effective technique revealing the chromosome numbers with an error of ± 2 chromosomes. Using the correlation curve and statistical analysis it was estimated that the SH 1508/5 has 63.53 chromosomes, while chromosome counts revealed 62 chromosomes (Fig. 1). The SH 1508/2 has 71.26 chromosomes as indicated by indirect calculation as compared to 68 after direct chromosome counts (Fig. 1).

Trichome morphology and density

Trichome diversity was evaluated based on the classification established by Luckwill (1943) and updated by Channarayappa et al. (1992) according to whom, on *Solanaceae* leaves 8 different types of thricomes might exist [13, 27]. The classification is based on morphological and physiological features like secretory capacity, basal cells number and morphology, dimension or glandular cells number. We identified 6 out of 8 possible trichome types
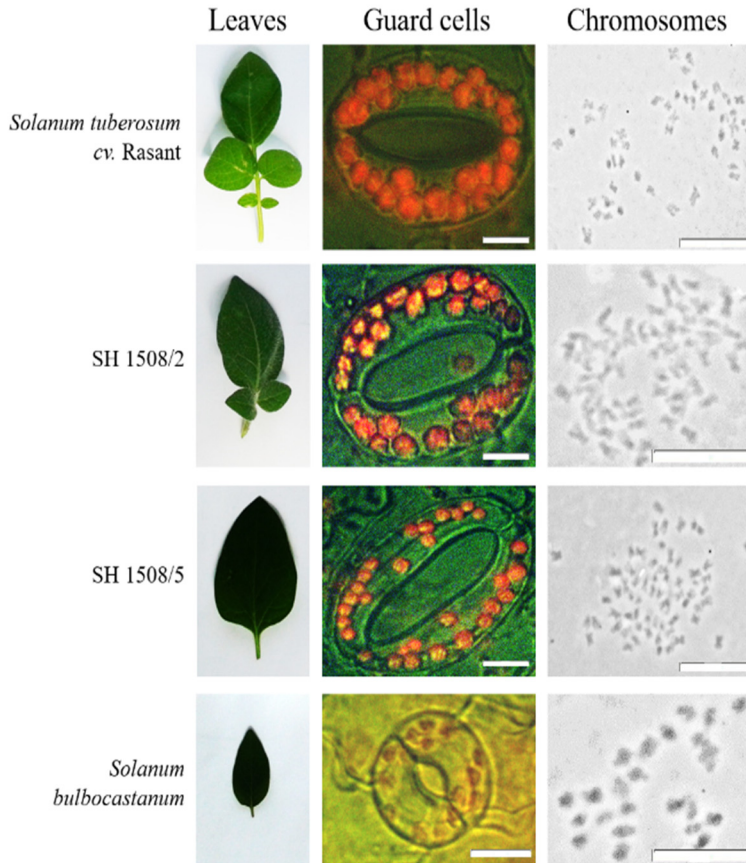
Figure 1. Comparative presentation of analyzed clones for leaf morphology, guard cells used for counting chloroplasts under epifluorescent microscopy (60X) and chromosome numbers (phase contrast pictures) (100X immersion). Bars: 10 µm

on the surfaces of our genotypes, but their diversity varies between genotypes (Fig. 2 and 3). Types II and III, part of the non-glandular subtype, and types VI and VII belonging to the glandular subtype were identified on all four analyzed genotypes. However, two additional types, IV (non-glandular) and V (glandular) were identified only on the leaves of *S. bulbocastanum* and the SH 1508/5 (Table 1).
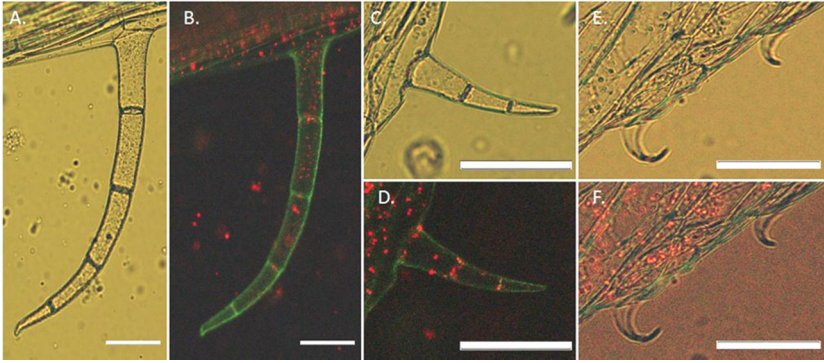
Figure 2. Non-glandular trichomes identified on the leaves of at least one genotype, under direct and UV light. Type II – under direct (A) and UV (B) light; Type III – under direct (C) and UV (D) light; Type V – under direct (E) and UV + direct (F) light. Note that Type V does not have fluorescence under UV light. Red fluorescence is emitted by chlorophyll. Bars: 100 µm
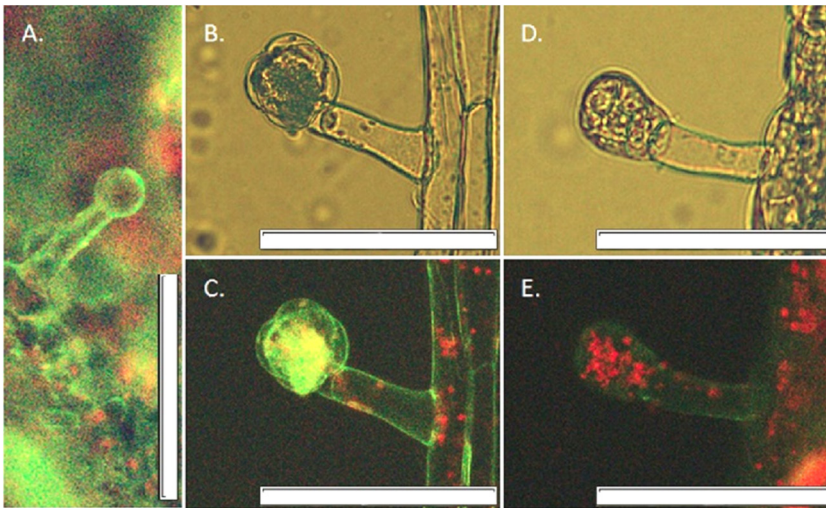
Figure 3. Glandular trichomes identified on the leaves of at least one genotype, under direct and UV light. Type IV – under UV light (A); Type VI, young trichome – under direct (B) and UV (C) light; Type VII, mature trichome – under direct (D) and UV (E) light. Bars: 100 µm

Table 1. Distribution of trichome types among all four analyzed genotypes: *S. bulbocastanum* (<u>S. blb</u>), *S. tuberosum* cv. 'Rasant' and two somatic hybrids (1508/5 and 1508/2). „+" represents the presence of each specific type on the leaves.

| Genotype	Type II	Type III	Type IV	Type V	Type VI	Type VII
S. blb	+	+	+	+	+	+
'Rasant'	+	+			+	+
1508/5	+	+	+	+	+	+
1508/2	+	+			+	+

In terms of native fluorescence under UV light, the non-glandular type II and III trichomes present red fluorescence inside the cells, showing chlorophyll content, and thus photosynthetic activity. On the other hand, type IV trichome does not show any kind of fluorescence. Regarding the glandular trichomes, all three types that were found on leaf surfaces presented either green or red fluorescence, or a combination of the two (Fig. 3).

Trichome densities determined for each genotype are presented in Fig. 4. The lowest total density is characteristic for *S. tuberosum* cv. Ransat, with only 340 ± 16.7 trichomes/cm^2, while the highest was found on the leaves of *S. bulbocastanum* (598 ± 17.5) and the SH 1508/5 (620 ± 15.3). The SH 1508/2 presented intermediate phenotype (522 ± 7.8) when compared to the two parents. The major differences between genotypes occurs in the glandular trichome density, even though significant differences ($p < 0.05$) are also observed in the non-glandular hair density, when comparing the cultivated potato with all the other genotypes.
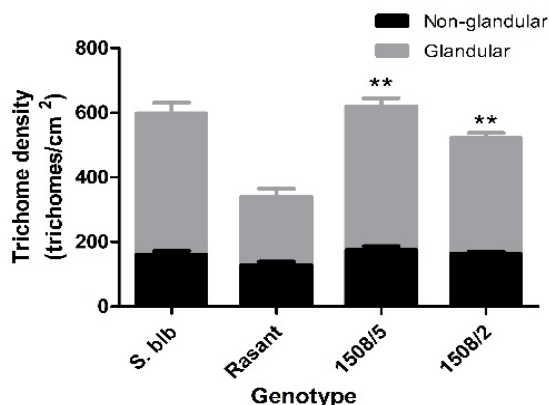
Figure 4. Non-glandular (black) and glandular (grey) trichome density for all four genotypes: *S. bulbocastanum* (S. blb), *S. tuberosum* cv. 'Rasant' (Rasant) and two somatic hybrids (1508/5 and 1508/2). For each somatic hybrid, ** shows a highly significant difference ($p < 0.01$) in comparison to *S. tuberosum* cv. 'Rasant'

Non-glandular trichomes are directly involved in plant stress response, being implicated in specific resistance mechanisms to both biotic and abiotic factors. They reduce the insect's movement on leaf surfaces [28], are a mechanical barrier to pathogen attacks [29], participate in temperature and humidity regulation [30] and in calcium ions homeostasis [31]. Thus, the presence of an additional non-glandular type on the surface of *S. bulbocastanum* and the somatic hybrid 1508/5 can be considered a morphological advantage, conferring resistance to all these environmental factors, when compared to the cultivar.

Glandular trichomes are known to secrete a vast variety of secondary metabolites, with implications in the physiological response to biotic stress factors. Type VI secrets different terpenoids [32], that are repellent or toxic for different parasites and insects, while type VII appears to synthesize protease inhibitors which affect the growth of insect larvae [33]. Type IV, the glandular type that was identified only on the leaves of the wild species and the 1508/5 somatic hybrid, is known to secrete sugar esters [33], which are toxic for the consuming insects [34]. In this context, *S. bulbocastanum* is superior in terms of resistance to consumers when compared to the cultivar. Furthermore, the 1508/5 somatic hybrid has presumably inherited the trichome diversity from the wild species, therefore it acquired novel resistance mechanisms in comparison with the cultivated potato.

Trichome density has an important contribution in regard to plant general resistance to environmental factors. Several reports demonstrate a correlation between hair density on leaves surface and resistance to different biotic stress factors [10, 35]. Therefore, both somatic hybrids might possess greater resistance towards these stress factors because they acquired higher trichome densities through somatic hybridization.

Total phenolic and flavonoid contents and the antioxidant activity

The TPC and TFC for each genotype, both under control conditions and after wounding are presented in Fig. 5 (A.) and (B.) The highest constitutive phenolic and flavonoid contents (under control conditions) were found in *S. bulbocastanum,* while *S. tuberosum* cv. 'Rasant' and the SH 1508/2 proved to have low TPC and TFC. The SH 1508/5 has intermediate phenotype in regard to both physiological traits, when compared to the parents.

The results for the AA are presented in Fig. 5 (C.). Similar to our data on TPC and TFC, the highest AA was found in *S. bulbocastanum* and low antioxidant capacity was observed in the cultivar and the SH 1508/2. Furthermore, the SH 1508/5 proved to be intermediate in regard to the AA, when compared with its parents. A strong correlation between TPC and AA was observed under both sets of conditions, the Pearson correlation coefficient being 0.995 ($p < 0.01$) in control plants.

All three parameters increased after wounding, for all the genotypes tested. *S. tuberosum* cv. 'Rasant' has high increasing rates for both TPC and TFC after wounding, but these secondary metabolites are found in lower final concentration, in comparison with the SH 1508/5. Thus, the somatic hybrid is still superior in regard to these physiological traits. The observed increase in AA after wounding is most probably caused by the accumulation of polyphenols and flavonoids, but also by other compounds with antioxidant capacity. This might explain the differences in the increasing rates observed for TPC on one hand and AA on the other hand.
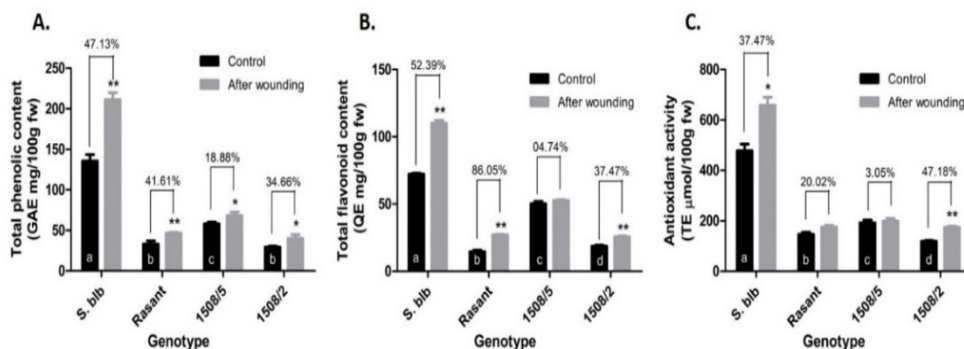
Figure 5. Total phenolic content (A.), total flavonoid content (B.) and Antioxidant activity (C.) under control conditions and after wounding, for all four analyzed genotypes: *S. bulbocastanum* (S. blb*), S. tuberosum* cv. 'Rasant' (Rasant) and two somatic hybrids (1508/5 and 1508/2). For each measurement after wounding, * shows a statistically significant difference at $p < 0.05$ and ** shows a highly significant difference at $p < 0.01$ in TPC/ TFC/ AA when compared to control conditions. The increased rates (%) for TPC/ TFC/ AA after wounding for each genotype are shown above each set of data. Significant differences ($p < 0.05$) between genotypes in control conditions are represented by different letters. Data are means ± SD (n=3)

Phenols, including flavonoids, found constitutively in plant tissues, are involved in resistance mechanisms to a wide variety of biotic and abiotic factors. They act as protective molecules against UV light, strong light, heavy metals in soils, high/low temperature [18] but also against herbivores, especially insects, their constitutive concentrations being correlated with broad-spectrum resistance to environmental attacks [23]. Nevertheless, in *Solanum* species, flavonoids proved to be directly involved in resistance to *E. carotovora* and *P. infestans* [36]. Therefore, the SH 1508/5 possesses relevant additional resistance features, due to its higher total phenolic and flavonoid content when compared to the cultivar.

Several reports prove that wounding causes TPC and TFC increase, both after artificial and biotic damage [37, 38]. Furthermore, an increase in TPC and TFC was observed for *Solanum* species, after wounding, irradiation or infection with pathogens [39]. Our results are consistent with these data, for all four genotypes increases in TPC and TFC being observed after artificial mechanical wounding.

Polyphenols and implicitly flavonoids, are part of plant resistance mechanisms due to their toxicity, repellent action or their role as phytoalexins, but also because of their strong antioxidant activity [15]. One of the first physiological events that occur in plants after stress is the generation of reactive oxygen species (ROS), molecules which have a dual role [40]. First, they act as signaling molecules in initiating defense responses, but they are also toxic for the cell if their intracellular concentration increases beyond a threshold value [17, 41]. In this context, polyphenols take part in maintaining the ROS intracellular concentration, due to their antioxidant capacity and thus are involved in plant stress responses. Our results demonstrate firstly that polyphenols are truly involved in the antioxidant activity of our genotypes, due to the strong correlation observed between TPC and AA. Furthermore, our data regarding the AA suggest that *S. bulbocastanum* is far better in comparison with the cultivar and also that the SH 1508/5 inherited in part its antioxidant capacity from the wild species. Therefore, both genotypes present better adaptation mechanisms to environmental stress factors along with already demonstrated presence of two late blight resistance genes (*Rpi-blb*1 and *Rpi-blb*3 – Rakosy-Tican et al. under publication*)*.

S. bulbocastanum proved to be superior in comparison with the cultivated potato in all studied aspects, having 2 additional trichome types, grater trichome density on its leaves and higher TPC, TFC and AA, both under control conditions and after wounding. We expected these results, *S. bulbocastanum* being resistant to different abiotic and biotic stress factors, like aphids, nematodes, or the oomycete *Phytophthora infestans*, while the cultivar is susceptible to these attacks. Thus, the wild species would presumably have multiple resistance mechanisms towards these environmental factors, assumption also demonstrated by our results on trichomes and some physiological responses to artificial wounding (this study) or the stress caused by *in vitro* culture [21].

The SH 1508/5 proved to be superior in regard to all studied morphological/physiological traits when compared with its cultivated genitor although it possessed fewer chromosomes than SH 1508/2. It is similar with the wild species when it comes to trichome diversity and density, and has intermediate TPC, TFC and AA under both sets of conditions tested in this study. This genotype previously proved to be resistant to late blight, due to the presence in its genome of two genes (*Rpi-blb1* and *Rpi-blb3*) that are known to be directly involved in the gene-for-gene durable resistance mechanism to the pathogen

(Rakosy-Tican et al. under publication). Correlating these results, the SH 1508/5 is a good candidate for future pre-breeding programs, due to the acquisition of multiple resistance traits/ mechanisms through somatic hybridization.

EXPERIMENTAL SECTION

Plant material

In this study we analyzed four different genotypes of *Solanum*: the wild diploid Mexican potato species *S. bulbocastanum* GLKS-31741 [blb41; Gross Lüsewitz Potato Collections (GLKS) of the IPK Gene Bank, Leibniz—Institute of Plant Genetics and Crop Plant Research, Germany]; a commercial potato cultivar*, S. tuberosum* cv. 'Rasant' (Nordring-Kartoffelzucht-und Vermehrungs-GmbH Gross Lüsewitz, Germany); and two asymmetric somatic hybrids - 1508/5 and 1508/2, produced by mesophyll protoplast electrofusion [9]. The starting material was represented by micro-tubers maintained *in vitro* on MS medium [42], with 10% sucrose at 4 °C. All four genotypes were cultivated *in vitro* for four weeks under controlled conditions (25 °C ± 2 °C, photoperiod 16 h/ 8 h day/night, 60% humidity and a light intensity of 135 µmol m^{-2} s^{-1}) and acclimatized subsequently under *ex vitro* conditions, in soil. They were cultured under uncontrolled environmental conditions (room temperature: 24 °C ± 3 °C, photoperiod: approximately 12 h, in sunlight during May), for eight weeks.

The hybridity of our somatic hybrids (SHs) was previously demonstrated through flow-cytometry while the use of SSR and AFLP markers proved their asymmetric status [9]. From a morphologic perspective, the somatic hybrids have intermediate phenotype when compared to the parents, both in regard to their biomass, plant height and leaf morphology (Fig. 1). They present intermediate leaf morphology, with the 1508/5 hybrid being more similar to the cultivated genitor and the 1508/2 genotype more likened with the wild species (Fig. 1) [21]. An extremely relevant aspect is that the 1508/5 somatic hybrid proved to be resistant to *P. infestans* in detached leaf assay and field assessments. Furthermore, its genome contains two genes (*Rpi-blb1* and *Rpi-blb3*) directly involved in the gene-to-gene durable resistance mechanism to late blight (Thieme R. personal communication) (Table 2).

Although flow cytometry data reveal that the two somatic hybrids used in this study are pentaploids, indirect and direct cytogenetic methods were applied to better characterize their genetic composition. As indirect method counting of chloroplasts per guard cell was applied. Three leaves from three individual plants for each genotype (parents and SHs) were harvested from three weeks old *in vitro* plants. The abaxial epidermis was peeled out and three different microscopic fields were randomly selected to count the chloroplasts

in each guard cell using epifluorescent microscopy (Olympus BX-60 – objective 60X). The chlorophyll auto-fluorescence facilitated the counting of the chloroplasts per 54 guard cells per analyzed genotype (Fig. 1). The mean number of chloroplasts per guard cell was used to calculate the number of chromosomes based on the correlation curve obtained for the parental genotypes with known ploidy level, *Solanum bulbocastanum* 2x = 24 diploid and *S. tuberosum* cv. 'Rasant' 2x = 48, tetraploid.

Table 2. Available data on the parents and somatic hybrids (SH) used in the present study: hybrid nature was confirmed by SSR markers and flow cytometry; resistance to late blight caused by oomycete *Phytophthora infestans* (Pi) was evaluated in detached leaf assays (DLA) and noted using a scale 1 for the most resistant and 9 for the most susceptible; two *Rpi* genes were followed by using specific molecular markers (data under publication)* For details on SSR markers see Rakosy-Tican et al. (2015)

Genotype	Hybridity/ molecular markers	Ploidy	Resistance to Pi – DLA	*Rpi* genes
S. bulbocastanum blb41	-	2x	Yes/ 1	*Rpi-blb*1 *Rpi-blb*3
S. tuberosum cv. Rasant	-	4x	No/ 5.35	none
SH 1508/2	Yes/SSR STIIKA, STM2022*	5x	ND	ND
SH 1508/5	Yes/SSR STIIKA, STM2022*	5x	Yes/ 2	*Rpi-blb*1 *Rpi-blb*3

Characterization of ploidy and chromosome numbers by using indirect and direct cytological tools

For direct chromosome counts root meristem was used. The roots were induced on nodal segments (n = 20 per genotype) cultured *in vitro* on MS medium with 0.05 mg L^{-1} NAA (α-naftalene acetic acid) pH 5.8. Roots, 10 mm long were harvested and maintained on ice overnight. Then the roots were fixed in ethanol:acetic acid 1:3 for 24 h and maintained at -20 °C until use. The fixed roots were transferred to citrate buffer for 25 min at room temperature. The roots were digested with enzyme solution made up of 0.4% pectolyase, 0.4% citohelycase and 1% celullase in citrate buffer pH 4.8. Enzymatic digestion was performed at 37 °C for 30 min. The roots were washed with citrate buffer for 20 min at 4 °C. Then the root tips containing the meristem were dissected under stereomicroscope with entomological needles. The slides were fixed with a flame and the chromosomes were counted under the microscope using phase contrast microscopy (microscope Olympus BX-60, objective 100X).

Trichome analysis

Trichome type: for each genotype, six fully expanded leaves with mature trichomes originating from two individuals were considered for the trichome morphological analysis. Epidermis from the leaf abaxial surface was peeled out and analyzed through optical microscopy (Olympus BX60), with the 10X objective, under direct light. Simultaneously, the trichomes were analyzed under UV light (filter cube: excitation filter at 450–480 nm, dichroic mirror at 500 nm, barrier filter at 515 nm), in order to highlight their content in bioactive molecules. Images were taken using the Olympus CX50 CCD camera and CellSense software. The morphological analysis was based on the latest *Solanaceae* trichome classification presented by Channarayappa et al. (1992) according to which eight different trichome types might be present on potato leaves surfaces [13].

Trichome density was determined based on the analysis of the third and fourth leaves down from apex, originating from 3 different individuals for each genotype. Detached leaves were maintained in 70% ethanol, in the dark, at room temperature, for three weeks to remove the chlorophyll. Three randomly selected microscopic fields on the abaxial epidermis of each leaf, one at the leaf tip and two on each side were analyzed through stereomicroscopy and pictures were taken with digital camera (Olympus 5060). Trichome density was determined using Photoshop counting tools.

Wounding procedure

For each genotype, two leaves from three different individuals were taken into consideration for this procedure. All individuals were cultivated in the same environmental conditions as unwounded plants. The leaves were incised using scissors, 30% of each leaf being removed. After 16 h, wounded leaves were detached and sample extraction was performed.

Sample extraction

For sample extraction, for both wounded and control plants, 1 g of leaf material derived from three different individuals was milled for each genotype, transferred in 10 mL extraction buffer [acidified methanol - 85:15 v/v, MeOH:HCl) [43] and incubated in the dark, at room temperature for 24 h. The supernatant was collected after centrifugation and the residual tissue was re-extracted under stirring, through repeated extraction buffer addition, centrifugation and collection, until the extraction solvent became colorless [44]. The total extracts for all samples were dried using a vacuum rotary evaporator (Heidolph Laborota 4000 Efficient), at 40 °C and re-dissolved in 2 mL extraction buffer, prior to further analysis.

Total phenolic and flavonoid content determination

Total phenolic content, for each sample, was determined using the colorimetric Folin-Ciocalteu method [45]. Samples of 25 μL were mixed with 1.8 mL distilled water and 120 μL Folin-Ciocalteu Reagent (FCR) for oxidation, and further neutralization was performed using 340 μL Na_2CO_3. After incubation 90 min in the dark, sample absorbance was measured at 750 nm through spectrophotometry (BioTek Instruments, Winooski, VT). The results were expressed as mg of gallic acid 100 g^{-1} of fresh weight (FW). All measurements were performed in triplicate.

The total flavonoid content was evaluated for each sample based on the colorimetric method elaborated by Kim et al. (2003) [46]. Aliquots containing 300 μL of the alcoholic extracts were diluted in 1.2 mL distilled water and 90 μl 5% $NaNO_2$ was added. After that, 90 μL 10% $AlCl_3$ was added, the mixtures were allowed to stay for 6 min and 600 μL 1N NaOH was added to each sample. The absorbance was measured at 510 nm through spectrophotometry (JASCO V-630 series, International Co.). All measurements were performed in triplicate and the results were expressed as mg quercetin equivalents /100 g^{-1} FW.

Antioxidant activity determination

The antioxidant capacity was determined through the ABTS assay (ABTS radical cation distaining assay), based on the capacity of the samples to scavenge ABTS radicals, in comparison with Trolox, a standard antioxidant [47]. The $ABTS^+$ solution was prepared 16 h before the experiment, by mixing 7 mM ABTS with 2.45 mM potassium persulfate in the dark, being diluted afterwards with 70% ethanol, until the solution absorbance at 734 nm reached 0.7. Aliquots containing 20 μL of each sample extract and Trolox were added in 170 μL $ABTS^+$ solution and left in the dark, at 30 ℃, for 6 min. The absorbance was measured at 734 nm on a 96 well microplate, through spectrophotometric means (BioTek Instruments, Winooski, VT). The results were expressed as μmole Trolox equivalents /100 g^{-1} FW and for each genotype 3 measurements were performed.

Statistical analysis

Data shown in Fig. 1 are expressed as means ± standard deviation of six different counts for each genotype, for both glandular and non-glandular trichomes. Unpaired tow-tailed t-tests were performed to determine if the difference between the trichome density on somatic hybrids leaves and the one on the parent's leaves is statistically significant.

DANIEL CRUCERIU, IMOLA ERDELY-MOLNAR, ZORITA DIACONEASA,
ANTONIA MARIA MARGINEANU, ADRIANA AURORI, ELENA RAKOSY-TICAN

Unpaired two-tailed t-tests were also performed to establish the differences between genotypes in regard with their phenolic content, flavonoid content and antioxidant activity, under control conditions. Furthermore, the same statistical analysis was used to assess the disparity in TPC, TFC and AA before and after wounding, for each genotype. Pearson correlation test was used to assess the relationship between TFC and AA. The increase rate of TPC, TFC and AA (parameter) presented by each genotype after wounding, was calculated as follows:

$$Increased\ rate\ (\%) = \left[\left(\frac{parameter\ in\ control}{parameter\ after\ wounding}\right) - 1\right] x\ 100$$

All statistical analyzes were performed using the GraphPad Prism software (Graph Pad Software Inc; San Diego, CA, USA). Significance of difference was defined at the 5% level ($p < 0.05$) for all the t-tests used in this study. Before each statistical analysis, our data were tested for their variances using the F-test.

CONCLUSIONS

Somatic hybridization proves to be a useful biotechnological tool for resistance mechanisms transfer from a wild species to a somatic hybrid. It overcomes the pre- and post-zygote incompatibility barriers, while its major advantage is the transfer of multiple genes, as it happened with the SH 1508/5. The drawback of somatic hybridization is uncontrollable transfer of different numbers of chromosomes from the wild species – as it is the case of the two SHs analyzed here, but this can be resolved by thorough characterization of resulted somatic hybrid clones. Plant genetic transformation is not always a viable method, taking into consideration that the transfer of only a few genes doesn't guarantee the acquisition of the targeted resistance mechanisms. This study highlights the usefulness of somatic hybridization in transferring multiple resistance mechanisms into potato gene pool.

ACKNOWLEDGEMENTS

REFERENCES

1. A.J. Haverkort; P.C. Struik; R.G.F. Visser; E. Jacobsen; *Potato Res*, **2009**, *52*, 249-264
2. L.F. Salazar; *Potato viruses after the XXth century: effects, dissemination and their control*; Crop Protection Department, Lima 12, Peru, **2003**
3. J. Elphinstone; I. Toth; *Erwinia chrysanthemi (Dickeya spp.): The Facts*; British Pototo Council Publications, **2007**
4. G.A. Forbes; W. Pérez; J. Andrade-Piedra; *Field assessment of resistance in potato to Phytophthora infestans*; International Center of Potato **2014**
5. R. Thieme; E. Rakosy-Tican; Somatic Cell Genetics and Its Application in Potato Breeding. In *The Potato Genome*; S.K. Chakrabarti, C. Xie and J.K. Tiwari Eds.; Springer International Publishing AG Cham, Switzerland, **2017**, pp. 217-269
6. D. Carputo; D. Alioto; R. Aversano; R. Garramone; V. Miraglia; C. Villano; L. Frusciante; *Plant Genet. Resour.*, **2013**, *11*, 131-139
7. R. Thieme; E. Rakosy-Tican; T. Gavrilenko; O. Antonova; J. Schubert; M. Nachtigall; U. Heimbach; T. Thieme; *Theor. Appl. Genet.*, **2008**, *116*, 691-700
8. R. Thieme; E. Rakosy-Tican; M. Nachtigall; J. Schubert; T. Hammann; O. Antonova; T. Gavrilenko; U. Heimbach; T. Thieme; *Plant Cell Rep.*, **2010**, *29*,
9. E. Rakosy-Tican; R. Thieme; M. Nachtigall; I. Molnar; T. E. Denes; *Plant Cell. Tiss. Org. Cult.*, **2015**, *122*, 395-407
10. G.G. Kennedy; *Annu. Rev. Entomol.*, **2003**, *48*, 51-72
11. A.T. Simmons; G. M. Gurr; D. McGrath; P. M. Martin; H. I. Nicol; *Aust. J. Entomol.*, **2004**, *43*, 196-200
12. A. Lai; V. Cianciolo; I. Chiavarini; A. Sonnino; *Euphytica*, **2000**, *114*, 165-174
13. S.G. Channarayappa; V. Muniyappa; R. H. Frist; *Can J Bot*, **1992**, *70*, 2184-2192
14. A.M. Mărgineanu; I. Erdelyi-Molnár; E. Rákosy-Tican; *Analele Ştiinţifice ale Universităţii „Al. I. Cuza" Iaşi s. II a. Biologie vegetală*, **2014**, *60*, 33-42
15. O. Blockhina; E. Virolainen; KV. Fagerstedt; *Ann. Bot.*, **2002**, *91*, 179-194
16. K.K. Mallikarjuna N, Jadhav DR, Kranthi S, Chandra S *J. App. Entomol.*, **2004**, *128*, 321-328
17. C.H. Foyer; B. Rasool; J.W. Davey; R.D. Hancock; *J. Exp. Bot.*, **2016**, *67*, 2025-2037
18. J. Mierziack; K. Kostyn; A. Kulma; *Molecules*, **2014**, *19*, 16240-16265
19. G. Guillet; V. De Luca; *Plant Physiol.*, **2005**, *137*, 692-699
20. M. Sisa; S.L. Bonnet; D. Ferreira; J.H. Van der Westhuizen; *Molecules*, **2010**, *15*, 5196-5245
21. D. Cruceriu; I. Molnar; Z. Diaconeasa; A. Aurori; C. Socaciu; E. Rakosy-Tican; *Notulae Botanicae Horti Agrobotanici*, **2017**, *45*, 75-81

22. J.S. Lorenc-Kukula K, Oszmianski J, Szopa, *J. Agric. Food. Chem.*, **2005**, *53*, 272-281
23. D. Treutter; *Environ. Chem. Lett.*, **2006**, *4*, 147-157
24. I. Yedidia; M. Shoresh; Z. Kerem; N. Benhamou; Y. Kapulnik; I. Chet; *Appl. Environ. Microbiol.*, **2003**, *69*, 7343-7353
25. G.S. Nuessly; B.T. Scully; M.G. Hentz; R. Beiriger; M.E. Snook; N.W. Widstrom; *J. Econ. Entomol.*, **2007**, *100*, 1887-1895
26. L.F. Reyes; L. Cisneros-Zevallos; *J. Agric. Food. Chem.*, **2003**, *51*, 5296-5300
27. L.C. Luckwill; *Aberd. Univ. Stud.*, **1943**, *120*, 1-44
28. H.B. Johnson; *Bot. Rev.*, **1975**, *41*, 233-253
29. G.A. Beattie; S.E. Lindow; *Phytopathology*, **1999**, *89*, 353-359
30. J. Ehleringer; Ecology and ecophysiology of leaf pubescence in North American desert plants. In *Biology and chemistry of plant trichomes*; E. Rodriguez, P.L. Healey and I. Mehta Eds.; Plenum Press, New York, **1984**, pp. 113-132
31. D.L. De Silva; T.A. Mansfield; M.R. McAinsh; *Planta*, **2001**, *214*, 158-162
32. A.L. Schilmiller; I. Schauvinhold; M. Larson; R. Xu; A.L. Charbonneau; A. Schmidt; C. Wilkerson; R.L. Last; E. Pichersky; *Proc. Natl. Acad. Sci. U.S.A.*, **2009**, *106*, 10865-10870
33. E.T. McDowell; J. Kapteyn; A. Schmidt; C. Li; J.H. Kang; A. Descour; F. Shi; M. Larson; A. Schilmiller; L. An; A.D. Jones; E. Pichersky; C.A. Soderlund; D.R. Gang; *Plant Physiol.*, **2011**, *155*, 524-539
34. G.J. Wagner; E. Wang; R. W. Shepherd; *Ann. Bot.*, **2004**, *93*, 3-11
35. G.G. Simmons AT; *Agric. Forest. Entomol.*, **2005**, *7*, 265-276
36. A. Kumar; V.S. Pundhir; *Potato Res.*, **1991**, *34*, 9-16
37. S. E. Hartley; R.D. Firn; *J. Chem. Ecol.*, **1989**, *15*, 275-283
38. H.M. Kang; M.E. Saltveit; *J. Agric. Food. Chem.*, **2002**, *50*, 7536-7541
39. C.E. Lewis; J.R.L. Walker; J.E. Lancaster; K.H. Sutton; *J. Sci. Food. Agric.*, **1998**, *77*, 58-63
40. G.R. Cramer; K. Urano; S. Delrot; M. Pezzotti; K. Shinozaki; *BMC Plant Biol.*, **2011**, *11*, 163
41. C.H. Foyer; G. Noctor; *Plant Cell.*, **2005**, *17*, 1866-1875
42. T. Murashige; F. Skoog; *Physiologia Plantarum*, **1962**, *15*, 473-497
43. M.A.A. El-Sayed; P. Hucl; *J. Agric. Food Chem.*, **2003**, *51*, 2174-2180
44. A. Bunea; D.O. Dugină; A.M. Pintea; Z. Sconta; C.I. Bunea; C. Socaciu; *Not. Bot. Horti. Agrobo.*, **2011**, *39*, 70-76
45. V.L. Singleton; R. Orthofer; R.M. Lamuela-Raventós; P. Lester; *Method. Enzymol.*, **1999**, *299*, 152-178
46. D.O. Kim; S.W. Jeong; C.Y. Lee; *Food Chem.*, **2003**, *81*, 321-326
47. M.B. Arnao; A. Cano; J.F. Alcolea; M. Acosta; *Phytochem. Anal.*, **2001**, *12*, 138-143

RADIOCARBON DATING OF MAKURI LÊ BOOM, A VERY OLD AFRICAN BAOBAB FROM NYAE NYAE, NAMIBIA

ROXANA T. PATRUT[a], ADRIAN PATRUT[b,c*],
DEMETRA RAKOSY[d], LASZLO RAKOSY[a], DANIEL A. LÖWY[e],
JENŐ BODIS[b,c], KARL F. VON REDEN[f]

ABSTRACT. The article reports the AMS (accelerator mass spectrometry) radiocarbon dating results of Makuri Lê boom, a very large African baobab from Nyae Nyae Conservancy, Namibia. The investigation of this superlative baobab shows that it consists of 12 independent stems of different dimensions, which belong to three generations. Makuri Lê boom has an open ring-shaped structure, a type of architecture which allows baobabs to reach very large sizes and old ages. The oldest sample has a radiocarbon date of 1602 ± 17 BP, which corresponds to a calibrated age of 1520 ± 35 calendar yr. By this value, Makuri Lê boom becomes one of the oldest dated baobabs and angiosperms with accurate dating results.

Keywords: *AMS radiocarbon dating, Adansonia digitata, tropical trees, dendrochronology, age determination, multiple stems.*

---

[a] *Babeş-Bolyai University, Faculty of Biology and Geology, 44 Republicii, RO-400015, Cluj-Napoca, Romania*
[b] *Babeş-Bolyai University, Faculty of Chemistry and Chemical Engineering, 11 Arany Janos, RO-400028, Cluj-Napoca, Romania*
[c] *Babeş-Bolyai University, Raluca Ripan Institute for Research in Chemistry, 30 Fantanele, RO-400294 Cluj-Napoca, Romania*
[d] *AG Spatial Interaction Centre, German Centre for Integrative Biodiversity Research, 5e Deutscher Platz, D-04103 Leipzig, Germany*
[e] *VALOR HUNGARIAE, Dept. of Science and Innovation, 4 Nagysándor József, 1054 Budapest, Hungary*
[f] *NOSAMS Facility, Dept. of Geology & Geophysics, Woods Hole Oceanographic Institution, Woods Hole, MA 02543, U.S.A.*
* Corresponding author: apatrut@gmail.com

ROXANA T. PATRUT, ADRIAN PATRUT, DEMETRA RAKOSY, LASZLO RAKOSY,
DANIEL A. LÖWY, JENŐ BODIS, KARL F. VON REDEN

INTRODUCTION

The African baobab (*Adansonia digitata* L.), which belongs to the Bombacoideae subfamily of Malvaceae, is the best known, the most utilized and widespread of the eight or nine species of the *Adansonia* genus. One or two species are endemic to the arid savanna of mainland Africa, six species are restricted to Madagascar and one species has a natural distribution in Australia [1-5].

In 2005, we started an extended research project to clarify several controversial aspects related to the architecture, development and age of the African baobab. Our approach consists of AMS (accelerator mass spectrometry) radiocarbon dating of tiny wood samples extracted from inner cavities, deep incisions in the stems, fractured stems and from the outer part/exterior of large baobabs [6-17]. Research results show that young baobabs are usually single-stemmed individuals, which develop into multi-stemmed trees, owing to their ability to generate new stems over time. We also established that superlative baobabs, i.e., very large and old specimens, preferentially exhibit ring-shaped structures. The oldest African baobabs were found to have ages up to 2,500 years. Thus, the African baobab becomes the longest-living angiosperm [9,11,13-15].

In 2013, our investigation on baobabs was extended to large and old individuals of the most representative three species of Madagascar, i.e., *Adansonia rubrostipa* Jum. & H. Perrier (Fony baobab), *Adansonia za* Baill. (Za baobab) and *Adansonia grandidieri* Baill. (Grandidier baobab) [19-22].

Namibia hosts several very big and old African baobabs. Most of them are in the north-east, in an area known during the colonial apartheid era as Bushmanlad, after its inhabitants. In 1990, after the end of the Independence War (also called South African Border War), South West Africa became Namibia. Since then, the new name of Bushmanland is Tsumkwe District and it is part of the Otjozondjupa region. The small town of Tsumkwe, which is the district capital, is the centre of the area populated by the Ju/'hoansi; they belong to the San people, also known as Bushmen.

We investigated and dated several African baobabs around Tsumkwe. Four of them have or had very large dimensions and ages between 1200 and 2000 years, namely Dorslandboom, Holboom, Grootboom and Makuri Campsite baobab [6, 9, 13, 18]. In a paper dedicated to the largest and oldest African baobabs, we mentioned the name of another very old tree in this region, the Makuri Lê boom [9]. Makuri Lê boom is the sixth oldest known African baobab with accurate dating results. Here we present the investigation and the radiocarbon dating results of this impressive baobab.

RESULTS AND DISCUSSION

The Makuri Lê boom and its area. The big baobab is located in the Nyae Nyae Conservancy, established in 1998, around the Nyae Nyae Pans. The Conservancy covers the eastern part of the Tsumkwe district (Bushmanland), up to the border of Namibia with Botswana. The baobab is situated at 32 km ESE of Tsumkwe, 9 km SE from the Makuri village and 10 km SW from the Baraka village. Its GPS coordinates are 19º39.404' S, 020º47.143' E and the altitude is 1169 m. The mean annual rainfall in the area is 467 mm, while the mean annual temperature reaches 21.5 °C (Tsumkwe station). The investigated baobab is a „laying tree", i.e., „Lê boom" in Afrikaans, such as the famous Dorslandboom, which can be found at 35 km NNE of Tsumkwe [13, 18]. We named it Makuri Lê boom.

Figure 1. Makuri Lê boom with the auxiliary constructions
of the hunting camp around its stems.

ROXANA T. PATRUT, ADRIAN PATRUT, DEMETRA RAKOSY, LASZLO RAKOSY,
DANIEL A. LÖWY, JENŐ BODIS, KARL F. VON REDEN

This monumental baobab, which grows in the proximity of a man-made waterhole, is known only at a local level by a limited number of San natives and a few hunters from Europe and America. Around and in between its stems there is a very unusual hunting camp, exclusively used a few times every year by rich hunters arriving here by private jets (Figure 1). In this area, they hunt the biggest African elephants and sometimes lions and leopards.

Makuri Lê boom exhibits an original structure, composed of 12 living stems of different dimensions and ages. Two stems are toppled, broken and lying on the ground, but still alive, 4 stems are leaning and severely broken/fractured, while the other 6 standing stems have many missing branches. The stems are partially blackened by previous fires. Several stems are missing. The stem numbering is presented in Figure 2.

This peculiar-looking baobab has an impressive circumference at breast height (cbh; at 1.30 m above ground level) of 34.23 m, the maximum height of the standing stems is 14.5 m and the overall wood volume (stems and branches) is around 200 m^3. The horizontal dimensions of the severely damaged canopy are 26.4 (NS) x 25.5 (WE) m.

Wood samples. Two tiny wood samples (marked as a and b), with the mass between 1-5 x 10^{-4} kg, were extracted from determined positions of 3 different stems each, by using a sharp instrument. The samples were labelled according to the initials of the tree name and the corresponding stem number, i.e., ML-1, ML-8 and ML-11.

AMS results and calibrated ages. Radiocarbon dates of the 6 samples are listed in Table 1. The radiocarbon dates are expressed in ^{14}C yr BP (radiocarbon years before present, i.e., before the reference year 1950). Radiocarbon dates and errors were rounded to the nearest year.

Calibrated (cal) ages, expressed in calendar years CE (CE, i.e., common era), are also shown in Table 1. The 1σ probability distribution (68.2%) was selected to derive calibrated age ranges. For three samples (1a, 8a, 11b), the 1σ distribution is consistent with one range of calendar years. For the other three segments (1b, 8b, 11a), the 1σ distribution is consistent with two ranges of calendar years. In these cases, the confidence interval of one range is considerably greater than that of the other; therefore, it was selected as the cal CE range of the sample for the purpose of this discussion. For obtaining single calendar age values of samples, we derived a mean calendar age of each sample from the selected range (marked in bold).

Figure 2. General view of Makuri Lê boom from the west (top)
and from the east (bottom), with stem numbering.

ROXANA T. PATRUT, ADRIAN PATRUT, DEMETRA RAKOSY, LASZLO RAKOSY,
DANIEL A. LÖWY, JENŐ BODIS, KARL F. VON REDEN

Table 1. Radiocarbon dating results and calibrated ages of samples
collected from Makuri Lê boom

Sample code (stem)	Depth[1] [height[2]] (m)	Radiocarbon date [error] (^{14}C yr BP)	Cal CE range 1σ [confidence interval]	Assigned year [error] (cal CE)	Sample age [error] (cal CE)
ML-1a (1)	0.51 [4.20]	1090 [± 18]	**994-1016 (68.2%)**	1005 [± 10]	1015 [± 10]
ML-1b (1)	1.02 [4.20]	1602 [± 17]	444-448 (2.3%) **466-539 (65.9%)**	502 [± 35]	1520 [± 35]
ML-8a (8)	0,45 [6.50]	930 [± 19]	**1152-1200 (68.2%)**	1176 [± 25]	845 [± 25]
ML-8b (8)	0.90 [6.50]	1360 [± 16]	670-685 (24.4%) **738-763 (43.8%)**	750 [± 15]	1270 [± 15]
ML-11a (11)	0.01 [1.98]	377 [± 18]	1496-1512 (12.6%) **1548-1623 (55.6%)**	1585 [± 35]	435 [± 35]
ML-11b (11)	0.97 [1.98]	1575 [± 15]	**529-574 (68.2%)**	551 [± 20]	1470 [± 20]

[1] Depth in wood from the exterior of the stem.
[2] Height/distance from the base.

Sample ages represent the difference between the year 2020 CE and
the mean value of the selected range, with the corresponding error. Sample
ages and errors were rounded to the nearest 5 yr. We used this approach for
selecting calibrated age ranges and single values for sample ages in our
previous articles on AMS radiocarbon dating of superlative angiosperms,
especially of baobabs [6-22].

Dating results of samples. The two samples ML-1 originate from the
end of the toppled and broken stem 1, which now has a horizontal length of
4.20 m. The remaining part of stem 1 is quasi-cylindrical and has a diameter
of 2.00 – 2.20 m with missing bark. The sample ML-1a was taken halfway
between the exterior of stem 1 and the theoretical pith, at a depth of 0.51 m
into the wood. It has a radiocarbon date of 1090 ± 18 BP, which corresponds
to a calibrated age of 1015 ± 10 calendar yr. The sample ML-1b was
extracted from the theoretical pith of stem 1, at a distance of 4.20 m from the
base. The radiocarbon date of 1602 ± 17 BP corresponds to a calibrated age
of 1520 ± 35 calendar yr. This is the oldest dated sample originating from
Makuri Lê boom.

The two samples ML-8 were collected from the fallen and broken stem 8, which now has a horizontal length of 10.90 m. Its diameter at breast height is dbh = 2.30 m. Similarly, to samples ML-1, the sample ML-8a was extracted halfway between the exterior of stem 8 and its theoretical pith, while the sample ML-8b originates from the theoretical pith, both at a distance of 6.50 m from the stem base. The radiocarbon dates of the two samples are 930 ± 19 BP and 1360 ± 16 BP. These values correspond to calibrated ages of 845 ± 25 and 1270 ± 15 calendar yr.

The samples ML-11 originate from the standing stem 11, which has a dbh = 3.05 m and is broken at the height of 6.2 m. They were collected from a long crack in the stem at the height of 1.98 m. Sample ML-11a consists of wood which was adjacent to the bark. However, the sample is not young as expected, but it has a radiocarbon date of 377 ± 18 BP. This value corresponds to a calibrated age of 435 ± 35 yr and it shows that stem 11 stopped growing over 400 years ago. The deepest sample ML-11b has a radiocarbon date of 1575 ± 15 BP, which corresponds to a calibrated age of 1470 ± 20 calendar yr. It was extracted from a depth of 0.97 m into the wood, while the theoretical pith at the sampling height of 1.98 m is positioned at a depth of 1.35 m.

Age of Makuri Lê boom. According to stem dimensions/diameters, Makuri Lê boom consists of stems which belong to at least three generations. Four stems (3, 5, 9, 12) have diameters around 1 m (0.8 – 1.3 m), five stems (1, 2, 6, 8, 10) have diameters close to 2 m (2.0 – 2.8 m) and three stems (4, 7, 11) have diameters of at least 3 m (3.0 – 3.5 m). As mentioned, the oldest dated sample was collected from the theoretical pith of stem 1, with a diameter of 2.2 m, and has an age of 1520 ± 35 years, which should be very close to the age of this stem.

As detailed in our previous papers, extrapolation to the center of the largest stems would yield older ages. For similar reasons, we consider that the largest stems of Makuri Lê boom are around 2000 years old.

Architecture of the baobab. By our research, we have identified a new architecture, which enables African baobabs to reach old ages and large sizes. In this multi-stemmed architecture, the stems define at ground level a circle or an ellipse, with an empty space between them. We named it ring-shaped structure (RSS). There are two subtypes of RSSs: the open RSS and the closed RSS [9, 12].

Makuri Lê boom exhibits an open RSS (Figure 3). In the open RSS, the stems are fused or knitted at the base, are pointed sideways, have cylindrical shapes and quasi-circular transversal sections [9, 12, 16].

Over time, stems may topple and die, while new stems emerge periodically from roots or from other fallen or broken stems. Such multi-stemmed and multi-generation baobabs with open RSSs are going through successive cycles of death and rebirth from their remains. In the case of open RSSs, the collapse and death of one or even of several stems does not usually affect the whole ring.
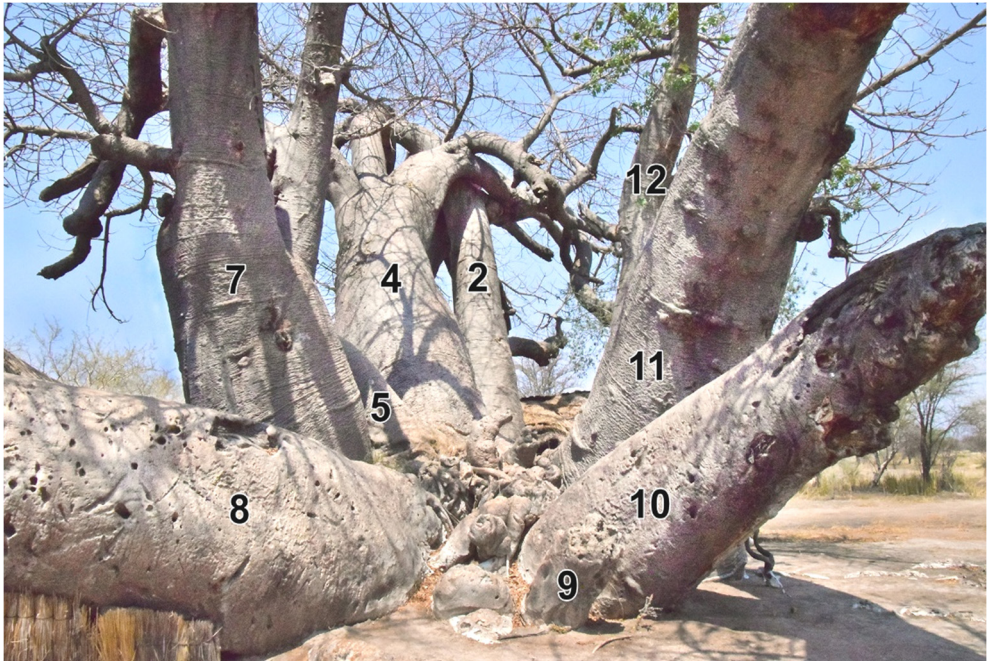
Figure 3. The photograph shows the common area from which the stems, that build the open ring-shaped structure, started growing.

Just like other famous very old baobabs with open RSSs, such as Dorslandboom or Glencoe, with toppled, standing and leaning knitted stems, some of them broken and a few regenerated with new shoots [12], Makuri Lê boom can be considered a kind of "Schrödinger's baobab", which is at the same time dead and alive.

CONCLUSIONS

The research presents the AMS radiocarbon investigation results of the Makuri Lê boom, a very large and old African baobab from Nyae Nyae Conservancy, Namibia. The aim of the research was to determine the age and the architecture of this baobab. Makuri Lê boom is composed of 12 living stems of different dimensions and ages.

Six wood samples extracted from three different stems were processed and dated by AMS radiocarbon. Four samples were found to have ages greater than 1000 BP. The oldest dated sample has a radiocarbon date of 1602 ± 17 BP, which corresponds to a calibrated age of 1520 ± 35 calendar yr. We consider that the largest stems of Makuri Lê boom are around 2000 years old. We also found that the largest and oldest stems stopped growing several centuries ago.

Makuri Lê boom exhibits an open ring-shaped structure, an architecture, which allows baobabs to reach very large sizes and old ages.

EXPERIMENTAL SECTION

Sample collection. Several tiny wood samples were extracted from predetermined positions of three stems with a sharp instrument. The samples were processed and investigated by AMS radiocarbon dating.

Sample preparation. The standard acid-base-acid pretreatment method was used for removing soluble and mobile organic components [23]. The pretreated samples were combusted to CO_2 by using the closed tube combustion method [24]. Then, CO_2 was reduced to graphite on iron catalyst, under hydrogen atmosphere [25]. Finally, the resulting graphite samples were analyzed by AMS.

AMS measurements. AMS radiocarbon measurements were performed at the NOSAMS Facility of the Woods Hole Oceanographic Institution (Woods Hole, MA, U.S.A.) by using the Pelletron ® Tandem 500 kV AMS system. The obtained fraction modern values, corrected for isotope fractionation with the normalized $\delta^{13}C$ value of -25 $^0/_{00}$, were ultimately converted to a radiocarbon date.

Calibration. Radiocarbon dates were calibrated and converted into calendar ages with the OxCal v4.3 for Windows [26], by using the SHCal13 atmospheric data set [27].

ROXANA T. PATRUT, ADRIAN PATRUT, DEMETRA RAKOSY, LASZLO RAKOSY,
DANIEL A. LÖWY, JENŐ BODIS, KARL F. VON REDEN

ACKNOWLEDGEMENTS

REFERENCES

1. G.E. Wickens, P. Lowe, "The Baobabs: Pachycauls of Africa, Madagascar and Australia", Springer, Dordrecht, **2008**, pp. 232-234, 256-257, 295-296.
2. D.A. Baum, *Ann. Missouri Bot. Gard.*,**1995**, *82*, 440-471.
3. J.D. Pettigrew, L.K. Bell, A. Bhagwandin, E. Grinan, N. Jillani, J. Meyer, E. Wabuyele, C.E. Vickers, *Taxon*, **2013**, *61*, 1240-1250.
4. G.V. Cron, N. Karimi, K.L. Glennon, C.A. Udeh, E.T.F. Witkowski, S.M. Venter, A.E. Assobadjo, D.H. Mayne, D.A. Baum, *Taxon*, **2016**, *65*, 1037-1049.
5. A. Petignat, L. Jasper, "Baobabs of the world: The upside down trees of Madagascar, Africa and Australia", Struik Nature, Cape Town, **2015**, pp. 16-86.
6. A. Patrut, K.F. von Reden, D.A. Lowy, A.H. Alberts, J.W. Pohlman, R. Wittmann, D. Gerlach, L. Xu, C.S. Mitchell, *Tree Physiol.*, **2007**, *27*, 1569-1574.
7. A. Patrut, D.H. Mayne, K.F. von Reden, D.A. Lowy, R. Van Pelt, A.P. McNichol, M.L. Roberts, D. Margineanu, *Radiocarbon*, **2010**, *52(2-3)*, 717-726.
8. A. Patrut, K.F. von Reden, R. Van Pelt, D.H. Mayne, D.A. Lowy, D. Margineanu, *Ann. Forest Sci.*, **2011**, *68*, 93-103.
9. A. Patrut, S. Woodborne, R.T. Patrut, L. Rakosy, D.A. Lowy, G. Hall, K.F. von Reden, *Nature Plants*, **2018**, *4(7)*, 423-426.
10. A. Patrut, D.H. Mayne, K.F. von Reden, D.A. Lowy, R. Van Pelt, A.P. McNichol, M.L. Roberts, D. Margineanu, *Radiocarbon*, **2010**, *52(2-3)*, 717-726.
11. A. Patrut, K.F. von Reden, D.H. Mayne, D.A. Lowy, R.T. Patrut, *Nucl. Instrum. Methods Phys. Res., B*, **2013**, *294*, 622-626.
12. A. Patrut, S. Woodborne, K.F. von Reden, G. Hall, M. Hofmeyr, D.A. Lowy, R.T. Patrut, *PLOS One*, **2015**, *10(1): e0117193.*
13. A. Patrut, S. Woodborne, K.F. von Reden, G. Hall, R.T. Patrut, L. Rakosy, J-M. Leong Pock Tsy, D.A. Lowy, D. Margineanu, *Radiocarbon*, **2017**, *59(2)*, 435-448.
14. A. Patrut, L. Rakosy, R.T. Patrut, I.A. Ratiu, E. Forizs, D.A. Lowy, D. Margineanu, K.F. von Reden, *Studia UBB Chemia*, **2016**, *LXI, 4*, 7-20.
15. A. Patrut, R.T. Patrut, L. Rakosy, D.A. Lowy, D. Margineanu, K.F. von Reden, *Studia UBB Chemia*, **2019**, *LXIV, 2 (II)*, 411-419.

16. A. Patrut, S. Woodborne, R.T. Patrut, G. Hall, L. Rakosy, C. Winterbach, K.F. von Reden, *Forests*, **2019**, *10*, 983-993.
17. A. Patrut, A. Garg, S. Woodborne, R.T. Patrut, L. Rakosy, I.A. Ratiu, *PLOS One*, **2015**, *15(1): e0227352.*
18. A. Patrut, K.F. von Reden, D.A. Lowy, D.H. Mayne, K.E. Elder, M.L. Roberts, A.P. McNichol, *Nucl. Instrum. Methods Phys. Res., B*, **2010**, *268*, 910-913.
19. A. Patrut, K.F. von Reden, P. Danthu, J-M. Leong Pock Tsy, R.T. Patrut, D.A. Lowy, *PLOS One*, **2015**, *10(3): e0121170.*
20. A. Patrut, K.F. von Reden, P. Danthu, J-M. Leong Pock-Tsy, L. Rakosy, R.T. Patrut, D.A. Lowy, D. Margineanu, *Nucl. Instrum. Methods Phys. Res., B,* **2015**, *361*, 591-598.
21. A. Patrut, R.T. Patrut, P. Danthu, J.-M. Leong Pock-Tsy, L. Rakosy , D.A. Lowy, K.F. von Reden, *PLOS One*, **2016**, *11(1)*, e0146977.
22. R.T. Patrut, A. Patrut, J-M Leong Pock-Tsy, S. Woodborne, L. Rakosy, P. Danthu, I-A. Ratiu, J. Bodis, K.F. von Reden, *Studia UBB Chemia*, **2019**, *LXIV, 4*, 131-139.
23. I.U. Olsson, Radiometric Methods. In: B. Berglung, editor, "Handbook of Holocene palaeoecolgy and palaeohydrology", Wiley, Chichester, **1986**, pp. 273-312.
24. Z. Sofer, *Anal. Chem.*, **1980**, *52(8)*, 1389-1391.
25. J.S. Vogel, J.R. Southon, D.E. Nelson, T.A. Brown, *Nucl. Instrum. Methods Phys. Res., B*, **1984**, *5*, 289-293.
26. C. Bronk Ramsey, *Radiocarbon*, **2009**, *51*, 337-360.
27. A.G. Hogg, Q. Hua, P.G. Blackwell, M. Niu, C.E. Buck, T.P. Guilderson, T.J. Heaton, J.G. Palmer, P.J. Reimer, R.W. Reimer, C.S.M. Turney, R.H. Zimmerman, *Radiocarbon*, **2013**, *55(4)*, 1889-1903.

THE INFLUENCE OF V_2O_5 ON SPECTROSCOPIC AND OPTICAL PROPERTIES OF MgO-KPO₃ GLASSES CO-DOPED WITH Ag_2O

CRISTINA SOMESAN[a], LIVIU CALIN BOLUNDUT[b*], LOREDANA OLAR[c*], VASILE POP[b], LEONTIN DAVID[a]

ABSTRACT. X-ray diffraction (XRD), Fourier transform infrared (FTIR), electron paramagnetic resonance (EPR), Ultraviolet-visible (UV-Vis) spectroscopies measurements have been employed to investigate the glasses from the $(V_2O_5)_x \cdot (KPO_3)_{80-x} \cdot (MgO)_{19} \cdot (Ag_2O)_1$ ($0 \leq x \leq 10$ mol%) system. The studied glasses had a fixed MgO and Ag_2O content of 19 mol% and 1 mol% respectively, and the V_2O_5:KPO₃ ratio was varied. XRD data confirms the vitreous nature of the studied samples. EPR, UV-Vis and IR data confirm the presence of vanadium in multiple valence states.

Keywords: V_2O_5-MgO-KPO₃ glasses, X-ray diffraction, FT-IR, EPR, UV-vis analysis

INTRODUCTION

During the last decades, glasses doped with transitional metal ions (TMI) have been the subject of many studies due to their interesting electrical, optical and magnetic properties which recommended them for potential application in many fields such as electrical memory switching, solid state lasers, phosphors, solar energy converters, catalysis and magnetic information storage, plasma display panels, electronic and optical devices [1-16]. Among different TMI, *vanadium ion* is considered extremely interesting due to the influences on some physical properties including electrical, optical, and

[a] *Babeş-Bolyai University, Faculty of Physics, Kogalniceanu str., Cluj-Napoca, Romania*
[b] *Technical University of Cluj-Napoca, Physics and Chemistry Depatment, 28 Memorandumului str., Cluj-Napoca, Romania*
[c] *University of Agiculture Sciences and Veterinary Medicine, 3-5 Calea Manastur, 400372 Cluj-Napoca, Romania*
* Corresponding authors: liviu.bolundut@chem.utcluj.ro, loredana.olar@usamvcluj.ro

magnetic properties of the glasses [2, 7-10, 12-14]. In glasses and glass ceramics vanadium ions can exists in different oxidation states: +3 (trivalent), +4 (tetravalent) and +5 (pentavalent). In the glass network V^{3+} ions occupy octahedral symmetry, V^{4+} ions appear in both square pyramidal and octahedral position and V^{5+} ions can be found in tetrahedral, square pyramidal and octahedral configurations [13]. The 5+ (diamagnetic) and +4 (paramagnetic) are the most frequent valence states of vanadium ions in glasses [10]. The content of vanadium ions in different coordination and valence states in the glass depending upon the quantitative properties of modifiers and glass formers, size of the ions in the glass structure, their field strength, mobility of the modifier cation, etc. The simultaneous presence of vanadium ions in different valence states in glasses bring interesting changes in electrical characteristics. Thus, the semiconducting behaviour of glasses doped with vanadium ions is due by the hopping of unpaired $3d^1$ electron between V^{4+} and V^{5+} ions [2, 13, 14]. To be specific, it is quite possible for the intervalence transfer of electrons between these ions and contribute more to the electronic component of the electrical conductivity of the glasses. Also, the presence of vanadium ions in the studied glasses offers the possibility to investigate the local structure by electron paramagnetic resonance (EPR) spectroscopy [9, 10, 17, 18]. EPR spectroscopy is a very powerful tool in obtaining information regarding the local environment of TMI in the glass network and to identify the site symmetry around these ions [17-25].

On the other hand, in the last years exist a large degree of interest concerning glasses co-doped with silver oxide due to their high ionic conductivity and potential applications such as biomaterials with antibacterial and antimicrobial effects, laser optical data recording and photonics [5, 26-29].

The aim of this paper is to present our results obtained by means of XRD, FTIR, EPR and UV-Vis spectroscopies measurements performed on some potassium phosphate glasses gradually doped with vanadium ions and co-doped with a constant content of silver oxide. The research is part of a comparative analysis program focused on the behaviour of TMI in glasses, to obtain generally valuable rules, which allow imposing and controlling the properties of such materials.

RESULTS AND DISCUSSION

1. XRD and density data

XRD patterns of studied samples within Bragg angles from 10 to 70° at room temperature are presented in Figure 1. For all the investigated samples the XRD patterns exhibit few diffused scattering peaks at low angles instead of any

sharp peak indicating the amorphous nature of the studied samples. These amorphous nature features are characterized by three halos centred at $2\theta \approx 16°$, $29°$ and $44°$.
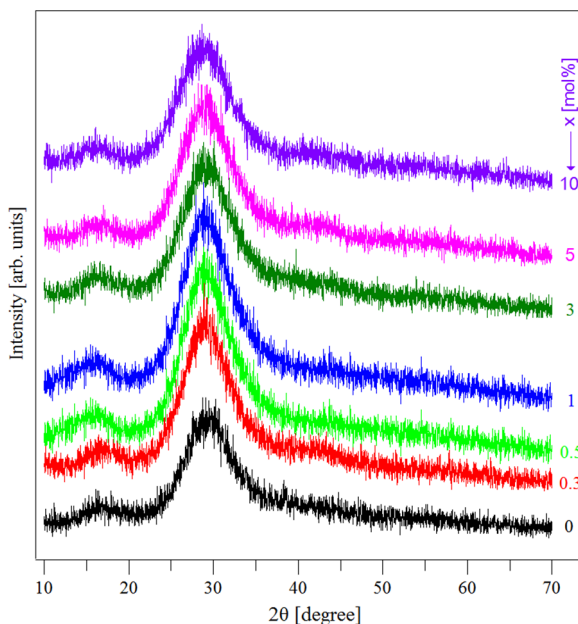

Figure 1. XRD patterns for the obtained samples

The compositional evolution of density for the studied glasses may provide important information concerning the possible structural changes that can occur in the host glass matrix by substitution of potassium metaphosphate by vanadium pentoxide. Figure 2 present the compositional dependence of the density for the studied glasses.

As can be seen from this figure the density increases with the increasing of V_2O_5 content in all the studies concentrations range. This evolution suggests that the increase of vanadium ions content in the studied glasses leads to a gradual inclusion of these ions in the host glass matrix. On the other hand, the non-linear compositional dependence of the density is due to the fact that the gradual addition of the vanadium ions leads not only to a simple incorporation of these ions in the host glass matrix but also generates structural changes in the glass network. Thus, the density data suggests that the vanadium ions play a network modifier role in the studied glasses.
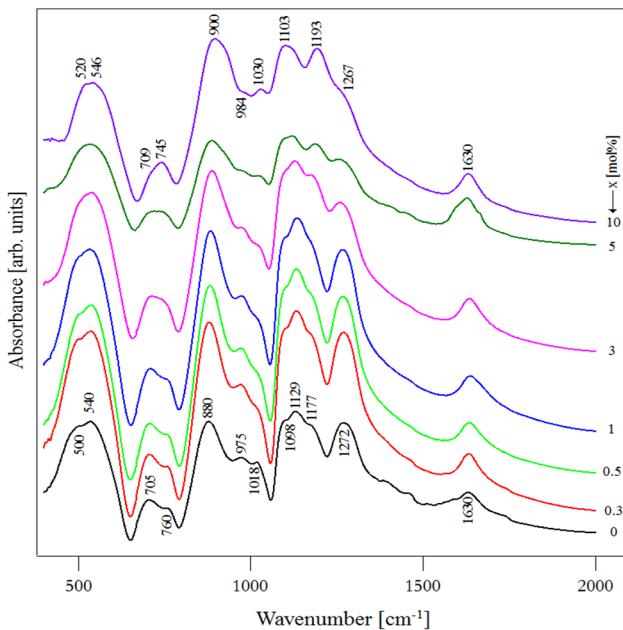
163
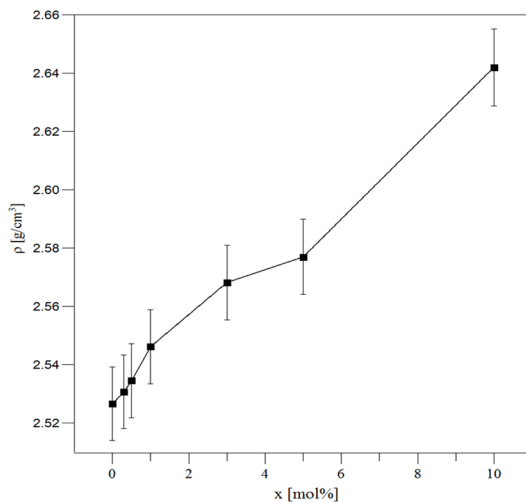
Figure 2. The density variation with the compositional evolution of the samples

2. FTIR data

Figure 3 present the FTIR spectra obtained for the studied glasses.

Figure 3. FTIR spectra for the studied samples

As can be observed the glass matrix and all the studied samples contain twelve absorption peaks in the range of 450-2000 cm^{-1} that can be assigned as follows, in accord with literature reports [19, 30-34]. Thus, the band from 500-520 cm^{-1} represent the bending vibration for P=O bonds in the case of matrix that is vanadium free, and bending modes for V-O-V bonds from the network that overlap with P=O vibration for the rest of the samples. The band from 540-546 cm^{-1} corresponding to the bending vibration in case of the O=P-O linkages. This band decrease when the concentration of the dopant (V_2O_5) increase. The behaviour is because the number of O=P-O bonds decrease (potassium monophosphate is replaced by vanadium pentoxide) and the number of V-O-V bonds increase. The first peak and the second form in the case of sample doped with 10 mol% of V_2O_5 an IR broad peak. The band from 705-709 cm^{-1} assigned to P-O-P symmetric stretching Q^2 type. 745-760 cm^{-1} represent the symmetric stretching vibration for P-O-P linkages. The band from 880-900 cm^{-1} assigned to asymmetric stretching vibration for P-O-P linkages from the glass network of matrix and for the rest of the samples is overlapped with symmetric vibrations of the V-O bonds from VO$_4$ tetrahedral that appear in the glass network when the dopant is added. The band from 975-984 cm^{-1} corresponds to the symmetric stretching vibration from $(PO_4)^{3-}$ group Q^0 type from the glass network. The band from 1018-1030 cm^{-1} for the matrix correspond to the asymmetric stretching vibration from $(PO_3)^{2-}$ groups, in the case of samples doped with vanadium can be assigned for the vibrations of V^{5+}=O double bond (in accord with UV-vis spectra that certifies the presence of pentavalent vanadium), also can correspond to the vibration of V-O bond from [V$_3$O] groups or to the stretching of O-V-O bonds. The band from 1098-1103 cm^{-1} corresponds to the asymmetric stretching vibration from $(PO_4)^{3-}$ group Q^0 type. 1129 cm^{-1} assigned to the symmetric stretching vibration from $(PO_2)^{-}$ group Q^2 type from the glass network. The band from 1177-1193 cm^{-1} is due to the asymmetric stretching vibration from $(PO_2)^{-}$ group Q^2 type that built up the amorphous network. The band from 1267-1272 cm^{-1} can be assigned to the symmetric stretching vibration of P=O bonds from the glass network while the band of 1630 cm^{-1} correspond to water vibration.

3. UV-VIS data

UV-Vis data were obtained at room temperature being presented in Figure 4. The Figure 4 reveals the presence of four peaks for the sample doped with 10 mol% of V_2O_5 (two in the UV region and another two in visible region) and three for the rest of the studied samples.
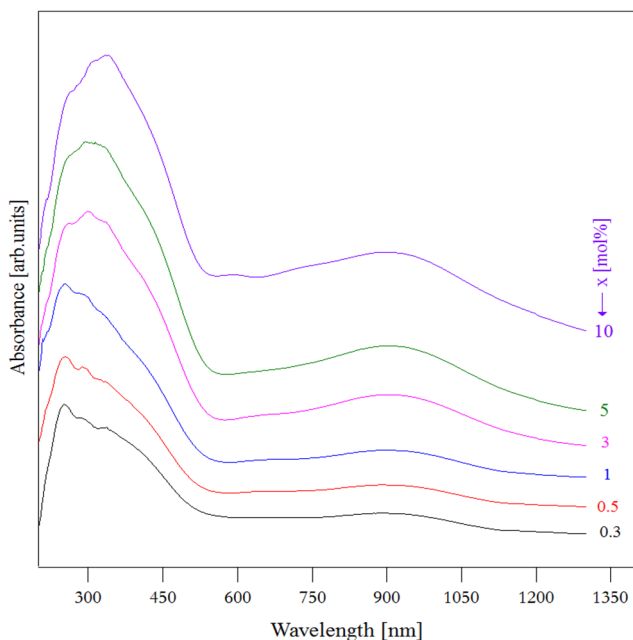
Figure 4. UV-vis spectra for samples from $(V_2O_5)_x \cdot (KPO_3)_{80-x} \cdot (MgO)_{19} \cdot (Ag_2O)_1$ $(0 \leq x \leq 10$ mol%) glass system

The samples were doped with V_2O_5 in this way the initial valence of vanadium is five. In glass according with the literature data [30], vanadium can exist in three different valence states V^{5+}, V^{4+}, V^{3+}. In the case of V^{5+} ion, the electronic structure is d^0 so the vanadium ion is incapable to give absorption peaks in the visible region of the optical spectrum because is not possible a d-d electronic transition (3d orbital being empty). But can be possible a charge transfer peaks that appear in UV region at about 290-340 nm according with the literature [31, 32] and confirmed by our results. It is interesting this behaviour, because phosphate glasses favour the presence of vanadium in low oxidation state (three and four) [31]. Our samples exhibit two charge transfer peaks in 285-340 nm region of the optical spectrum due to the presence of vanadium in highest oxidation state (V^{5+}).

In the visible region of the spectrum appears a very small peak at 597 nm. This peak it is observable only for the sample doped with 10 mol% of V_2O_5. According with other research data, this absorption can be attributed to the presence of vanadium in V^{3+} valence state [30], where vanadium is surrounded by six oxygen atoms in a distorted octahedral coordination. This absorption is due to $^3T_{1g}$ to $^3T_{2g}$ electronic transition.

Another peak in our case, for the studied samples appears at 930 nm. This absorption seems to be due to the presence of tetravalent vanadium as VO^{2+} in accord with other research data [30] and confirmed by our EPR data.

The intensity of absorption peaks increases when increase the concentration of the dopant (V_2O_5).

4. EPR data

To find more structural information related to the investigated system, EPR measurements were performed, at room temperature and the obtained spectra are illustrated in Figure 5.
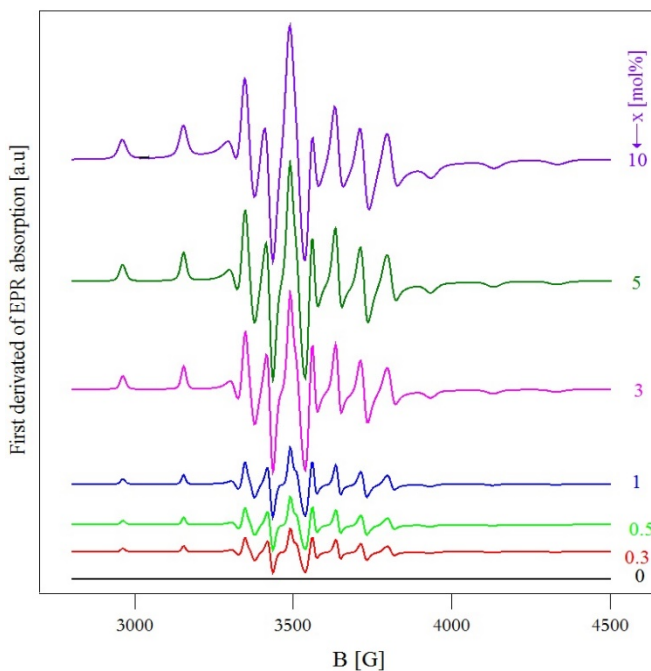
Figure 5. EPR data of the studied samples

The most significant finding in the EPR spectra, is the presence of the very well resolved hyperfine structure, with all features, for all prepared concentrations (up to x=10 %). These features are connected with very homogeneous distribution of the paramagnetic V^{4+} ions, which leads to very weak dipolar interactions or even to their absence.

Eight hyperfine lines (I=7/2) are expected for vanadyl (V^{4+}) ion in glasses, as a result of spin-orbit interaction in parallel band and same lines number in perpendicular one as the atom is aligned with field [35].

Other interesting result is the high ability of this system to incorporate V_2O_5 is the constant width of the hyperfine constant for all concentration ($A_{||}$ = 195 G)

The vanadium V^{4+} content increases constantly with V_2O_5 addition in the initial mixture, being illustrated by the increase in lines intensities, proving that during the melting process V^{5+} is reduced by the melting condition.

The V^{4+} ions built up vanadyl complexes with oxygen's from its neighbourhood and is located in octahedral field, with a tetragonal distortion, i.e. one V-O bond oriented axially, is shorter than the other [36]. Also, it was deduced from experimental data that, when the bond between the V^{4+} and on oxygen atom axially located is too long, caused by a lack in oxygen in the glass the complex can we considered as a pure tetrahedral one [37].

CONCLUSIONS

New samples from $(V_2O_5)_x \cdot (KPO_3)_{80-x} \cdot (MgO)_{19} \cdot (Ag_2O)_1$ ($0 \le x \le 10$ mol%) glass system were obtained.

XRD data confirm the amorphous state of the studied samples. The density measurement suggest that the vanadium ions play a network modifier role in our case.

IR and UV-vis data show the presence of vanadium in the glass network in multiple valence state.

EPR data also confirm the presence of V^{4+} ions in the glass network. So, all obtained data confirm the fact that at the working temperature a part of pentavalent vanadium is reduced to inferior oxidation states. Also, the vanadium ions seem to be octahedral surrounded by six oxygens fact confirmed by our obtained results.

EXPERIMENTAL SECTION

Glasses of the $(V_2O_5)_x \cdot (KPO_3)_{80-x} \cdot (MgO)_{19} \cdot (Ag_2O)_1$ ($0 \le x \le 10$ mol%) system were prepared by conventional melting and quenching method using V_2O_5, KH_2PO_4, MgO and Ag_2O of high purity (99.9%) in suitable proportion. The mechanically homogenized mixtures were melted in sintered corundum crucibles at 1100 °C for 10 minutes.

The X-Ray diffraction measurements of the samples were recorded with an XRD – 6000 Shimadzu diffractometer with a monochromator of graphite for Cu-Kα radiation (λ = 1.54060 Å) at room temperature.

The density of each sample was measured based on Archimedes principle at room temperature using toluene as immersing liquid. The samples were weighted on a KERN digital balance with an uncertainty of ± 0.00001 g.

The FTIR absorption spectra of the studied glasses and glass ceramics were obtained in the 360 - 1500 cm^{-1} spectral range with a resolution of 2 cm^{-1} using a JASCO FTIR 6200 spectrometer. The IR absorption measurements were done using the KBr pellet technique.

UV-VIS absorption spectra of the prepared samples were investigated with a JASCO V-550 spectrometer, in the wavelength range of 300-1380 nm having a resolution of 2 nm.

The EPR measurements of powder samples were carried out in the X-band (~ 9.79 GHz) at room temperature using a Bruker E-500 ELEXSYS spectrometer. The spectra processing was performed by Bruker Xepr software. To avoid the alteration of the glass structure due to the ambient conditions, especially humidity, samples were poured immediately after preparation and enclosed in tubular holders of the same calibre. The EPR spectra were recorded using equal quantities of samples.

REFERENCES

1. I. Ardelean; R. Ciceo-Lucacel; S. Filip; *J. Magn. Magn. Mater.*, **2004**, *272-276*, 337-338.
2. R. Balaji Rao; N.O. Gopal; N. Veeraiah; *J. Alloy Compd.*, **2004**, *368*, 25-37.
3. I. Ardelean; S. Cora; R. Ciceo Lucacel; O. Hulpus; *J. Non-Cryst. Solids,* **2007**, *7*, 1438-1442.
4. Hirofumi Akamatsu; Katsuhisa Tanaka; Koji Fujita; Shunsuke Murai; *J. Magn. Magn. Mater.*, **2007**, *310*, 1506–1507.
5. R. Ciceo-Lucacel; I. Ardelean; *J. Non-Cryst. Solids*, **2007**, *53*, 2020–2024.
6. P. Bergo; W.M. Pontuschka; J.M. Prison; *Mater. Chem. Phys.*, **2008**, *108*, 142-146.
7. P. Pascuta; *J. Mater. Sci: Mater. Electron.*, **2010**, *21*, 338-342.
8. H. Wen; P.A. Tanner; *J. Alloy Compd.*, **2015**, *625*, 328-335.
9. G. Swapna; M. Upender; M. Prasad, *Optik,* **2016**, *127*, 10716-10726.
10. M. Montesso; D. Manzani; J. Donoso; C.J. Magon; I D.A. Silva; M. Chiesa; E. Morra; M. Nalin; *J. Non-Cryst. Solids*, **2018**, *500*, 133-140.

11. S. Kapoor; D. Brazete; I.C. Pereira; G. Bhatia; M. Kaur; L.F. Santos; D. Banerjee; A. Goel, J.M.F. Ferreira, *J. Non-Cryst. Solids*, **2019**, *506*, 98-108.
12. Sk. Jani Basha; M. Kostrzewa; A. Ingram; A. Siva Sesha Reddy; N. Purnachand; V. RaviKumar; M. Piasecki; N. Veeraiah; *J. Non-Cryst. Solids*, **2019**, *521*, 119529.
13. S. Das; A. Madheshiya; M. Ghosh; K. K. Dey; S. S. Gautam; J. Singh; R. Mishra; C. Gautam; *J. Phys. Chem. Solids*, **2019**, *126*, 17-26.
14. J. Fan; Y. Zhang; G. Li; Y. Yue; *J. Non-Cryst. Solids*, **2019**, *521*, 119491.
15. F.H. Margha; G.T. El-Bassyouni; G. M. Turky; *Ceram. Int.*, **2019**, *45*, 11838-11843.
16. L.C. Bolundut; V. Pop; *Studia UBB Chemia,* **2016**, *4*, 223-232.
17. J.L. Kumari; J.S. Kumar; S. Cole; *J. Non-Cryst. Solids*, **2011**, *357*, 3734-3739.
18. M. Rada; L. Rus; S. Rada; P. Pascuta; S. Stan; N. Dura; T. Rusu; E. Culea; *J. Non-Cryst. Solids*, **2015**, *414*, 59-65.
19. S. Bale; S.Rahman; *J. Non-Cryst. Solids*, **2009**, *355*, 2127-2133.
20. M. Subhadra; P. Kistaiah; *J. Non-Cryst. Solids*, **2011**, *357*, 3442-3446.
21. R. Stefan; P. Pascuta; A. Popa; O. Raita; E. Indrea; E. Culea; *J. Phys. Chem. Solids*, **2012**, *73*, 221-226.
22. T.D. AbdelAziz; N.A. Elalaily; F.M. Ezz-Eldin; J. Radiat; *Res. Appl. Sci.*, **2015**, *8*, 84-90.
23. V. Volpi; M. Montesso; S.J.L. Ribeiro; W.R. Viali; C.J. Magon; I.D.A. Silva; J.P. Donoso; M. Nalin; *J. Non-Cryst. Solids*, **2016**, *431*, 135-139.
24. R. Stefan; M. Karabulut; A. Popa; E. Culea; L. Bolundut; L. Olar; P. Pascuta; *J. Non-Cryst. Solids*, **2018**, *498*, 430-436.
25. C. Lin; J. Liu; L. Han; H. Gui; J. Song; C. Li; T.Liu; A. Lu; *J. Non-Cryst. Solids*, **2018**, *500*, 235-242.
26. J. Massera; Y. Shpotyuk; F. Sabatier; T. Jouan; C. Boussard-Plédel; C. Roiland; B. Bureau; L. Petit; N. G. Boetti; D. Milanese; L. Hupa; *J. Non-Cryst Solids*, **2015**, *425*, 52–60.
27. Y. Petit; K. Mishchik; N. Varkentina; N. Marquestaut; A. Royon; I. M. Honninger; T. Cardinal; L. Canioni; *Opt. Lett.*, **2015**, *40*, 4134-4137.
28. Y. Daiko; K. Segawa; S. Honda; Y. Iwamoto; *Solid State Ionics*, **2018**, *322*, 5-10.
29. A.A. Ahmed; A.A. Ali; A. El-Fiqi; *J. Mater. Res. Technol.*, **2019**, *8*, 1003-1013.
30. A.M. Abdelghany; A.H. Hammad; *Spectochim. Acta A*, **2015**, *137*, 39-44.
31. F.H. ElBatal; M.A. Marzouk; A.M. Abdelghany; *J. Non-Cryst. Solids*, **2011**, *357*, 1027-1036.
32. N. Laorodphan; P. Pooddee; P. Kidkhunthod; P. Kunthadee; W. Tapala; R. Puntharod; *J. Non-Cryst. Solids*, **2016**, *453*, 118-124.
33. P. Pascuta; G. Borodi; N. Jumate; I. Vida-Simiti; D. Viorel; E. Culea; *J. Alloy Compd.*, **2010**, *504*, 479-483.
34. D.A. Magdas; N.S. Vedeanu; D. Toloman; *J. Non-Cryst. Solids*, **2015**, *428*, 151-155.
35. D. Kivelson; S.K. Lee; *J. Chem. Phys.*, **1964**, *41*, 1896-1903.
36. D.L. Griscom; *J. Non-Cryst. Solids*, **1980**, *40*, 211-272.
37. N. Vedeanu; O. Cozar; I. Ardelean; B. Lendl; D. A. Magdas; *Vib. Spectrosc.*, **2008**, *48*, 259-262.

CHARACTERIZATION AND APPLICATION OF NEW EFFICIENT NANOSORBENT Fe$_2$O$_3$ PREPARED BY A MODIFIED LOW-TEMPERATURE UREA METHOD

MILJANA RADOVIĆ VUČIĆ[a*], JELENA MITROVIĆ[a], MILOŠ KOSTIĆ[a], NENA VELINOV[a], SLOBODAN NAJDANOVIĆ[a], DANIJELA BOJIĆ[a], ALEKSANDAR BOJIĆ[a]

ABSTRACT. In this work, low-cost non-conventional nanostructured Fe$_2$O$_3$ was produced by a modified low-temperature urea method (MLTUM-Fe$_2$O$_3$). Non-magnetic amorphous nanoparticle MLTUM-Fe$_2$O$_3$ with a bouquet like morphology is found to play as an effective sorbent media to remove textile dye Reactive Blue 19 from textile industries dye effluents over a wide range of pH. The nanoparticles were characterized by X-ray powder diffraction analysis (XRD), scanning electron microscopy (SEM), energy dispersive X-ray spectroscopy (EDX), FTIR and TGA. The surface area was measured by Brunauer-Emmett-Teller (BET) analysis. SEM image reveals bouquet like morphology with average particle size about 50 nm. The maximum sorption capacity of the sorbent is found to be 271.00 mg g^{-1} for Reactive Blue 19 and the data fitted with different isotherm models. Study on sorption kinetics shows that sorption of Reactive Blue 19 onto iron oxide follows pseudo-second-order kinetic.

Keywords: Amorphous materials, Nanostructures, Iron oxide, Chemical synthesis, Thermogravimetric analysis (TGA), X-ray diffraction

INTRODUCTION

One of the most important industries using synthetic dyes is the textile and garment, which produces a strongly colored wastewater, typically with a concentration in the range of 10–200 mg dm^{-3} [1,2]. During the dyeing process, the competition between the colouring reaction and the hydrolysis of the reactive group results in a loss of unfixed dye of approximately 20–

---

[a] *The University of Niš, Faculty of Sciences and Mathematics, Department of Chemistry, Višegradska 33, 18 000 Niš, Serbia*
* *Corresponding author: mimaradovic@gmail.com*

MILJANA RADOVIĆ VUČIĆ, JELENA MITROVIĆ, MILOŠ KOSTIĆ, NENA VELINOV, SLOBODAN NAJDANOVIĆ, DANIJELA BOJIĆ, ALEKSANDAR BOJIĆ

25% [3], thus leading to the production of coloured effluents [4,5]. Reactive Blue 19 (RB 19) dye is commonly used in the textile and leather industry and may be mutagenic and toxic because of the presence of electrophilic vinylsulfone groups [6,7].

Sorption is one of the most powerful methods for the removal of various forms of wastewater contaminants [8–12]. High efficiency, non-toxic, simplicity and low cost, have made the sorption processes preferable among the other conventional methods. A lot of studies have been reported on the kinetics, equilibrium and thermodynamics of various classes of dyes sorption onto numerous synthetic and natural sorbents, including activated carbon, biomaterials, silica, MgO, chitosan, peat, clay, bentonite and feather [13–27]. There are few papers that describe the RB 19 dye sorption on metal oxides. Table S1 in Supplementary material section shows a summary of some sorbents for the removal of RB 19 from wastewater.

Among numerous metal oxides, iron oxide has been paid intensive attention due to its stability, eco-friendly, high efficiency non-toxic and inexpensive nature. In this study, a new nanosorbent based on Fe_2O_3 was prepared using a modified low-temperature urea method. For practical application of Fe_2O_3 produced by a modified low-temperature urea method (MLTUM-Fe_2O_3) for treatment of dye contaminated wastewater, it is important to determine the optimal experimental conditions. The present work involves the effects of parameters, such as pH, sorbent dose, and sorbate concentration on RB 19 dye removal, the kinetic and equilibrium studies of RB 19 dye sorption onto MLTUM-Fe_2O_3. Desorption of RB19 and reused of MLTUM-Fe_2O_3 nanosorbent are also done.


RESULTS AND DISCUSSIONS

Characterization and sorption study

To analyse and quantify the pore structure and surface area of the obtained sorbent, the N_2 adsorption-desorption isotherms were carried out and shown in Fig. S3 in Supplementary material section (a). The pore size distribution, calculated via BJH method based on desorption curve, is presented in Fig. S3 in Supplementary material section (b). The sample has a BET surface area of 206.9 m^2 g^{-1}. The measured micropore (pores below 2 nm) area by the t-plot method was 30 m^2 g^{-1}. The micropore volume was 0.011911 cm^3 g^{-1}, while the pore volume in range of 1.7 to 300 nm was 0.205275 cm^3 g^{-1}. The average pore size was 4.1378 nm. A high surface area and mesoporous nature of MLTUM-Fe_2O_3 would be beneficial to sorb more organic pollutants on its surface.

Figure 1 presents the SEM images of MLTUM-Fe$_2$O$_3$. It can be seen that the surface is porous in nature. The sorbent particles are irregular in respect of size and shape. The sample consisted of particles below 5 μm in size with a textured structure of 100 nm which were elongated. The EDX results are presented in Fig. 2. The sample consisted of Fe and O only. XRD showed that the sample is amorphous with no crystalline fractions.
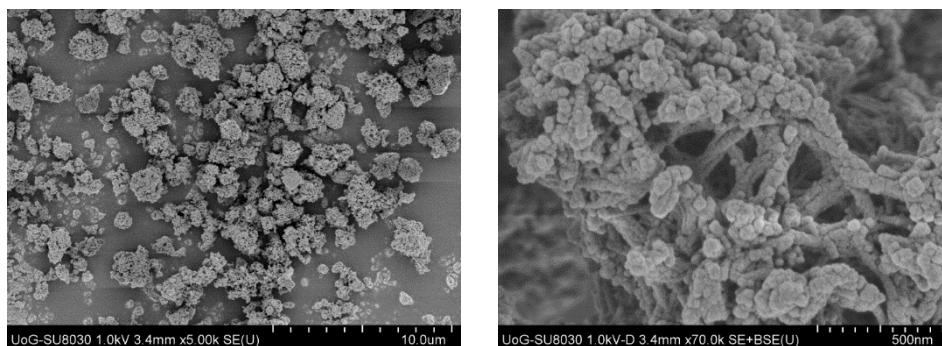
Figure 1. SEM images of MLTUM-Fe$_2$O$_3$
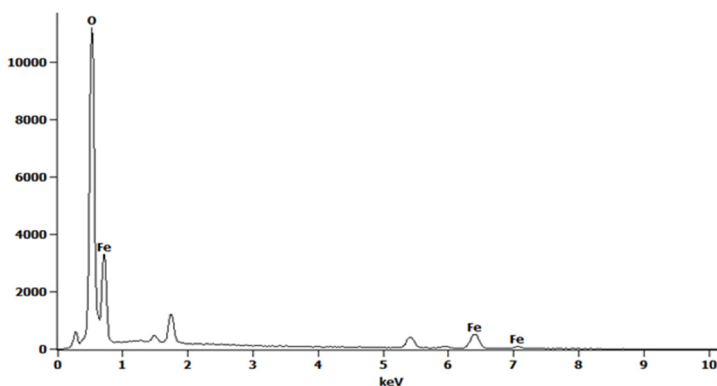
Figure 2. EDX spectra of MLTUM-Fe$_2$O$_3$

Thermogravimetric analysis (TGA) of MLTUM-Fe$_2$O$_3$ was carried out up to 700ºC (Fig. 3). The weight loss was observed to take place in two steps. The first weight loss is computed to be 20.76% at 375ºC. This weight loss in the temperature range 0–375ºC may be attributed to the loss of physisorbed and interstitial water. Further warming over 400ºC leads to a slight loss of weight (0.55%). The results of TG analysis show that the total weight loss is 21.31%. This confirms that a chemical transformation of hydroxide into the oxide has occurred.
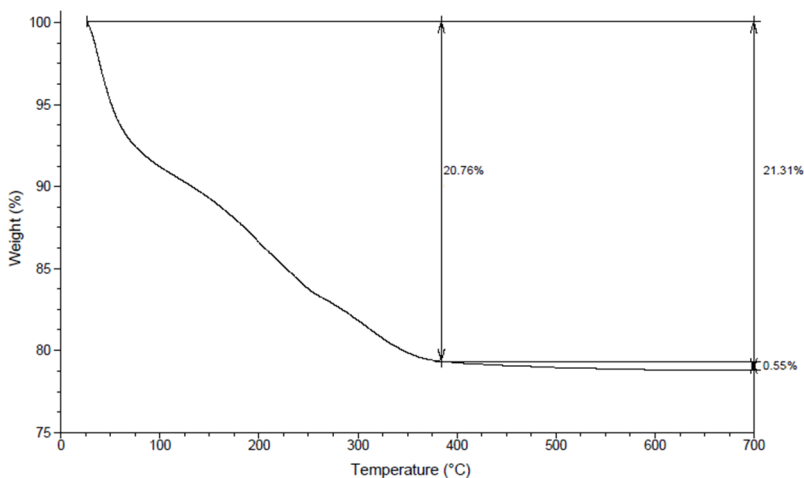
Figure 3. TGA of MLTUM-Fe$_2$O$_3$

Fig. 4. shows the FTIR spectra of MLTUM-Fe$_2$O$_3$. The band centred at 3416.23 and 1633.39 cm^{-1} are ascribed to O–H bonding stretching and bending vibrational modes [39]. It suggested the presence of very small amount of free and sorbed water on the surface of the sample. As shown in figure, a peak at 530.32 and 451.25 cm^{-1} is ascribed to the stretching between iron and oxygen in Fe$_2$O$_3$ [40].
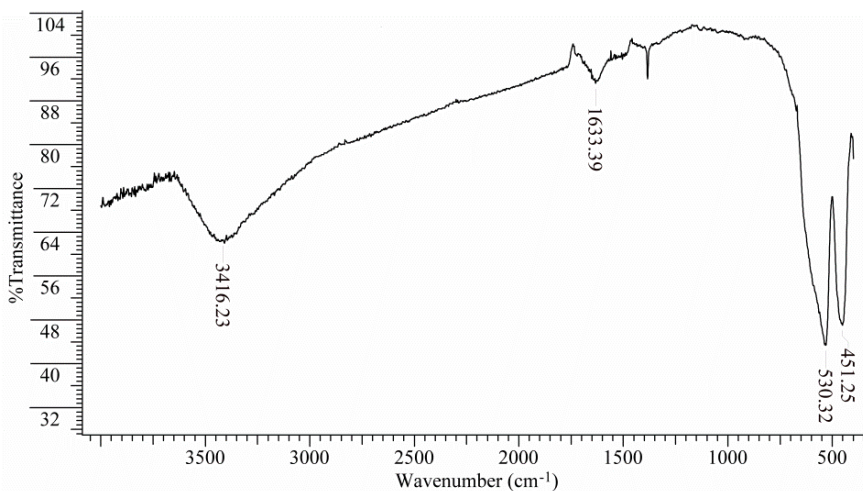
Figure 4. FTIR spectra of MLTUM-Fe$_2$O$_3$

Determination of the point of zero charge

The point of zero charge (PZC) is an important parameter that indicates the linear range of pH sensitivity and the sorption ability of the surface. The PZC value was determined by a simplified mass potentiometric titration method [41,42]. pH of solution after sorption vs pH before sorption is plotted and PZC value of MLTUM-Fe$_2$O$_3$ nanoparticle is found to 2.78.

Effects of contact time

Results on Fig. 5. indicates the effect of contact time on the removal efficiency and here it is followed that the rapid sorption of RB 19 took place within 5 min. Subsequently, sorption became slow and almost reached equilibrium within 15 min. However, the experimental data were measured at 180 min to make sure that full equilibrium was attained.
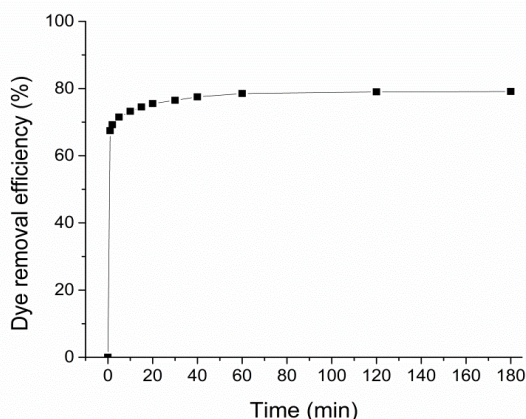
Figure 5. Effect of contact time on RB 19 removal using MLTUM-Fe$_2$O$_3$.
Initial dye concentration 100 mg dm^{-3}, sorbent dose = 0.5 g dm^{-3},
native pH, temperature = 25 ± 0.5ºC

Effect of sorbent dosage

To optimize the minimum dosage required for bringing down the RB 19 level, the dosage of sorbent was varied from 0.1 g dm^{-3} to 1 g dm^{-3}. The removal efficiency of RB 19 with different sorbent dosage is shown in Fig. 6. The percentage removal of RB 19 significantly increased with sorbent dosage. In all the subsequent experiments 0.5 g dm^{-3} of sorbent was fixed as the optimum dosage.

MILJANA RADOVIĆ VUČIĆ, JELENA MITROVIĆ, MILOŠ KOSTIĆ, NENA VELINOV,
SLOBODAN NAJDANOVIĆ, DANIJELA BOJIĆ, ALEKSANDAR BOJIĆ
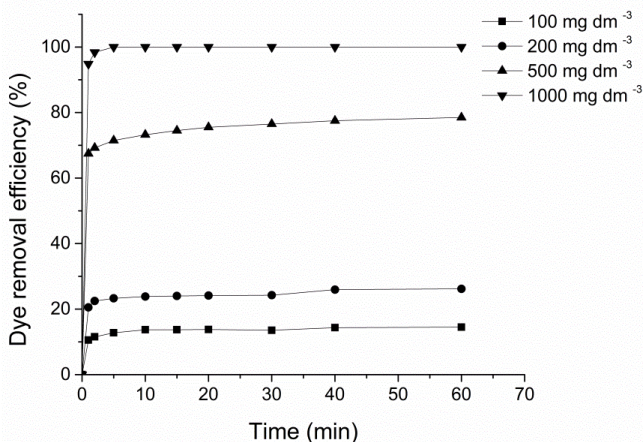
Fig. 6. Effect of sorbent dosage on RB 19 removal using MLTUM-Fe$_2$O$_3$. Initial dye concentration 100 mg dm^{-3}, native pH, temperature = 25 ± 0.5ºC

Effect of initial dye concentration

The effect of initial dye concentration was studied in the concentration range 1–500 mg dm^{-3} at native pH value. It was evident that for lower initial concentrations of RB 19, the sorption was very fast (Fig. 7). The removal of RB 19 decreased with increase in initial dye concentration and took longer time to reach equilibrium.
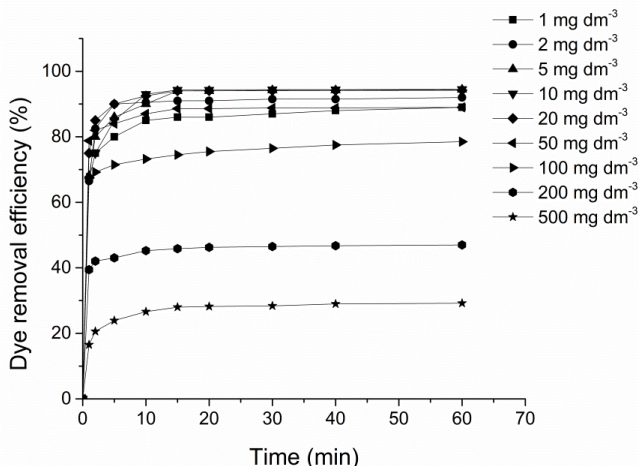
Fig. 7. Effect of initial dye concentration on RB 19 removal using MLTUM-Fe$_2$O$_3$. Sorbent dose = 0.5 g dm^{-3}, native pH, temperature = 25 ± 0.5ºC

Effect of pH

To study the effect of pH on the sorption of RB 19, experiments were carried out in the pH range of 2–11. Anionic dye sorption is favoured at pH < pH$_{pzc}$ where the surface becomes positively charged [43]. It can be observed that the sorption of RB 19 increases in the acidic medium (Fig. 8). Although the dye removal efficiency decreased from 89.35% to 14.90 when pH was raised from 2 to 11. This can be explained on the basis of the point of zero charge [44]. Therefore, the surface of MLTUM-Fe$_2$O$_3$ is positively charged below the PZC and negatively charged above the PZC.
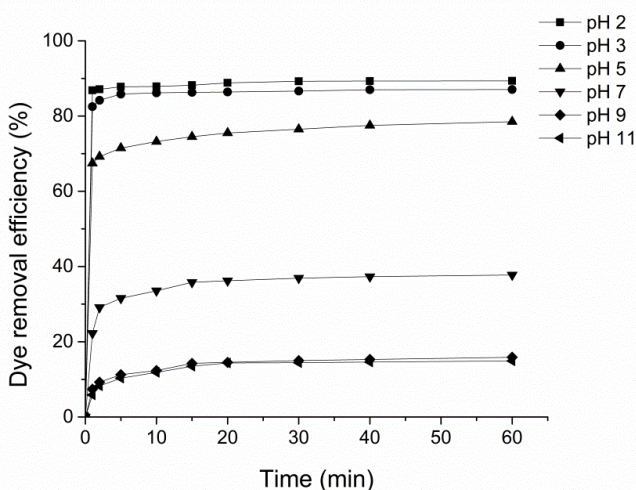
Figure 8. Effect of pH on RB 19 removal using MLTUM-Fe$_2$O$_3$. Initial dye concentration 100 mg dm^{-3}, sorbent dose = 0.5 g dm^{-3}, temperature = 25 ± 0.5ºC

Sorption kinetics

The rate of sorption was determined by studying the sorption kinetics at nine different initial RB 19 concentrations (1, 2, 5, 10, 20, 50, 100, 200 and 500 mg dm^{-3}) at optimum sorbent dose. It was observed that RB 19 removal increased with the lapse of time and the rate was initially rapid, after which the rate slowed down as the equilibrium approached. The values of the kinetic models parameters calculated non-linearly are given in Table 1. The experimental data showed that pseudo-second-order model better fitted experimental data than pseudo-first-order model.

MILJANA RADOVIĆ VUČIĆ, JELENA MITROVIĆ, MILOŠ KOSTIĆ, NENA VELINOV,
SLOBODAN NAJDANOVIĆ, DANIJELA BOJIĆ, ALEKSANDAR BOJIĆ

Table 1. Pseudo-first order and pseudo-secoond-order kinetic parameters for the RB 19 dye sorption onto MLTUM-Fe_2O_3

C_0 (mg dm^{-3})	1	2	5	10	20	50	100	200	500
q_e, exp (mg g^{-1})	1.800	3.725	9.448	18.977	37.774	89.341	157.224	189.014	271.002
Pseudo-first-order model									
q_e, cal (mg g^{-1})	1.720	3.647	9.242	18.548	37.245	87.576	150.492	183.159	259.704
k_1 (min^{-1})	1.367	1.271	1.221	1.092	1.084	1.052	1.012	0.953	0.801
R^2	0.983	0.995	0.987	0.979	0.995	0.993	0.984	0.988	0.969
Pseudo-second-order model									
q_e, cal (mg g^{-1})	1.766	3.731	9.506	19.139	37.982	88.819	153.093	186.585	273.015
k_2 (min^{-1})	1.656	0.772	0.263	0.110	0.103	0.091	0.039	0.026	0.004
R^2	0.997	0.996	0.999	0.997	0.999	0.998	0.994	0.997	0.994

Since neither the pseudo-first-order nor pseudo-second-order model can identify the diffusion mechanism, the kinetic results were further analyzed by intraparticle diffusion model [45]. Values of the parameters of the intraparticle diffusion model are shown in Table S4 in Supplementary.

Based on k_{id1} and k_{id2} values it can be concluded that film diffusion is more efficient than intraparticle diffusion. The calculated intra-particle diffusion rate constants k_{id3} (Table S4) increased with increasing initial RB 19 which can be related to faster diffusion.

Chrastil's diffusion model describes sorption kinetics in diffusion-controlled systems. The original equation for Chrastil's diffusion model is presented in detail in paper by Chrastil (1990) [46]. The parameters of the model were determined by a non-linear regression analysis of experimental data and given in Table S5 in Supplementary material section. The results obtained for the diffusion resistance coefficient show that n values decrease from 0.652 to 0.051 (Table S5) for initial RB 19 concentration from 1 up to 500 mg dm^{-3}, meaning that the sorption rate is strongly limited by the diffusion [47].

Sorption isotherms

In this work, different equilibrium models of two (Langmuir, Freundlich, Temkin, and Dubinin-Radushkevich) and three (Sips) parameters were evaluated to fit the experimental MLTUM-Fe_2O_3 sorption of RB 19 isotherm. Fig. S6 in Supplementary material section shows the comparison of different isotherms studied at 25ºC. The isotherm parameters of all the above-mentioned models, along with their corresponding r^2 values are presented in Table 2.

Table 2. Characteristic parameters of different isotherm models for RB 19 sorption for the RB 19 dye sorption onto MLTUM-Fe_2O_3

Equilibrium model	Parameter	Value
Langmuir isotherm	K_L (dm^3 mg^{-1})	0.088
	q_m (mg g^{-1})	241.779
	R^2	0.970
Freundlich isotherm	K_F, (dm^3 g^{-1})$^{1/n}$	43.212
	n	3.171
	R^2	0.952
Tempkin isotherm	K_T (dm^3 mg^{-1})	5.082
	b (J mol^{-1})	31.823
	R^2	0.969
Dubinin-Radushkevich isotherm	q_{DR} (mg g^{-1})	207.022
	K_{DR} (mol^2 kJ^{-2})	5.024·10^{-6}
	E (J mol^{-1})	315.557
	R^2	0.909
Sips isotherm	q_m (mg g^{-1})	299.383
	K_S (dm^3 mg^{-1})	0.126
	n	1.578
	R^2	0.988

Langmuir isotherm

The Langmuir isotherm [48] is often used to describe the adsorption in homogeneous surfaces based on the assumptions that monolayer adsorption occurs on uniformly energetic adsorption sites with no interactions between adsorbate molecules.

The highest correlation factors ($R^2 > 0.97$) of Langmuir model for RB 19 indicates that the Langmuir model gives the best fit to the experimental data and so the nature of sorption of dyes on the sorbents is more compatible

with Langmuir assumptions and imply that sorption of investigated pollutant on the sorbent is mono-layer and after saturation of this layer no further sorption took place. The maximum RB 19 sorption capacity determined from the Langmuir isotherm model was 241.77 mg g^{-1} (Table 2), which is consistent with the experimental value (271.002 mg g^{-1}).

Freundlich isotherm

The Freundlich isotherm [49] is used for adsorption which involves system with heterogeneous surface energy. It is assumed that the stronger binding sites are occupied first and that the binding strength decreases with the increasing degree of site occupation.

Differences between the monolayer (chemisorption) and multilayer (physisorption) process can be detected by applying the Freundlich model. From the data in Table 2, that value of $1/n = 0.315$ while $n = 3.171$ indicating that the sorption of RB 19 onto MLTUM-Fe$_2$O$_3$ is favourable, as noted in the previous adsorption works [50–53]. These values also suggest formation of an almost homogeneous surface.

Temkin isotherm

The Temkin isotherm assumes that the heat of sorption of all the molecules in a layer decreases linearly due to sorbent–sorbate interactions and that sorption is characterized by a uniform distribution of binding energies, up to some maximum binding energy. The original non-linear equation is presented in paper by Temkin and Pyzhev (1940) [54]. The relatively high value of parameter b (31.8232), indicated that there is a significant ionic interaction between RB 19 and MLTUM-Fe$_2$O$_3$ sorbent and suggested predominance of chemical sorption.

Dubinin–Radushkevich isotherm

Dubinin–Radushkevich model is used to distinguish between physisorption and chemisorption and also to assess the mechanism of RB 19 sorption on MLTUM-Fe$_2$O$_3$. Values q_{DR}, K_{DR} and ε should be determinate from a non-linear plot of q_e versus C_e. Radushkevich (1949) [55] and Dubinin (1965) [56] have reported that the characteristic sorption curve is related to the porous structure of the sorbent. According to the calculated E value, which was 315.557 J mol^{-1}, physical sorption can be involved in RB 19 sorption onto MLTUM-Fe$_2$O$_3$. Considering determination coefficient value ($R^2 = 0.909$), it can be concluded that the D-R model doesn't fit well with experimental data (Table 2).

Sips isotherm

The Sips isotherm [57] is a combined form of Langmuir and Freundlich expressions used for predicting the heterogeneous adsorption systems and circumventing the limitation of the rising adsorbate concentration associated with Freundlich isotherm model. The relatively high value of parameter *n* (Table 2) indicates that the Langmuir will be preferable isotherm. This is consistent with the results obtained for other isotherms.

Desorption of RB19 and reused of MLTUM-Fe_2O_3 nanosorbent

Regeneration and reusability of sorbents is an important factor for industrial and practical applications because of the reduction of the need for new amount of sorbent and lowering of synthesis costs of the sorbent materials. It was found that for MLTUM-Fe_2O_3, the removal efficiency (*RE* %) decreased from 78.59% to 75.40% in the first three cycles and then reached 72.47% in the fourth cycle and the fifth cycle reached 70.32%. The maximum desorption efficiency by NaOH was obtained after 15 min and amounted about 82% in the first desorption cycle. In the next cycles desorption efficiency by using NaOH was higher than 92%. The minor decrease of the sorption capacity can be attributed to the loss of the sorbents in the sorption desorption processes and the irreversible binding (chemisorption) of RB19 on MLTUM-Fe_2O_3. Desorption of RB19 using NaCl solution was very low with *DE* % of 21.78%. Therefore, the MLTUM-Fe_2O_3 can be reutilized, with previously desorption using NaOH.

CONCLUSION

The Fe_2O_3 nanoparticles have been synthesized using simple and fast modified low-temperature urea method and successfully characterized by BET, SEM, EDX, XRD, TGA and FTIR techniques. MLTUM-Fe_2O_3 can be used as potential sorbent for the removal RB 19 from water with a maximum sorption capacity of 271.00 mg g^{-1} for dye at room temperature. The kinetic data shows that the present system follows pseudo-second-order model. Equilibrium sorption data fit better to Langmuir followed by Sips, Tempkin, Freundlich and Dubinin-Radushkevich sorption models, respectively. Hence, this study could provide a simple route to synthesize a cost-effective nanostructured Fe_2O_3 sorbent for dyes removal in environmental treatment.

MILJANA RADOVIĆ VUČIĆ, JELENA MITROVIĆ, MILOŠ KOSTIĆ, NENA VELINOV, SLOBODAN NAJDANOVIĆ, DANIJELA BOJIĆ, ALEKSANDAR BOJIĆ

EXPERIMENTAL

Materials

Ferric nitrate $Fe(NO_3)_3 \cdot 9 H_2O$ (Sigma Aldrich, USA) and urea $(NH_2)_2CO$ (Merck, Germany) with 99% and 99.5% purities respectively, were employed as the starting materials. The dye Reactive Blue 19 (RB 19) was obtained from Sigma Aldrich (USA) and used without further purification. The properties and molecular structure of RB 19 are shown in Table S2 in Supplementary material section.

Synthesis

Iron oxide nanoparticles was synthesized by a modified low-temperature urea method. The effect of the fuel in controlling particle size and microstructure of the product under different fuel-to-oxidant ratios is investigated by a few scientists [37,38]. Initially, three aqueous solutions of the ferric nitrate nonahydrate $Fe(NO_3)_3 \cdot 9 H_2O$ and urea $(NH_2)_2CO$ with Fe:urea molar ratio 1:2.5, 1:5 and 1:7.5 were added to three flasks with reflux condenser, which were maintained at 90ºC for 3 h. After that the suspensions were cooled to room temperature, filtered and washed with hot deionized water for effective removal of ions. The final products were dried at 100ºC for 10 h. For further research, the iron oxide obtained with molar ratio 1:2.5 was used because with the further increase in the amount of urea there was no increase in the sorption of the material. The material with Fe:urea molar ratio 1:2.5 will be marked as MLTUM-Fe_2O_3 further in the text.

Characterization

The structure of MLTUM-Fe_2O_3 was determined by X-ray powder diffraction (XRD). Data were collected with a Siemens D5000 X-ray Diffractometer in theta-theta geometry in reflection mode with Co Kα. Data collection was between 20-80º 2θ, step size of 0.02º. For SEM-EDX analysis samples were attached to aluminum stubs using Leit-C carbon cement. A Hitachi SU8030 cold FEG-SEM was used for imaging the samples with Thermo-Noran NSS system 7 ultra-dry x-ray detector for semi-quantitative EDX analysis (Thermo Scientific NORAN System 7, USA). An infrared spectrum of MLTUM-Fe_2O_3 was obtained using a Fourier transform infrared spectrometer (Bomem Hartmann & Braun MB-100 spectrometer).

The specific surface area was evaluated by the BET method using N_2 adsorption. A full gas sorption isotherm was run on a Micromeritics Gemini 5 Surface Area Analyser. The pore size distribution was calculated from the desorption branch of the isotherm by the Barrett, Joyner, and Halenda (BJH)

method. Thermogravimetric analysis (TGA) was performed using TGA Q5000 (TA Instruments, USA). The sample was heated in air at a flow rate of 25 cm^3 min^{-1} from ambient temperature to 600ºC in aluminum pan, at a heating rate of 2ºC min^{-1}.

Sorption experiments

Studies on the sorption of dye RB 19 by MLTUM-Fe_2O_3 were carried out in batch conditions. 100 cm^3 of each of working dye solution was contacted with 0.05 g sorbent, stirred at 250 rpm, at room temperature 25.0 ± 0.5°C. Aliquots of solutions (5.0 cm^3) were withdrawn at desired time intervals and the sorbent was removed immediately by filtration through a 0.20 µm regenerated cellulose membrane filter (Agilent Technologies, Germany). Absorbance at 592 nm was measured using a UV/vis spectrophotometer Shimadzu UV-1800 PC (Shimadzu, Japan). The amount of dye sorbed q_t (mg g^{-1}) was determined by using the following equation 1:

$$q_t = \frac{(c_i - c_t)}{m}$$
(1)

The percentage of removal was evaluated using equation 2:

$$RE\ (\%) = \left(1 - \frac{c_t}{c_0}\right) \times 100$$
(2)

where c_0 and c_t are the initial and final concentrations of the dye in solution (mg dm^{-3}), V is the solution volume (dm^3) and m is the mass of the sorbent (g).

Desorption of RB19 and reused of MLTUM-Fe_2O_3 nanosorbent

In order to investigate the reusability performance of the MLTUM-Fe_2O_3 nanosorbent, five successive sorption–desorption (regeneration) cycles were performed. In the adsorption test, 0.05 g of MLTUM-Fe_2O_3 was loaded with 100 cm^3 of RB19 solution with concentration of 100 mg dm^{-3} and stirred for 180 min. To regenerate the adsorbent, the used MLTUM-Fe_2O_3 was contacted with 100 cm^3 of desorption solutions (0.1M NaOH and 1M NaCl), with stirring for 1 h. The desorption efficiency (DE %) was calculated as follows:

$$DE\ (\%) = \left(\frac{m_{desorbedRB\ 19}\ [mg]}{m_{previously\ sorbed}\ [mg]}\right) \times 100$$
(3)

MILJANA RADOVIĆ VUČIĆ, JELENA MITROVIĆ, MILOŠ KOSTIĆ, NENA VELINOV,
SLOBODAN NAJDANOVIĆ, DANIJELA BOJIĆ, ALEKSANDAR BOJIĆ

ACKNOWLEDGEMENTS

REFERENCES

1. C. O'Neill; F.R. Hawkes; D.L. Hawkes; N.D. Lourenco; H.M. Pinheiro; W. Delee; *Chem. Technol. Biot*., **1999**, *74*, 1009-1018.
2. I. Arslan-Alaton; B.H. Gursoy; J.E. Schmidt; *Dyes Pigm.*, **2008**, *78*, 117-130.
3. J. (Ed.) Shore; *Dyeing with Reactive Dyes*, Formerly of BTTG-Shirley and ICI (now Zeneca), Manchester, UK, **1995**.
4. P. (Ed.) Gregory; *Toxicology of Textile Dyes*, Heriot-Watt University, UK, **2007**.
5. Y. Verma; *Toxicol. Ind. Health*, **2011**, *27*, 41-49.
6. J.E.B. McCallum; S.A. Madison; S. Alkan; R.L. Depinto; R.U. Rohas Wahl; *Environ. Sci. Technol*., **2000**, *34*, 5157-5164.
7. M. Siddique; R. Farooq; Z.M. Khan; Z. Khan; S.F. Shaukat; *Ultrason. Sonochem*., 2011, *18*, 190-196.
8. A. Dabrowski; *Adv. Coll. Interface Sci*., **2001**, *93*, 135-224.
9. T. Robinson; G. McMullan; R. Marchant; P. Nigam; *Bioresour. Technol*., **2001**, *77*, 247-255.
10. O. Aktas; F. Cecen; *Int. Biodeterior. Biodegrad*., **2007**, *5*9, 257-272.
11. E. Hosseini Koupaie; M.R. Alavi Moghaddam; S.H. Hashemi; *Int. Biodeterior. Biodegrad*., **2012**, *71*, 43-49.
12. J. Zolgharnein; N. Asanjarani; T. Shariatmanesh; *Int. Biodeterior. Biodegrad*., **2013**, *85*, 66-77.
13. R.S. Juang; R.L. Tseng; F.C. Wu; S.H. Lee; *J. Chem. Technol. Biot*., **1997**, *70*, 391-399.
14. K.Y. Ho; G. McKay; K.L. Yeung, *Langmuir*, **2003**, *19*, 3019-3024.
15. Q.Y. Sun; L.Z. Yang; *Water Res*., **2003**, *37*, 1535-1544.
16. M. Valix; W.H. Cheung; G. McKay; *Langmuir*, **2006**, *22*, 4574-4582.
17. B.H. Hameed; A.A. Ahmad; N. Aziz; *Chem. Eng. J*., **2007**, *133*, 195-203.
18. I.A. W. Tan; B.H. Hameed; A.L. Ahmad; *Chem. Eng. J*., **2007**,*127*, 111-119.
19. A. Mittal; L. Kurup; J. Mittal; *J. Hazard. Mater*., **2007**, 146, 243-248.
20. I.A. W. Tan; A.L. Ahmad; B.H. Hameed; *J. Hazard. Mater.*, **2008**, *154*, 337-346.
21. E. Eren; B. Afsin; *Dyes Pigments*, **2008**, *76*, 220-225.
22. A.P. Vieira; S.A.A. Santana; C.W.B. Bezerra; H.A.S. Silva; J.A.P. Chaves; J.C.P. de Melo; E.C. da Silva Filho; C. Airoldi; *J. Hazard. Mater*., **2009**, *166*, 1272-1278.

184

23. B.K. Nandi; A. Goswami; M.K. Purkait; *Appl. Clay. Sci.*, **2009**, *42*, 583-590.
24. O. Gok; A.S. Ozcan; A. Ozcan; *Appl. Surf. Sci.*, **2010**, *256*, 5439-5443.
25. A.R. Khataee; F. Vafaei; M. Jannatkhah; *Int. Biodeterior. Biodegrad.*, **2013**, *83*, 33-40.
26. R. Darvishi Cheshmeh Soltani; A.R. Khataee; M. Safari, S.W. Joo; *Int. Biodeterior. Biodegrad.*, **2013**, *85*, 383-391.
27. N.K. Nga; P.T.T. Hong; T.D. Lam; T.Q. Huy; *J. Colloid. Interf. Sci.*, **2013**, *398*, 210-216.
28. U. A. Isah; G. Abdulraheem; S. Bala; S. Muhammad; M. Abdullahi; *Int. Biodeterior. Biodegrad.*, **2015**, *102*, 265-273.
29. D.C. dos Santos; M.A. Adebayo; E.C. Lima; S.F.P. Pereira; R. Cataluna; C. Saucier; P.S. Thue; F.M. Machado; *J. Braz. Chem. Soc.*, **2015**, *26*, 924-938.
30. S. Karimifard; M. R. A. Moghaddam; *Process Saf. Environ. Prot.*, **2016**, *99*, 20-29.
31. N.K. Nga; H.D. Chinh; P.T.T. Hong; T.Q. Huy; *J. Polym. Environ.*, **2017**, *25*, 146-155.
32. G. Ciobanu; S. Barna; M. Harja; *Arch. Environ. Protec.*, **2016**, *42*, 3-11.
33. Y. Liu; M. Yan; Y. Geng; J. Huang; *Appl. Sci.*, **2016**, *6*, 232-245.
34. M. Shanehsaz; S. Seidi; Y. Ghorbani; S.M.R. Shoja; S. Rouhani; *Spectrochim. Acta., Part* A, **2015**, *149*, 481-486.
35. G. Moussavi; M. Mahmoudi; *J. Hazard. Mater.*, **2009**, *168*, 806-812.
36. Z.M. Khoshhesab; M. Ahmadi; *Desalination Water Treat.*, **2016**, *57*, 20037-
37. R.D. Purohit; B.P. Sharma; K.T. Pillai; A.K.Tyagi; *Mater. Res. Bull.*, **2001**, *36*, 2711-2721.
38. J.C. Toniolo; M.D. Lima; A.S. Takimi; C.P. Bergmann; *Mater. Res. Bull.*, **2005**, *40*, 561-571.
39. L.M. Song; S.J. Zhang; *Colloids Surf. A: Physicochem. Eng. Asp.*, **2010**, *360*, 1-5.
40. R.M. Cornell; U. Schwertmann; The Iron Oxides: Structure, Properties, Reactions, Occurrences and Uses, Wiley-VCH, New York, **2003**.
41. P. Balderas-Hernandez; J.G. Ibanez; J.J. Godinez-Ramirez; F. Almada-Calvo; *Chem. Educator*, **2006**, *11*, 267-270.
42. J.G. Ibanez; M. Hernandez-Esparza; C. Doria-Serrano; A. Fregoso-Infante; M.M. Singh; *Environmental Chemistry: Microscale Laboratory Experiments*, Springer, New York, **2008**.
43. D. Savova; N. Petrov; M. Yardim; E. Ekinci; T. Budinova; M. Razvigorova; V. Minkova; *Carbon*, **2003**, *41*, 1897-1903.
44. S. Al-Qaradawi; S. R. Salman; *J. Photochem. Photobiol. A: Chem.*, **2002**, *148*, 161-168.
45. W.J. Jr. Weber; J.C. Morris; *J. Sanit. Eng. Div.*, 1964, *89*, 31-60.
46. J. Chrastil; *Text. Res. J.*, **1990**, *60*, 413-416.
47. F. Carrillo; M.J. Lis; X. Colom; M. Lopez-Mesas; J. Valldeperas; *Process Biochem.*, **2005**, *40*, 3360-3364.
48. I. Langmuir; *J. Am. Chem. Soc.*, **1916**, *38*, 2221-2295.
49. H.Z. Freundlich; *J. Phys. Chem.*, **1906**, *57A*, 385-470.
50. A.A. Ismaiel; M.K. Aroua; R. Yusoff; *Chem. Eng. J.*, **2013**, *225*, 306-314.

51. H.K. Boparai; M. Joseph; D.M. O'Caroll; *J. Hazard. Mater*., **2011**, *186*, 458-465.
52. G. Vazquez; M. Sonia Freire; J. Gonzalez-Alvarez; G. Antorrena; *Desalination*, **2009**, 249, 855-860.
53. N. Asasian; T. Kaghazchi; M. Soleimani; *J. Ind. Eng. Chem*., **2012**, *18*, 283-289.
54. M.I. Temkin; V. Pyzhev; *Acta Physicochim.*, **1940**, *12*, 217-222.
55. L.V. Radushkevich; *Zhurnal Fizicheskoi Khimii* **1949**, *23*, 1410-1420.
56. M.M. Dubinin; *Chem. Rev.*, **1960**, *60*, 235-266.
57. R. Sips; *J. Chem. Phys*., **1948**, *16*, 490-495.

KINETICS OF GLICLAZIDE AFTER SINGLE DOSE ORAL ADMINISTRATION OF GLICLAZIDE 60 MG MODIFIED RELEASE TABLET

DIANA IOANA POP[a,b], ADRIANA MARCOVICI[b], MONICA OROIAN[a,b], ANA-MARIA GHELDIU[c,*], LAURIAN VLASE[a]

ABSTRACT. The current study aimed to establish and describe the basic pharmacokinetics of a single dose of gliclazide 60 mg modified release formulation manufactured by Ranbaxy Laboratories Limited, now Sun Pharmaceutical Industries Limited, India. Ten mathematical models were created for analyzing the experimental data resulted from two bioequivalence studies conducted at Clinical Pharmacology and Pharmacokinetics Department of Terapia S.A. Model discrimination was done using the Akaike index value and it was observed that model number 10 (M10) is the model that best describes the gliclazide disposition. This model has two compartments (peripheral and central), mixed order absorption process (1st and zero order kinetics) with a lag time of around 3 hrs and 1st order kinetics of elimination. Applying this model in Phoenix software version 6.3 (Pharsight Corp., Mountain view, CA, USA) the main pharmacokinetic parameters of gliclazide were also computed.

Keywords: gliclazide, compartmental pharmacokinetic analysis, bioequivalence clinical trials, best model

INTRODUCTION

Gliclazide, available on market as immediate and modified release formulations, is a second-generation sulphonylurea used as an oral

---

[a] *University of Medicine and Pharmacy 'Iuliu Hațieganu', Faculty of Pharmacy, Department of Pharmaceutical Technology and Biopharmaceutics, 8 Victor Babeș str., RO-400012, Cluj-Napoca, Romania*
[b] *Terapia SA – a Sun Pharma Company, Department of Clinical Pharmacology and Pharmacokinetics, 124 Fabricii str., RO-400632, Cluj-Napoca, Romania*
[c] *University of Medicine and Pharmacy 'Iuliu Hațieganu', Faculty of Pharmacy, Department of Pharmaceutical Botany, 23 Marinescu str., RO-400337, Cluj-Napoca, Romania*
* Corresponding author: anamaria.gheldiu@yahoo.com

hypoglycaemic agent for the treatment of type 2 diabetes (T2DM) [1,2,3]. Gliclazide is part of the World Health Organization (WHO) list with essential drugs and it was first used in 1972, thus having a long history of clinical use and several generics available on the market [4,5,6].

Gliclazide is chemically known as 1-(3,3a,4,5,6,6a-hexahydro-1H-cyclopenta[c] pyrrol-2-yl)-3-(4-methylphenyl)sulfonylurea (IUPAC name) (see Figure 1).
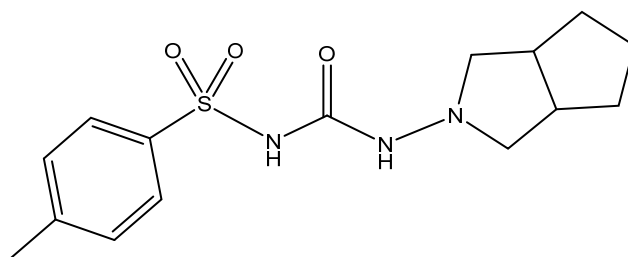
Figure 1. Chemical structure of gliclazide

It is different from other sulphonylureas as it has an N-containing heterocyclic ring and an endocyclic bond. It has a molecular weight of 323.4 g/mol and the molecular formula $C_{15}H_{21}N_3O_3S$ [7,8,9].

The levels of blood glucose are reduced by gliclazide as it stimulates the insulin secretion of pancreatic islets β-cells. It binds to sulfonylurea receptors available on the surface of pancreatic beta cells (SUR-1) selectively, inducing insulin release. It shows a good safety profile and ensures cardiovascular protection, as gliclazide has no affinity for sulfonylurea receptors in the heart (SUR-2A) [7,9,10,11,12]. Moreover, gliclazide presents extra-pancreatic effects and hemovascular properties [7,13,14].

The main organ for gliclazide's metabolization is the liver. In plasma were not found any active metabolites. In urine were detected at least eight metabolites. The major metabolic pathway of gliclazide metabolization involves the tolylmethyl hydroxylation and then oxidation to the corresponding carboxylic acid. Seven monohydroxylated metabolites could be obtained after the hydroxylation of the azabicyclo-octyl moiety. Transporters were not proved to be involved in gliclazide's disposition [15,16,17].

The main role in gliclazide metabolic clearance is attributed to cytochrome P450 2C9 (CYP2C9) and possibly CYP2C19 and CYP2C18. CYP2C9 polymorphism and other pharmacodynamic factors could explain the gliclazide individual differences that have been reported [16,18, 19,20,21].

The pharmacokinetics describes how a drug is disposed in the human body and studies the processes like absorption, distribution, metabolism and excretion (ADME), processes that occur in time after drug administration. It analyses the relationship between the pharmacological effect that is exerted by the active substance and the administered drug dose and gives a deep insight into the mechanisms that are involved in the physiologic process that a drug undergoes in the body [22,23,24].

Using the pharmacokinetic compartmental analysis the ADME processes can be characterized by establishing the pharmacokinetic (PK) parameters. Individualized therapy or specific dose-adjustment for patients could be determined considering the PK profile of the drug. In addition, the PK parameters and the drug profile are very useful for the formulations that undergo bioequivalence studies for approval of generic products [22,23,24]

Therefore, it is essential that the disposition in the human body and the basic PK model of gliclazide should be described before the approval of a new generic 60 mg modified release tablet.

The aim of the presented study was to establish and describe the best PK model that accurately reflects the kinetics processes of ADME processes for gliclazide, after a single 60 mg oral dose in healthy Caucasian volunteers of the newly developed modified release formulation. The predicted values were compared with the actual experimental data that resulted from two bioequivalence studies conducted under fasting and fed conditions at the Clinical Pharmacology and Pharmacokinetics Department of Terapia S.A.

RESULTS AND DISCUSSION

Ten mathematical models were created with the purpose of analyzing the PK profile of gliclazide and are given in Table 1.

The differences between the ten PK models consisted in different assumptions about the absorption kinetics of gliclazide, number of compartments for the drug, and existence of lag time from the time of drug administration until the beginning of drug absorption. The corresponding mathematical differential equations were written and run for each PK model with Phoenix 6.3 software package (Pharsight Corp., Mountain view, CA, USA).

Table 1. Pharmacokinetic models of gliclazide used in compartmental analysis

Pharmacokinetic model	Absorption kinetics	Lag time	Number of compartment
M1	1st order	No	1
M2	1st order	Yes	1
M3	Zero order	No	1
M4	Zero order	Yes	1
M5	1st order	No	2
M6	1st order	Yes	2
M7	Zero order	No	2
M8	Zero order	Yes	2
M9	1st order and zero order	Yes	1
M10	1st order and zero order	Yes	2

The PK scheme for model 10 (M10) is shown in Figure 2.
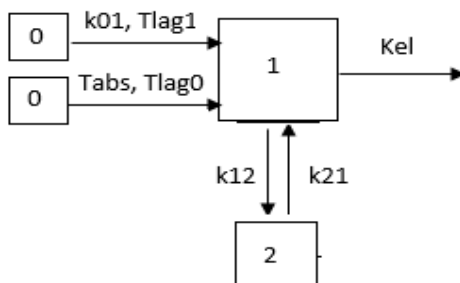
Figure 2. Schematic representation of kinetic processes for model M10, where "0" are absorption compartments of gliclazide; "1" is the central compartment of gliclazide; "2" is gliclazide peripheral compartment; T_{lag0} and T_{lag1} are the latency times for absorption; Tabs is the time needed for zero order absorption and k_{01} is the 1st order absorption rate constants of gliclazide; k_{12} and k_{21} are the distribution rate constants for gliclazide; K_{el} is the elimination rate constant for gliclazide

The mean plasma concentrations of gliclazide were analysed using the ten kinetic models described, after they were implemented in Phoenix software. The same settings of minimisation engine was used for the evaluated models: weighting scheme was 1/y (1/observed concentration), minimisation method was Gauss-Newton (Levenberg and Hartley variant), and convergence criterion was 0.0001.

The Akaike index value (AIC) was automatically calculated for each PK model and further used for model discrimination, considering that a smaller value of this index would be attributed to the model that best fits the experimental data [23,24]. The Akaike values for the ten PK models that were evaluated for the study under fasting condition are given in Figure 3, while the Akaike values for PK models assessed for the study under fed condition are shown in Figure 4.
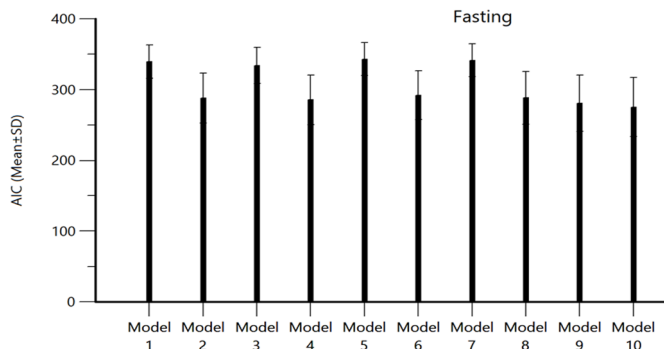
Figure 3. Akaike index values for mathematical evaluated for characterisation of gliclazide disposition in the body, after administration of a single dose 60 mg modified release tablet in subjects under fasting condition
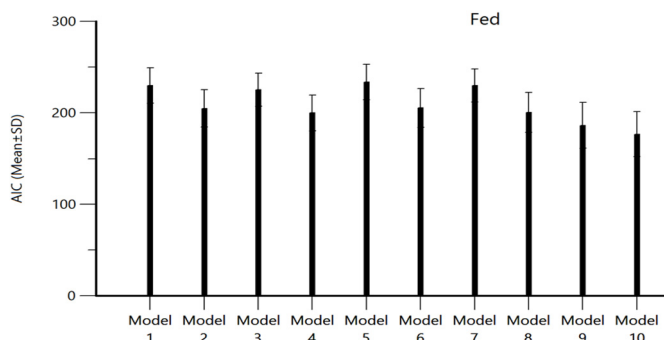
Figure 4. Akaike index values for mathematical evaluated for characterisation of gliclazide disposition in the body, after administration of a single dose 60 mg modified release tablet in subjects under fed condition

In Figure 5 are presented typical fitting of four data sets for subjects from the bioequivalence fasting study, while in Figure 6 are illustrated other four typical fitting of data sets from subjects who participated in the bioequivalence fed study. The best model to describe gliclazide disposition was M10, with the lowest AIC value.
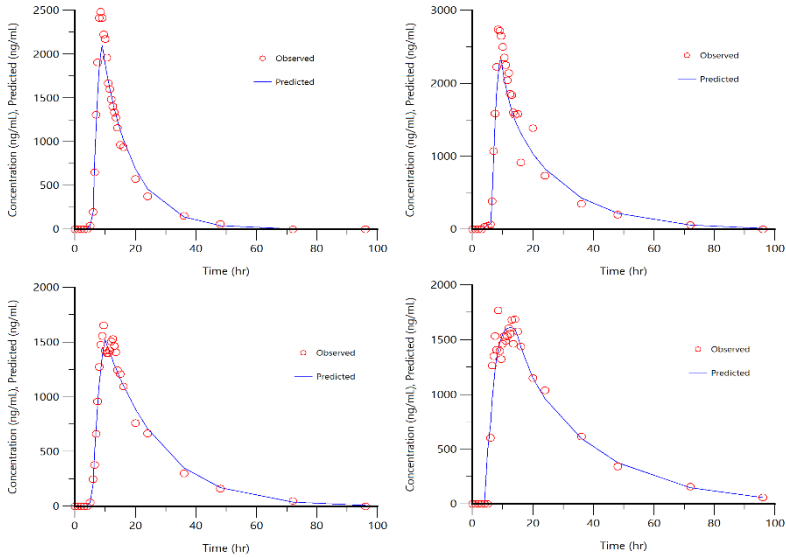
Figure 5. Typical fitting of model M10 for four data sets of experimentally determined plasma concentrations of gliclazide (data from clinical trial under fasting condition)
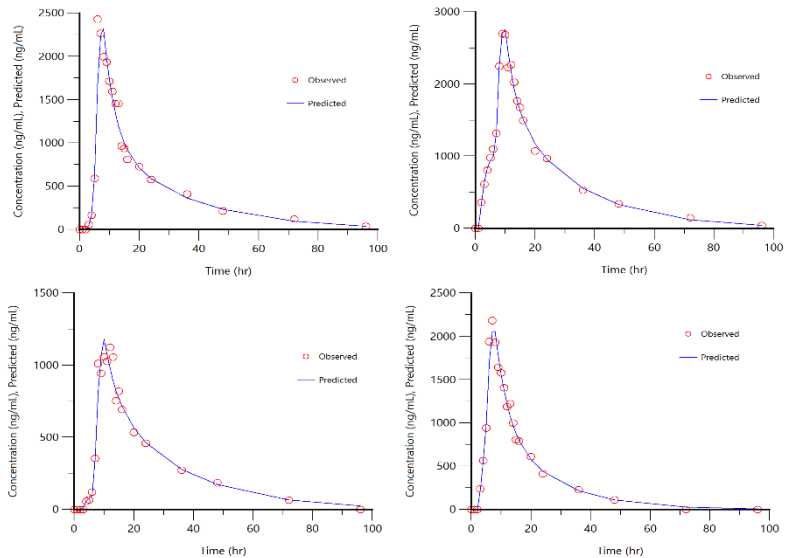
Figure 6. Typical fitting of model M10 for four data sets of experimentally determined plasma concentrations of gliclazide (data from clinical trial under fed condition)

After applying the representative kinetic model for gliclazide (M10) in Phoenix software for fitting all data sets, its characteristic individual PK parameters were computed, for both studies (fasted and fed). In Table 2 are shown the mean PK parameters for fasting study and fed study, side-by-side.

Table 2. The mean pharmacokinetic parameters of gliclazide
calculated with M10, for fasting and fed study

PK parameter (units)	Food					
	Fasting			Fed		
	Mean	SD	CV%	Mean	SD	CV%
f	0.20	0.14	71.55	0.15	0.11	72.35
T_{lag1} (hr)	2.96	1.04	34.99	2.85	0.84	29.51
K_1 (hr^{-1})	0.48	0.53	109.95	0.44	0.30	67.45
T_{lag0} (hr)	5.51	0.93	16.91	5.53	0.84	15.21
T_{abs} (hr)	4.21	1.91	45.36	3.72	1.44	38.70
K_{12} (hr^{-1})	0.07	0.05	71.64	0.06	0.04	61.20
K_{21} (hr^{-1})	0.40	0.27	69.00	0.19	0.18	91.96
K_{el} (hr^{-1})	0.07	0.02	31.77	0.07	0.02	32.35
V_d_F (L)	17.21	7.40	43.03	18.44	5.28	28.66

*f – fraction of dose absorbed following first order kinetics.

By evaluating Figures 3 and 4, it can be observed that model M10 fits the experimental data better than its concurrent models, having the smallest AIC value. Thus, it was selected as representative for gliclazide disposition after single dose oral administration. According to M10, the pharmacokinetics of gliclazide is characterised by a mixed absorption kinetics, 1st order and zero order kinetics, and bicompartmental distribution. Gliclazide is further eliminated from the body following a 1st order kinetics.

The obtained data revealed the importance of the latency time of absorption (T_{lag} was approximately 3 hrs), which is consistent with the fact that gliclazide was administered as a single dose modified release tablet. This is supported by lower AIC values for models that considered lag time. The latency time could be attributed, in addition, to gastric emptying time or to lesser extent, to food intake. It was noticed an insignificant difference between latency time of absorption under fasting versus fed condition (2.96±1.04 hr versus 2.85±0.84 hr), which implies no significant food effect on the T_{lag} of absorption [25].

On the other hand, unitary absorption kinetics was found to be not relevant for the data, neither in fasting study nor in fed study, fact highlighted by the significantly higher AIC values for the models that considered that absorption process follows a single order kinetics. Hence, two new complex

models were created and evaluated, namely M9 and M10, which assumed that gliclazide is subjected to a mixed order absorption of 1st and zero order. Based on the AIC value, it was concluded that M10 is the best model for describing the gliclazide disposition.

The dose fraction (f) that is absorbed following a 1st order kinetics was higher in the case of fasting than fed condition (20% vs 15%, see Table 2), the rest of the dose being absorbed by zero order kinetics.

CONCLUSIONS

The basic PK model for gliclazide that best describes its disposition in the body was determined and characterized. It consists of two compartments, a central and a peripheral compartment, a mixed order absorption (1st order and zero order kinetics), and a lag time of approximately 3 hrs for the onset of absorption process after drug administration.

EXPERIMENTAL SECTION

Subjects: The clinical study data (plasma concentration versus time profile) were obtained from two bioequivalence trials that were conducted at the Clinical Unit of Clinical Pharmacology and Pharmacokinetics Department of Terapia S.A. 41 Caucasian healthy volunteers completed the first bioequivalence study conducted under fasting state, while 23 volunteers finalized the second bioequivalence study, carried out under fed state of subjects. The eligibility of the volunteers for both clinical studies was assessed based on their medical records, on-site physical examination, vital signs, and clinical laboratory tests results. The study protocols were approved by the Ethics Committee of the University of Medicine and Pharmacy "Iuliu Hatieganu", from Cluj-Napoca (Romania) and by the National Agency for Medicines and Medical Devices, Romania [26,27]. The clinical trials were conducted in accordance with all applicable regulatory requirements. All volunteers signed the written informed consent before initiation of any study procedure.

Study design: Each bioequivalence study was designed as an open-label, randomized, single-dose, crossover study that consisted of two periods during which the subjects were given the test product developed by Ranbaxy Laboratories Limited, now Sun Pharmaceutical Industries Limited, India, and the reference product Diamicron® MR, Servier, France [26,27].

Drug administration: For the fasting study the subjects were required to have a fasting period of at least 10 hours before administration of the investigational products. For the fed study after a 10 hours fasting period, all

subjects were given a standard meal (high-fat, high-calorie) with 30 minutes before drug administration. The investigational products were administered with 240 mL of 20% glucose solution [26,27].

Sample collection: The blood samples of 4 mL each were collected in K_3EDTA vacutainers prior to drug administration and up to 96 hours post-dose in each bioequivalence study. The samples were centrifuged, plasma was separated and stored at -50°C until analysis [26,27].

Drug analysis from plasma samples: The plasma concentrations of gliclazide were obtained by using the validated high-throughput liquid chromatography-tandem mass spectrometry (LC-MS/MS) using Gliclazide D4 as internal standard. The limit of quantification was 5.00 ng/mL, required plasma volume of 150 µL and a run time of approximately (2.5 min) [26,27].

Pharmacokinetic and statistical analysis: For both bioequivalence clinical trials, the pharmacokinetic analysis (noncompartmental) was performed with WinNonlin® PK software version 5.2 and the main PK parameters C_{max}, T_{max}, AUC_{0-t}, $AUC_{0-\infty}$, AUC% Extrap and $T_{1/2}$ were calculated. Statistical analysis was performed with SAS software version 9.1.3 for log-transformed C_{max}, AUC_{0-t} and $AUC_{0-\infty}$ using ANOVA. Ratios of means and the 90% confidence intervals were calculated and the obtained values were between 80% and 125%. For the analysis of gliclazide's disposition in the body, the compartmental analysis module of WinNonlin® PK software version 5.2 was used. [26,27].

ACKNOWLEDGMENTS

REFERENCES

1. Z.X. He; Z.-W. Zhou; Y. Yang; T. Yang; S.-Y. Pan; J.-X. Qiu; S.-F. Zhou; *Clin. Exp. Pharmacol P.*, **2015**, *42*, 125-138
2. M. Alsharidah; M. Algeffari; H. Abdel-Moneim; M.F. Lutfi; H. Alshelowi; *Saudi Pharm. J.*, **2018**, *26*, 1-6
3. G.W.D. Landman; G.H. de Bock; K.J.J. van Hateren; P.R. van Dijk; K.H. Groenier; R.O.B. Gans; S.T. Houweling; H.J.G. Bilo; N. Kleefstra; *PLoS ONE.*, **2014**, *9*, article number e82880

4. C.J. Bailey; A.J. Krentz; Oral Antidiabetic Agents. In *Textbook of Diabetes*, 4th ed.; R.I. G. Holt, C.S. Cockram, A. Flyvbjerg, B.J. Goldstein Eds.; Wiley-Blackwell, Oxford, UK, 2010, Part 6 – Chapter 29, pp. 452-477

5. S. Colagiuri; D. Matthews; L.A. Leiter; S.P. Chan; G. Sesti; M. Marre; *Diabetes Res. Clin. Pract.*, **2018**, *143*, 1-14

6. D.I. Pop; A. Marcovici; M. Oroian; A.-M. Gheldiu; L. Vlase; *Studia UBB Chemia*, **2019**, *LXIV*, 217-229

7. O. Ziegler; P. Drouin; *Diabetes Res. Clin. Pract.*, **1991**, *14*, S83-S89

8. M.S. Arayne; N. Sultana; M.K. Zaman; *Pak. J. Pharm. Sci.*, **2003**, *16*, 35-49

9. A. Sarkar; A. Tiwari; P.S. Bhasin; M. Mitra; *J. Appl. Pharm. Sci.*, **2011**, *01*, 11-19

10. H. de Wet; P. Proks; *Biochem. Soc. Trans.*, **2015**, *43*, 901-907

11. G. Müller; Y. Satoh; K. Geisen; *Diabetes Res. Clin. Pract.*, **1995**, *28*, S115-S137

12. C.L. Lawrence; P. Proks; G.C. Rodrigo; P. Jones; Y. Hayabuchi; N.B. Standen; F.M. Ashcroft; *Diabetologia*, **2001**, *44*, 1019-1025

13. P.E. Jennings; *Metabolism*, **2000**, *49*, 17-20

14. S. Zoungas; J. Chalmers; A.P. Kengne; A. Pillai; L. Billot; B. de Galan; M. Marre; B. Neal; S. Harrap; N. Poulter; A. Patel; *Diabetes Res. Clin. Pract.*, **2010**, *89*, 126-133

15. N. Rojanasthien; T. Autsavakitipong; B. Kumsorn; M. Manorot; S. Teekachunhatean; *ISRN Pharmacol.*, **2012**, *2012*, article ID 375134

16. H. Xu; K.M. Williams; W.S. Liauw; M. Murray; R.O. Day; A.J. McLachlan; *Br. J. Pharmacol.*, **2008**, *153*, 1579-1586

17. T.M.E. Davis; F. Daly; J.P. Walsh; K.F. Ilett; J.P. Beilby; L.J. Dusci; P.H.R. Barrett; *Br. J. Clin. Pharmacol.*, **2000**, *49*, 223-230

18. D.J. Elliot; H.N. Suharjono; B.C. Lewis; E.M.J. Gillam; D.J. Birkett; A.S. Gross; J.O. Miners; *Br. J. Clin. Pharmacol.*, **2007**, *64*, 450-457

19. W. Zeng; Y. Guo; P. Chen; Z. Liu; D. Chen; C. Han; *J. Diabetes Investig.*, **2016**, *7*, 764-768

20. F. Yang; X. Xiong; Y. Liu; H. Zhang; S. Huang; Y. Xiong; X. Hu; C. Xia; *Sci. Rep.*, **2018**, *8*, article number 10994

21. Y. Yao; W.W. Han; Y.H. Zhou; Z.S. Li; Q. Li; X.Y. Chen; D.F. Zhong; *Eur. J. Med. Chem.*, **2009**, *44*, 854-861

22. M. Oroian; A. Marcovici; D.I. Pop; S. Bhardwaj; A. Khuroo; A.-M. Gheldiu; L. Vlase; *Studia UBB Chemia*, **2019**, *LXIV*, 297-308

23. A.-M. Gheldiu; A. Csavdari; M. Achim; L. Vlase; I. Tomuta; D.M. Muntean; *Studia UBB Chemia*, **2017**, *LXII*, 179-188

24. A.-M. Gheldiu; D.M. Muntean; I. Cristea; I. Antonescu; R. Chira; C. Ureche; L. Vlase; *Rev. Chim. (Bucharest)*, **2016**, *67*, 702-705

25. D.I. Pop; A.-M. Gheldiu; M. Oroian; A. Marcovici; S. Bhardwaj; A. Khuroo; R. Kochhar; L. Vlase; *Acta Med. Marisiensis*, **2018**, *64*, 161-168

26. D.I. Pop; M. Oroian; S. Bhardwaj; A. Marcovici; A. Khuroo; R. Kochhar; L. Vlase; *Clin. Pharm. Drug Dev.*, **2019**, *8*, 16-21

27. D.I. Pop; M. Oroian; S. Bhardwaj; A. Marcovici; A. Khuroo; R. Kochhar; L. Vlase; *Farmacia*, **2018**, *66*, 597-601

EFFECT OF *AGARICUS BISPORUS* AND *ORIGANUM MAJORANA L* EXTRACT ON THE SHELF-LIFE AND NUTRITIONAL PROPERTIES OF PORK LIVER PÂTÉ

DORIN TIBULCA[a], MELINDA FOGARASI[a]*, SONIA A. SOCACI[b], SZABOLCS FOGARASI[c], CARMEN POP[b], DAN SALAGEAN[a] , MARIA TOFANĂ[b], DELIA MICHIU[a]

ABSTRACT. The current study aimed to examine the effects of *Agaricus bisporus* and *O. marjorana* extract and their beneficial impact on the shelf-life and nutritional changes occurring in pork liver pâté during storage time. Based on the obtained result, regarding the characterization of *O. marjorana* essential oil (OMEO) and mushroom powder, three types of pork liver pâté were formulated with different proportion of OMEO and mushroom powder and they were sensory evaluated using the 9-point hedonic test. In order to determine the stability during storage time, the selected sample and the control sample were sampled initially, after 30, 60, 90 and 120 days of storage than subjected to physicochemical (protein, fat, moisture, ash, total carbohydrates, and energy) evaluation.

Keywords: Agaricus bisporus, *biochemical changes, essential oil, Origanum majorana L.,* pork liver pâté, *sensory evaluation, volatile profile*

INTRODUCTION

The partial replacement of animal fat by plant extracts is one of the most effective strategies to reduce the saturated fatty acid content of meat products, which has gained importance due to the consumer's concern about

---

[a] *Department of Food Engineering, University of Agricultural Sciences and Veterinary edicine of Cluj-Napoca, Cluj-Napoca, Romania, Calea Mănăştur 3-5, 400372 Cluj-Napoca, Romania*
[b] *Department of Food Science, University of Agricultural Sciences and Veterinary Medicine of Cluj-Napoca, Cluj-Napoca, Romania, Calea Mănăştur 3-5, 400372 Cluj-Napoca, Romania*
[c] *Babeş-Bolyai University, Faculty of Chemistry and Chemical Engineering, Department of Chemical Engineering 11 Arany Janos Str., Cluj-Napoca, RO-400028, Romania*
*Corresponding author: melinda.fogarasi@usamvcluj.ro

DORIN TIBULCA, MELINDA FOGARASI, SONIA A. SOCACI, SZABOLCS FOGARASI, CARMEN POP, DAN SALAGEAN, MARIA TOFANĂ, DELIA MICHIU

the harmful effects of saturated fat [1]. Currently, many consumers demand low-fat foods with healthy ingredients. Some vegetable oils and vegetables are the important source of poly unsaturated faty acids (PUFAs) as well as minor components such as phytosterols and tocopherols. They have been employed as saturated fat replacers in meat products. However, the reduction and substitution of lipids can affect the physicochemical characteristics of high fat foods like sausages, burgers and pâté [2]

Liver pâté is a traditional food manufactured using liver from pig, by-products of pork and other characteristic ingredients. It is consumed all over the world, especially in European countries and is generally considered an added value product with high nutritional and sensory qualities. On the other hand, liver pâté is considered as a high-caloric food product with large amounts of saturated fats. The contribution of this type of fat to the development of cardiovascular diseases, cancer, diabetes and other degenerative diseases, has led to meat industry to seek strategies to reformulate these products with increasing levels of PUFA. A good option could be the replacement of animal fat with vegetable one rich in unsaturated fatty acids [3].

A. bisporus is an edible species that is extensively cultivated throughout Europe and an appreciated nutritional source for humans' diet due to their low caloric intake and their high content in proteins, dietary fibre and phenolic compounds [4]. From the functional perspective, mushrooms are low in fat and cholesterol. The bioactivity exhibited by these compounds is also linked with the presence of phenolic compounds, polyketides, terpenes, steroids, β-carotene, and some vitamins, such as A and C, all of them related with antimicrobial, antiviral, antioxidant or anti-inflammatory activities [5].

A great diversity of species of plants has gained the attention of the food industry as food preservatives. These plants are made up of bioactive compounds that act to protect plants from microbiological attacks, but they have also been exploited and employed by humans as food and medicinal sources for thousands of years. *O. marjorana* essential oil is a unique cooking additive with many additional internal and external benefits. *O. majorana* essential oil possesses antioxidant, antimicrobial, cytotoxic and acetycholinesterase properties, thus providing strong support for their promising candidacy for use as natural agents in various applications, including food preservation, cosmetic preparations, medical or therapeutic products. It also has a positive effect on the nervous system.

Therefore, the aim of this study was to evaluate the effect of *Agaricus bisporus* powder and the essential oil extracts of *O. majorana* on pork liver pâtés by evaluating the physico-chemical and sensory characteristics of the product during the storage time.

RESULTS AND DISCUSSION

1. Chemical composition of *Agaricus bisporus*

We studied the chemical composition of the *Agaricus bisporus cultivated mushroom*, which are most popular and regularly consumed by the population in Romania. The results concerning the nutritional value of the selected mushroom are presented in Table 1. Carbohydrates (55,85 %) were the major constituents, followed by proteins (26,42 %) and ash (8,63 %). Fat contents were low what is understandable because many studies reveal that A. bisporus are regarded as an important dietary supplement for people interested in calorie restriction [4, 6]. The result for this specie is in agreement with the literature [7], and it gave the lowest content in fat, but the highest energetic contribution, due to the highest protein levels. The total fat, protein and ash values obtained for *A. bisporus* in this work, is also in agreement with the values reported by Kalac et al. [8]. Nevertheless, the total fat found in our cultivated mushroom is lower than the values reported for wild edible mushroom in the same species [4]. On the other hand, the protein content in wild edible Agaricus bisporus is more higher than in cultivated Agaricus bisporus. These differences may be attributed to a number of factors that can influence the mushrooms protein contents, namely the type of mushroom, the stage of development, the part sampled, level of nitrogen available and the harvest location.

Table 1. Nutrition value of *Agaricus bisporus* mushroom

	Agaricus bisporus
Fat (g/100 g)	1,98±0,08
Protein (g/100 g)	26,42±0,12
Moisture (g/100 g)	7,12±0,20
Ash (g/100 g)	8,63±0,06
Total carbohydrates (g/100 g)	55,85±0,10
Energy (kcal/100 g)	346,9±0,14

2. Chemical composition of essential oil

The volatile compounds detected by ITEX-GC/MS analysis of the O. marjorana essential oil with their percentage composition are summarized in Table 2.

DORIN TIBULCA, MELINDA FOGARASI, SONIA A. SOCACI, SZABOLCS FOGARASI, CARMEN POP, DAN SALAGEAN, MARIA TOFANĂ, DELIA MICHIU

Table 2. Volatile compounds profile of *O. majorana* essential oil

Compounds	OMEO Conc. (%, of total peaks area)
α-Thujene	0,56
4(10)-Thujene	0,69
α-Pinene	6,7
β-Pinene	0,4
β-Myrcene	1,44
α-Phellandrene	0,36
α-Terpinene	7,12
p-Cymene	2,9
D-Limonene	1,62
β-Phellandrene	1,64
Eucalyptol	0,2
γ-Terpinene	12,03
n.i.	3,97
Terpinolene	2,81
Bicyclo[3.1.0]hexan-2-ol, 2-methyl-5-(1-methylethyl)-, (1.alpha.,2.alpha.,5.alpha.)-	15,06
n.i.	1,63
n.i.	1,02
1-Terpinen-4-ol	27,97
α-Terpineol	4,4
n.i.	0,05
2-Cyclohexen-1-ol, 3-methyl-6-(1-methylethyl)-, trans-	0,5
Carvone	0,06
Linalool acetate	2,25
n.i.	0,11
1-Terpinen-4-ol acetate	0,2
Caryophyllene	2,74
α-Caryophyllene	0,07
n.i.	1,27
n.i.	0,17

OMEO- O. majorana essential oil
n.i. – not identified

The results from the GC–MS analysis of the volatile EO constituents revealed the presence of a total of 29 components, their abundance being expressed as percentage of total peaks area. The most abundant constituents were 1-terpinen-4-ol (27,97%) followed by bicyclo[3.1.0]hexan-2-ol,2-methyl-5-(1-methylethyl)-,(1.alpha.,2.alpha.,5.alpha.) (15,06%) γ-terpinene (12,03%),

α-terpinene (7,12%) and α-pinene (6,7%). 1-Terpinen-4-ol is a characteristic volatile constituent of marjoram leaves that contribute to the fruity, floral, terpenous aroma. These results are in accordance with previous studies reported by Hajlaoui H. that also found 1-terpinen-4-ol (23,2%), and γ-terpinene (10.5%) as the major components of *O. majorana* EO [9].

3. Antibacterial activity of *O. majorana* essential oil

In order to evaluate the antibacterial activity, minimum inhibitory concentration tests of the studied essential oil were performed. According to the results shown in Table 3, minimum inhibitory concentrations values differ significantly.

Table 3. Minimum inhibitory concentrations (MIC) of OMEO

Essential Oil	*E. coli* ATCC 25922	*S. aureus* ATCC 25923	*S. enteritidis* ATCC 13076	*L. monocytogenes* ATCC 19114
	μl/ml			
OMEO	2.45±0,00	5.14±0,00	5.14±0,00	10.80±0,00
Gentamicin	0.05±0,00	0.05±0,00	0.11±0,00	0.11±0,00

The results show that *O. marjorana* has the most bacteriostatic effect against all four of the selected bacteria, considering that it displayed the lowest MIC values. In the case of bacteria S. aureus and S. enteritidis had the same antibacterial activity (5.14 μl/ml). The antibacterial activity of *O. marjorana* was also the most bacteriostatic against E. coli, followed by S. aureus, S. enteritidis and L. monocytogenes. These findings are in agreement with the data reported in the literature regarding the MIC values of *O. marjorana* [9, 10].

4. Sensorial analysis

Sensory science has been recognized as a scientific discipline, and sensory evaluation of meat is used as a component of meat quality, shelf life, and consumer-acceptance studies. It has long been recognized that the sensory attributes of meat are important for consumer acceptability, and by understanding these relationships, the meat industry can improve or decrease variability in specific meat sensory properties and increase consumer satisfaction. The Hedonic testing was used to determine consumer's attitude towards all three liver pâté samples by measuring the degree of acceptance of the new

products. It is very important to note that the organoleptic properties of liver pâté enhanced with mushroom powder and essential oil remained acceptable to consumers and the quality level similar to the current commercially available products. This is also confirmed by the results shown in the Table 4 for sensorial evaluation of liver pâté samples containing different level of mushroom powder and essential oil compared to the control sample (without EOs).

Table 4. Results of sensorial evaluation

Sample	Appearance	Color	Texture	Odor	Taste	Overall acceptability
C.S.	7	8,2	8,5	6,4	7,2	7,4
M1OMEO	7,2	8,5	8	7,4	7	7,6
M2OMEO	8,5	8,4	8,7	8	8,5	8,4

C.S. – control sample, M1OMEO - 15% mushroom powder and 0,02% OMEO and M2OMEO - 25% mushroom powder and 0,01% OMEO

The enriched liver pâté showed significant differences for sensory descriptors compared to the control sample. Moreover, the enriched liver pâtés were characterized by more intense color, odor and taste as the concentration of mushroom power increased.

The *O. majorana* essential oil has given a fresh taste and smell to the product and it reduces the fatty taste of the product. Moreover, the liver pâté with 25% mushroom powder and 0,01% OMEO reached the highest hedonic score, having a mean sensory score for the visual appearance color, odor and taste of 8.4, 8 and 8.5 respectively, as showed in the Table 4.

5. The physicochemical evaluation of the liver pâté

The results of the proximate composition presented in Table 5 shows the moisture, lipid, protein, ash, carbohydrates and energy values of pork liver pâté samples with and without mushroom powder and O. marjorana essential oil in glass containers stored under refrigeration.

In this study the analyzed samples proximate composition showed significant difference between two samples considering that M2OMEO pork liver pâté sample had higher protein and lower lipids content. These differences may be attributed to the replaced of pork subcutaneous fat with mushroom powder.

Table 5. The compositional parameters percentage values
according to the storage time

Sample	Storage time	Fat (%)	Protein (%)	Moisture (%)	Ash (%)	Carbohyd-rates (%)	Energy (kcal)
C.S.	initial state	22,15±0,02	12,59±0,12	58,24±0,24	3,41±0,11	3,61±0,26	264,15±0,17
	30 days	22,18±0,16	12,62±0,41	58,2±0,25	3,42±0,08	3,58±0,10	264,42±0,15
	60 days	22,21±0,14	12,53±0,08	58,27±0,27	3,42±0,35	3,57±0,21	264,29±0,22
	90 days	22,31±0,01	12,49±0,10	58,32±0,31	3,43±0,57	3,45±0,40	264,55±0,11
	120 days	22,39±0,06	12,43±0,36	58,39±0,32	3,43±0,05	3,36±0,18	264,67±0,50
M2OMEO	initial state	17,41±0,04	21,18±0,48	53,80±0,26	3,50±0,20	4,11±0,20	257,85±0,05
	30 days	17,45±0,12	21,22±0,51	53,75±0,32	3,5±0,24	4,08±0,10	258,25±0,42
	60 days	17,48±0,24	21,25±0,54	53,71±0,37	3,51±0,11	4,05±0,47	258,52±0,28
	90 days	17,51±0,31	21,29±0,22	53,68±0,13	3,52±0,10	4,00±0,18	258,75±0,25
	120 days	17,56±0,04	21,34±0,47	53,64±0,30	3,52±0,01	3,94±0,24	259,16±0,10

The use of cold storage had a significant effect on the lipid and protein content, since the lipid and protein content gradually increased with storage time. This increase can be attributed to the reduction of moisture content with storage time. In contrast, the fluctuations in composition in the case of the controil sample can be attributed to protein oxidation. Regarding the packing, Amaral et al. analysed lamb pâté during repining [11] and reported that the polyamide casing system showed lower values of moisture, indicating a greater permeability when compared with glass packing, differing statistically only in the first 15 days of storage. Similar behavior was observed by Amaral et al., the only difference being that they used raw material from another species of animal (sheep, goat) [11, 12].

CONCLUSIONS

The obtained original results proved that *Agaricus bisporus* and *Origanum majorana l.* extract can improve the shelf-life and nutritional properties of pork liver pâté, leading to viable alternative to add value to pork 'variety meat', as well as providing greater profitability. It was found, that the

stability of the product is due to the antimicrobial activity of the OMEO which has not only bacteriostatic effect but contributes to the attractive texture, taste and color of the product together with Agaricus bisporus. As an overall conclusion it can be stated that the liver pâté with 25% mushroom powder and 0,01% OMEO is the best option considering that it reached the highest hedonic score, showed good physicochemical characteristics and did not indicate a possible protein and lipid oxidation, thus did not affect the protein content throughout the storage period.

EXPERIMENTAL SECTION

1. Plant Materials and Essential Oils Extraction

The selected mushroom specie (*Agaricus bisporus*) was purchased from a local producer and the dried marjoram leaves were procured from a company that markets food ingredients (Solina Group, Alba Iulia, Romania). Fresh and cleaned mushrooms were randomly divided and dried using a laboratory plant dryer at 45 °C until reaching a constant mass. Afterwards, the mushroom material was ground into a fine powder using a laboratory mill, mixed to obtain a homogeneous sample, and kept at 4 °C, for further analyses. *O.Marjorana* essential oil (OMEO) was obtained by hydrodistillation using 50 g dried leaves. The extraction was performed for 3 h with 750 mL distilled water in a Clevenger-type apparatus (S.C. Energo-Metr S.R.L., Odorheiu Secuiesc, Romania). The essential oils were dried over anhydrous sodium sulphate and stored at 4°C until analysis.

2. Nutrition value of *Agaricus bisporus*

The chemical composition of *Agaricus bisporus* mushroom, including moisture, ash, total carbohydrates, total energy, crude fat and crude protein, were determined according to AOAC procedures[4]. To obtain the moisture content, sample of the mushroom were dried at 105 °C until constant weight. The ash content was determined by incineration at 600 ± 15 °C for 6 h. The crude protein content of the samples was estimated by the Kjeldahl method. For the calculation of crude protein in mushroom, the nitrogen content was multiplied by a factor of 4.38 [13]. The crude fat content of the samples was determined by extracting a know weight of powdered mushroom sample (3g) with petroleum ether as a solvent, using Soxhlet apparatus [14]. The amount of total carbohydrate was calculated by difference [15]: 100 - (g moisture + g protein + g fat + g ash). The total energy was calculated according to the following equations [15]: energy (kcal) = 4 × (g protein + g carbohydrate) + 9 × (g lipid)

3. ITEX/GC-MS Analysis of Volatile Components

The extraction of volatile oil performed by hydrodistillation using a Clevenger type apparatus according to Socaci et al., 2008 [16]. The extracted essential oil was collected and 1 µL of essential oil solution was used for analysis of volatile compounds on a GCMS QP-2010 (Shimadzu Scientific Instruments, Kyoto, Japan) model gas chromatograph-mass spectrometer. The volatile constituents were separated on a Zebron ZB-5ms capillary column of 30 m × 0.25 mm i.d. × 0.25 µm film thickness. In all determinations, the carrier gas was He, 1 ml/min and the split ratio 1:100. The temperature program used for the column oven was: from 50 ℃ (kept at this temperature for 2 min) to 160 ℃ at 4 ℃/min, then raised to 250 ℃ at 15 ℃/min (kept at this temperature for 10 min). The injector, ion source and interface temperatures were set at 250 ℃ and the MS mode was electron impact (EI) at ionization energy of 70 eV. The scanned mass range was 40–500 m/z. Volatile compounds were tentatively identified using the spectra of reference compounds from NIST27 and NIST147 mass spectra libraries and verified by comparison with retention indices drawn from www.pherobase.com or www.flavornet.org (for columns with a similar stationary phase to the ZB-5ms column). Compounds were considered "tentatively identified" only in the case in which their mass spectra similarity value was above 85%. All peaks found in at least two of the three total ion chromatograms (TIC) were considered when calculating the total area of peaks (100%) and the relative areas of the volatile compounds.

4. Bacterial Strains

The antimicrobial activity of *O. marjorana* essential oil was determined using the methods presented in the scientific literature [17].The following microorganisms were tested: Escherichia coli (ATCC 25922), Staphylococcus aureus (ATCC 25923), Salmonella enteritidis (ATCC 13076) and Listeria monocytogenes (ATCC 19114). All strains were grown into a test tube containing 10 mL sterile nutrient broth (Oxoid Ltd., Basingstoke, Hampshire, England) at 37 ◦C for 24 h in the case of E. coli, S. aureus and S. enteritidis, while L. monocytogenes at 37 ◦C for 30 h. The purity of the inoculums was confirmed by plating on appropriate selective media and microscopic examination of the Gram-stained smear (Optika microscope, B-252, M.A.D. Apparecchiature Scientifiche, Milan, Italy). A loopful of inoculums was transferred by streaking onto a selective medium: TBX for E. coli, BP (baird parker) for S. aureus, XLD agar (Oxoid Ltd., Basingstoke, Hampshire, England) for S. enteritidis and Palcam agar base (Oxoid Ltd., Basingstoke, Hampshire, England) with added Palcam selective supplement for L. monocytogenes. Plates were incubated at 44 ℃ for 24 h E. coli, at 37 ℃ for 24 h in the case of S. Aureus, and

S. enteritidis and at 37 $°$C for 30 h in the case of L. monocytogenes. Bacterial morphology was confirmed by optical microscopy. Several colonies were collected with a sterile inoculating loop, transferred into sterile saline solution (8.5 g L^{-1}), and adjusted to match the turbidity of a McFarland 0.5 standard (1.5×108 $CFUmL^{-1}$) [31]. Then, three serial 10-fold dilutions (107, 106, and 105 CFU mL^{-1}) were prepared using the sterile saline solution as diluent.

5. Manufacture of the pâtés

All pork liver pâtés samples were elaborated in the Experimental Laboratory of Meat Products (pilot scale) of the Faculty of Food Science and Technology, Cluj-Napoca (University of Agricultural Sciences and Veterinary Medicine Cluj-Napoca, Romania). Three batches of liver pâté were prepared by replacing pork with mushroom powder: CS (control sample without addition of mushroom powder and OMEO), M1OMEO (with 15% mushroom powder and 0,02% oMEO) and M2OMEO (with 25% mushroom powder and 0,01% OMEO). An identical formula was used for all the batches, except for the addition of the different antioxidants. The recipes (%) used for the preparation of the control sample were as follows: pork subcutaneous fat (52,5%), broth (the boiling water in which the fat was cooked) (7%), liver (35%), sodium chloride (1,4%), nutmag (0,01%), pepper (0,07%), onion (3%), sugar (1%) and paprika (0,02%). During the manufacturing process the pork subcutaneous fat and liver were cut into cubes of about 15 mm side and scalding at 65$°$C for 60 min. The cooked liver and subcutaneous fat was mixed in the cutter with the other ingredients until a homogeneous raw batter was obtained. For the M1OMEO and M2OMEO samples the corresponding ingredients were added. Finally, the batter was manually distributed into glass flasks until completely full (250 g) and these were then hermetically closed which were subjected to a heat treatment in a stainless steel autoclave. In the core of the pâtés, temperature remained constant at 80 ± 2$°$C for 30 min being monitored with a Cu-Constantan type T thermocouple. Subsequently, the flasks were cooled to room temperature and stored in the dark at 4 ± 1 $°$C for 120 days.

6. Sensory evaluation of liver pâté

Sensory characteristics of pork liver pâté samples were evaluated by a panel of 50 untrained assessors, with a mean age of 20-40, consisted of students and staff members of the department. All samples were coded numerically and supplied in plastic dishes randomly. The 9-point hedonic scale test (1 being "dislike extremely" and 9 being "like extremely") was used to evaluate all liver pâté samples. The main sensory attributes used in the assessment of the samples were appearance, color, texture, odor, taste, and overall acceptability.

7. Physicochemical parameters of pork liver pâté samples

Protein, fat, and moisture content were analysed using the Food ScanTM Lab 78810 (Foss Tecator Co., Ltd., Denmark). Three replicates were run for each sample. The results were expressed as g/100 g sample. The liver pâté samples samples ash content was established by incineration at 600±15 °C. The amount of total carbohydrate resulted as a difference based on the following equation: 100 - (g moisture + g protein + g fat + g ash) [15]. The total energy was calculated using the following equation from the literature: energy (kcal) = 4 × (g protein + g carbohydrate) + 9 × (g lipid) [15].

ACKNOWLEDGEMENTS

REFERENCES

1. R.T. Heck, B.N. Lucas, D. Santos, M.B. Pinton, M.B. Fagundes, M. de Araujo Etchepare, A.J. Cichoski, C.R. de Menezes, J.S. Barin, R. Wagner, P.C.B. Campagnol, *Meat Sci,* **2018**, *146,* 147-153.
2. A.M. Terrasa, M. Dello Staffolo, M.C. Tomás, *LWT - Food Sci and Tech,* **2016**, *66,* 678-684.
3. R. Agregan, D. Franco, J. Carballo, I. Tomasevic, F.J. Barba, B. Gomez, V. Muchenje, J.M. Lorenzo, *Food Res Int,* **2018**, *112,* 400-411.
4. M. Fogarasi, S.A. Socaci, F.V. Dulf, Z.M. Diaconeasa, A.C. Farcas, M. Tofana, C.A. Semeniuc, *Molecules,* **2018**, *23,* 12,
5. M. Ramos, N. Burgos, A. Barnard, G. Evans, J. Preece, M. Graz, A.C. Ruthes, A. Jimenez-Quero, A. Martinez-Abad, F. Vilaplana, L.P. Ngoc, A. Brouwer, B. van der Burg, M. Del Carmen Garrigos, A. Jimenez, *Food Chem,* **2019**, *292,* 176-187.
6. M. Nagy, S. Socaci, M. Tofana, E.S. Biris-Dorhoi, D. ȚIbulcĂ, G. PetruȚ, C.L. Salanta, *Bulletin USAMV. Food Sci and Tech,* **2017**, *74,* 1, 1.
7. N. CHERNO, S. OSOLINA, A. NIKITINA, *Food and Envi Saf journal,* **2013**, *XII,,* 4, 291 - 299.
8. P. Kalač, *Food Chemistry,* **2009**, *113,* 1, 9-16.

9. H. Hajlaoui, H. Mighri, M. Aouni, N. Gharsallah, A. Kadri, *Microbial pathogenesis,* **2016**, *95,* 86-94.
10. J.d.L. Marques, L.M. Volcão, G.D. Funck, I.S. Kroning, W.P. da Silva, Â.M. Fiorentini, G.A. Ribeiro, *Industrial Crops and Products,* **2015**, *77,* 444-450.
11. D.S. Amaral, F.A.P. Silva, T.K.A. Bezerra, N.M.O. Arcanjo, I.C.D. Guerra, P.S. Dalmás, M.S. Madruga, *Food Pack and Shelf Life,* **2015**, *3,* 39-46.
12. D. Amaral, F.A.P.d. Silva, T.K.A. Bezerra, I.C.D. Guerra, P.S. Dalmás, K.M.L. Pimentel, M.S. Madruga, *Semina: Ciências Agrárias,* **2013**, *34,* 4,
13. A. Mocan, A. Fernandes, L. Barros, G. Crisan, M. Smiljkovic, M. Sokovic, I. Ferreira, *Food & function,* **2018**, *9,* 1, 160-170.
14. M. Nagy, C. Mureşan, S.A. Socaci, M. Tofană, A. Fărcaș, S.E. Biriş, *Bulletin USAMV Food Sci and Tech,* **2015**, *72, 2,*
15. M. Obodai, I.C. Ferreira, A. Fernandes, L. Barros, D.L. Mensah, M. Dzomeku, A.F. Urben, J. Prempeh, R.K. Takli, *Molecules,* **2014**, *19,* 12, 19532-19548.
16. Sonia A. Socaci, Maria Tofană, C. Socaciu, *Bulletin UASVM, Agriculture,* **2008**, *65, 2,*
17. M. Fogarasi, S.A. Socaci, S. Fogarasi, M. Jimborean, C. Pop, M. Tofană, A. Rotar, D. Tibulca, D. Salagean, L. Salanta, *Studia UBB Chemia,* **2019**, *64,* 2 T2, 527-537.

EPR FINGERPRINTING AND ANTIOXIDANT RESPONSE OF FOUR SELECTED *PLANTAGO* SPECIES

ANCA D. FARCAȘ[a,b], CEZARA ZĂGREAN-TUZA[c], LAURIAN VLASE[d], ANA-MARIA GHELDIU[d], MARCEL PÂRVU[a], AUGUSTIN C. MOȚ[c,b]*

ABSTRACT. In this study we compare the phytochemical composition and antioxidant properties of four *Plantago* species (*P. cornuti, P. lanceolata, P. major* and *P. media*), in terms of radical scavenging ability and their reductive properties in corroboration with EPR spectroscopy profiling. We found that *Plantago* extracts possess very low prooxidant activity while being efficient radical scavengers and electron donors. *P. media* showed the strongest antioxidant activity from the four species investigated. The relative composition derived from the EPR spectra of the studied extracts was compared to the phytochemical composition determined by HPLC-MS analysis. Downhill Simplex algorithm simulation of EPR experimental signals revealed that all four *Plantago* extracts display luteolin and chlorogenic acid profiles, as well as quercetin glycosides, especially rutin. EPR spectroscopy appears to be a useful tool for discrimination of radical-based complex mixture, rendering it as an alternative method for predicting chemical behaviour, regardless of synergistic or antagonistic effects.

Keywords: Plantago, Antioxidants, EPR fingerprinting

INTRODUCTION

A genus comprising more than 200 species, *Plantago* herbs are known throughout the world as medicinal plants[1]. Known for their effects since Antiquity, aerial parts of these plants are still used as natural remedies

---

[a] *Babeş-Bolyai University, Faculty of Biology and Geology, Cluj-Napoca 400028, Romania*
[b] *National Institute for Research and Development of Isotopic and Molecular Technologies, Cluj-Napoca 400293, Romania*
[c] *Babeş-Bolyai University, Faculty of Chemistry and Chemical Engineering, Cluj-Napoca 400028, Romania*
[d] *Iuliu Haţieganu University of Pharmacy and Medicine, Faculty of Pharmacy, Cluj-Napoca 400012, Romania*
* *Corresponding author: augustinmot@chem.ubbcluj.ro*

for several diseases, including inflammation, skin, respiratory, digestive and reproductive organs issues, as well as cancer [1-4]. Nowadays, there is an upsurge of interest in the therapeutic potential of medicinal plants, mostly because of their effectiveness in prevention, as well as for their low toxicity, which triggers less side effects as compared to the synthetic conventional remedies. In many countries, *Plantago* herbs, especially *P. lanceolata*, are also appreciated for their nutritional values in both humans and animals [5], [6].

The most renowned *Plantago* species still used in modern medicine are *P. major*, *P. lanceolata*, *P. media*, *P. indica*, *P. ovata*, *P. asiatica* and *P. sempervirens* [11]. Among others, a widely used therapeutic perspective is the antioxidant nature of the medication which helps in prevention, neutralization of harmful reactive species and maintainance of a normal redox balance of the cells. The antioxidants are chemical compounds known to have the ability of scavenging reactive oxygen or nitrogen species [12]. Many *Plantago* species have been investigated for their antioxidant capacity [2,3,6,13] by employing various assays, both *in vitro* and *in vivo*. Thereby, there is a particular interest in the study of new sources of natural antioxidants, which have less side effects compared to classic drugs and could be used to prevent and to treat a large spectrum of disorders.

We have explored in a previous study [14] the phytochemical composition, antioxidant and anti-inflammatory effects of *P. sempervirens* Crantz. Following this, we decided to survey the phytochemical potential of other *Plantago* species mentioned above. Therefore, our paper aims at making a general *in vitro* investigation of four *Plantago* species (*P. cornuti, P. lanceolata*, *P. major* and *P. media*), determining their antioxidant and pro-oxidant activity and highlighting their major phytochemical constituents, with a strong focus on an EPR spectroscopy method, which enables a degree of fast fingerprinting.

RESULTS AND DISCUSSION

Polyphenolic profile of the four *Plantago* samples (*P. cornuti, P. lanceolata, P. major* and *P. media*) follows a common composition, but each extract distinguishes itself by different amounts of polyphenols (Table 1). The basic phytochemical profile for all four species was made from luteolin and apigenin; regarding luteolin, by far *P. lanceolata* extract holds the highest amount as compared to the other *Plantago* counterparts. The highest concentration of chlorogenic acid was found in *P. lanceolata* and *P. media*.
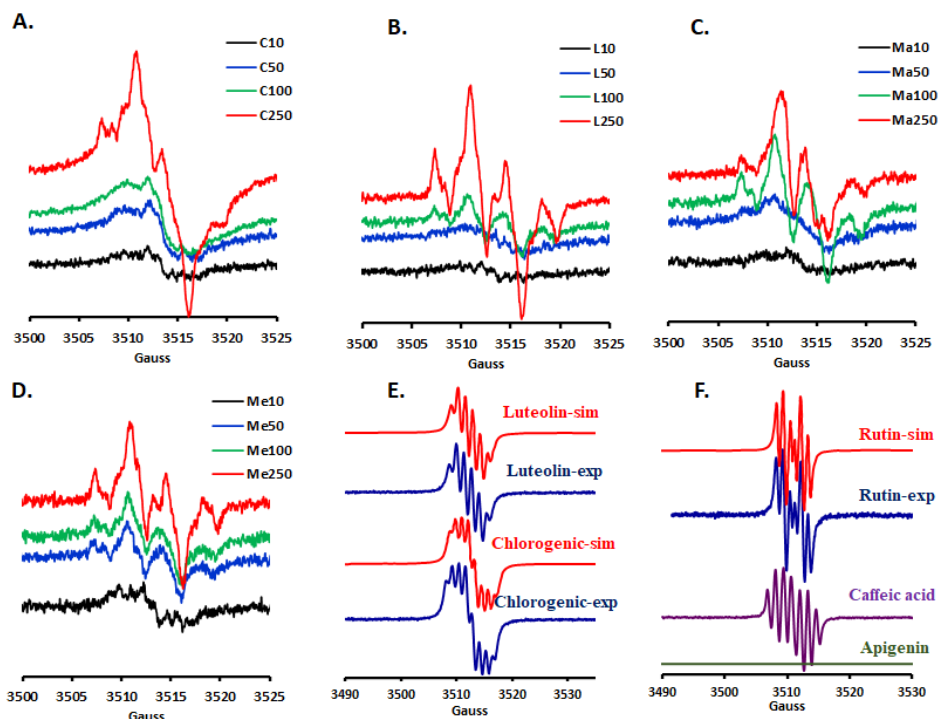
Increasing the plant extracts pH with basic reagents like sodium hydroxide gives rise to EPR signals due to oxidation of secondary metabolites, mainly polyphenols, in the presence of molecular oxygen. In this way, flavonoids and phenolic acids are prone to transformation into reactive anionic radicals exhibiting specific EPR features due to their distinct hyperfine coupling of protons in the vicinity of the unpaired electron. However, not every phytoconstituent can be converted into an anionic radical; in fact, there are some structural features that give rise to a relatively stable intermediate such as extensive conjugation, presence of a phenyl substituent as the center for radical formation and hydroxyl groups in key position [15]. Also, the reactivity of these intermediates varies greatly, thus affecting their half-life.

Table 1. The polyphenolic composition in the studied species (ug/g plant material)

Polyphenolic compounds	*P. cornuti*	*P. lanceolata*	*P. major*	*P. media*
Gentisic acid	<0.2	<0.2	<0.2	<0.2
Caffeic acid	<0.2	<0.2	<0.2	<0.2
Chlorogenic acid	<0.2	8.253	<0.2	1.836
p-**cumaric acid**	<0.2	<0.2	<0.2	0.501
Ferulic acid	<0.2	<0.2	<0.2	<0.2
Rutin	<0.2	8.253	<0.2	<0.2
Luteolin	6.487	23.214	1.021	0.951
Apigenin	0.383	0.677	1.755	0.285
Quercitrin	<0.2	<0.2	<0.2	<0.2

The EPR profiles of the studied extracts at four different concentrations are presented in Figure 1. The EPR spectrum at the highest dilution, corresponding to each *Plantago* extract was simulated using HPLC identified components: luteolin, chlorogenic acid and an rutin. Apigenin exhibits no EPR spectrum in our conditions, indicating a higher redox potential or a low stability of the generated radicals in basic medium.

ANCA D. FARCAȘ, CEZARA ZĂGREAN-TUZA, LAURIAN VLASE, ANA-MARIA GHELDIU,
MARCEL PÂRVU, AUGUSTIN C. MOȚ

Figure 1. EPR spectra profiles for the four extracts of *Plantago*. (A) *P. cornuti*, (B) *P. lanceolata*, (C) *P. major*, (D) *P. media*, using different dilutions in 75% ethanol (10x, 50x, 100x and 250x times). EPR spectra of luteolin, chlorogenic acid and rutin, experimental and simulated and experimental EPR spectra of caffeic acid and apigenin, measured in the same conditions as extracts (E, F).

The entry parameters for all three components were those previously optimized for the pure standard; for each signal, optimization occurred *via* Downhill Simplex algorithm, thus determining the relative contribution for each component. The results are presented in Table 2; the simulated and their corresponding experimental spectra are depicted in Figure 2. All simulations exhibited correlation coefficients with experimental signal higher than 0.98.

Table 2. EPR signal contribution for main phytochemical components
in the four *Plantago* extracts

| Simulated EPR signal	*P. cornuti*	*P. lanceolata*	*P. major*	*P. media*
Luteolin	53.9%	37.2%	33.2%	50.8%
Chlorogenic acid	22.9%	26.3%	21.7%	31.9%
Rutin	23.2%	36.5%	45.1%	17.3%
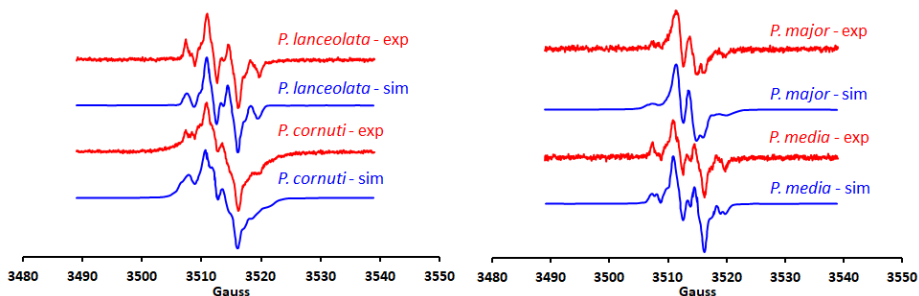
Figure 2. Experimental (exp) and simulated (sim) EPR spectra profiles
for the four studied extracts of *Plantago.*

Each of standards determined using HPLC analysis was simulated separately, considering possible hyperfine couplings with neighbouring protons: luteolin radical lone electron interacts with four different protons, whereas chlorogenic acid possesses five distinct protons that are coupled with the single electron. The third EPR standard considered was rutin, as HPLC results pointed out. At a glance, it is obvious that the width and signal shape is influenced by chlorogenic acid, whilst the hyperfine splitting are due to luteolin and rutin.

The EPR contribution for each component was in accord with the HPLC results. Regardless of HPLC detected concentration magnitude in each extract, luteolin displayed a notable contribution in the EPR spectrum. It is interesting to note that *P. lanceolata* did not exhibit the highest luteolin simulated contribution, despite the fact that HPLC analysis pointed out to the highest concentration of this flavonoid; a possible explanation for this observation can be the existence of antagonistic effects that arise due to the phytochemical complexity of the extract, which can alter the signal shape as well as the semiquinone radical half-life. When it comes to chlorogenic acid, the second simulated standard, all extracts display a relatively similar EPR contribution, mostly according to HPLC results. Interestingly, *P. cornuti* and *P. major* do not exhibit detectable levels of this phenolic acid in HPLC. This can be explained by the fact that some compounds have strong EPR fingerprints that can be seen even in much lower concentrations. As for rutin, the variation in area value is great. *P. major* followed by *P. lanceolata* have the strongest resemblance to rutin signal shape; indeed, HPLC analysis pointed to detectable levels of rutin in the latter. Still, the third component of the simulated signals might be due not only rutin, but also to other quercetin derivatives like quercitrin and isoquercitrin. Indeed, all four signal are mainly similar in appearance to luteolin and chlorogenic acid spectra, whereas additional hyperfine features may arise from rutin and other quercetin glycosides.

ANCA D. FARCAȘ, CEZARA ZĂGREAN-TUZA, LAURIAN VLASE, ANA-MARIA GHELDIU,
MARCEL PÂRVU, AUGUSTIN C. MOȚ

The antioxidant properties of polyphenolic compounds still represent a topic of scientific interest, due to phytoconstituents potential as alternative treatments or food supplements [16]. A first line of assessments used to test the protective potential of ethanolic extracts was made in terms of *in vitro* antioxidant activity. Artificial free radicals such as DPPH and ABTS can be used as targets for antioxidant routine tests, whereas Folin-Ciocâlteu method quantifies the total phenolic content, indirectly related to free radical quenching ability. Figure 3 (A, B and C) depicts a comparative antioxidant analysis of the four tested extracts; *P. media* showed a significant higher antioxidant activity as compared to its *Plantago* counterparts.
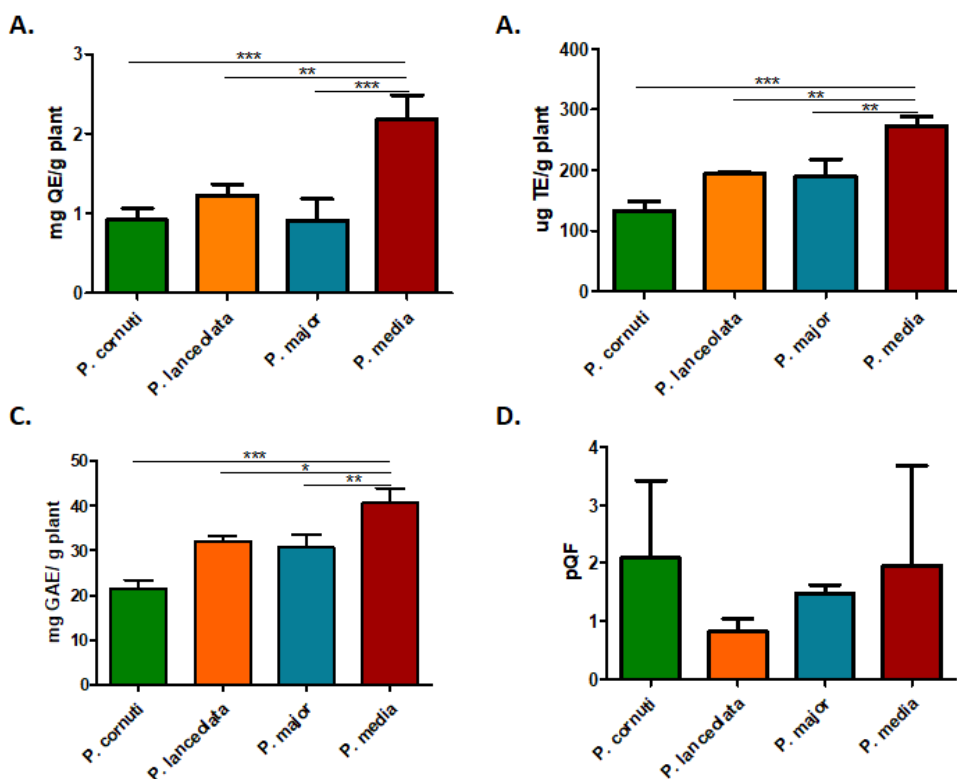
Figure 3. Antioxidant activity of the four studied extracts of *Plantago* as determined using DPPH bleaching assay (A), ABTS scavenging method (B), total phenolic content using Folin-Ciocâlteau assay (C) and the pro-oxidant enzymatic method (D). Statistical comparison using ANOVA test: ***Significant at p<0.001 as compared to *P. cornuti*, *P. lanceolata*, *P. major* and *P. media*, ##Significant at p<0.01 as compared to *P. cornuti*. Values are the mean ± SD (n = 3).

The TEAC results correlate well with the DPPH values; *P. media* once again ranks first (p<0.001) as compared to its *Plantago* counterparts. Regarding Folin-Ciocâlteu (FC) assay, *P. media* expressed significant reduction ability (40.65±1.85 mg GAE/g, p<0.01) as opposed to *P. cornuti*, *P. lanceolata* and *P. major*. Therefore, three different assays designate *P. media* as displaying the strongest antioxidant potential within the four species we have investigated. None of the four hydroalcoholic extracts exhibited significant pro-oxidant activity, as seen in Figure 3D. Such information might lead to further investigations regarding the beneficial effects of the *Plantago* extracts.

Many herbs have been found to possess antioxidant properties, which should therefore minimise redox imbalances or counteract the effects of free radicals. It is well known that antioxidants could scavenge reactive species (ROS/NOS) [5]. A strong antioxidant activity was yielded by *P. media* against DPPH and ABTS radicals, whereas use of Folin-Ciocâlteu reagent underlined a high concentration of reductive species. These results are in a reasonable agreement with the quantitative chromatographic analysis, due to higher amounts of polyphenols found in this extract. There have been many papers regarding *Plantago* species, starting with phytochemical analysis and other biological activities [5,8,13,17-22]. In addition, the antioxidant function derived from *in vitro* assays confirms the high potential of *P. media* extract and supports its further use in more complex tests. There were considerable variations between the samples from the perspective of antioxidant and chromatographic methods employed in this preliminary work. Previous studies discussed the antioxidant activity and polyphenolic content in *P. lanceolata*, *P. cornuti* and *P. major* [3,4,6,12,23,24], without *P. media*. It is noteworthy that there are a few remarks concerning *P. major* and its antioxidant potential which is not exactly proper for therapeutic purposes since the free radical generation does not resemble the physiological conditions [23]. Depending on the pH of the environment, dose and enzymatic interactions, polyphenolic compounds can behave as antioxidants or can display pro-oxidant properties [26,30]. Therefore, a strong antioxidant activity can operate in two different ways: antioxidant or pro-oxidant. Considering this, antioxidant/pro-oxidant balance represents a key factor for an efficient natural therapy, which could be elucidated by continuing research in a multiple dimension, such as *in vitro* or *in vivo* studies. Studies conducted on model biosystems, such as laboratory animals, offer the possibility of investigating the antioxidant/pro-oxidant properties of plant extracts rich in polyphenolic compounds and of tracking the physiological effects in various experimental patterns of oxidative stress.

CONCLUSIONS

The antioxidant potential and the pro-oxidant reactivity of the four *Plantago* extracts (*P.cornuti*, *P. lanceolata*, *P.major* and *P. media*) were investigated using radical scavenging assay and, hemoglobin-oxidation, respectively in presence of laccase. No significant pro-oxidant activity was found by this enzymatic assay. Follow up the EPR fingerprintion in alkali medium, all *Plantago* extracts are dominated by luteolin and chlorogenic acid, as well as rutin. The signals might comprise other phytochemical fingerprints that, due to smaller concentration or shorter half-life, could have not been detected through this method. Sinergistic and antagonistic effects should be taken into consideration as far as they can give rise to higher reactivity and, as a result, a shorter radical lifespan. Thus, EPR spectroscopy in combination with a simulating tool software such as WinSim can offer a sneak peek into plant extracts relative composition. The highest antioxidant activity was attributed to *P. media* extract, thus nominating it as a strong candidate for further *in vitro* and *in vivo* tests.

EXPERIMENTAL SECTION

Plant material and extracts preparation

The leaves of *P. cornuti*, *P. lanceolata*, *P. major* and *P. media* were collected from the Botanical Garden "Alexandru Borza" from Cluj-Napoca, Romania in September 2015 and were identified at the Herbarium of the Botanical Garden, where a voucher specimen was deposited for each plant (*P. cornuti*- CL663371, *P. lanceolata*- CL663372, *P. major*- CL663369, *P. media*- CL663370). The *Plantago* extracts were prepared by the percolation method at room temperature for three days by using small fragments (0.5-1 cm) of fresh leaves and 70% ethanol. The fluid extract of *Plantago* contained 35% ethanol and was: 1:1.4 for *P. cornuti*; 1:1.7 for *P. lanceolata*; 1:1.3 for *P. major* and *P. media* [27].

Chemicals

Folin-Ciocâlteu reagent, DPPH (di(phenyl)-(2,4,6-trinitrophenyl) iminoazanium), ABTS (2,2'-azino-bis(3-ethylbenzothiazoline-6-sulfonic acid)), N-(1-naphtyl)ethilenediaminedihidrochloride, sulphuric acid, hydrochloride acid, glycerol, trolox (6-hydroxy-2,5,7,8-tetrametyl-croman-2-carboxylic acid) were obtained from several companies (Sigma, Fluka, Merck). Standards: rutin, kaempferol, chlorogenic acid were purchased from Sigma, Germany. Ferulic acid, galic acid, luteolin and quercetin were obtained from Roth, Germany. All other chemicals and solvents used in the study were of analytical grade.

HPLC-MS analysis

The phytochemical analysis was carried out using an Agilent Technologies 1100 HPLC Series system (Agilent, Santa Clara, CA, USA) assisted by mass spectrometry, an Agilent 1100 Ion Trap SL (LC/MSD Ion Trap VL) equipped with an electrospray or ACPI ion source. For the separation, a reverse-phase analytical column was employed (Zorbax SB-C18 100x3.0 mm i.d., 3.5 µM particle). All chromatographic operations were carried out at 48°C. The compounds were detected with both UV (330 nm) source and in MS mode (electrospray ion source in negative mode). The chromatographic data were processed using a software from Agilent, ChemStation and DataAnalysis. The mobile phase was made up of methanol and acetic acid 0,1% (*v/v*). The flow rate was 1 mL/min and injection volume was 5 µL. Based on the chromatographic conditions described above and preliminary experiments, the compounds eluted in less than 40 minutes. There were a few compounds that were not quantified due to overlapping (gentisic acid and caffeic acid), but they were identified using MS detection. The limit of quantification was around 0.5 µg/mL. We also performed quantitative determination, using external standard method. The calibration curves (0.5-50 µg/mL) range with $R^2 > 0.999$ and detection limits between 17-90 ng/mL. All reagents were of analytical grade purity.

EPR Measurements

The protocol for the Electron Paramagnetic Resonance (EPR)-based investigation is fully described elsewhere [28]. All measurements have been performed using an ELEXSYS 580 X- band EPR spectrometer. The simulation of EPR spectra has been carried using WinSim 2002 software [29] on the signal with the highest resolution from all four dilutions, namely diluted 250 times. The standards chosen for comparison are luteolin and chlorogenic acid, along with rutin. Each EPR signal of the employed standards was simulated separately, then optimized by use of Downhill Simplex algorithm.

Pro-oxidant activity assays

The prooxidant reactivity of the extract was evaluated using a previously developed method that is described in detail elsewhere [30]. Briefly, the extract is treated with catalytic amount of laccase that generates radicals from the components of the extract which are responsible of oxidation of the ferrous oxy hemoglobin (oxyHb) into the oxidized form (metHb) which is unable to transport molecular oxygen. The kinetic profile and the rate of the oxyHb oxidation is a marker for the reactivity of the generated radicals and it is expressed as relative quercetin prooxidant factor using a quercetin standard (pQF).

ANCA D. FARCAȘ, CEZARA ZĂGREAN-TUZA, LAURIAN VLASE, ANA-MARIA GHELDIU, MARCEL PÂRVU, AUGUSTIN C. MOȚ

Antioxidant activity assays and total phenolic determination
DPPH bleaching assay

The DPPH solution (900 µM) was prepared in ethanol and 111 µL was added alongside with 50 µL of *Plantago* extract. The final volume (1 mL) was adjusted with a solution made of ethanol and water (1:1). The bleaching of DPPH was examined after 40 minutes incubation at 517 nm, using a UV-vis spectrophotometer (Varian, Cary 50) and expressed in quercetin equivalents using a quercetin-based calibration curve (n=6, R=0.999) [31]. The measurements were carried out in triplicates.

Trolox equivalent antioxidant capacity (TEAC) assay

In a quartz cuvette, 100 µL of ABTS radical were added along with 10 mM sodium acetate buffer pH 5.5 and 50 µL 10 times diluted *Plantago* sample. The final volume was 1mL. The decreasing ABTS absorbance was monitored for 15 minutes at 420 nm, using a UV-vis spectrophotometer (Varian, Cary 50). The measurements were done in triplicates. The results were expressed as trolox equivalent (TE) *via* a calibration curve (n=6, R=0.999) using trolox standard solutions.

Determination of total polyphenols content (GAE) of the extract

Total polyphenols content of the *Plantago* extracts was determined using Folin-Ciocâlteu method [28]. The extract was diluted 10 times and 10 µL diluted solution was mixed with 790 µL of ultrapure water, 50 µL of Folin-Ciocalteu reagent and 150 µL of 20% sodium carbonate. The final concentration of the plant extract in the assayed solution was 0.01 mg/mL. The measurements were done in triplicates, both for the samples and for the standards. Gallic acid (21 mg/mL) was used as standard stock solution for calibration curve. Standards from 0.5 to 30 mg/L were prepared and treated along with the samples, then incubated for 30 minutes in the dark. The solutions turned blue and the absorbance was recorded at 750 nm, using a UV-vis spectrophotometer (Varian, Cary 50). For each sample, the level of phenolics were determined in terms of gallic acid equivalents (GAE).

Statistical analysis

All data are reported as the mean ± SD. The Gaussian distribution was checked by the Shapiro-Wilk normality test. One-way analysis of variance ANOVA, followed by Bonferroni's Multiple Comparison test procedure was performed. Statistical significance was at $p < 0.05$. Statistical values were obtained using Statistica 12.

ACKNOWLEDGMENTS

REFERENCES

1. A.B. Samuelsen; *J. Ethnopharmacol.,* **2000**, *71*,1–21.
2. M. Nikolova; L. Evstatieva; D. Nguyen; *Garden*, **2011**, *35*, 43–48.
3. T. Janković; G. Zdunic; I. Beara; K. Balog; D. Pljevljakusic; D. Stesevic; K. Savikin; *Biochem. Syst. Ecol.*, **2012**, *42*, 69–74.
4. I. Stanisavljevic; S. Stojicevic; D. Velickovic; M. Lazic; V. Veljkovic; *Sep. Sci. Technol.*, **2008***, 43*, 3652–3662.
5. S. Gonçalves; A. Romano; *Ind. Crops Prod.*, **2016**, *83*, 213–226.
6. M. Gálvez; C. Martín-Cordero; P.J. Houghton; M.J. Ayuso; *J. Agric. Food Chem.*, **2005**, *53,* 1927–1933.
7. N. Ronsted; E. Gobel; H. Franzyk; S.R. Jensen; C.E. Olsen; *Phytochemistry*, **2000**, *55*, 337-348.
8. M. Zubair; A. Ekholm; H. Nybom; S. Renvert; C. Widen; K. Rumpunen; *J. Ethnopharmacol.*, **2012**, *141*, 825–830.
9. P. Lukova; I. Dimitrova-Dyulgerova; D. Karcheva-Bahchevanska; R. Mladenov; I. Iliev; M. Nikolova; *Int. J. Med. Res. Pharm. Sci.,* **2017**, *4*, 20–26.
10. W. Reardon; D.A. Fitzpatrick; M.A. Fares; J.M. Nugent; *Plant Mol. Biol.,* **2009**, *71*, 241–250.
11. I.N. Beara; M.M. Lesjak; E.D. Jovin; K.J. Balog; G.T. Anackov; D.Z. Orcic; N.M. Mimica-Dukic; *J. Agric. Food Chem.***, 2009**, *57*, 9268–9273.
12. F. Pourmorad, S.J. Hosseinimehr; N. Shahabimajd; *African J. Biotechnol.*, **2006**, *5*, 1142–1145.
13. I.N. Beara; M.M. Lesjak; D.Z. Orcic; N.D. Simin; D.D. Cetojevic-Simin; B.N. Bozin; N.M. Mimica-Dukic; *LWT - Food Sci. Technol.,* **2012**, *47*, 64–70.
14. A. D. Farcaș; A.C. Moț; A.E. Pârvu; V.A. Toma; M.A. Popa; M.C. Mihai; B. Sevastre; I. Roman; L. Vlase; M. Pârvu; *Oxid. Med. Cell. Longev.* **2019**, *2019*, 1-13.
15. S. Fiorucci; J. Golebiowski; D. Cabrol-Bass; S. Antonczak; *J. Agric. Food. Chem.*, **2007**, *55(3)*, 903.
16. J. B. Silva; R.F. Mendes; V. Tomasco; N.C.C. Pinto; L.G. deOliveira; M.N. Rodrigues; D.M.O. Aragao; J.A.K. Aguiar; M.S. Alves; M.C.N.M. Castagnon; A. Ribeiro; E. Scio; *J. Ethnopharmacol.*, **2017**, *198*, 399-406.
17. A. Venditti; *Nat. Prod. Res.*, **2011**, *26(21)*, 2035-2039.

18. E. Reina; N. Al-Shibani; E. Allam; K.S. Gregson; M. Kowolik; L.J. Windsor; *J. Tradit. Complement. Med.,* **2013**, *3*, 268–272.
19. E.F. Al-Jumaily; H.A. Abdul-Ratha; R.H. Raheema; *DAMA Int.,* **2012**, *1*, 17–21.
20. H. Ravn; L. Brimer; *Phytochemistry,* **1988**, *27*, 3433–3437.
21. H. Fleer; E.J. Verspohl; *Phytomedicine,* **2007**, *14*, 409–415.
22. J.L. Hu; S.P. Nie; F.F. Min; M.Y. Xie; *J. Agric. Food Chem.,* **2012**, *60*, 11525–11532.
23. J.C. Mello; M.V.D. Gonzalez; V.W.R. Moraes; T. Prieto; O.R. Nascimento; T. Rodrigues; *Molecules*, **2015**, *20(10)*,17747–17759.
24. R. Taskova; N. Handjieva; L. Evstatieva; S. Popov; *Phytochemistry,* **1992**, *52*, 1443–1445.
25. A.D. Farcaș; A.C. Moț; C. Zăgrean-Tuza; V.A. Toma; C. Cimpoiu; A. Hosu; M. Pârvu; I. Roman; R. Silaghi-Dumitrescu; *PLoS ONE*, **2018**, 13(7):e0200022.
26. D. Procházková; I. Boušová; N. Wilhelmová; *Fitoterapia*, **2011**, *82*, 513–23
27. M. Pârvu; O. Roșca-Casian; M. Pușcaș, G. Groza; *Contribuții bot.*, **2009**, *44*, 125–129.
28. A.C. Moț; G. Damian; C. Sârbu; R. Silaghi-Dumitrescu; *Redox. Rep.*, **2009**, *14*, 267–74.
29. D.R. Duling, *J. Magn. Reson. B*; **1994**, *104*, 105–10.
30. A.C. Moț; C. Coman; C. Miron; G. Damian, C. Sârbu, R. Silaghi-Dumitrescu; *Food Chem.,* **2014**, *143*, 214–22.
31. A. Karadag; B. Ozcelik; S. Saner; *Food Anal. Methods*, **2009**, *2*, 41–60.

HIGH-TEMPERATURE SOLID-STATE SYNTHESIS OF Mg-DOPED ZrO₂: STRUCTURAL, OPTICAL AND MORPHOLOGICAL CHARACTERIZATION

**ANTONELA BERAR[a], MARIETA MUREȘAN-POP[b],
LUCIAN BARBU-TUDORAN[c,d], RÉKA BARABÁS[e,*], LILIANA BIZO[f,*]**

ABSTRACT. 15 at% Mg-doped ZrO_2 ceramic material was synthesized by solid-state reaction at 1600 ºC. Particle size analysis of raw materials mixture depicts the formation of a narrow particle size distribution (PSD) with a mean particle size of about 56 nm. The structural analysis confirms that the as-synthesized Mg-doped ZrO_2 product is of pure tetragonal phase (*t*-ZrO_2) with a crystallite size of 55.76 nm. The UV–VIS diffuse reflectance spectrum (DRS) showed a maximum %R at 550 nm and the estimated optical bandgap was about 3.83 eV. The morphology of the sample examined by scanning electron microscopy (SEM) shows interconnected grains in the sintered ceramics. Moreover, EDX analyses confirm the presence of Mg, Zr, and O, with a homogenous distribution throughout the sample.

Keywords: *Mg-doped ZrO_2, solid-state reactions, XRPD, UV-VIS spectroscopy, SEM/EDX*

INTRODUCTION

There is increasing interest in zirconia ceramics known as important candidates for functional and structural applications due to their properties which

---

[a] *"Iuliu Hațieganu" University of Medicine and Pharmacy, Faculty of Dentistry, Department of Prosthetic Dentistry and Dental Materials, 32 Clinicilor str., RO-400006, Cluj-Napoca, Romania*
[b] *Babes-Bolyai University, Interdisciplinary Research Institute on Bio-Nano-Sciences, 42 Treboniu Laurian str., RO-400271, Cluj-Napoca, Romania*
[c] *Babeş-Bolyai University, Faculty of Biology and Geology, Department of Molecular Biology and Biotechnology, 1 Mihail Kogălniceanu str., RO-400084, Cluj-Napoca, Romania*
[d] *National Institute for Research and Development of Isotopic and Molecular Technologies, 67-103 Donath Street, RO-400293, Cluj-Napoca, Romania*
[e] *Babeş-Bolyai University, Faculty of Chemistry and Chemical Engineering, Department of Chemistry and Chemical Engineering of Hungarian Line of Study, 11 Arany Janos str., RO-400028, Cluj-Napoca, Romania*
[f] *Babeş-Bolyai University, Faculty of Chemistry and Chemical Engineering, Department of Chemical Engineering, 11 Arany Janos str., RO-400028, Cluj-Napoca, Romania*
Corresponding authors: breka@chem.ubbcluj.ro, lbizo@chem.ubbcluj.ro

ANTONELA BERAR, MARIETA MUREȘAN-POP, LUCIAN BARBU-TUDORAN,
RÉKA BARABÁS, LILIANA BIZO

are different and considerably improved compared with conventional ceramics. Due to its properties as excellent chemical and thermal stability, good mechanical strength, high ionic conductivity, low thermal conductivity at high temperature, high porosity and large surface area, they have been used for a wide range of industrial applications such as sensors, microelectronic devices, refractory materials, fuel cells, catalyst or catalyst support, solid-state electrolytes, thermal barrier coatings, electro-optical materials and biomaterials [1-8].

Nowadays, different types of zirconia ceramics are used for several medical applications, in replacing hard tissue due to its properties to emphasis the mechanical stability and biocompatibility [9-11]. It is widely used in medicine for replacement of the bone (hip prosthesis) but also in dentistry [12-14]. In the prosthetics domain, zirconia ceramics are used especially for fabrication of veneers, full and partial crowns, fixed partial dentures, posts and/or cores, implant abutments [15-16].

It is well known that the physical properties of ZrO_2 are strongly influenced by its crystal structure. Three different forms of ZrO_2 have been recognized, depending upon the growth temperature. The monoclinic phase (m-ZrO_2) exists at low temperatures below 1150 ºC and is a thermodynamically stable phase, the tetragonal phase (t-ZrO_2) exists at intermediate temperatures within the range of 1150–2370 °C, and cubic (c-ZrO_2) which exists at very high temperatures greater than 2370 °C [17]. The transformation from the t-ZrO_2 to the m-ZrO_2, which is more stable, is associated with a volume increase of 3%-5%. Stresses generated by this expansion originate cracks in pure zirconia ceramics that, after sintering at temperatures in the range of 1500 ºC -1750 ºC break into pieces at room temperature. These crystal phases strongly depend on the thermal condition and preparation method [18]. To stabilize the t-ZrO_2 phase at room temperature, zirconia can be mixed with other metallic oxides, e.g. CaO, MgO, CeO_2, La_2O_3, Y_2O_3, etc. The addition of these oxides to pure zirconia allows to generate multiphase materials known as partially stabilized zirconia (PSZ) whose microstructure at room temperature generally consists of cubic zirconia as the major phase, with monoclinic and tetragonal zirconia precipitates as the minor phase [19-20]. The well-known system ZrO_2-Y_2O_3 (yttria-stabilized zirconia, YSZ) has been extensively studied due to its excellent properties which make this material of special scientific and industrial interest. However, YSZ is expensive as compared with CaO- or MgO-based zirconia systems. Also, magnesia is found to be an effective dopant for stabilizing zirconia [21].

In the present paper, the facile preparation of 15 at% MgO-doped ZrO_2 ceramic material by solid-state reaction at high temperature is reported. The effect of Mg doping on the structural, optical, and morphological properties, have been studied and discussed.

RESULTS AND DISCUSSION

Particle size analyses

Because particle size distribution (PSD) of the precursor oxide mixture is a key factor in the evolution of the solid-state reaction, laser diffraction analysis was carried out on precursor oxides, ZrO$_2$ and MgO, and precursor oxides mixture. The PSD is presented in Figure 1.
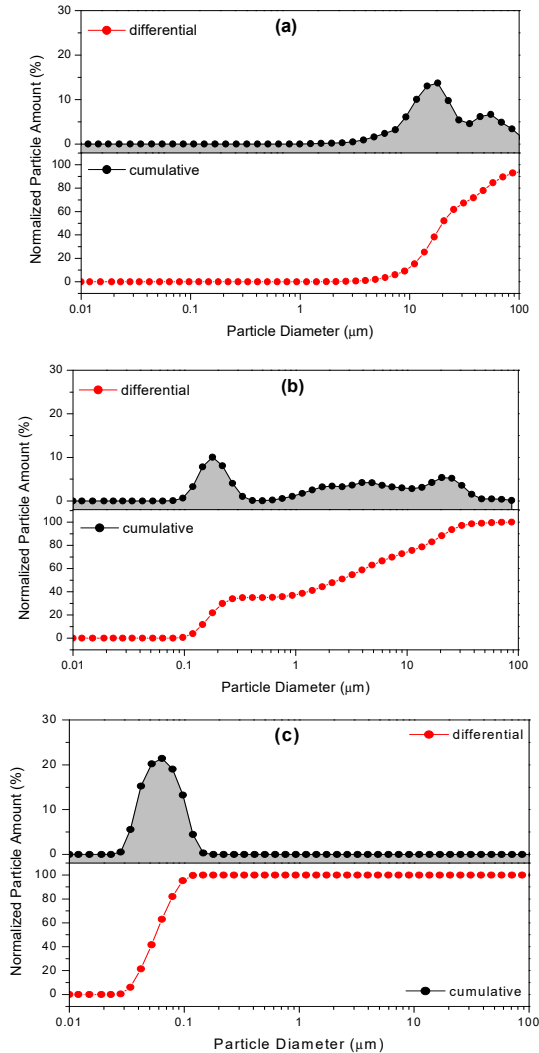

Figure 1. PSD (cumulative and differential curves) for (a) ZrO$_2$, (b) MgO and (c) raw materials mixture.

As observed from Figure 1a, for ZrO_2 powder was characteristic a bimodal grain size distribution with a mean particle size of 1,780 µm (SD=0.359). In the case of the MgO (Figure 1b) a wide PSD of the initial ZrO_2 powder, consisted of three main grain populations with a mean value of 23.257 µm (standard deviation, SD=0.359) was observed.

The mixture was homogenized by dry milling using an agate mortar and pestle and subsequently passed through a 63 µm sieve. After the homogenization, the mixture consisted of a narrow PSD of particles (Figure 1c) with a mean value of 0.056 µm (SD=0.146). As visible from Figure 1, the volume fraction of particles smaller than 1 µm is much higher for the mixture than for the pure ZrO_2 and MgO precursor powders.

X-ray powder diffraction (XRPD) analysis

To determine the structural properties of the prepared ceramic material, XRPD analysis was performed on 15 at% MgO-doped ZrO_2 sintered at 1600°C for 12 hours. The typical XRPD patterns shown in Figure 2 provided structural information on the processed ceramic. Analysis of powder pattern of the investigated sample showed peaks at 2θ angle of 30.5º, 35.28º, 50.76º, 60.38º, 63.36º and 74.7º which correspond to the (111), (200), (220), (311), (101), and (400) crystallographic planes of t-ZrO_2 (JCPDS no. 88-1007). As evidenced from Figure 2, high peak intensity confirms the high crystallinity of the prepared material. No peaks belonging to the m-ZrO_2 or MgO phases were observed at this Mg doping level, confirming the solubility of Mg in the ZrO_2.
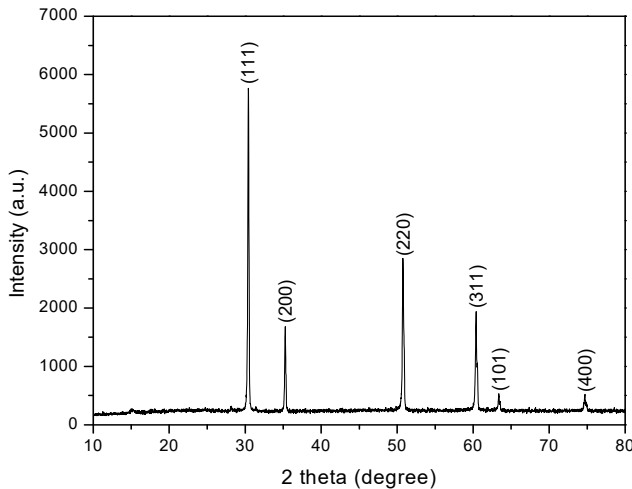
Figure 2. XRPD pattern of Mg-doped ZrO_2.

The small difference between ionic radii of the Zr^{4+} (0.84 Å) and Mg^{2+} (0.72 Å) [22] should provide the easier solubility of Mg in the ZrO$_2$ lattice, as previously observed. Consequently, the Zr^{4+} on its lattice site is substituted by the Mg^{2+} ion. Furthermore, since Mg has the oxidation state of +2, some oxygen vacancy is induced in the structure. It has been previously reported that oxygen vacancies are the main reason for the stabilization of the tetragonal phase [23].

The crystallite size (D) of the prepared composition was calculated by Scherrer formula for (111) reflection:

$$D_{hkl} = 0.9\lambda/(\beta\cos\theta) \tag{1}$$

where: D - crystallite size along (hkl) direction, β - full width half maximum (FWHM) of the most intense diffraction line, λ - wavelength of X-ray, θ - the Bragg angle [24].

The calculated crystallite size of Mg-doped ZrO$_2$ was about of 55.67 nm. Compared with data obtained by laser diffraction it can be stated that the size of particles remains practically unchanged after sintering. This phenomenon was previously observed on the sintering of nanostructured ZrO$_2$ ceramics by colloidal processing. The inhibition of the grain growth may have been caused by inter-diffusion of cations during the sintering [25].

UV-VIS spectroscopy

The optical properties of the prepared composition were considered in terms of UV-VIS diffuse reflectance spectrum (DRS) as shown in Figure 3a. The DRS spectrum shows a sharp and prominent maximum %R around 550 nm which can arise due to the transition between valence band to the conduction band.

Figure 3b revealed the optical bandgap (Eg) value estimated from DRS by Tauc plot using Kubelka-Munk function F(R) [26]. The determination of Eg by applying the Kubelka–Munk (K–M or F(R)) method is based on the following equation:

$$F(R) = (1-R)^2/2R \tag{2}$$

where R is the reflectance; F(R) is proportional to the extinction coefficient (α).

The bandgap of ZrO$_2$ is dependent on heat treatment temperature as shown by Lavisa et al. [27]. Their result indicates that the exponential optical absorption edge and optical bandgap are controlled by the degree of structural defects in the lattice. Hence, the increase of optical bandgap value with the heat treatment temperature promotes a reduction of the intermediary energy levels, as a result of the structural organization in the lattice [27, 28]. The bandgap can be also influenced by the formation methods and type and

amount of dopant introduced in the ZrO_2 lattice. Depending on the types and chemical states of metal ions, the bandgaps of metal-doped ZrO_2 varied, the differences being mainly associated with the electronic configurations of the ions, which control the energy levels in the ZrO_2.
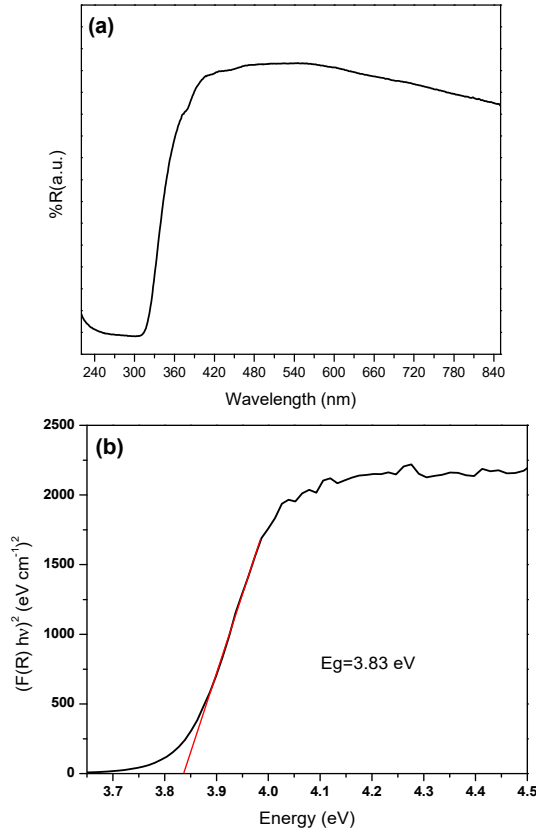


Figure 3. (a) DRS of Mg-doped ZrO_2 and (b) the Tauc plot depicting the optical bandgap.

In our work, the bandgap determined for the bulk Mg-doped ZrO_2 ceramic material from the DRS spectrum is about 3.83 eV. ZrO_2 has a wide bandgap, and the reported value is about 5.0 eV [29]. The reduced value of bandgap obtained for Mg-doped ZrO_2 may be due to the incorporation of magnesia. In the case of Mg doping in ZrO_2, Mg^{2+} ions are moved to the substituted sites in the ZrO_2 matrix and may act as a donor impurity. The doped Mg^{2+} ions increase the donor density and thus result in the formation of a donor level below the conduction band thereby reducing the bandgap of ZrO_2 [30].

Scanning electron microscopy (SEM) / Energy dispersive X-ray (EDX) spectroscopy

SEM was employed to analyze the morphological characteristics of the prepared Mg-doped ZrO$_2$ ceramic material. From the images shown in Figure 4(a, b, c), it can be seen that irregular and agglomerated shapes like morphology was formed in the ceramic sample.
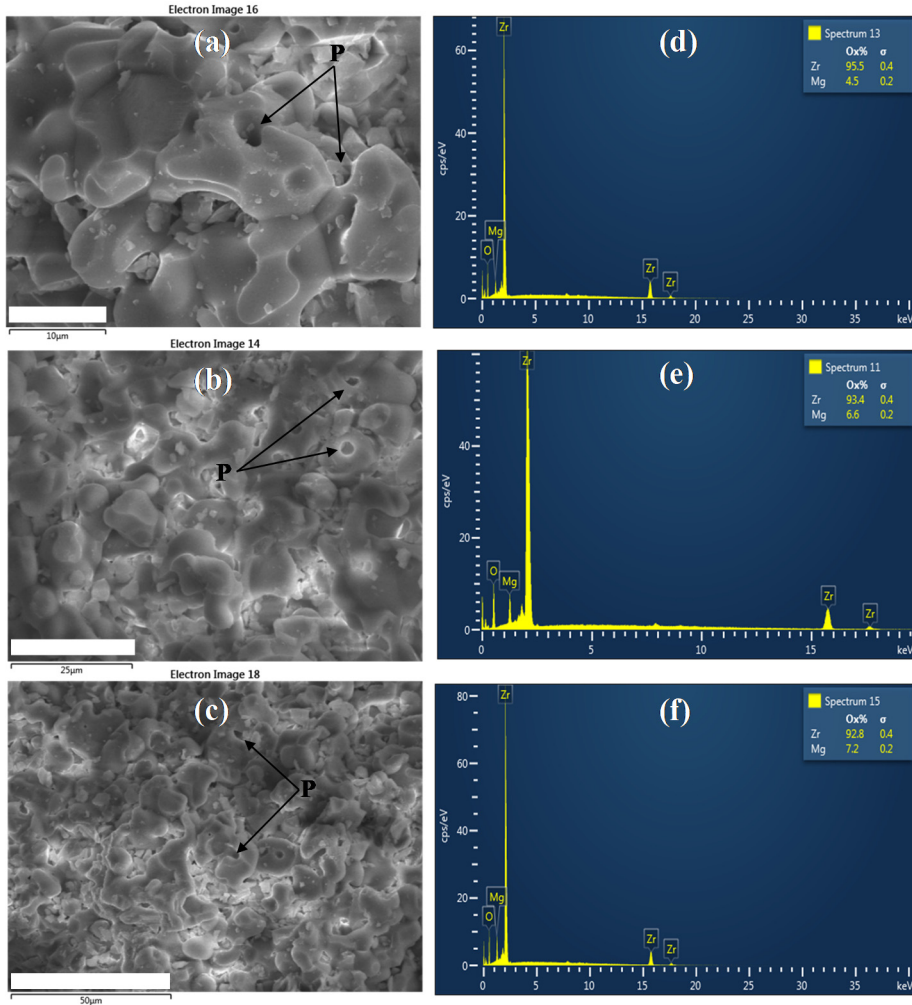

Figure 4. SEM images at different magnifications (a, b and c) and typical corresponding EDX spectra (d, e and f) of Mg-doped ZrO$_2$ ceramics. The corresponding scale bars are (a) 10 μm, (b) 25 μm and (c) 50 μm, respectively.

227

SEM data reveals also that the grains are stronger interconnected to each other. This typical interconnected structure in zirconia-based ceramics was previously observed for yttria-stabilized zirconia (YSZ) ceramics or ZrO_2-based composites, sintered at 1550 °C [31, 32]. As stated before, this strong network provided by the interconnection of grains allows to obtain high mechanical strength [31]. In addition, the microstructural observations reveal the presence of pores as seen in Figure 4. From point of view of technological applications one of the most important characteristics of the porous YSZ is low thermal conductivity, which is greatly influenced by the presence of pores into the microstructure. The air trapped in the pores represents a better thermal insulator [33]. For biomedical applications finer pores and less volume fraction of porosity should be beneficial for biological cell attachment. The presence of finer pores could favor the initial osteoblast cell attachment by a mechanical anchorage process. Consequently, once cells are attached at the initial stage of implantation, the attached cell assembly would subsequently favor formation of multiple cells and thereby lead to *in vivo* tissue formation [34, 35].

The chemical composition of the obtained Mg-doped ZrO_2 ceramic material was analyzed using EDX as displayed in Figure 4(d, e, f). The EDX result confirms the presence of elements such as magnesium, oxygen and zirconium by the appearance of Mg, Zr and O peaks. It indicates the purity of the product and without any other signal present in the product.

Qualitative analysis of elements present in Mg-doped ZrO_2 ceramic sample was further evaluated by elemental mapping. The elemental mapping micrographs are presented in Figure 5.
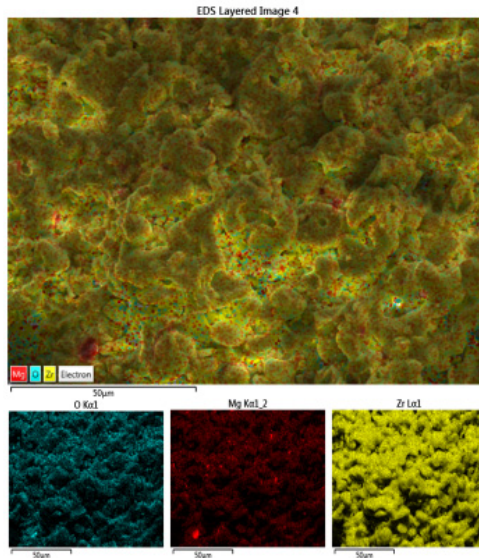
Figure 5. SEM mapping photographs for the Mg-doped ZrO_2 ceramic.

These micrographs confirmed the homogenous distribution of the elements in the sample. It was found that magnesia is distributed uniformly throughout the imaged area, which clearly indicates that the ZrO$_2$ is surface modified by magnesia.

CONCLUSIONS

15 at% Mg-doped ZrO$_2$ ceramic material was successfully obtained by solid-state reaction method at 1600°C, followed by their characterization using XRPD, UV-VIS, and SEM techniques. The analyses indicated the presence of t-ZrO$_2$ phase. No trace of the m-ZrO$_2$ or MgO phase was noticed in the sample. The SEM micrographs confirmed the homogenous distribution of the elements through the mixed oxide. Further, optical properties evaluated in terms of UV-VIS DRS spectrum, revealed that the Mg-doped ZrO$_2$ showed a smaller bandgap compared with pure ZrO$_2$, which may be due to the incorporation of magnesia in the ZrO$_2$ matrix. Moreover, through this study, we have confirmed the significant role played by the Mg^{2+} aliovalent dopant cation concerning t-ZrO$_2$ phase stabilization. The study also should be helpful in the development of potential applications using Mg-doped ZrO$_2$, like catalysis, sensors, energy conversion and storage, coating, or in the biomedical domain.

EXPERIMENTAL SECTION

PREPARATION

Ceramic preparation

Mg-doped ZrO$_2$ ceramic sample was synthesized by solid-state reaction at high temperature following the scheme from Figure 6.

Commercial pure ZrO$_2$ (Riedel-de Haën AG, Seelze, Germany, 99%) and MgO (Alfa Aesar, Germany, 99.99%) powdered oxides were used as starting materials in order to obtain 15 at% MgO in ZrO$_2$. Proper amounts of starting precursors in a corresponding atomic ratio were homogenized using an agate mortar and pestle. The resultant powder was mixed with 5% PVA and uniaxially cold-pressed in a metallic dye into cylindrical pellets of 1 g with 10 mm in diameter at a pressure of 400 kgf/cm^2 using a Carver Inc. hydraulic press (Carver Inc, Wabash, IN, USA). The obtained pellets were further sintered at 1600 ºC under the air atmosphere using a high-temperature Nabertherm LHT 04/16 furnace, with a heating and cooling rate of 5 °C/min and dwell time of 12 h at the maximum temperature.
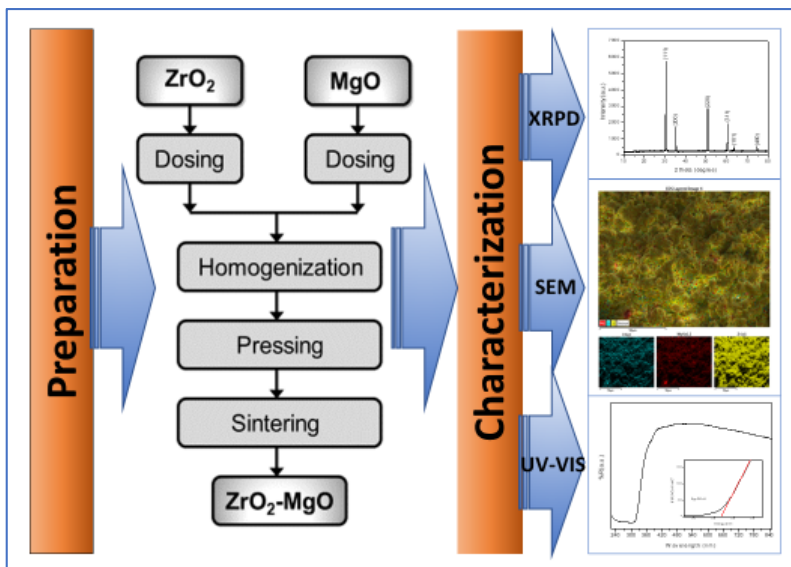
Figure 6. Schematic flowchart for Mg-doped ZrO_2 ceramic preparation.

CHARACTERIZATION METHODS

Particle size analysis

A Shimadzu Sald-7101 (Japan) micro- and nano- particle size analyser was used for investigating the particle size distribution (PSD) of raw materials and raw materials mixture powders. Samples were immersed for 15 s in distilled water used as a solvent, with aggregation being reduced using treatment with ultrasounds.

X-ray powder diffraction (XRPD)

XRPD analysis was performed in order to investigate the structure of the samples, using a Shimadzu XRD-6000 (Japan) diffractometer operating at 40 kV, 30 mA with a monochromator of graphite for CuKα (λ=1.5418 Å). The diffraction patterns was recorded in the 2θ range of 10–80° at a scan speed of 2 °/min.

Scanning Electron Microscopy (SEM)/ Energy dispersive X-ray (EDX) spectroscopy

SEM analysis was performed using a Hitachi SU8230 (Tokyo, Japan) microscope. The electron microscope was coupled with an Aztec X-Max 1160 EDX detector (Oxford Instruments).

UV-VIS spectroscopy

UV-VIS spectroscopy was employed to characterize the influence of the dopant on the optical properties of the ZrO$_2$ based ceramic. Diffuse reflectance spectrum (DRS) was registered with a double-beam JASCO V-650 (Japan) spectrophotometer, equipped with an ISV-722 Integrating Sphere, in the wavelength range from 200 to 800 nm, with a scan rate of 400 nm/min.

ACKNOWLEDGEMENTS

REFERENCES

1. S. Shukla; S. Seal; *Int. Mater. Rev.,* **2005**, 5, 45–64.
2. D.R. Clarke; C.G. Levi; *Annu. Rev. Mater. Res*., **2003**, 33, 383–417.
3. J.Y. Thompson; B.R. Stoner; J.R. Piascik; R. Smith; *Dental Mater.*, **2011**, 27, 71–82.
4. V. Fiorentini; G. Gulleri; *Phys. Rev. Lett.,* **2002***, 89, 266101, 1–4.
5. P. Li; I. W. Chen; J.E. Penner-Han; *J. Am. Ceram. Soc*., **1994**, 77, 118–128.
6. D. Ysoutsou; G. Apostolopoulos; S. Galata; A. Sotiropoulos; G. Mavrou; Y. Panayiotatos; A. Dimoulas; *Microelect. Eng*., **2009**, 86, 1626–1628.
7. S. Manjunatha; M.S. Dharmaprakash; *J. Luminescence*, **2016**, 180, 20–24.
8. S. Somiya; N. Yamamato; H. Yanagina; *Science and Technology of Zirconia (III),* vol. 24 A and 24B, American Ceramic Society, Westerville, **1988**.
9. S. Raveendrana; M.I.K. Khanb; A. Dhayalanb; S. Kannan; *Ceram. Int*, **2020**, 46, 641-652.
10. P.F. Manicone; P. Rossi Iommetti; L. Raffaelli; *J. Dent.,* **2007***, 35*, 819–826.
11. I.G. Tredici; M. Sebastiani; F. Massimi; E. Bemporad; A. Resmini; G. Merlati; U. Anselmi-Tamburini; *Ceram. Int.*, **2016**, *42*, 8190-8197.
12. S. Kargozar; S Ramakrishna; M. Mozafari. *Curr. Opin. Biomed. Eng.*, **2019**,10, 181-190.
13. S. Soon; B. Pingguan-Murphy, K.W Lai; S.A. Akbar; *Ceram. Int.*, **2016**, 42(11), 12543–12555.
14. O.S. El-Ghany; A.H Sherief; *Future Dent. J.,* **2016,** 2(2), 55–64.
15. S.A. Ali; S. Karthigeyan; M. Deivanai; R. Mani; *Pak. Oral Dent. J.,* **2014**, 34, 177-183.

16. M. Ferrari; A. Vichi; F. Zarone; *Dent. Mater.*, **2015**, 31(3), e63–e76.
17. S. Kumar, S. Bhunia, A.K. Ojha, *Chem. Phys. Lett.,* **2016**, 644, 271–275.
18. L. Renuka, K.S. Anantharaju, S.C. Sharma, H.P. Nagaswarupa, S.C. Prashantha, H. Nagabhushana, Y.S. Vidya, *J. Alloys Compd.*, **2016**, 672, 609-622.
19. E.C. Subbarao. Zirconia-an overview. In: *Advances in ceramics*, A.H. Heuer, L.W. Hobbs, Science and Technology of Zirconia, Amsterdam: Elsevier, **1981**, vol 3, 1-24.
20. C. Piconi; G. Maccauro; *Biomaterials,* **1999**, 20, 1-25.
21. L Keerthana; C. Sakthivel; I. Prabha; **2019***, 3-4, *Materials Today Sustainability*, 100007, 1-15.
22. R.D. Shannon; C.T. Prewitt; *Acta Cryst.*, **1969**, B25, 925-946.
23. S. Shukla; S. Seal; **2005**, *Int. Mater. Rev.* 50(1), 45-64.
24. A.L. Patterson; *Phys. Rev.*, **1939**, 56, 978-982.
25. G. Suárez; Y. Sakka; T. S Suzuki; T. Uchikoshi; X. Zhu; E.F. Aglietti; *Sci. Technol. Adv. Mater.,* **2009***, 10(2), 025004, 1-8.
26. P. Kubelka; F. Munk-Aussig; *Physik*, **1931**, 12, 593-601.
27. L.X. Lovisa; V.D. Araújo; R.L. Tranquilin; E. Longo; M.S. Li; C.A. Paskocimas; M.R.D. Bomio; F.V. Motta; *J. Alloys Compds.*, **2016**, 674, 245-251.
28. M.D. Gonçalves; L.S. Cavalcante; J.C. Sczancoski; J.W.M. Espinosa; P.S. Pizani; E. Longo; I.L.V. Rosa; *Opt. Mater.*, **2009**, 31, 1134-1143.
29. A. Emeline; G.V. Kataeva; A.S. Litke; A.V. Rudakova; V.K. Ryabchuk; N. Serpone, *Langmuir*, **1998**, 14, 5011-5022.
30. Y. Nian-Qi; L. Zhi-Chao; G. Guang-Rui; W. Bao-Jia; *Chinese Physics B*, **2017**, 26(10), 106801, 1-5.
31. L. Hu; C. Wang; Y. Huang; *J. Mater. Sci*, **2010**, 45, 3242–3246.
32. L. Bizo; K. Sabo; R. Barabas; G. Katona; L. Barbu-Tudoran; A. Berar; *Studia UBB Chemia*, LXV, 1, **2020**, 137-148.
33. G. Pia; C. Siligardi; L. Casnedi; U. Sanna, *Ceram. Int.*, **2016**, 42(8), 9583-9590.
34. B. Annaz; K.A. Hing; M. Kayser; T. Buckland; L. Di Silvio; *J. Microsc.*, **2004**, 215, 100-110.
35. S. Nath; S. Baja; B. Basu; *Int. J. Appl. Ceram. Technol.*, **2008**, 5(1), 49-62.

SCREEN-PRINTED ELECTRODES MADE ON STONE PAPER SUBSTRATE FOR URIC ACID ELECTROCHEMICAL DETECTION

CODRUTA VARODI[a], FLORINA POGACEAN[a], MARIN GHEORGHE[b], LUCIAN BARBU-TUDORAN[a] and STELA PRUNEANU[a,*]

ABSTRACT. Flexible screen-printed electrodes on stone paper substrate (HP) and modified with gold nanoparticles (HP-AuNPs) or AuNPs-poly-methylene blue (HP-AuNPs-PMB) were fabricated and morphologically investigated by SEM/EDS. The electrochemical properties of the new electrodes were studied by cyclic voltammetry (CV). The best electrocatalytic properties for uric acid detection were obtained with HP-AuNPs electrode: 0.16 µM Limit of Detection, 5×10^{-7}- 10^{-4} M linear range and 20.7 mA/M sensitivity.

Keywords: *uric acid detection, stone paper substrate, AuNPs modified electrodes*

INTRODUCTION

Uric acid is a waste product created during the metabolism of proteins. It is normally cleaned out of the blood by the kidneys, and passes out of the body along with urine. The high concentration of uric acid in the blood will eventually convert the acid into urate crystals, which can then accumulate inside the body leading to various diseases like gout, Lesch-Nyhan syndrome, urolithiasis, kidney damage, leukemia, lymphoma [1]. The detection of UA in human body has considerable importance for clinical analysis and diagnosis.

[a] *National Institute for Research and Development of Isotopic and Molecular Technologies, Donat Street, No. 67-103, RO, 400293, Cluj-Napoca, Romania*
[b] *NANOM MEMS srl, G. Cosbuc Street, No. 9, RO, 505400, Rasnov, Brasov, Romania*
* *Corresponding author: stela.pruneanu@itim-cj.ro*

Various methods for the determination of UA have been reported, such as chemiluminescence [2], fluorimetry [3], spectrophotometry [4], enzyme assay [5], chromatography [6-8], electrophoresis titration [9], gamma radiolysis [10] and electrochemical methods [11-15].

The interest for the development of a new generation of biodegradable electronics [16-17] made by non-toxic materials and for renewable and waste-based materials as substrates for electrochemical electrodes is highly increasing in the last decades. The electrodes based on textile, hydro chars waste, carbon rod from zinc-carbon batteries, CD/DVD, ITO from photovoltaic device, PVC, ceramic, paper or other types of materials re-designed in a greener approach the analytical electrochemistry [18].

In this context, stone paper is very attractive for flexible device applications. It is a composite material made of calcium carbonate and a non-toxic resin, *high-density polyethylene* (HDPE). It is not biodegradable but is *photo-degradable* under suitable conditions [19]. The production of paper from stone offers significant environmental benefits such as no major deforestation.

In this research, we used stone paper as substrate for developing new modified electrodes, with excellent electrocatalytic activity for the oxidation of uric acid.


RESULTS AND DISCUSSION

The flexible screen-printed electrodes on stone paper substrate (HP) can be connected to a laboratory potentiostat. Two HP electrodes were modified either with gold nanoparticles (HP-AuNPs) or gold nanoparticles and poly-methylene blue (HP-AuNPs-PMB) and were morphologically characterized before the electrochemical testing for uric acid detection.

Morphological characterization of the flexible screen-printed electrodes (HP, HP-AuNPs and HP-AuNPs-PMB)

SEM technique coupled with EDS analysis was used for the morphological characterization of the new flexible screen-printed electrodes (HP and HP-AuNPs).

The image of bare HP electrode (Figure 1a) reveals a porous surface with graphite particles have irregular shapes and the size in the range of hundred of nm. After AuNPs electrodeposition, round particles attached to the electrode surface can be observed. The changed morphology of modified electrode is presented in Figure 1b. The effect of poly-methylene blue was to cover the electrode surface, including the gold nanoparticles as can be seen in Figure 1c.
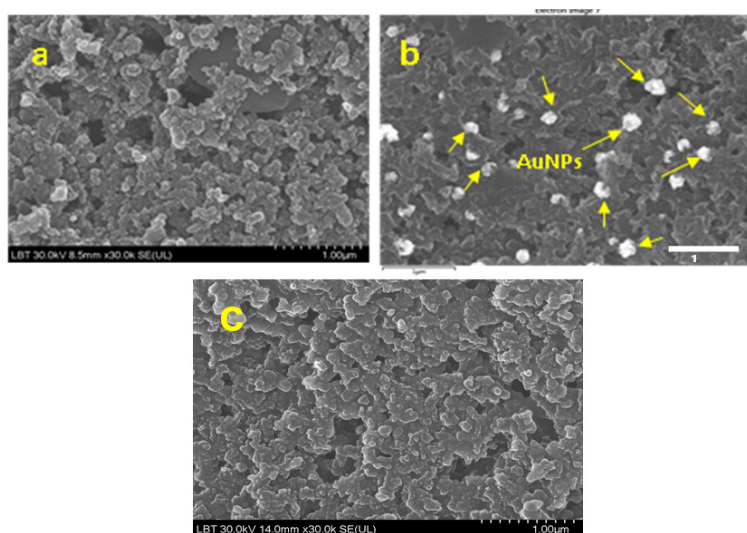
Figure 1. SEM image of HP electrode (a), AuNPs modified electrode (HP-AuNPs) (b) and PMB-AuNPs modified electrode (HP-AuNPs-PMB) (c); scale bar: 1 µm.

The EDS analysis (Figure 2) confirmed that the paper surface printed with carbon ink has carbon in its composition (yellow) and the nanoparticles from the modified electrode surface were gold (red).
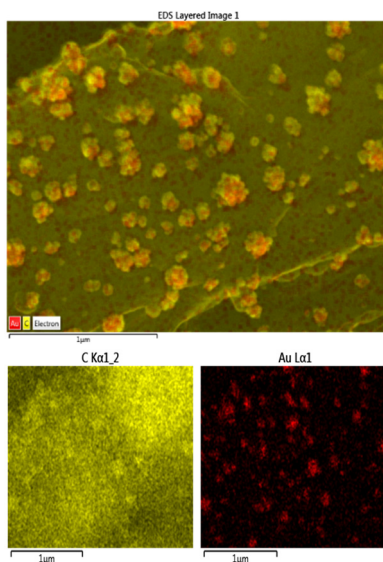

Figure 2. EDS analysis of HP-AuNPs electrode, confirming the presence of carbon (yellow) and gold (red) elements within its surface; scale bar: 1µm

CODRUTA VARODI, FLORINA POGACEAN, MARIN GHEORGHE,
LUCIAN BARBU-TUDORAN, STELA PRUNEANU

Electrochemical active areas of the flexible screen-printed electrodes

The new flexible screen-printed electrodes were electrochemically characterized by cyclic voltammetry in a redox couple solution (1 mM $K_4[Fe(CN)_6]$ + 0.2 M KCl), between -0.2 V and +0.65 V potential range. In this one-electron redox reaction (Scheme 1), the ferricyanide ion $Fe(CN)_6^{3-}$ is an oxidant and the ferrocyanide ion $Fe(CN)_6^{4-}$ is a reductant. This reversible redox couple is a standard in electrochemistry [20].

$$Fe(CN)_6^{4-} - e^- \underset{\text{Reduction}}{\overset{\text{Oxidation}}{\rightleftarrows}} Fe(CN)_6^{3-}$$

Ferrocyanide ion   Ferricyanide ion
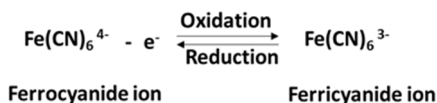
Scheme 1. Potassium ferrocyanide/ferricyanide reversible one-electron redox reaction

Their active areas were calculated with Randles-Sevick equation, after recording cyclic voltammograms at different scanning rate (2, 5, 10, 15, 20, 30, 40, 50, 100 mVs^{-1}). The linear plots obtained between the anodic peak current (I_p) of each electrode and the square root of scan rate ($v^{1/2}$) are presented in Figure 3.
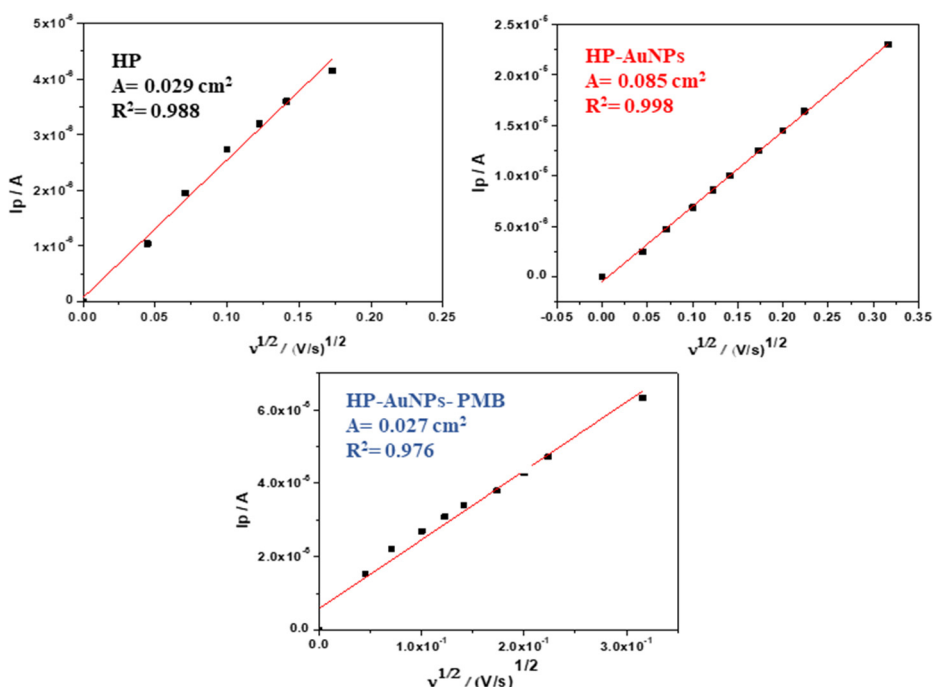
**Figure 3.** The linear plots obtained between anodic peak current (I_p) and the square root of scan rate ($v^{1/2}$) with new flexible screen-printed electrodes in the presence of 1.0 mM $K_4[Fe(CN)_6]$ + 0.2 M KCl, at different scanning rates

As can be seen in these figures, AuNPs had a benefic effect leading to a considerably increase of the active area of the modified electrode (~ 3 times, from 0.029 cm^2 to 0.085 cm^2). In contrast, the electrodeposition of PMB over the electrode modified with AuNPs had an opposite effect and the active area considerably decresed (0.027 cm^2).

Electrochemical detection of uric acid (UA) with HP, HP-AuNPs and HP-AuNPs–PMB flexible electrodes

In order to investigate the analytical applicability of new flexible screen-printed electrodes *HP, HP-AuNPs and HP-AuNPs–PMB*, they were tested for uric acid detection. Cyclic voltammograms recorded with the electrodes in pH 6 PBS solution containing 0.1 mM uric acid are shown in Figure 4. The signals generated by the three electrodes are different. In the case of bare HP electrode (blue), the oxidation wave is broad and small. The electrode modified with AuNPs-PMB gives a higher signal, but the best signal was that recorded with HP-AuNPs. In addition, the electrocatalytic effect of HP-AuNPs electrode was indicated by the clear shift of the peak potential, from 0.45 to 0.205 V.
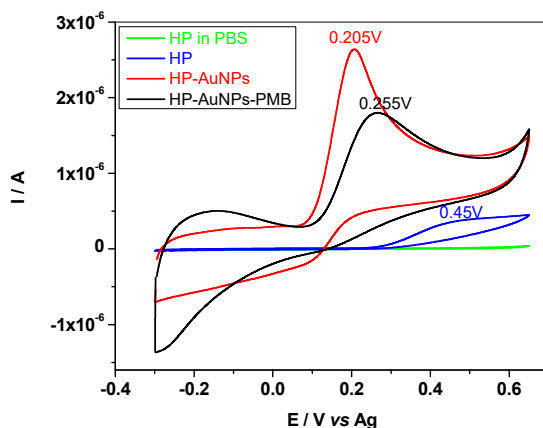
Figure 4. Cyclic voltammograms recorded with HP, HP-AuNPs and HP-AuNPs-PMB flexible electrodes in the absence and presence of 0.1 mM uric acid. Supporting electrolyte: pH 6 PBS; scan rate 10 mVs^{-1}.

The bare and modified electrodes were next employed to record cyclic voltammograms in solutions containing various concentrations of uric acid (10^{-7}-10^{-4} M; pH6 PBS supporting electrolyte). For exemplification, in Figure 5a are shown the CVs recorded with HP-AuNPs. The superior performances of the HP-AuNPs modified electrode are further confirmed by the obtained calibration plot, Figure 5b. A higher sensitivity of the AuNPs modified electrode (20.7 mA/M) in comparison with bare (1.23 mA/M) or AuNPs-PMB electrode (11.7 mA/M) can be clearly observed.
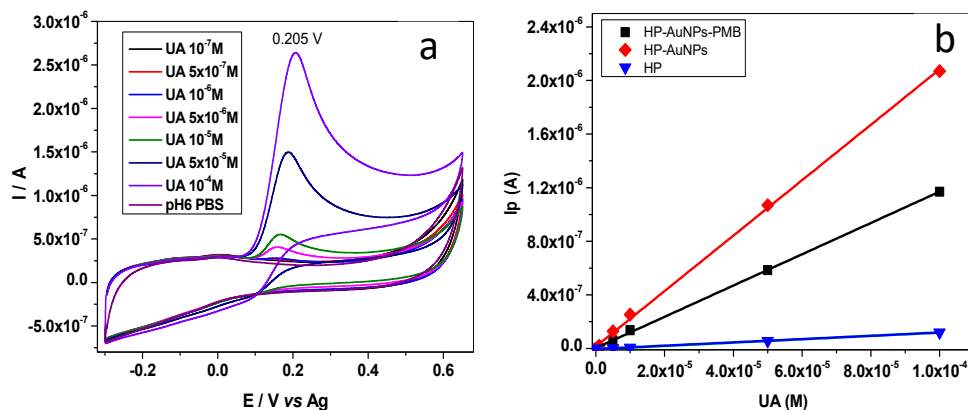
Figure 5. Cyclic voltammograms recorded with HP-AuNPs flexible electrode in the absence and presence of different concentration of uric acid; supporting electrolyte: pH 6 PBS; scan rate 10 mVs^{-1} (a); Calibration plots for HP (5×10^{-6}-10^{-4} M UA), HP-AuNPs (5×10^{-7}-10^{-4} M UA) and HP-AuNPs-PMB (10^{-6}-10^{-4} M UA) electrode (b)

The electro-analytical parameters of screen-printed electrodes made on the stone paper substrate for uric acid detection are presented in Table 1.

Table 1. The electro-analytical parameters of HP, HP-AuNPs and HP-AuNPs-PMB electrodes for UA detection

Electrode	Sensitivity (mA/M)	Linear range (M)	Detection limit (M)
HP	1.23	5×10^{-6}- 10^{-4}	1.6×10^{-6}
HP-AuNPs	20.7	5×10^{-7}- 10^{-4}	1.6×10^{-7}
HP-AuNPs-PMB	11.7	10^{-6}-10^{-4}	3.3×10^{-7}

Here one can see that the limit of detection of HP-AuNPs electrode is considerably lower than that of HP (10 times) or HP-AuNPs-PMB electrode (2 times). In addition, it has the largest linear range for UA, from 5×10^{-7} to 10^{-4} M. In Table 2 are shown the analytical performances of the new screen-printed electrodes made on the stone paper substrate for UA detection, in comparison with other types of electrodes. The low detection limit and the wide linear range highly recommend the HP-AuNPs electrode for practical applications.

Table 2. Analytical performances of new screen-printed electrodes made on the stone paper substrate for UA detection, compared with other types of electrodes

Electrode	Substrate	Technique	LOD (µM)	Linear range (M)	Ref.
HP	Stone paper	CV	1.6	5×10^{-6}- 10^{-4}	This work
HP-AuNPs	Stone paper	CV	0.16	5×10^{-7}- 10^{-4}	This work
HP-AuNPs-PMB	Stone paper	CV	0.33	10^{-6}-10^{-4}	This work
PAMTA/PG	PG	DPV	2.74	5×10^{-6}- 1.2×10^{-3}	[11]
AuNPs/GO/Uricase	optical fiber	LSPR	206	1×10^{-5}-8×10^{-4}	[12]
CNCo/GCE	GCE	DPV	0.83	2×10^{-6}- 1.1×10^{-4}	[13]
PEDOT/GCE	GCE	CV	7	6×10^{-6}- 10^{-4}	[14]
α-Fe2O3/PAnNTs/GCE	GCE	DPV	0.038	10^{-8}- 5×10^{-6}	[15]

PAMTA-2-amino-5-mercapto-1,3,4-thiadiazole; PG- pencil graphite, GO- graphene oxide, CNCo- N,Co-doped porous carbon, LSPR- localized surface plasmon resonance, PEDOT-poly(3,4-ethylenedioxythiophene, GCE- glassy carbon electrode, PAnNTs- polyaniline nanotube

CONCLUSIONS

In conclusions, flexible electrodes (HP) printed on stone paper and modified with AuNPs or AuNPs-PMB were employed for the electrochemical detection of uric acid, in standard laboratory solutions (pH 6 PBS). The results were compared with those of bare electrode (HP). The best performances in terms of limit of detection (0.16 µM) and linear range (5×10^{-7}- 10^{-4} M uric acid) were those of HP-AuNPs electrode.

EXPERIMENTAL SECTION

Chemical and reagents

All chemicals, including KH_2PO_4, KCl, Potassium ferrocyanide $K_4 [Fe(CN)_6]$ and KCl were purchased from Sigma-Aldrich. Uric acid was purchased from Alfa-Aesar. Double-distilled water was obtained with a Fistreem Cyclon water purification system and used to prepare all the solutions. Stone paper was purchase from MIQUELRIUS (Spain) and used as substrate for screen-printed electrode fabrication.

Apparatus

Cyclic voltammograms (CV) were recorded with a potentiostat/ galvanostat Instrument (PGSTAT-302N, Metrohm-Autolab B.V., Netherlands). The experimental data were fitted using Nova 1.11 software.

A Hitachi SU8230 High Resolution Scanning Electron Microscope equipped with a cold field emission gun was used for obtain Scanning electron microscopy (SEM) images and energy-dispersive X-ray spectroscopy (EDS) analyses of stone paper electrodes.

Fabrication of flexible screen-printed electrodes on stone paper substrate

Stone paper, more durable than normal paper [21], was the flexible and water proof substrate for screen-printed electrode fabrication. The working electrode (4 mm diameter) and the counter were printed with carbon ink, while the reference electrode was printed with silver paste using a semiautomatic screen-printer (LC-TA-250 Model; NANOM MEMS SRL, Rasnov). The size of the obtained HP screen-printed electrode was: 3.4 x 1.0 x 0.05 cm (L x W x H) (Figure 6).
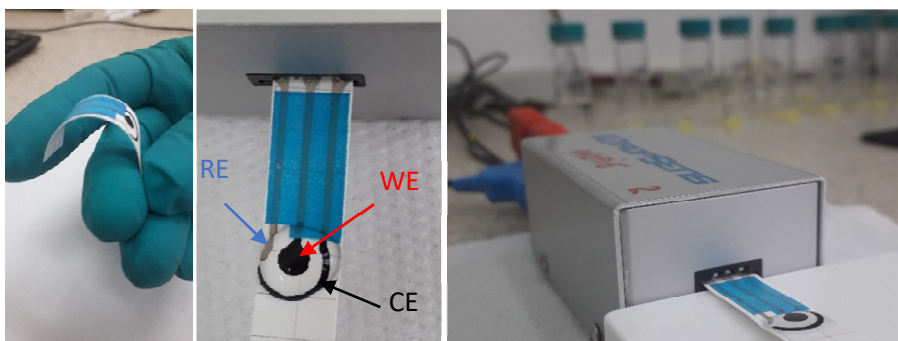
Figure 6. Flexible screen-printed electrodes on stone paper substrate (HP)
(optical images)

In order to modify the working electrode with gold nanoparticles (AuNPs) the chronoamperometric method was employed. A drop of 60 µL solution containing 1 mM $HAuCl_4$ (in 0.5 M H_2SO_4) was put on top of HP electrode and a potential of -0.2 V *versus* silver pseudo-reference electrode was applied, for 120 seconds. After AuNPs deposition, the electrode was cleaned with distilled water several times and was ready for further electrochemical investigation. The electrode was denoted HP-AuNPs.

After AuNPs deposition, a Methylene Blue aqueous solution (10^{-4} M in pH 7 PBS) was added on top of HP-AuNPs electrode in order to form a polymeric film on its surface. The poly-methylene blue (PMB) layer was electro-deposited by sweeping the potential from -1 to 0.9 V at a scan rate of 50 mV·s^{-1}, for 30 cycles (Figure 7). The electrochemical signal of MB was observed at E_{pa} = -0.3 V.
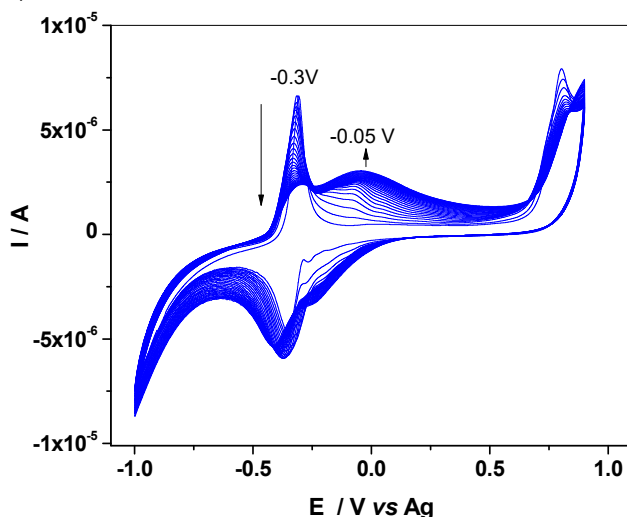
Figure 7. The electro-polymerization of Methylene Blue by
cyclic voltammetry; 50 mV·s^{-1} for 30 cycles

During the successive cycles the peak decreased in intensity and another peak grow-up at -0.05 V, corresponding to PMB. After polymerization, the modified electrode was thoroughly rinsed with double distilled water, air-dried and denoted HP-AuNPs-PMB.

ACKNOWLEDGMENTS

REFERENCES

1. G. Wurzner, J.C. Gerster, A. Chiolero, M. Maillard, C.L. Fallab-Stubi, H.R. Brunner, M. Burnier, *J. Hypertens.*, **2001**, *19*, 1855–1860
2. J. Yu, S. Wang, L. Ge, S. Ge, *Biosens. Bioelectron.*, **2011**, *26,* 3284–3289
3. J. Arora, S. Nandwani, M. Bhambi, C.S. Pundir, *Anal. Chim. Acta*, **2009**, *647 (2)*, 195-201
4. T. Yamaguchi, K. Hasegawa, S. Kamino, K. Iyachi, H. Tominaga, Y. Fujita, *Anal. Sci.*, **2007**, *23,* 223–226
5. R. Mundaca-Uribe, F. Bustos-Ramírez, C. Zaror-Zaror, M. Aranda-Bustos, J. Neira-Hinojosa, C. Pena- Farfal, *Sens. Actuators B*, **2014**, *195,* 58–62
6. A. Rodrigueza, R.M. Gomilab, G. Martorellb, A. Costa-Bauzaa, F. Grasesa, *J. Chromatogr.* B, **2017**, *1067,* 53–60
7. D. Remane, S. Grunwald, H. Hoeke, A. Mueller, S. Roeder, M. von Bergen, D. K. Wissenbach, *J. Chromatogr. B*, **2015,** *998-999,* 40–44
8. *R. Ferin, M. L. Pavão, J. Baptista, Clin. L. Biochem.,* **2013**, *46,* 665–669
9. M.I. Khan, Q. Zhang, Y. Wang, S. Saud, W. Liu, S. Liu, H. Kong, C. Wang, A. Uzzaman, H. Xiao, L.-Y. Fan, C.-X. Cao, *Sens. Actuators: B. Chem.,* **2019**, *286,* 9–15
10. N. Misra, V. Kumar, L. Borde, L. Varshney*, Sensor Actuat. B-Chem.*, **2013,** *178,* 371-378
11. R.G. Krishnan, R.Rejithamol, B. Saraswathyamma, *Microchem. J.*, **2020**, *155*, 104745
12. L. Singh, R. Singh, B. Zhang, S. Cheng, B.K. Kaushik, S. Kumar, *Opt. Fiber Technol.*, **2019**, *53,* 102043
13. L. Liu, L. Liu,Y. Wang, Bang-Ce Ye, *Talanta,* **2019**, *199,* 478-484
14. M. Motshakeri, J. Travas-Sejdic, A.R.J. Phillips, P.A. Kilmartin, *Electrochim. Acta*, **2018**, *265*, 184-193
15. M.R. Mahmoudian, W.J. Basirun, M. Sookhakian, P.M. Woi, E. Zalnezhad, H. Hazarkhani, Y. Alias, *Adv. Powder Technol.,* **2019**, *30, 2,* 384-392
16. V.R. Feig, H. Tran, Z. Bao, *ACS Cent. Sci.* **2018**, *4*, 337–348
17. X. Chen, J.H Ahn, *J. Mater. Chem. B*, **2020**, *8*, 1082–1092
18. G. Moro, F. Bottari, J. Van Loon, E. Du Bois, K. De Wael, L.M. Moretto, *Biosens. Bioelectron.* **2019**, *146*, 111758
19. C. Chu, P. Nel, *AICCM Bull.*, **2019**, 40, 37-49
20. Z.N. Nkunu, G.N. Kamau, J.G. Kithure, C.N. Muya, *Int. J. Innov. Res. Sci. Eng. Technol*. **2017**, 4 (5), 53
21. J. He, M. Luo, L. Hu, Y. Zhou, S. Jiang, H. Song, R. Ye, J. Chen, L. Gao, J. Tang, *J. Alloys Compd.* **2014**, *596*, 73–78.6

CHARACTERIZATION OF BOTSWANA COAL FROM TWO COAL FIELDS: MABESEKWA AND MMAMABULA TO DETERMINE ITS COAL RANK

MMOLOKI MAKOBA[a]*, TABOKA MOALOSI[a], PAUL S. AGACHI[a,b], EDISON MUZENDA[a], TIRIVAVIRI A. MAMVURA[a]

ABSTRACT. Coal samples from two different coal fields: Mabesekwa and Mmamabula were collected (with six seams from each coal field) to characterize using X-Ray diffractometer (XRD), Scanning Electron Microscopy (SEM) and Fourier Transform Infrared (FT-IR) spectroscopy. Proximate and ultimate analysis are also given. Clay minerals kaolinite, pyrite, dolomite, siderite and calcite, and quartz were discovered. Comparing measurements of C, VM, GCV, MC and FC obtained from the samples with literature, Botswana coal identifies as lignite grade A coal suitable for applications in coal gasification and ammonia based fertilisers due to its high volatile matter and high reactivity of char. The paper looks to use different methods to analyse Botswana coal and recommend its potential applications based on literature.

Keywords: Botswana coal, characterization, XRD, SEM, FT-IR, coal rank

INTRODUCTION

Botswana coal is not extensively studied despite the country's huge coal resources of around 212 Billion tons[1]. There are currently 8 coal fields across the country lying on the eastern side. Coal samples for this paper have been collected from two different mining points; Mabesekwa and Minergy (see Figure 1) to study how coal varies across the Karoo supergroup which is a belt that runs in the southern part of the African continent [2] covering 2/3rd of Botswana's geological strata.

[a] *Department of Chemical, Materials and Metallurgical Engineering, Faculty of Engineering and Technology, Botswana International University of Science and Technology, Palapye, Botswana*
[b] *Department of Chemical Engineering, Faculty of Chemistry and Chemical Engineering, University Babes-Bolyai, Cluj-Napoca, Romania*
* Corresponding author: mmoloki.makoba@studentmail.biust.ac.bw

MMOLOKI MAKOBA, TABOKA MOALOSI, PAUL S. AGACHI, EDISON MUZENDA,
TIRIVAVIRI A. MAMVURA

This study of coal composition and rank was influenced by research on gasification of Botswana coal for synthetic gas production. Coal is considered complex and heterogeneous in nature, therefore in order to understand coal before any process it is important to know its structure specific to its location. In an attempt to understand coal, different analyses can be carried out.

Mabesekwa coal field is located in the north eastern part of Botswana currently being explored by Shumba coal while Mmamabula coal field is located in the south eastern part of Botswana (Figure 1) with Minergy coal currently mining there for export to South Africa. These two constitute one of the key coal fields in the Botswana and can be well representative of the country's deposit (North and South). It is important to study all coal seams as mining of coal can change from shallow to deep.

X-ray diffraction (XRD) presents an average of the coal sample intensities rather than local properties of coal [4] which represents coal well because it is heterogeneous in nature. XRD is a non-destructive method that has been established to determine crystalline materials contained in coal.

FT-IR spectroscopy is also a non-destructive analytical tool which allows for study of functional groups. It identifies molecular vibrations in stretching and bending groups extensively identifying chemical structure of coal. The morphological structure was determined using the scanning electron microscopy (SEM). These analytical tools have been coupled with thermogravimetric analyzer (TGA) to give thermodynamic properties of coal.

In this work, we report information on structural parameters of Botswana coal determined by X-Ray diffraction, FT-IR spectroscopy and Scanning electron microscopy. Volatile matter, gross calorific value and fixed carbon are used to establish coal ranks. Volatile matter increases with decrease in rank [1].

RESULTS AND DISCUSSION

1.1 Proximate & ultimate analysis

Characterization of Botswana coal is reported in a table form as proximate analysis, ultimate analysis and gross calorific value of six (6) coal seams from Mabesekwa coal mine in the north eastern part of Botswana. The coal was floated in a fluid of specific gravity 1.80 using dense medium separator (DMS).

Table 1. Proximate and ultimate analysis of Mabesekwa coal

| Sample Identification			SHUMBA COAL					
			A	B	C	D	E	F
	Yield	mass (g)	143	1362	1090	381	50	167
Proximate analysis		%	0.4	4.4	2.9	1.0	0.1	0.6
	AC	%	33.4	39.8	45.0	37.2	35.2	35.9
	MC	%	3.1	4.6	4.2	4.2	5.4	5.2
	VM	%	24.4	22.9	20.7	24.0	23.6	24.8
	FC	%	39.1	32.7	30.2	34.6	35.9	34.2
	GCV	(MJ/kg)	15.3	12.7	12.1	14.0	14.2	13.6
Ultimate analysis	C	%	41.2	35.4	33.2	38.2	38.3	37.0
	H	%	2.01	2.07	2.20	2.20	1.97	2.01
	N	%	0.87	0.81	0.78	0.82	0.83	0.85
	O	%	18.1	17.2	14.6	17.2	18.3	19.0

Proximate analysis reports the physical characteristics of coal being moisture content, ash content, volatile matter, fixed carbon and total Sulphur contained. Fixed carbon is obtained by difference in percentage.

Seam A contains the least ash and subsequently the most fixed carbon. Coal is amorphous in nature; it depends on what was dumped and buried at the time when that layer/ seam was formed. Seam A seems to be purer with the highest amount of volatile matter and hence highest calorific value. High moisture content is generally believed to reduce the value of coal as indicated in Table 1. This will in turn lead to a large decrease of product gas efficiency due to the increase of the equivalence ratio in an attempt to keep the exit temperature of the gasifier at the specified value [5].

Table 1 also reports ultimate analysis of the elements i.e. C, H, N and O contained in six seams from Mabesekwa coal field. These elements form a typical structure of coal but it is how they are bonded together that makes coal unique and of certain value. The bonds in coal are identified through FT-IR spectroscopy as explained in section 3.2. According to analysis of coal ranks by [6]–[8] Botswana coal identifies as lignite grade A coal with C content of 40%, VM – 24%, GCV – 13.6 MJ/kg and MC – 4%. Lignite type coal proves to be more efficient as a coal gasification feedstock [9] because of its high volatile matter content and high reactivity of char therefore Botswana coal will fit best for application for gasification process.

With these elements together with functional groups analysis, a chemical formula for Botswana coal can be predicted. According to [1], all coals have nearly identical infrared spectra but differ in relative intensity of component bands which are broad and poorly defined due to a wide range of coal structures.

Mmamabula West coal had 6 seams and the proximate analysis results are represented in Table 3. This coal has at most 10% moisture compared with Mabesekwa coal with only 5% moisture. TGA analyses inherent moisture. Moisture reduces heating value of coal [10] therefore low inherent moisture coal is promising for a better-quality coal. Seam A for both Mabesekwa and Mmamabula coals show the least amount of moisture. This can be explained by the hot weather in Botswana that evaporates off water from the top surfaces compared to water that tends to settle at the bottom of the rock bed.
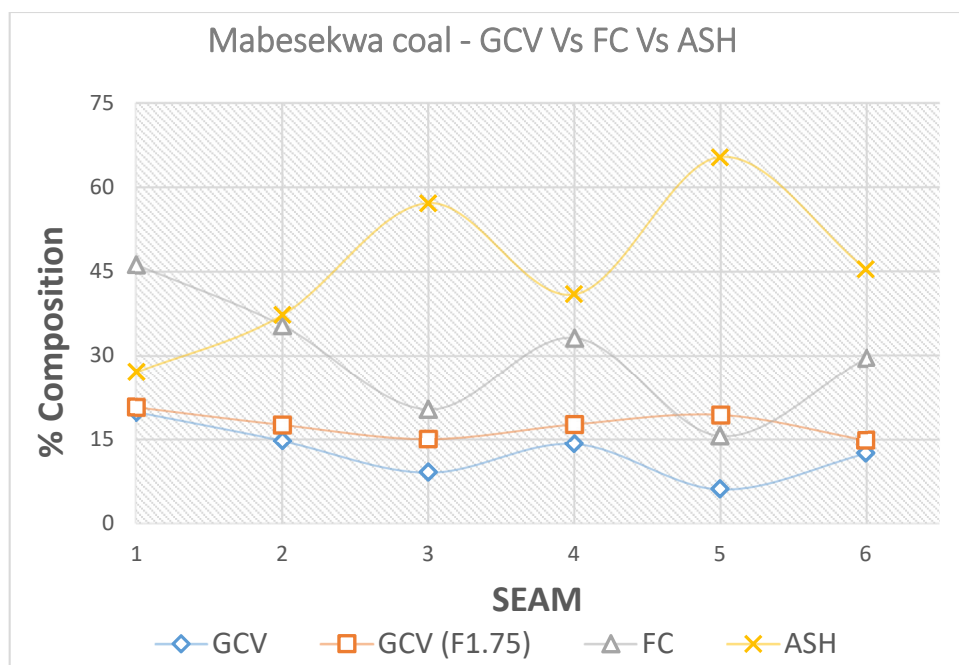
Figure 1. Proximate analysis variations across coal seams.

Fixed carbon for coal that was floated in low density medium (1.75) before testing is higher than raw coal because what weighs the most is usually invaluable inorganic material that sunk.

Table 2. Proximate and ultimate analysis of Minergy coal

| Sample Identification			MINERGY COAL					
			A	B	C	D	E	F
Proximate analysis	Yield							
	AC	%	63.9	25.2	17.7	18.3	21.2	29.9
	MC	%	3.2	7.2	7.3	6.5	5.4	4.7
	VM	%	15.4	26.2	21.8	26.9	26.0	25.0
	FC	%	17.5	41.4	53.2	48.3	47.4	40.4
Ultimate analysis	C	%	20.9	51.3	58.1	58.5	55.9	49.8
	H	%	2.01	3.52	3.82	4.07	3.66	3.68
	N	%	0.37	1.05	1.30	1.20	1.12	1.03
	S	%	0.19	2.47	2.57	1.60	3.21	1.90

% FC shows to decrease with increase in density medium as expected. This increase is proportional to ash content, the more the ash content the more increase in fixed carbon after dense medium separation. this is because ash composes of predominantly inorganic matter which does not add value to coal. Looking at the GCV for each seam.

From graph, FC and AC follow a similar pattern showing to complement each that proving that coal is indeed made up of organic matter that burns out completely leaving inorganic matter that is ash. GCV and AC are indirectly proportional, the higher the heating value, the lower the ash content and vice versa. Seam E shows to have 65% ash content; coal was made from dead plants and animals that were buried thousands of years ago. Coal which was floated at density 1.75 of liquid medium has more value than raw coal, this is explained by higher gross calorific value.

1.2 FT-IR

Combining elemental analysis with functional groups analysis enables a chemical formula for that particular coal can be predicted. Functional groups present show to be aromatic C=C bending groups at wavenumber 1700 - 1500, C=C bending alkene and CH_2 bend at 730 – 665 and 1480 – 1440 respectively. According to [1], all coals have nearly identical infrared spectra but differ in relative intensity of component bands which are broad and poorly defined due to a wide range of coal structures.

The coal samples showed intense peaks between 400 cm^{-1} and 1100 cm^{-1}. According to [11] these peaks indicate clay minerals (kaolinite, pyrite, siderite, dolomite) and quartz. These results can be correlated with XRD results as they also showed intense peaks of these clay minerals. From the graph it can be noticed that seam A had the highest intensities of the clay minerals. The peaks around 1600 cm^{-1} indicate C=C bonds.
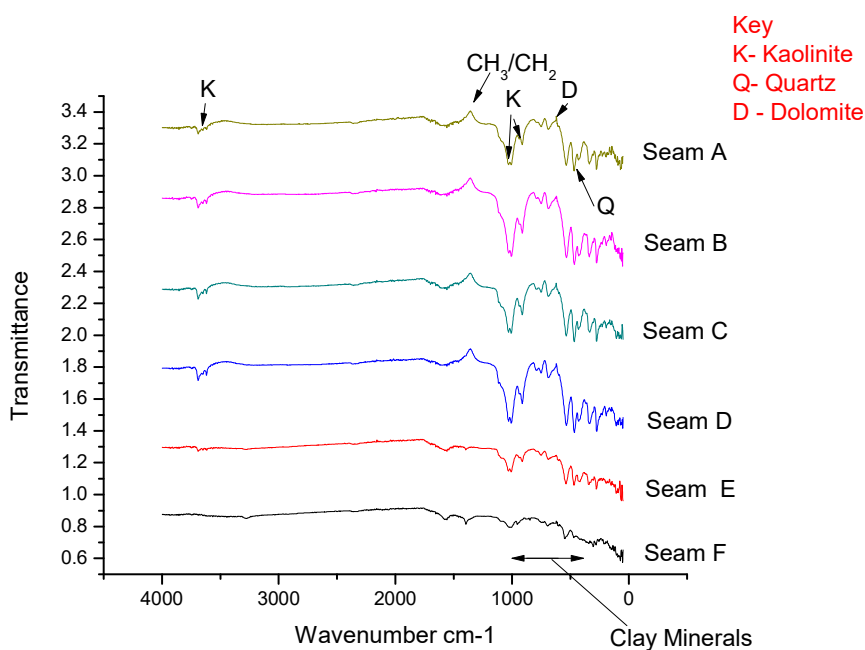
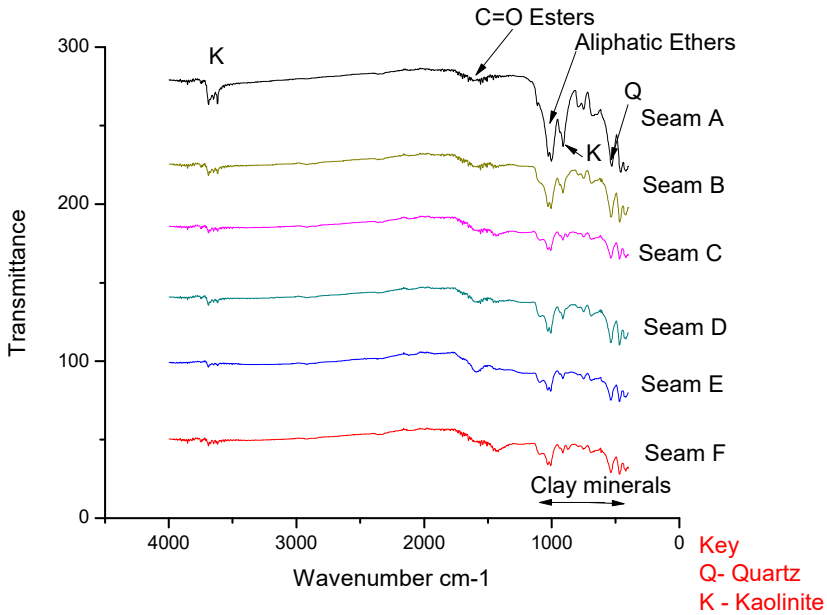**Figure 2.** FT-IR spectra for six Mabesekwa coal samples.

Figure 3. FT-IR spectra for 6 Mmamabula coal samples.

1.3 X-Ray diffraction

XRD analysis showed the presence of minerals in their varying intensities in the coal samples. These minerals included analcime, quartz, kaolinite, dolomite, calcite, pyrite and siderite. Minerals identified by FTIR analysis are also detected by XRD. Its only about 2 % of unidentified peak area which are minerals that are unclassified. [3] states that coal is made up of mineral and organic matter. The mineral matter contained in coal influences the type of ash and gaseous components to be produced when coal burns. For example, pyrite (FeS_2), which was one of the minerals found in the coal, would produce iron oxide (ash) and SiO_2 (gas).
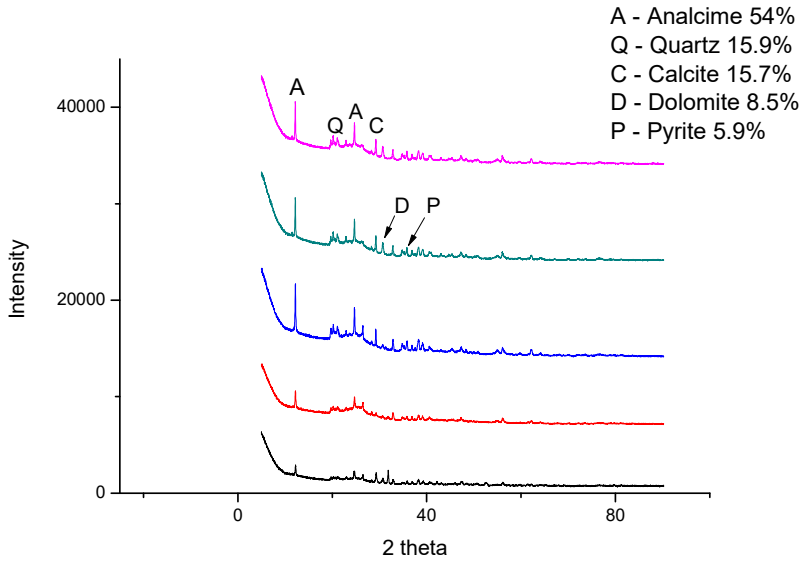
Figure 4. XRD analysis for Mabesekwa coal samples seams A – F from top to bottom.
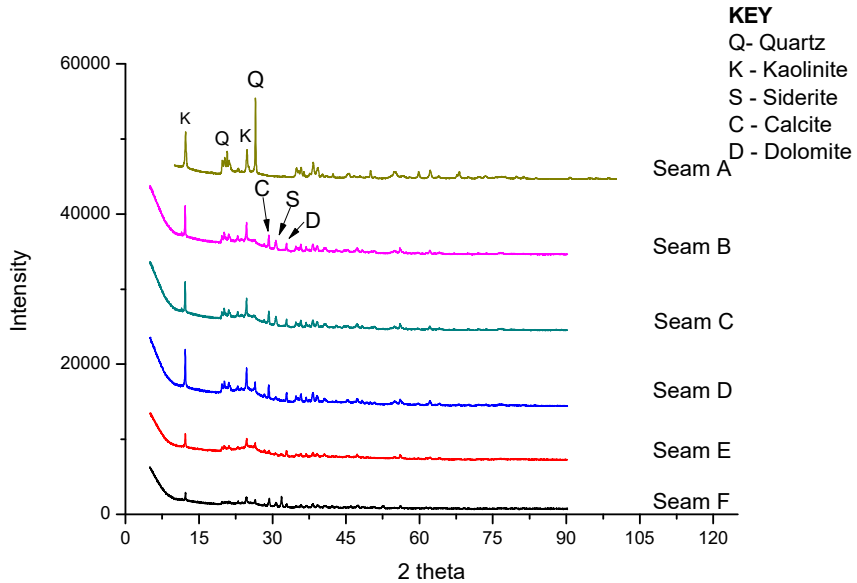
Figure 5. XRD analysis showing an estimate of crystallinity in Mmamabula coal samples, seams A – F from top to bottom.

That is why it is important to understand and quantify the mineral matter contained in coal. Mineral matter is thought of as a geochemical indicator.

XRD analyses crystalline materials which are materials with long range of order, amorphous content in samples cannot be identified but can be calculated from the data collected.

It is necessary to assess the beneficial and detrimental effects that the mineral matter (before and after processing) may have both on the process in which it is involved and on its ultimate disposal.

Ash indicates the incombustible inorganic material that remains after coal burns. It can include clay minerals such as carbonates and Sulphur compounds, and quartz. It is also viewed as an unwanted coal property that degrades coal value [2]. Sulphur content is at an average 1.99% in Botswana coal.

1.4   SEM

Figure 5 shows the SEM images of the 6 Minergy coal samples. SEM describes surface morphology by visual magnification of the surface. This SEM is equipped with energy dispersive x-ray spectrometers (EDX) that allow qualitative and quantitative chemical analysis. SEM images can provide valuable information such as particle size, swelling of the particles during conversion, and the structure of char/ash. The images are used to estimate particle size and porosity in samples.
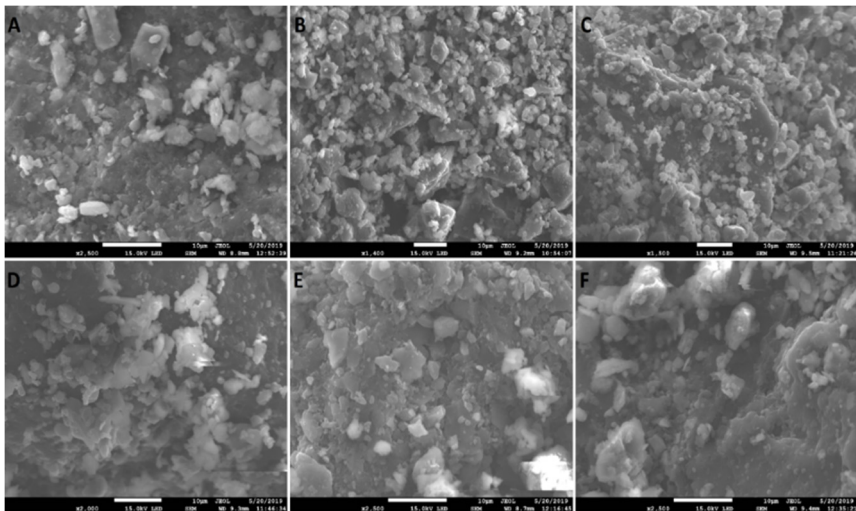

Figure 6. 2-D SEM images for porosity comparison of 6 Minergy coal samples.

SEM details topography, crystallography and composition of the material being investigated. A good knowledge of the morphology of coal is necessary in proposing suitable ways of cleaning coal.

Energy Dispersive X-ray (EDX) analysis produced elemental analysis of the seams. Table 4 shows the EDS results of Seam C at 12m to 13m. these results show dominant carbon in the sample followed by oxygen. These are other trace elements in the sample. Hydrogen is not present in the EDX spectrum because EDX is related to the K-shells which are not the valence shell[12]. H has only a K shell in covalent bonding and this is the only shared electron.

Table 3. EDS results of Seam A showing the elements contained

Element Line	Weight %	Atom %	Formula
C K	65.72	73.78	C
O K	27.50	23.18	O
Mg K	0.10	0.06	Mg
Al K	2.38	1.19	Al
Si K	2.46	1.18	Si
S K	0.53	0.22	S
K K	0.03	0.01	K
Ca K	0.77	0.26	Ca
Fe K	0.52	0.12	Fe

EDX is not reliable in characterizing the whole coal as it only analysis a certain point which cannot be taken as a representation of the whole coal sample. It shows that coal has trace elements including Titanium, Iron, Calcium and Potassium varying through the coals. EDX is used to observe compositional analysis of coal, elements contained are determined by x-ray peak intensity.

CONCLUSIONS

Botswana coal is Lignite grade A. Clay minerals; kaolinite, dolomite, siderite and calcite, and quartz were discovered. The depth of coal has no relevance in the degree of coalification. Preconcentrating coal with density of 1.75 enriched it to 37% more purity.

According to Lignite Energy Council in the US, 13.5% of lignite is used in the production of synthetic natural gas while 7.5% is used in ammonia-based fertilizers. Low rank coals are preferable for application in gasification process as they produce better syngas yield compared to caking high rank bituminous coals.

Characterization is an initial stage in the plan to carry out gasification of Botswana coal. These results will enable the prediction in the design of a gasifier being able to predict the yield from the process and ash content.

Seams B to F are highly recommended for gasification process with higher contents of fixed carbon and Hydrogen which will yield high quality synthetic gas.

EXPERIMENTAL

Sample Selection

Coal is heterogenous in nature and given this complexity is it necessary to select a representative sample of the main sample.

To ensure a representative sample is collected, correct sampling procedures were followed and certain rules adhered to. The main sample was thoroughly mixed; seams are layers of these composites; they vary depending on how much was buried at that time.

Figure 7. Botswana coal fields map indicating two coal fields for this study: Mabesekwa (North) and Mmamabula west (South) [3]

Sample preparation

Samples were collected from two different coal fields (Mabesekwa & Mmamabula, shown in Figure 1) with each having a set of six samples termed as coal seams A to F. A total of 12 samples were further sampled to get a representative sample enough to be ground to 45 – 100 μm size fractions in a ball mill pulverisette after drying in an oven. Either than grinding, the pulverisette allowed for proper mixing and homogenizing of coal sample. The top most seam was at least 10 m below the ground for both coal fields.

Coal characterization

Proximate and ultimate analysis

A thermogravimetric analyzer Lego TGA701 was used for proximate analysis to determine moisture, ash, volatile matter, and fixed carbon contents of Botswana coal. About 1 g of each sample was loaded into a crucible in a thermogravimetric analyzer. The six coals were then subjected to devolatilization and combustion at temperature of 105 °C, for moisture content analysis temperature rose to 950 °C for volatiles and 750 °C for ash. Fixed carbon was calculated using differences in percentages.

Ultimate analysis was performed under standard laboratory conditions with Bureau Veritas South Africa.

XRD Analysis

The pulverized coal was further crushed using a laboratory porcelain mortar to further increase the surface area. A smaller holder was filled up with the sample ensuring a smooth surface which was put into the XRD for analysis. XRD data were obtained from a Bruker D8 Advance powder diffractometer with a 3.0 kW generator, a Copper (Cu) tube X-ray source, and a LynxEye XE energy-dispersive strip detector. The radiation used is a Copper K alpha with a wavelength of 1.54056. The machine was run at 40V and 40mA for 20 minutes for one sample. The sample data was collected from the angles 10 to 70 an increase of 0.029 degrees per step for a total time of about 20 minutes.

FT-IR measurements

An FT-IR spectrometer of model Vertex 70x was used. The sample was placed on the sample stand on the equipment. The process ran with infrared light incident to coal sample such that some light was absorbed and some reflected. The information collected was interpreted by the computer which produced data. The range of wavelength specifically for coal was specified. The process was repeated three times for the 12 different samples.

SEM analysis

A JSM-7100F scanning electron microscope was used. The pulverized samples were placed on 6 different specimen mounts with carbon coating before being placed in the sample holder.

Nomenclature

VM	volatile matter
GCV	gross calorific value
MC	moisture content
FC	fixed carbon
TGA	thermogravimetric analyzer

ACKNOWLEDGEMENTS

REFERENCES

1. R. Grynberg;*BIDPA*, **2012**, 1, 1-46.
2. M.R. Johnson; C.J. Van Vuuren; W.F. Hegenberger; R. Key; U. Shoko; *J. of Afr Earth Sci*., **1996**, *23*, 3-15.
3. R. Graeme; *Extr Ind Soc*., **2015**, *2*, 827-839.
4. L. Lu; V. Sahajwalla; C. Kong; D. Harris; *Carbon*., **2001**, *39*, 1821-1833.
5. H. Morita; F. Yoshiba; N. Woudstra; K. Hemmes; H. Spliethoff; *J. Power Sources*., **2004**, *138*, 31-40.
6. R.M. Flores; Coalification, Gasification, and Gas Storage. In Coal and coalbed gas: fueling the future, 1st Ed.; Elsevier, Oxford, UK, 2014; 167–233.
7. D.A. Bell; B.F. Towler; M. Fan;. The nature of coal. In Coal gasification and its applications, 1st Ed.; William Andrew Publishing, 2010; 1-15.
8. J.A. Mikhlin; Approach to direct liquefaction of high ash low rank coals. In Energy Developments: New Forms, Renewables, Conservation, 1st Ed.; Fred A. Curtis; Pergamon, Regina, Canada,1984; 25–29.

9. S. Toshiyuki; L. Zhihong; T. Makoto; H. Koki;T. Hidehisa; *IHI Eng. Rev.*, **2012**, *45*, 15–20.

10. F.H. Selvig; W.A. Gibson;*Chem. coal Util.*, **1945**, *1*, 139.

11. A. Georgakopoulos; A. Iordanidis;V. Kapina; *Energy Sources*, **2003**, *25*, 995–1005.

12. N. Stojilovic; *J. Chem. Educ.*, **2012**, *89*, 1331–1332.

DETERMINATION AND ASSESSMENTS OF PHYSICO-CHEMICAL PARAMETERS OF THE WATER FROM ANTHROPO-SALINE LAKES LOCATED IN THE PROTECTED AREA "SALINA TURDA", ROMANIA

LILIANA RUS[a], SIMONA-ELENA AVRAM[a], VALER MICLE[a]

ABSTRACT. It was carried out the monitoring of the qualitative parameters for the "Ocnei" and "Rotund" lakes located in the protected area "Salina Turda", Romania, and as well it was made a comparative analysis of the results with previous determinations. It was determined the evolution of the physico-chemical parameters on 5 segments of depth. The monitoring was carried out within 2 measurement campaigns. It has been determined that the lakes tend to lose basicity and it was found that the heliotherm phenomenon represents a stable index in comparison with previous determinations.

Keywords: anthropo-saline lakes, water quality, physico-chemical parameters

INTRODUCTION

Saltwater is a natural resource useful for health, its therapeutic qualities being known from the 19th century, and its exploitation must be done in an appropriate way. Improving human's health and prophylactic action is the major objective of the therapeutic use of water with a high salinity content. Salty lakes are the basis of the spa activity.

As a result of the increased demands of the body, generated by the modern lifestyle, new aspects of morbidity appear, with the predominance of degenerative diseases, sequelae after trauma or accidents, diseases that have a debilitating potential picked up. In these cases, balneary medicine is not limited to medicinal treatment, widening the scope of therapeutic interventions by applying natural remodeling, here as well as the therapeutic action of salt lakes and baths in salted water.

[a] Technical University of Cluj-Napoca, Faculty of Materials and Environmental Engineering, 103-105 Muncii Bd., 400641 Cluj-Napoca, Romania
* Corresponding author lilianarus@mail.utcluj.ro

Saline aquatic systems are classified into two categories: thalassohaline (derived from sea water) or athalassohaline (i.e., of land origin) [1].

"Ocnei" and "Rotund" lakes are anthropo-saline and they have chlorinated-sodic mineral waters, with mineralization ranging between 19.27 mg/l and 225 mg/l. These lakes are sensitive to climate change through alterations, precipitation patterns and evaporation potential that may lead to dilution, further concentration, or even drying [2].

The therapeutic value of organic-rich sediments and the physico-chemical peculiarities of salt waters (e.g., heliothermy) represents one of the most important two characteristics of values, so that they contribute to their scientific valorization [3]. Stratification and currents in lakes are determined by the weather conditions [4].
Ocnei lake was formed by the collapse of an old salt mine around 1800 [3].

The high chlorine concentration in theses lakes is reflected in the salinity of the water, which is why the lake is very pleasant during the hot season for salt baths for therapeutic purposes [5].

Sodium chloride (NaCl), which is a thermophile molecule has an impact on the salinity of the warm layer by increasing it during the day [6].

Where salt lakes occur, they represent the dominant aquatic resource and they also are the critical components of the natural environment. What makes them important research model systems in microbial niche differentiation and biogeochemical cycling is their physical stability coupled with vertical water column partitioning [7].

The purpose of this paper is to determine the water quality status of the salty lakes located in the protected area "Salina Turda" after 7 years from opening.

There have been 2 measurement campaigns for the physico-chemical parameters of the lakes water, on 5 segments of depth, in order to determine their quality status.

For the knowledge of the water quality of the lakes located in the protected area "Salina Turda", namely "Ocnei" and "Rotund" lakes, during the course of the research, were organized 2 measurement campaigns in order to determine the basic parameters.

The lakes are fed by rainfall and freshwater springs and the level of the water is maintained constant by an artificial drainage channel towards the sărata Valley [8]. They are located in Transylvania which is an area with residual relief and diapiric areas [9]. This perimeter is on the western border of the Transylvanian basin, in a diapiric zone that appears in the form of salt masses [10].

"Ocnei" lake is one of the most important and representative lacustrine units of the existing nine lakes in Turda area (Cluj County), Romania, mainly because of its considerable depth (around 33 m) and volume (around 26,000 m^3 by 2001) [11]. The ionic composition of Ocnei Lake is similar to seawater [12].

Previous analyzes have shown that the limit values of certain physico-chemical and microbiological parameters of lakes water are exceeded. This is due to the exploitation of lakes in an unorganized setting [13].

In order to establishing the measurement periods, it was considered the behavior of the two lakes under different natural condition. For comparisons there are the results of the studies carried out in previous years.

RESULTS AND DISCUSSION

Experimental research on "Rotund" lake

The experimental research was developed between 2 measurements campaigns.

Following the analyzes carried out on April 14th, 2016 (first campaign), on the "Rotund" lake, were found the following:

The climatological data identified: 33.1% atmospheric humidity; 26.5 °C air temperature; 3.8 ÷ 5.6 m/s air currents; 26 °C air temperature at the level of the water; 37% water humidity at the level of the water; clear sky.

Since the equipment is dedicated for measuring at different depths, on the sensor immersion cable, were made 5 signs corresponding to each depth of measurement.

The lake water has a neutral character with a pH value of 8.14 at a depth of - 0.3 meters and 6.43 at a depth of - 4 meters, therefore the variation of the parameter is within the neutrality range of water.

The water conductivity exceeds 200 mS/cm at a depth of - 4 meters and on other deep segments it increases slightly.

The water temperature on the water mirror is 21.73 °C, having an increase up to a depth of - 2 meters followed by a slight decrease up to a depth of - 4 meters where was recorded 18.71 °C.

The salinity of the lake exceeds 70 units of PSU in all segments of depth.

The total solids dissolved (TDS) into the water of the lake increases with the depth, so at the level of the water mirror was identified the amount of 61.29 g/l and at the depth of - 4 meters it was identified 116 g/l dissolved solids.

From the results of the analyzes carried out on 11 August 2005 by the specialists of the S.C. Salina Turda S.A., it was found a basic pH with a limit value of 8.5 [14]. The analyzes resulted from the pH monitoring during April 2016 are confirmed in the literature by S.C. Salina Turda S.A. in August 2005, and in both cases, it was found that the pH is slightly basic, having the tendency to decrease the basicity, which requires a constant monitoring of this indicator.

Following the analyzes carried out on June 08th, 2016 (second campaign), on the "Rotund" lake, were found the following:

The lake water is slightly basic with a pH value of 8.79 at a depth of - 0.2 meters and 6.78 with a neutral character at a depth of - 4 meters, therefore the variation of the parameter lies in the field of water neutrality; water conductivity exceeds 200 mS/cm at a depth of - 4 meters and on other deep segments it increases slightly.

The water temperature at a depth of - 0.2 meters is 25.39 °C with a first increase up to a depth of - 1 meter followed by a slight decrease up to a depth of - 3 meters, where was recorded 29.07 °C and at - 4 meters was determined a temperature of 22.84 °C.

The salinity of the lake exceeds 70 units of PSU (Maximum Sensor Limit) on most deep segments, except for the water mirror level where was recorded 44.11 units of PSU.

The total dissolved solids (TDS) in the lake water are growing with the increasing of the depth, so it was found 32.99 g/l at the water mirror level and at a depth of - 4 meters a quantity of 117.76 g/l solids dissolved.

The pH determined, in the second measurement campaign had a higher value, across all the segments of depth, than the value determined in the first measurement campaign.

At S.C. Salina Turda S.A., it was found the results of the analyzes carried out during the period of August 2005, prior to the touristic arrangement of the lakes. At that time, water was neutral at the upper permissible limit (pH = 8.5).

As a result of the analyzes in the second campaign it was found that the water has a slightly basic character (pH = 8.79).

Considering the tendency to decrease basicity, is required to monitor the pH of the lake once a year, possibly, in the same period.

Table 1. The evolution of the physico-chemical parameters on depth for the "Rotund" lake

Depth (m)	pH		Temperature (°C)		TDS (mg/l)		Conductivity (mS/cm^A)	
	First campaign	Second campaign	First campaign	Second campaign	First campaign	Second campaign	First campaign	Second campaign
-0.2		8.79		25.39		32.99		72.18
-0.3	8.14	8.31	28.29	38.36	61.29	58.24	130.44	145.62
-1	8.07	8.26	28.57	39.17	63.5	61.1	135.25	151.02
-2	8.07	8.34	25.71	35.76	65	65.68	131.94	158.4
-3	7.62	7.58	22.1	29.07	84.08	91.19	158.83	196.65
-4	6.43	6.78	18.71	22.84	116	117.76	204.45	226.46

In 2016, in terms of thermal regime for the first campaign, it was recorded the temperature of, approximately 28 °C at the level of the water mirror (- 0.3 meters) with a slight increase of 0.3 °C up to a depth of - 1 meter. It was noticed that the temperature is dropping up to 22 °C at a depth of - 3 meters and 18 °C at a depth of - 4 meters.

In the second research determination, it was recorded the temperature of 25.39 °C at the water mirror level (- 0.2 meters) with a significant increase up to a depth of – 0.3 meters where the temperature was 38.36 °C. As for the depth of - 1 meter, the temperature recorded a slight increase up to 39.17 °C. On the other segments of depth, the temperature is in a slight decrease, at a depth of - 3 meters, recording 29.07 °C and at a depth of - 4 meters, the temperature dropped sharply up to 22.84 °C.

The water conductivity of the lake has an increasing value starting with the first segment of depth studied.

For the first campaign, it was recorded a value of 130.44 mS/cm^A at the water mirror level, followed by a steady increase up to the level of the last segment of depth where the conductivity exceeded the value of 200 mS/cm^A.

In the second campaign it was recorded a value of 72.18 mS/cm^A at the water mirror level, followed by a steady increase up to the last segment of depth where the conductivity was 226.46 mS/cm^A.

The total of solids dissolved in the water of the "Rotund" lake increase with the increasing of the depth. From the measurements made in April, 14th, at the water mirror level was determined a value of 61.29 mg/l TDS and at a depth of - 4 meters 116 mg/l TDS. In June, 08th, it was found at the water mirror level a value of 32.99 mg/l TDS and at the depth of - 4 m 117.76 mg/l TDS.

The salinity determined in the water of the "Rotund" lake exceeds 70 units of PSU.

Analyzing the results obtained, it was observed that with the increasing of the depth, the conductivity of the water also increases.

The amount of dissolved oxygen is maintained constant (0 mg/l) throughout the depth due to a long period of stagnation of the lake because of the interruption of the spa activity due to the unfavorable climatic conditions for bathing.

The results are compared with the analyzes conducted during the warm season of the year, namely August 2005, where was recorded a value of 9.21 mg/l dissolved oxygen [14]. The value of dissolved oxygen is directly influenced by the water disorder due by the balnear treatment.

Experimental research on "Ocnei" lake

In order to determine the values of the quality parameters of the "Ocnei" lake, a number of 17 sampling points have been established as a result of its sketching.

By following the analyzes carried out on April 14th, 2016 (first campaign), on "Ocnei" lake, it was found:

The climatological data identified: 42% atmospheric humidity; 24.2 °C air temperature; 0.7 ÷ 3.1 m/s air currents; 23.8 ° C air temperature at the water level; 46% water humidity at the water level; clear sky.

The lake water has a neutral character with a pH value of 8.38 at a depth of - 0.3 meters and 6.45 at a depth of - 4 meters, therefore the variation of the parameter is in the neutral range of water.

The water conductivity exceeds 200 mS/cm at a depth of - 4 m and on other deep segments it slightly increases.

The water temperature on the mirror is 21.73 °C, having an increase up to a depth of - 2 meters followed by a slight decrease up to a depth of - 4 m where the temperature recorded was 25.14 °C.

The salinity of the lake exceeds 70 units of PSU in all segments of depth.

The total dissolved solids (TDS) in the water of the lake grow with the increasing of the depth, so at the water mirror level it was found 61.29 g/l TDS and at a depth of - 4 m it was recorded 116.51 g/l TDS.

The second determination was carried out in June 08th, 2016 (second campaign), for the "Ocnei" lake and it was observed the following issues:

The lake water has a neutral character with a pH value of 8.63 at a depth of - 0.2 meters and 6.56 at a depth of - 4 meters, therefore the variation of the parameter is in the neutral range of water.

The water conductivity exceeds 200 mS/cm at a depth of - 4 meters and on other deep segments the conductivity increases.

The water temperature, at a depth of - 0.2 meters, was 22.66 °C, having a first increase up to – 1 meter, followed by a slight decrease up to - 3 meters, where was recorded a temperature of 33 - 34 °C. At a depth of - 4 meters it was recorded 30.95 °C.

The salinity of the lake exceeds 70 units of PSU in most deep segments, except for the water mirror level where was recorded 62.29 units of PSU.

The total dissolved solids (TDS) in the water of the lake increases with the depth, so at the water mirror level was identified a quantity of 61.29 g/l TDS and at a depth of - 4 meters 118.72 g/l TDS.

By following the analyzes performed on April 14th, on "Ocnei" lake, it was found a basic pH between 8.38 in the water mirror level and a near neutral pH with a value of 6.45 at a depth of - 4 meters. For the second campaign it was determined a basic pH with a value of 8.63 on the water mirror and a neutral pH with a value of 6.56 at a depth of - 4 meters.

From the results of the analyzes carried out on 11.08.2005, by the specialists of the S.C. Salina Turda S.A,. it was found a pH of 8.8 [14].

Table 2. The evolution of the physico-chemical parameters on depth for the "Ocnei" lake

Depth (m)	pH		Temperature (°C)		TDS (mg/l)		Conductivity (mS/cm^A)	
	First campaign	Second campaign	First campaign	Second campaign	First campaign	Second campaign	First campaign	Second campaign
-0.2		8.63		22.66		61.29		85.8
-0.3	8.38	8.39	21.73	33.48	61.29	54.26	94.62	124
-1	8.16	8.25	26.03	35.49	64.96	64.3	132.36	132.36
-2	8.15	8.23	26.06	33.2	65.32	64.39	133.26	148.85
-3	7.28	7.3	25.59	33.93	99.04	105.7	199.65	246.72
-4	6.45	6.56	25.14	30.95	116.51	118.72	233.41	264.1

The analyzes resulted from the pH monitoring during April 2016 are confirmed in the literature by S.C. Salina Turda S.A. carried out in August 2005, and in both cases it was found that the pH is slightly basic, having the tendency to decrease the basicity of the lake.

In the first campaign, in terms of thermal regime, the temperature of 21.73 °C was found at the water mirror level, with a significant increase up to a depth of - 2 meters where was recorded a temperature of 26.06 °C. In June, 2016, it was recorded 22.66 °C at the water mirror level, at a depth of – 0.2 meters, with a significant increase up to a depth of – 0.3 meters where the temperature determined was 33.48 °C. As for the depth of - 1 meter, in the second campaign, the temperature was slightly increased up to 35.49 °C. As far as the temperatures on the other segments of depth are concerned, they are in a slight decrease, at a depth of - 4 meters being recorded 30.95 °C. For the depth of - 3 and - 4 meters, the temperature recorded a slight decrease up to 25.59 °C at a depth of - 3 meters and 25.14 °C at a depth of - 4 meters.

The salinity determined in the water of Lake "Ocnei" exceeds 70 units of PSU.

The water conductivity has an increasing process starting with the first segment of depth up to the las one.

The conductivity of the lake, determined on April 14th, 2016, recorded a value of 94.62 mS/cm^A at the water mirror level, followed by a steady increase up to the last segment of depth, where the conductivity exceeded 200 mS/cm^A. On the other hand, on June 08th, 2016, has an increasing value starting with the first depth segment studied. A value of 85.8 mS/cm^A was recorded at the water mirror level, followed by a steady rise up to a depth of - 2 meters, where was recorded a slight decrease in conductivity.

The total dissolved solids in the water of the "Ocnei" lake increases with the increasing of the depth.

From the measurements developed in April 2016 at the level of the water mirror was determined 55.53 mg/l and at a depth of - 4 meters was recorded a value of 116.51 mg/l.

In June, 2016, the total dissolved solids in the water of "Ocnei" lake grow with the increasing of the depth, so the measurements made at the water mirror level determined a value of 43.93 mg/l and at the depth of - 4 m was recorded the value of 118.72 mg/l.

The amount of dissolved oxygen in April 2016 is maintained constant, 0 mg/l, throughout the depth of the water due to a long period of stagnation of the lake because the spa activity was interrupted due to the unfavorable climatic conditions for bathing. Compared with the results of the analysis performed during the warm season of the year, namely August 2005, where a dissolved oxygen value of 11.22 mg/l was recorded [14]. This value being directly influenced by the water disorder followed by the balnear treatment.

CONCLUSIONS

The pH determined in the two measurement campaigns was lower compared to the measurements made in 2005, but is in the neutral pH range (6.5 ÷ 8.5). From these determinations it was found that lakes tend to lose basicity.

There is a high influence on the temperature of the water caused by the climatic conditions. The temperature of the lakes is steadily increasing up to the half of the depth of the study, following a gradual decrease with the increasing of the depth.

This temperature variation is observed in both measurement campaigns. Temperature is strictly influenced by the weather conditions and the heliotherm phenomenon. In the second campaign, the temperature of the water mirror level was lower compared to the one determined in the first campaign, due to a rainy period. Measurements made in 2005 do not influence the findings of the 2016 analysis, climatic issues being variable.

Conductivity of the lake increases progressively with increasing of the depth in both measurement campaigns.

The water salinity exceeds the detection limit of the sensor. The determination of the parameter value was achieved only at the level of the water mirror, at the depth of - 0.2 meters.

EXPERIMENTAL SECTION

In order to carry out physico-chemical analyzes of the water lakes from the "Salina Turda" area, the water samples were taken from different depths, namely: from the level of the water mirror (- 0.3 meters), -1 meter, - 2 meters, - 3 meters and as well as - 4 meters.

Figure 1. Location of the salt lakes from the protected area "Salina Turda"

This environment is called meromictic because the water is stratified and the water column is clearly divided into distinct water masses that mix slowly or do not intermix at all [15].

The measurement campaign took place in April 2016 (the first measurement campaign), as well as in June 2016 (the second measurement campaign). The second measurement campaign was based on the results obtained from the first analysis campaign.

To determine the quality parameters of the lakes, the following are set:
• the maximum depth of analysis is - 4 meters, depth at which changes may occur from bathing pads;
• depth sampling - 0.3 meters, - 1 meter, - 2 meters, - 3 meters, - 4 meters;
• collecting samples on the lake water mirror.

General Work Steps:
- the sketch of the analysis lake;
- making the grid for establishing the sampling points;
- preparation of registration forms;
  - instrument calibration and ground preparation for sampling;
  - analysis of microclimate parameters (air temperature, atmospheric humidity, wind speed and water temperature);
- boat movement at the originally set points and in-situ depth analysis;
- registration of values;
- the interpretation of the results.

For the "Rotund" lake, the first research was accomplished in April, 14th, 2016, and the second one in June, 08th, same year. In the first measurement campaign, a number of 9 cropping points per diameter were chosen depending on the surface of the lake (figure 2).
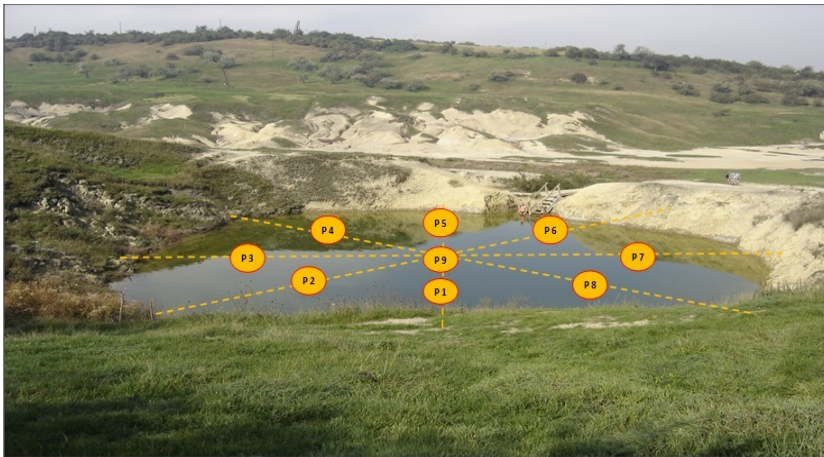
Figure 2. Distribution of the sampling points for "Rotund" lake

At each point, 5 samples were collected on depths of - 0.2 meters, - 0.3 meters, - 1 meter, - 2 meters, - 3 meters and - 4 meters. In the vicinity of the banks, where the depth of the lake is smaller, the measurement took place at the bottom of the lake.

As for the "Ocnei" lake, a number of 17 picking points per diameter were chosen depending on the surface of the lake (figure 3). The research was carried out at the same depths as for the "Rotund" lake.
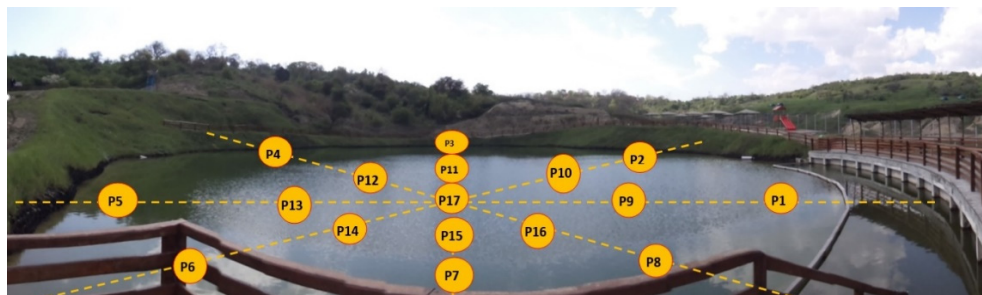
Figure 3. Distribution of the sampling points for "Ocnei" lake

From the physical point of view, samples were taken and analyzed to determine the following properties: pH, turbidity, conductivity, resistivity, sea water density, temperature and TDS, and from the chemical point of view samples were also taken and analyzed in order to determine the chemical properties characteristic of the lakes studied, namely: dissolved oxygen and salinity.

These analyzes were performed using the Hanna HI 9829 multiparameter instrument with which determinations were performed on site.

Research on the distribution of physico-chemical water quality parameters in the two lakes took place in April and June, 2016, when measurements were made using the Hanna HI 9829 multi-parameter instrument on 5 deep segments.

Hanna HI 9829 is a multi-parameter instrument which monitors 14 essential water quality parameters (7 measured and 7 calculated). The device is portable and is equipped with a multi-sensor probe that makes possible the measurement of the following parameters: pH, ORP, turbidity, dissolved oxygen, conductivity, chlorine, nitrate, ammonia and temperature. The Hanna turbidity sensor conforms to ISO 7027.

In order to determine the microclimate parameters (on-site determinations) during the deployment of the measurement campaigns, it was used the Almemo 2390-5 multifunctional instrument.

The *Almemo 2390-5* multifunctional measuring instrument is a device for measuring microclimate parameters.

This instrument comprises 3 detection sensors:
- Sensor for measuring the light intensity;
- Air speed sensor;
- Humidity and temperature sensor.

ACKNOWLEDGEMENTS

REFERENCES

1. Hammer UT, *Saline lake ecosystems of the world,* Kluwer Academic, Dordrecht, **1986**;
2. John M. Zacharaa, James J. Morana, Charles T. Rescha, Stephen R. Lindemanna, Andrew R. Felmyab, Mark E. Bowdena, Alexandra B. Corya, James K. Fredricksona, *GCA*, **2016,** *181*, pp. 144-163;
3. Romanescu G., *Sciendo*, PESD, **2019**, *3*, no. 1;
4. Boehrer B., Schultze M., *Rev Geophys*, **2008**, *46*, 2006RG000210;
5. Mera O., Ştefănie T., Vişinescu V., *Cetatea din muntele de sare*, Turda, România, **2010**, pp. 65;
6. Sonnenfeld P., Hudec P.P., *Dev Sed*, **1980**, *28*, pp. 93-100;
7. Andrei Adrian-Ştefan, Robeson Michael S, Baricz Andreea, Coman Cristian, Muntean Vasile, Ionescu Artur, Etiope Giuseppe, Alexe Mircea, Sicora Cosmin Ionel, Podar Mircea , Banciu Horia Leonard, *ISME J.*, **2015**, *9*, pp. 2642–2656;
8. Mircea Alexe, Gheorghe Şerban, Andreea Baricz, Adrian-Ştefan Andrei, Adorján Cristea, Karina P. Battes, Mirela Cîmpean, Laura Momeu, Vasile Muntean, A. Porav, Horia I. Banciu, *J. Limnol.,* **2018**, *77(1)*, pp. 17-34;
9. Alexe M, Şerban G, *Proceedings of the 14th Geoconference on Water resources, Forest, Marine and ocean ecosystems*, Albena, Bulgaria **2014**, *2*, pp. 793-800;
10. Alexe M., *Studiul lacurilor sărate din Depresiunea Transilvaniei*, Ed. Presa Universitară Clujeană, Cluj Napoca, Romania, **2010**;
11. Alexe M., Furtună P., *Water resources and wetlands*, Tulcea, Romania, **2012**, pp. 244–247;
12. Baricz Andreea, Coman C., Andrei A.Ş., Muntean V., Keresztes Z.G., Păuşan Manuela, Alexe M., Banciu H.L., Extremophiles, **2014**, *18*, pp. 399–413;
13. Mera O., Bican-Brişan N., Petrescu I., Varga I., Bunea L., *Environ, Prog.*, **2007***, 11*, pp. 291-300;
14. Bercea A., Bunea A*., Buletine de analiza fizico-chimica si bacteriologica a apei din lacurile Durgau- Lacul Rotund, Subteran -Mina Terezia, Durgau- Lacul Ocnei. Eliberat de RATAC Turda*, data **11.08.2005**;
15. Bayly I, Williams WD, *Inland waters and their ecology*, Longman Australia, Melbourne, **1973,** pp. 483-484.